Fall 2013

An Experimental Investigation of Wind Turbine Aerodynamic Interaction

Brandon Lee Ennis
Purdue University

Graduate School ETD Form 9
(Revised 12/07)

PURDUE UNIVERSITY
GRADUATE SCHOOL
Thesis/Dissertation Acceptance

This is to certify that the thesis/dissertation prepared

By Brandon Lee Ennis

Entitled
An Experimental Investigation of Wind Turbine Aerodynamic Interaction

For the degree of Doctor of Philosophy

Is approved by the final examining committee:

Prof. Sandy Fleeter
Chair

Prof. Doug Adams

Prof. Jun Chen

Prof. Karen Marais

To the best of my knowledge and as understood by the student in the *Research Integrity and Copyright Disclaimer (Graduate School Form 20)*, this thesis/dissertation adheres to the provisions of Purdue University's "Policy on Integrity in Research" and the use of copyrighted material.

Approved by Major Professor(s): Prof. Sandy Fleeter

Approved by: David Anderson 11/26/2013
Head of the Graduate Program Date

AN EXPERIMENTAL INVESTIGATION OF WIND TURBINE AERODYNAMIC INTERACTION

A Dissertation

Submitted to the Faculty

of

Purdue University

by

Brandon Lee Ennis

In Partial Fulfillment of the

Requirements for the Degree

of

Doctor of Philosophy

December 2013

Purdue University

West Lafayette, Indiana

"I can do all things through Jesus Christ, who gives me strength." Philippians 4:13

Thank you Lord for your love displayed through faithfulness to me both in times of great abundance and times of great need. With your help, may I be faithful to you and only love you more for the rest of my days.

ACKNOWLEDGEMENTS

The highest thanks and praise and all glory goes to the Lord and my Savior, Jesus Christ, for this work. It is by his grace and strength that I was able to accomplish this work and it is his divine plan which has led me here and has seen me through this program.

I also want to sincerely thank Prof. Sandy Fleeter. Prof. Fleeter has such great understanding and insight into choosing novel research projects which provide needed and significant results. I have enjoyed my six years as his graduate student and the opportunities to learn from him in the classroom, to learn from him about research, and to simply learn about him through the many conversations. Without Prof. Fleeter's guidance and willingness and trust to put me on big projects I would not be where I am or the researcher I am today. Prof. Fleeter is one of the Great's of Purdue, and I am truly privileged to have worked under his guidance. Thank you for always supporting me financially and emotionally. I hope that I have honored you with this work.

I would be remiss to not also express my deep gratitude to Ronnie McGuire, the most talented and caring machinist that has ever worked at Purdue. Ronnie has gone above and beyond what I could ever think to ask of him. He has come in on Saturday's to work with me outside in the cold, he has worked early hours and late hours, and he always makes great parts. Ronnie's friendship and his generous heart and all the conversations we've shared will always stand out to me when I think back on my time at Purdue. Thank you for your seemingly endless experience and for your willingness to always help, I literally couldn't have completed this dissertation without you.

Finally, to my family, friends, roommates and brothers and sisters in Christ; you have held me up when I have been weak, you have given me joy when I have felt sorrow, and you have prayed for me without ceasing. I owe this accomplishment, in part, to you also. Thank you for your love and encouragement, and for making life so much better.

TABLE OF CONTENTS

Page

Page

LIST OF TABLES

Table Page

LIST OF FIGURES

Figure Page

Figure Page

ABSTRACT

Ennis, Brandon L. Ph.D., Purdue University, December 2013. An Experimental Investigation of Wind Turbine Aerodynamic Interaction. Major Professor: Dr. Sanford Fleeter, School of Mechanical Engineering.

Wind turbine installed capacity in the United States has seen an exponential growth over the last decade and mostly coming in the form of large wind farm installations. The wind farms themselves too have been increasing in size, incorporating more wind turbines in larger areas than ever before.

Wind turbines have become a viable component in the overall energy makeup of the United States due to improved economics where energy prices have risen and production costs dropped. For a fixed cost, the effectiveness of a wind turbine financially is highly related to its performance. Considering the size of current wind farms, a minor performance improvement will result in large additional sums of revenue. A problem that has received attention with wind farms is that while the fixed costs of the development do get spread out further to reduce the installed cost of each wind turbine, the wind turbines have been observed to perform at lower performance values in the wind farm setting.

Development work is performed to predict maximum theoretical levels of performance describing a wind turbine. This work is extended to include predictions of the limiting power for a two-rotor, counter-rotating wind turbine configuration. Wind farm performance losses are also modeled for the dominant modes of interaction when operating a wind turbine within the wake of upstream machines; covering single-, multiple-, and lateral-wake scenarios.

A year's worth of wind speed data are analyzed to reveal seasonal trends of the wind turbine input condition. Wind turbine performance is simulated using this data and compared amongst small and large wind turbines.

Predictions of wind farm wake models are compared to data generated using the Purdue University Micro Reconfigurable Wind Farm facility. This facility contains four small wind turbines in an in-field experimental setting where wake scenarios are created and performance comparisons measured. Model validation is obtained using the experimental results which provides insight into the model's assumptions' range of effectiveness, and resultant predicted wake behavior. The physical mechanisms of wake operation power losses are also observed from the data showing the relative contribution of the wake loss constituents in different wind farm configurations.

CHAPTER 1: INTRODUCTION

1.1 Problem Background

Wind turbines have become a significant component in the overall energy makeup in the United States. Between 1999 and 2012 total installed capacity of wind turbines in the U.S. alone has grown from 2.5 to 60 GW. This tremendous growth is indicative of market variables aligning with the product capabilities.

A noted problem with wind turbines in the wind farm setting is efficiency losses due to the passage of upstream wind turbine wake vortex structures impinging upon downstream wind turbines. This effect has been seen to result in 10-20% losses in the total farm predicted power for large wind farms [1]. There is a need for better understanding of Windfarm Aerodynamic Interaction/Wake Dissipation Testing.

A variable that limits the performance of wind turbines regardless of the turbine efficiency or farm losses is simply the wind input variability. This factor can be controlled to a degree by appropriate siting of the wind turbine but the variability is an inherent quality of the atmosphere. To support making accurate performance predictions for a wind turbine the wind statistics need to be understood and accounted for. These predictions can be made by first performing a Study of the Statistical Analysis of Wind Data.

1.2 Problem Description

Windfarm Aerodynamic Interaction/Wake Dissipation Testing

Experimental and analytical studies point to significant energy losses in wind farm arrays spaced less than seven turbine diameters apart [2]. Guidelines for wind turbine spacing in a wind farm due to wake effects have been introduced as a result of these losses.

In the wakes of upstream wind turbines the turbulence levels may increase sufficiently to cause measurable damage from fatigue and dynamic loads. Lift-type turbines develop less intense wakes than drag-type turbines, but the single rotor turbine introduces a turbulent, highly viscous, swirl component of velocity in the flow that both degrades the performance of downstream turbines and adds to their loads [3].

It has been experimentally observed from several turbines in a line that the interaction produces a significant decrease in the power of the second turbine, with practically no further loss in successive machines [3]. Equally, there is an increase in turbulence intensity which has been found to reach an equilibrium value after 3 to 4 rows of turbines [4]. The equivalent loads under these single- and multiple-wake conditions are also very similar [5]. These findings have implications which mean the wakes of upstream wind turbines also need to be considered for small wind farms. The reduced power and increased loads of every turbine downstream of another makes this an important phenomena to better understand and quantify.

1.3 Technical Literature

Counter-Rotating Wind Turbine High Efficiency Design Modeling

Significant research has been performed to study counter-rotating propeller (CRP) systems arising from the aeronautics industry. This research, which peaked interest in the late 1980’s and 1990’s, was performed because of the predictively known improvement in efficiency of the CRP over single-rotor propeller (SRP) systems. Predictions and early experiments reveal an 8-16% increase in efficiency over SRP systems [6], derived primarily from the recovery of axial momentum imposed on the flow by the first rotor considered part of the SRP loss mechanism. The research for CRP systems eventually faded out as noise concerns were greater than fuel concerns, and efficiency, at the time.

Explanation of Agrawal's CRWT design

Agrawal performed a design and analysis for a low-TSR counter-rotating wind turbine [7]. The work first involved an optimization of the Froude-Momentum theory (Actuator Disk Theory) with two disk planes representing the two rotor planes in the counter-rotating configuration. This theory guided the design of the rotor disk areas and resulted in a forward rotor with an airfoil over only the outer 25% of the blade as the optimum design. Blade Element theory was applied to construct the optimum blade pitch and chord length as functions of the radius for both rotors. Design parameters were chosen with the optimum TSR set to 2.86, and having a rated wind speed of 24.6 mph. The airfoil selected for this low speed turbine was the NREL S-833, with optimum angle of attack of 5.4°. The turbine performance was calculated using a Prandtl tip loss factor to account for three-dimensional effects and a commercial computational fluid dynamics program was used to determine the swirl input to the second rotor. The maximum power coefficient after taking losses into account was determined to be 65% for this turbine.

Explanation of Interaction

CRP systems operate in unsteady flow fields due to the interaction between the two rotors and any holding struts/towers. This interaction arises from the potential field pressure gradients and viscous wakes impinging on downstream flow objects and from potential fields impinging on upstream flow objects. These are primarily 2D effects that depend on object geometry, rotational speed, incoming freestream wind speed, and object spacing up/downstream. There are also 3D effects which arise from blade tip losses present for both rotors and a resulting horseshoe vortex structure which impinges on the back rotor. Denner documents the analysis of calculating the velocity triangles and CRP performance and loading due to these interference effects [8]. There are induced velocity components caused by the propeller on itself and on a blade segment caused by the other propeller that are superimposed over the axial and tangential velocity components.

The flowfield interaction mechanisms for a CRP arise from the bound potential field of the other propeller, viscous wakes from the front propeller on the back, and tip vortices of the front propeller blades. The bound potential is described to strongly depend on the distance between the two propellers, and tip vortices mainly influence only the outer radial positions of the rear propeller. In the experiment of Lolgen and Neuwerth [9], thermal anemometry was used to measure the circumferential velocity component between the two propellers. It was found that the wakes cause sharp, high peaks whereas potential fields cause a smoother, lower amplitude sinusoidal in the measured circumferential velocity. By testing at different radial locations they also found that at 80% of the front propeller radius tip effects can be neglected, at 93% the induced velocity is dominated by tip vortices (with a nearly 500% fluctuation over the steady value) and that the tip vortex core passes through the rear plane at 96% of the front rotor radius.

Chung performed tests to quantify the flow interaction of a CRP system using thermal anemometry to measure 1-D axial velocity fluctuations and 3-D interference effects [10] [11].

The initial study presents a method [10] for measuring decay and spreading of the forward blade wakes and the upstream propagation of the rear blade disturbances using thermal anemometry for a 3x4 (3 blades in the forward rotor and 4 in the rear) CRP configuration. The influence the rotors have on each other is the cause of the interaction mechanism which alters the performance from the mean values and introduces a new source of sound generation.

The results from measuring the axial flow velocity between the two rotors show a large peak velocity associated with the potential field of the forward blade. This peak can be reduced by the disturbance from the rear blades as a function of the relative phase angle between them. The addition of the rear rotor to the CRP configuration yields increased mean peak velocities and a much more complicated time history over the SRP performance. The forward rotor viscous wakes diffuse and separate from each other radially with distance downstream from forward rotor, while the rear disturbance remains at a nearly constant angular position due to its propagation speed near the speed of sound.

As the rear blade passes through the forward blade potential flow it causes a slight reduction in the average axial velocity. This is an asymmetrical effect that is more pronounced as the measurement section moves axially closer to the rear rotor. When the rear blade, hence the disturbance, is offset from the forward blade potential wake by half of the rear rotor blade spacing, 45 degrees, there is little influence. At less than 12 degrees the peak velocity begins to degrade quickly. When the rear blade is at about -25 degrees the rear blade enhances the axial flow, and as the rear blade becomes aligned with the velocity peak the axial velocity is retarded. The results show that the rear rotor will increase and decrease the axial flow between rotors of a CRP in a complicated manner depending on the relative locations of forward and rear rotor blades and rotor to rotor spacing.

Chung et al. [11] performed a second study using 3-D thermal anemometry to measure the aerodynamic interaction between the forward and rear rotors in a CRP with a 3x4 blade configuration. From this study it was observed that the rear rotor potential field has little influence at the forward rotor, but that the potential fields and viscous wakes are significantly altered before they impinge upon the rear rotor. This upstream disturbance from the rear rotor on the potential field and viscous wakes of the forward rotor blades occurs in all three flow components and varies with distance from the rear rotor and with radial location, which is entirely due to the passing of the rear potential field.

The measurements revealed an axial velocity which varies with radius, with a maximum value around r/R_{tip} of 0.7-0.9 for this configuration. The radial velocity is negative, towards the hub/axis of rotation, for this compressor (turbine would be positive radial expansion). Circumferential flow vectors plotted in 3d space cause the tip vortex from the forward blade rotor to be detectable in the mean flow. Circumferential velocity is increased by the rotor interaction (more positive, in forward rotor direction).

The forward rotor viscous wakes are seen to be delayed into the rear rotor plane by the convection time dependent upon rotor and freestream speeds, causing a drop in the axial velocity. The primary peaks in axial velocity through rotation are due to the potential wakes of the forward rotor. Periodicity of the forward rotor wake is disturbed by the rear rotor, as a function of blade number and the rotational speed ratio. Peaks in axial velocity arise from the potential wakes of the forward blades with the local minima caused by the forward blade viscous wakes. The flow from the rear blade may either increase or decrease the axial velocity between rotors due to the variation of effects upon the flow as rear blade passes. Axial velocity would be symmetric around the blades if rear rotor was removed. At any axial location the difference between the largest and smallest peak from the potential wake of the forward blade is a measure of the influence of the rear blade field. The peak axial velocity was observed to decrease by approximately 7% with a location shift of about 15 degrees (relative to the front rotor) pulled in the direction of rotation of the rear rotor as the rear rotor passes through the viscous wake.

<u>Explanation of prediction tools</u>

Denner and Korkan [8] detail an analytical prediction method which utilizes the method proposed by Lock and Theodorsen for prediction of the steady CRP performance and the vortex lattice method of Lesieutre for calculation of the unsteady forces. The Davidson method, derived from Lock and Theodorsen, calculates the steady performance averaged over one revolution. No information can be directly obtained regarding the time dependence of these forces from

Davidson. The Lesieutre method is used for inviscid, incompressible, unsteady aerodynamic calculation of the force variation about these mean levels. In this method the unsteady loads are then added to the steady loads to reflect time-variation of the forces on the propeller blades due to the interference velocities. With the time-dependent variation of the induced velocity components known, the variation of the unsteady loads can be obtained. Blades are modeled by a vortex with its circulation determined by the section blade lift force. A strip-analysis method is used for calculating the steady time-averaged loadings. The unsteady interference effects are determined by superimposing the axial and circumferential velocity components over the induced velocities from the counter-rotation. The Sears function is used to calculate the loads experienced by the airfoils, in which a sinusoidally-varying velocity component is superimposed.

Lolgen and Neuwerth [9] used a method where steady blade loading is computed according to the classical theory of Goldstein with the influence of the bound potential field calculated from potential theory. Unsteady blade forces arising from velocity fluctuations caused by blade passage through a flow distortion are predicted by calculation of the unsteady vorticity shed from the blades. The unsteady forces are then added to the steady forces to predict the overall performance.

McKay [12] studied the problem of optimization of a CRP system by combining existing propeller theory from Glauert, Lock, and Theodorsen. The solution method studied both Goldstein and Theodorsen optimization techniques which vary the radial circulation distribution. Propeller characteristics and trends were sufficiently determined using this ideal induced methodology. Glauert's axial and rotational interference factors were used to represent the induced flow from the aerodynamic interaction. Lock's assumption for a close pair of CRP accounts for front-to-rear rotor aerodynamic interactions. This quantifies the axial induced velocity added to both rotors and the rotational induced velocity added to the rear rotor. Betz criterion for minimum-induced-propellers is used which states that the optimum loading distribution occurs when the rearward wake displacement velocity is radially constant. Theodorsen's optimum criterion is also applied where radial spanwise circulation distribution is identical for both rotors.

In this analysis, radial flow was accounted for by comparing a Prandtl tip loss factor with a radial flow factor developed by Davidson based on Theodorsen. These calculations yielded similar efficiencies with a 0.5% difference. The comparison was made in solving for the optimum-loaded minimum-induced-loss efficiency using two different procedures: (1) Goldstein ideal circulation function (2) Theodorsen's ideal circulation function. The Goldstein method was seen to produce a similar, but lower efficiency for a given configuration and power, confirming Theodorsen's distribution as the optimum. The Theodorsen method may also be desirable because it minimizes loading in high-Mach number radially outward regions yet produces similar efficiencies, which likely would be better in terms of sound generation. Other results indicated that the rear rotor efficiency is more sensitive to increasing rotor speed than the front rotor; that for all practical purposes the optimum torque split is 50/50; but also that CRP systems can achieve higher levels of performance if the total power is biased in favor of the rear rotor, done by operating rear rotor at higher rotational speeds.

Leseiutre and Sullivan performed a study to examine unsteady forces acting on CRP blades [13]. In this model the vortex lattice model of counter-rotation is used to predict quasi-steady solutions to the propeller loadings in order to predict the overall performance. Total unsteady velocity is composed of the (1) inflow (freestream) velocity, (2) the rotational velocity (rotational speed times radius), (3) the self-induced velocity of the propeller on itself, and (4) the interference velocity induced by the other propeller. Self-induced and interference velocities from the vortex lattice system are determined using the Biot-Savart Law and unsteady loadings on the propeller blades are obtained by applying an unsteady Sears correction to the quasisteady results from vortex lattice. Sears showed an airfoil in a sinusoidal gust exhibits an amplitude reduction about the mean and a phase shift of the quasi-steady results. The results revealed that unsteady effects diminish with increasing reduced frequency. Also that unsteady loadings are minimized with large number of blades and large blade chord for a given operating condition; where peak-to-peak variation about the mean caused by unsteady loads varied from 9% for a 2x2 to 2% for an 8x8 CRP.

Page and Liebeck extended the vortex-blade element propeller design procedure developed by Adkins and Liebeck to analyze CRP systems [14]. This analytical method confirms an optimum loading distribution for CRP systems using a finite number of blades. The Theodorsen method for optimum CRP operation, calculated for minimum induced energy losses, assumes that the far-field vortex wake acts as two rigid screw helices of equal pitch but opposite rotation. The velocity profiles are affected by the vortex fields on the two rotor disks, with the front rotor influenced by its own vortex and the rear rotor influenced by both vortices. Velocity profiles for the optimum loading case occur where the induced motion of the fluid is normal to the local vortex sheet. Calculation of the loading function defining the optimum propeller is done for specific advance ratios (wake helix angles) and number of blades. The optimum CRP calculation has a 50/50 split between the two rotors in this derivation. Theodorsen gives an optimum loading for the case of infinite blades with a circulation function equal to 1. The circulation function for a finite number of blades is a constant, which varies from 1. In these calculations the effect of varied propeller disk spacing is not present and the equations apply to a "closely-coupled" pair of propellers, with no measure or specification given. The theory was compared with actual data and found close agreement for the limited range of comparison.

Playle et al derived a numerical method to design and analyze the theoretical performance of CRPs by combining existing theoretical models for the design and analysis of CRPs [6]. They discussed CRP findings from literature which state that the performance of a CRP is significantly improved at lower advance ratios, high Tip Speed Ratio (TSR). Also that CRPs exhibit many advantages over SRPs including higher peak efficiency and better off-design performance. In this study, three previously developed models for the design of CRPs were considered and examined; methods by Ginzel, Naiman, and Lock and Theodorsen as described by Davidson. Earlier comparisons showed that the Lock and Theodorsen method, given by Davidson, was most accurate. The Davidson method calculates the interference of one disk upon the other using an interpolation scheme which requires the circulation as the input for the entire configuration. Advantages of this method are the ability to modify for drag and compressibility, and that it is adaptable to include off-design analysis, disk spacing, blade sweep, and different angular velocities on each propeller disk. This method of designing and analyzing a CRP is 2D by nature of the strip-analysis method; however, the propeller is a 3D flow phenomena. To account for the difference between these effects a method is included by Davidson in a version of Lock's tip loss factor for CRPs. For their design the rear disk results in a higher integrated thrust coefficient than the front propeller disk. And the propeller efficiencies vary front to back from 0.798 to 1.93, with total efficiency of 0.946.

This theoretical model designs a CRP configuration for a given operating condition and specified geometric constraints. Playle also showed how to perform off-design calculations, which begin with the propeller blade geometry and flight conditions as specified from the design analysis. In the analysis of the CRP system, the design point yields maximum power coefficient. The results show that there is a very broad efficiency map across a large variance of advance ratio (1/TSR), and that CRPs perform very efficiently even in off-design flight conditions; an improvement upon typical SRPs.

Gazzaniga and Rose tested the efficiency improvement for a propeller by adding a vane row downstream to recover swirl from the propeller [15]. Improvements for this study were found at 2% for the design speed and up to 4.5% at off-design speeds. The addition of the swirl recovery vanes shifted the efficiency peak to a higher operating speed. CRP systems have increased efficiency over SRP's due to their ability to recover the swirl present in the propeller slipstream which is originally considered into the SRP loss mechanism. The aim of this test was to achieve improvement in efficiency without the complexity of a second rotating stage. The maximum rotor power coefficient changed from 2.3 to 2.85 at advance ratios of 3.3 and 2.7 for Mach numbers from 0.80 to 0.60.

Explanation of performance improvements

Counter-rotating turbomachinery configurations have higher efficiencies than their single rotor counterparts due to the recapture of the swirl of the front rotor being transformed into additional torque by the rear rotor [9]. A repeated finding point to another advantage of the CRP which is that they operate with significantly higher efficiencies in off-design conditions [8] [6].

Explanation of noise sources and directivity

Denner's methodology for calculating the loads extended to predicting the acoustics for CRP devices [8]. The procedure is summarized as follows: (1) Davidson approach is used to calculate the steady loads, pressure forces, on the blades, (2) Leseiutre's method is used to calculate the unsteady loads, (3) Succi acoustic prediction is made, using a compact source assumption, to determine the acoustic response. Aerodynamic interference, as experienced with a CRP, alters the magnitude and velocity of the airflow over the blade surfaces. This results in a periodic variation of the thrust and torque force creating a highly directional noise component that dominates the noise pattern in front of and behind the propellers. This method was found to be useful in predicting noise level in the disk-plane of the propeller and the frequency characteristics in the disk-plane and on-axis. The prediction is valid in the far-field in order to satisfy the compact source assumption where $x \gg D_{source}$. The acoustics were calculated with the need only to determine the loads on the front and rear propellers as functions of time.

Lolgen measured noise emission of a CRP along with aerodynamic interaction, measured by velocity distortions and pressure fluctuations on the rear prop blades [9]. Two additional effects have to be considered for a CRP configuration, (1) the aerodynamic interaction, and (2) the acoustic interference between the two propellers. In this study, CRP noise was found to be dominated by that due to aerodynamic interaction. This noise was mainly radiated in the upstream and downstream directions, and is strongly influenced by the thrust ratio between forward and rear propeller. Propeller noise generation is generally dominated by discrete tones, caused by noise sources located on the rotating blades. When the flowfield where the propeller operates is distorted, the unsteady blade loading generates additional dipole-type noise sources (for CRP second rotor). The interaction tone is the additional noise source introduced with a CRP configuration which occurs at the sum of the forward and rear propeller BPF's and originates from the rear blades chopping the wakes of the upstream prop. The individual propeller tones peak in the propeller plane (90° from V_{inf}), whereas the interaction noise was found to have a maximum radiation at an emission angle of 30 to 45degrees with a minimum near the propeller planes. The Bessel function was found to fit well with the prediction of directivity. Other results revealed that increasing the thrust of one propeller leads to an increase of the interaction noise radiated by the other propeller, and that the propeller speed also influences the directivity pattern of each propeller due to a change of radiation efficiency of the tones.

Chung measured acoustic data, collected with an emphasis on the blade pass frequencies (BPF) and interaction tone of the CRP [11]. The rear rotor upstream influence affects the wakes of the forward rotor, which affects the radiated noise and the performance of the rear rotor. Increasing rotor spacing improves noise, but has an adverse effect on aerodynamic performance at larger spacings. They found that the forward rotor tended to dominate the noise spectra (which they noted could be due to having higher power per blade for this rotor). The interaction tone, with frequency $BPF_f + BPF_r$, has a minimum for directivity near 90 degrees, and exceeds both the forward and rear BPFs in the forward most measurement location. Interaction tones are stronger with reduced rotor spacing. Rear rotor noise is most affected (3x4 rotor) by the CRP operation. The increase in SPL for a CRP is caused by the interaction between the forward and rear rotors, which mostly affects the rear rotor operating in the unsteady wakes from the forward blades.

Squires did an early experimental study on the role of the leading-edge vortex due to stall on the forward rotor on CRP noise [16]. The study utilized a 3x4 configuration CRP where the forward rotor could be configured with forward sweep or aft sweep. Forward sweep on a CRP was found to eliminate the leading edge vortex of the upstream blades; significantly altering the SPL of the interaction tone. The leading edge vortex is different from tip vortex, and studies have shown that the leading edge vortex may be more important than the tip vortex for noise generation. The purpose of this study was to manipulate the path of the leading edge vortex as it convects into the rear rotor and determine its effect on interaction tone noise. The leading edge vortex develops as a result of the high sweep of the rotor blades. By altering the rotor to a forward sweep no leading edge vortex was found to form. Velocity fluctuations imposed by the vortex when sampled along the radius yields a circumferential velocity that is skewed alternately positively, then negatively at the bottom and top of the vortex. By this test, results appear that there is no leading edge vortex for the forward swept configuration. BPF tone SPL's were not greatly affected by sweep of the forward blades, forward or rear. With thrust and torque held constant between the two tests the BPF noise sources were unaffected. The SPL in the interaction tone was actually found to increase when the leading vortex is removed or altered to reduce the interaction. This result was not expected or explained. By reducing the leading edge vortex the interaction tone SPL increased. The mechanisms for the interaction tone are not greatly understood.

Windfarm Aerodynamic Interaction/Wake Dissipation Testing

Wake Development and Physical Mechanisms

The physical mechanics of a wind turbine wake are classified into two distinct regions, the near-wake and the far-wake. The dividing flow properties are that at the onset of the far-wake region, the pressure drop across the rotor is fully recovered into the wake and the wake is fully developed.

The physical mechanics producing, and therefore describing, the wake are the rotor's axial thrust and torque extraction. Immediately downstream of the rotor, the onset of the near-wake, there are non-uniform pressure and velocity deficits in the flow. The pressure and axial velocity reduction arise from the axial thrust, and there is also an introduced tangential component of velocity related to the torque on the machine. From the loading of the blade, which relates to the bound circulation on the blade, vorticity is shed into the wake. Variation in circulation, due to the loading along the blades, sheds vorticity from the blade trailing edge which combines together radially outward and combines with the tip vortices which map out a helical trajectory opposite the rotor rotation direction. These trajectories create the shear layer between the slow moving wake flow and the adjacent freestream. Progressing downstream of the rotor, the shear layer expands as the pressure seeks to normalize back to atmospheric with associated velocity decreasing in the wake until the driving pressure gradient force is reduced to zero. Turbulent diffusion of momentum arising from the velocity shear between the wake and atmospheric flows becomes the main mechanism causing the wake to diffuse. This diffusion mechanism causes the shear layer thickness to increase (inward) with axial distance leading to the ultimate transition to the far-wake region defined where the shear layer thickness reaches the rotor axis. This transition from the near-wake to far-wake occurs 2 to 5 rotor diameters downstream. The far-wake region has a fully developed wake with axisymmetric and self-similar velocity deficit and turbulence intensity profiles (in the absence of an atmospheric boundary layer). In this region only the overall properties of the turbine appear as parameters, the rotor thrust coefficient and the total turbulent kinetic energy produced by the rotor itself.

Vermeer and Sorensen performed a survey of wind turbine aerodynamic experiments within these two distinct regions [17]. The near wake studies reviewed are restricted to controlled environments. The near wake survey concluded that good near wake experiments are hard to find in wind energy research. The survey's far wake studies focus on both single turbines and combined effects in wind farm settings; including analytical and experimental results. It was concluded that far wake experimental results can be extended to other turbines if the overall drag of the turbine that produces the wake is estimated correctly. From this survey, Vermeer determined that engineering rules developed for describing the problems with aerodynamics need more fundamental understanding. Also, that while the aerodynamics of wind turbines seem simple, some of the most basic mechanisms of the fluid flow are not well or fully understood, such as the unsteady effects from operating in the atmosphere, presence of stall, three-dimensional effects which change the airfoil performance, and the production of and operation with turbulence.

The testing parameters of the near wake wind tunnel experiments analyzed by Vermeer are summarized, where the most promising results come from full-scale experiments of which there was only one at the time. The limitation to this practice is the model to tunnel area ratio, which was given for the experiments and was between 1:1.7 and 1:125 for the different experiments. The dependency of rotor inflow and wake structure cause this dimension to be of concern where the rotor performance is influenced by the possibility, or not, of free wake expansion. Good practice before studying wakes in a wind tunnel is to first thoroughly test the wind turbine rotor. Flow visualization immediately behind the rotor or along the blades produces valid insight into the flow in the vicinity of the rotor, mostly qualitative, and can reveal areas of interest to be related to the wake dynamics.

Averaged data from these experiments dealing with velocity distribution in the wake are mostly used to analyze global properties of the wind turbine, such as power and thrust. These data, however, does not reveal much about the physical process of power extraction. Detailed wake data from high response sensors including thermal anemometry, laser doppler velocimetry, and particle image velocimetry are needed to provide a better understanding of wind turbine aerodynamics. Data using these high response sensors reveals fundamentally insightful patterns regarding wind turbine aerodynamics. For example; vortex spirals from a two bladed wind turbine set at two different pitch angles have two different trajectories and converge on each other, the propagation speed of a tip vortex spiral is lower than the local flow velocity. Vermeer summarized that tip vortices, in addition to wake properties, are worth noting because they likewise determine the physical behavior of the wind turbine rotor as a whole. These properties include wake expansion measured by viewing the tip vortex path at distances downstream, the vortex spiral twist angle, and the strength of tip vortex itself.

While properties of the rotor can be discerned in near-wake flow, for the far-wake region experiments and modeling, the rotor geometry is less important and focus is placed on wake models, wake interference, turbulence models, and topographical effects. Emphasis from the studies reviewed was on the influence of the wind turbines in wind farm settings, not the individual turbines themselves. Vermeer reiterated key results from these studies. The effects of the far-wake are expected to vanish sufficiently far downstream due to turbulent diffusion of the wake, implying the relation to atmospheric conditions such as turbulence and stability. Results using static simulators, confirmed later by wind turbine research, reveal a saturation of turbulence reaching an equilibrium value within a wind turbine cluster after several rows of turbines. It was also found that turbulence intensity in the far-wake decreases with downstream distance and increases with the thrust coefficient. Turbulence effects have been found to be more persistent downstream of a wind turbine with its decay less rapid as the decay of velocity.

Experiments found turbulence effects noticeable at 12 and 10 rotor diameters downstream of a wind turbine, where velocity deficits are nearly negligible. Vermeer restated additional results which showed that the wake of a downstream machine recovers more rapidly than the initial upstream machine at the same relative position, which is likely due to the increased turbulence and atmospheric mixing present with downstream inflow. A shift in the turbulence spectrum to higher frequencies accompanies wake flow with the turbulent length scale observed to decrease to a quarter of the free stream value.

Wake/Wind Farm Modeling

Crespo et al. [3] performed a survey in 1999 on the modeling methods for wind turbine wakes and wind farms. The attempts at modeling the wake of a wind turbine and their combined effects in a farm setting were reviewed and categorized into the different forms.

The two methods for farm modeling include the early approach of modeling turbines as distributed roughness elements which alter the atmospheric flow, and the most common approach which considers individual turbine wakes and examines the interaction and superposition with neighboring wakes in the farm. For calculating individual turbine wakes the two approaches are using a kinematic model or a field model. Kinematic models are explicit models which depend on adjustable coefficients and provide acceptable results if the coefficients are appropriate. Field models are implicit models which calculate the flow magnitudes at every point of the flow field and produce an acceptable representation of the flow field.

Wind farm modeling by describing the turbines as distributed roughness elements assumes a log wind profile including a parameter to describe the ground roughness and the presence of a turbine increased this value. Some models use two parameters in their profile calculation; one to describe the profile below the hub height, and a second to describe the height above that related to the drag of the machine. Both methods have the same ultimate process for power calculation which is to obtain the wind velocity incident on each machine and derive the power produced in those distributed locations to obtain overall wind farm performance. These models however are said to not be used much, but that they could be of interest in predicting the overall effects of large wind farms on wind characteristics.

Kinematic models to calculate individual wakes for farm approximation have the far-wake property of self-similarity as their basis. Self-similar velocity deficit profiles used in these models are obtained from experimental and theoretical work from co-flowing jets. The initial value for the velocity deficit comes from the thrust coefficient of the machine, with subsequent reference values at each section acquired from global momentum conservation. Larsen [18] proposed a simple analytical model based on work by Schlichting [19] for classical wake theory and compared results with empirical relations and obtained relative differences lower than 5% in all cases where the downstream distance was greater than 2 diameters. Kinematic models have been shown to provide results in good agreement with experimental measurements if appropriate values are chosen for the parameters appearing in them [20].

Crespo reviewed the field model approach and found that they all solve the Ryenolds-average turbulence flow equations and use a closure scheme, based on zero-, one-, or two-equation models to calculate the turbulence transport terms. An isotropic turbulence field is implicitly assumed in these models through the use of an eddy viscosity. Wakes are described using a linearized momentum equation in the main flow direction with constant advective velocity and eddy diffusivity and a parabolic approximation. This model was compared to small scale experiments with agreement for velocity deficit and wake growth within 10% for cases not having high thrust loading, where the error could reach 20%. Considering the model simplicity this is seen as a reasonable approximation. Crespo et al. [21] developed the UPMWAKE model based on the field model approach for calculating wind farm performance. This model calculates the 3D wake model for a wind turbine operating in a non-uniform flow corresponding to the atmospheric boundary layer. UPMWAKE uses conservation equations of mass, momentum, energy, and turbulence kinetic energy and its dissipation rate. This model has been verified with experimental data to describe accurately the velocity deficits from the wake, even in the near-field. Results have been shown in agreement from wind tunnel experiments and field experiments using full-scale machines, along with CFD numerical computation using CFD PHOENICS. In general, field models give an acceptable respresentation of the flow field and better insight into the governing processes of wake development than the kinematic models.

Crespo described the process which wind farm codes typically implement where the results of single-wake calculations are relied upon, with a superposition assumption made which takes into account the combined effect of different wakes [3]. Linear superposition fails for larger perturbations where the velocity deficits are overpredicted, and this assumption could even lead to non-physical result of negative velocities given sufficient wakes. Katic et al. [22] used linear superposition of the squares of the velocity deficits in the PARK model, which in general produces better agreement with experimental results than linear superposition. UPMPARK is an extension of the parabolic UPMWAKE code for calculations in a farm with many turbines. This model requires no assumptions about the superposition or type of wake to be used as all the wakes and interactions are calculated directly by the code. The model solves the same conservation as for the single-wake code with turbulence closed using a k-ε model. This model is especially suited for the case of turbines in a row, and can handle moderately irregular terrain.

Wind farm models typically make the simplifying assumption that the terrain is flat and that the unperturbed wind velocity is uniform, in the absence of the atmospheric boundary layer. A simple method to account for the terrain effects is adding the velocity perturbations arising from the upstream wakes with those arising from the terrain as an approximate. This procedure has been applied with a relative order of the errors of 10%, less than 20%, validating the method for moderately irregular terrain but less valid for highly irregular terrain. Van Oort et al. [23] found that terrain irregularity creates additional turbulent diffusion towards the ground, diminishing the wake effects. Additionally, above the apex a hill where streamlines concentrate wake effects are increased. In offshore applications where there is a smaller surface roughness, and associated reduced atmospheric boundary layer, turbulence intensities will be lower than for equivalent inland locations reducing the turbulent diffusion of the wake resulting in wake effects that persist further downstream. Stefanatos et al. [24] and Helmis et al. [25] give some guidelines for studying the interaction between wake and terrain, derived from experimental results in wind tunnel and large-scale tests.

Analytical expressions and semi-empirical expressions have also been studied to estimate the order of magnitude and the tendencies of the most relevant parameters which describe wake evolution. Regressions or correlations have been obtained by many authors in describing single wake properties for velocity deficit and width of the wake, along with expressions for turbulence intensity. Taylor [26] performed a parametrization of calculated wake magnitudes as functions of dimensionless parameters. Most of these studies describe wake diffusion as a function of downstream distance and hub height normalized with the rotor diameter, thrust coefficient, and ambient turbulence intensity. Magnusson and Smedman considered the effect of atmospheric stability by including the Richardson number in their correlation for velocity deficit decay [27]. Crespo summarized that all the correlations show an acceptable degree of agreement but suggests that more work is needed for confirmation with experimental results.

Loading Effects Caused by Wakes in Wind Farms

Crespo summarizes that wake measurements and modeling associated with wind farm operation have since been primarily focused on energy production and loads, however relatively few direct measurements of structural loads under wake conditions have been performed. The most serious and expected effects of turbines operating in wakes of other turbines is fatigue and dynamic loading. In the near wake, flap-wise bending moments depend primarily on the distance to the neighboring machine. Volund performed an early study utilizing a 250kW turbine 2 diameters downstream of another revealed that loads were largest when the machine was exposed to half-wake conditions [28]. Frandsen and Thomson [29] studied an offshore wind farm with eleven 450kW turbines separated by approximately 8 diameters and determined the equivalent fatigue load as a function of wind direction, and therefore upstream wake participation. The Alsvik wind farm in Sweden was studied by Dahlberg [30] which has 300kW turbines in three rows with one instrumented wind turbine exposed to 5-, 7-, or 9.5-diameter spacing from single-wakes depending on the wind direction. Some results found were that there were no significant half-wake loads when the instrumented machine was within 7 to 9.5 diameters downstream. It was also found that under full-wake conditions the equivalent load was increased by 10% at 9.5 diameters, and up to 45% at 5 diameters.

The data from these early studies reveal that there is no appreciable difference when operating in single- or multiple-wake loads, repeating the trend of power losses when operating in wake flows. Adams et al. [5] also concluded that equivalent loads were very similar under single- and multiple-wake conditions.

Crespo concludes that there have only been limited efforts toward directly estimating wake loads from modeling. Frandsen and Thomson [29] developed a model which has been demonstrated to work for turbine separations larger than 3 to 4 diameters. The modeled value of turbulence intensity depends on the thrust coefficient, wind turbine spacing, and ambient turbulence. At high wind speeds the wake effects decrease due to the reduced thrust coefficient.

Experimental and Computational Wind Turbine Wake Studies

Bathelmie [1] compared multiple analytic and computational fluid dynamics (CFD) wake models to data from the Horns Rev offshore wind farm. The wind farm consists of 80 Vestas V80 wind turbines in an 8x10 arrangement with a 7-diameter spacing each. In predictions power loss should encompass the entire range of wind speeds and directions at each turbine location, but with CFD this is limited to a few directions and wind speeds for only a small number of turbines. When modeling wakes the power curve and thrust coefficients must be known. Atmospheric stability has been shown to strongly impact power losses due to wakes offshore, however, few models incorporate this parameter. Wake recovery is determined by the transfer of momentum into the wake region which is primarily controlled by turbulence, hence, also with atmospheric stability. For large wind farms on land ambient turbulence is significantly higher than off-shore, enhancing atmospheric mixing and reducing the wake recovery length.

The models used in the comparison are described. The WAsP model uses the one-dimensional linear wake expansion model with a constant velocity profile in the wake and does not account for complex terrain. The CRES model accounts for wake effects through the amended wake model proposed by Dekker and Pierek [31], and includes the effects of multiple wakes on mean wind speed and turbulence. WindFarmer from GH utilizes the WAsP model with mean flow parameterized with turbine and wake-generated turbulence modeled using empirical relationships, solved using a CFD Reynold's averaged Navier-Stokes (RANS) solver. WAKEFARM from ECN is a CFD solver based on the UPM code described earlier, which uses a Gaussian velocity profile for the far-wake downstream boundary condition which must be tuned with experimental data. CENER is based on the CFD package Fluent and simulates the rotor effects on the flow as axial momentum sinks with model inputs of thrust coefficient and topography. NTUA solves the 3d incompressible RANS equations with wind turbines modeled as axial momentum sinks defined by the turbine thrust coefficient.

Power observations from the wind farm were compared to the models in sorted data sets composed of 10 minute averages, then averaged along each row. There was a minimum of fourteen 10-minute averaged points in each case. Three cases of alignment with the wind direction were chosen which resulted in a 7-, 9.4-, or 10.4-

diameter turbine spacing's along the row. These cases were sorted by the averages of the yaw alignment and filtered by the degree of alignment with the wind direction. When aligned ± 1° the wind farm row seems to reach a limit power of 60% freestream. For the 7-diameter spacing case this result was realized at the first wind turbine in wake operation and remained near constant up to the eighth wind turbine in the row. A 9.4-diameter spacing dropped performance to 70% and reached 60% at the fourth or fifth wind turbine. A 10.4 diameter spacing did not reach the limit over the five turbine row, but the increments between each turbine were more constant beyond the first wake operated turbine's 90% power. When focusing on narrow wind direction sectors the power at the second wind turbine drops significantly. However, if wider sectors are chosen the power drop to the second turbine is less severe with power in the row and continues to drop at a higher rate. The effect of yaw alignment on the wake loss is proven significant, changing the performance from 60% to 80% in some cases for only a 15° misalignment.

The predictions of the experimental results showed that the wind farm models typically under-predicted wake losses, particularly in partial wake flow scenarios, while CFD models over-predicted the wake losses. The errors from the predictions were substantial in the comparison, revealing the need for more accurate models for wind farms. The main issue is that models seem to be in good agreement when used for single wakes but vary substantially for large wind farm settings.

Barthelmie [32] performed a study using SODAR, a device used to measure velocity profiles, to compare several commonly used models for predicting a wake downstream of a wind turbine with measured velocity data. The SODAR measurements were taken at distances between 1.7 and 7.4 rotor diameters downstream, between 30-90 meters with a 5-m resolution. This study tested single wake scenarios only. The thrust coefficient used in the models was determined based on the hub-height wind speed, with three methods used for calculating the velocity profile which were also compared and seen to differ significantly in some cases.

The models used for the comparison are as described. The Risoe engineering model consists of a collection of sub-models for mean wind wake deficit, turbulence intensity, and turbulent length scale, among others. The model assumes a circular symmetric wake deficit and uses a similarity assumption for the shape. The sub-models dealing with wake turbulence are purely empirical. Risoe WAsP model is a simple wake model based on linear expansion of the wake. The expansion slope has suggested values of 0.05 offshore and 0.075 onshore, where higher turbulence levels are present. The wake is assumed to have a constant value velocity profile that changes with axial location. The near wake is not modeled specifically so this model is only valid for distances of over 3-diameters. Risoe Analytical Model calculates momentum deficit behind each turbine which is conserved as the wake expands. Velocity deficit is calculated assuming a circular wake area until the wake expands to hit the ground or lateral wakes. UO FLaP model solves the governing equations of the flow numerically with suitable parameterization. Wake flow is assumed to be axisymmetric and incompressible with no external forces or pressure gradients. This flow is then described with the two-dimensional Reynold's equation in the thin shear layer approximation without viscous terms. Eddy viscosity is used for turbulence closure, and an empirical wake profile is used as a boundary condition at the end of the near wake. The ECN Wakefarm model is based on the UPMWake model, which is a parabolized Navier-Stokes solver with k-ε model for turbulence. The velocity profile is defined to fit a Gaussian distribution. RGU CFD model requires inputs of atmospheric velocity and turbulence intensity profiles and approximates the rotor as a semi-permeable disk with pressure drop across it.

Estimation of the free-stream wind speed was seen to have profound effects on model results and the comparison. Reviewing the results, all of the models under predict the in the near-wake flow (1.7D) and over predict the deficit at 7.4D compared to the measured values. Risoe Analytic model tends to give lowest values, and UO flap and Risoe Engineering also typically predict lower values than other models. WAsP seems to perform as well as the other models despite use of the constant velocity profile among other simplifications. Average errors at the varying distances downstream varied from between 11-17% for the different models. The WAsP model with the simple linear wake approximation had the highest correlation coefficient with the data of the models studied. A large discrepancy remains between the model predictions and the experimental measurements with no clear identification of its cause. No particular model gave a consistently better performance than the others. Overall, higher turbulence conditions were not more accurately represented by the wake models than lower conditions, or vice versa. Comparing momentum deficit instead of velocity deficit produced more consistent results between the models. Wake meandering results in a measured wake which may be partial and not a full wake condition, causing the models to over predict the velocity deficit, particularly at larger spacing's. Correcting for wake meandering brings some of the modeled values closer to observed, but the change is not uniformly an improvement. Insight into the near wake transition was provided from the experiments where a near wake shape was seen at 1.7 and 2.8-diameters but not at 2.9-diameters, possibly due to higher turbulence levels or wind speeds.

Barthelmie summarized that the spread of wake model predictions is considerable even for the relatively simple offshore single wake cases studied, suggesting a need for more and better quality measurements and further model evaluation.

Cleve analyzes data at the Nysted offshore wind farm in Denmark and compares them with the Jensen linear wake model [33]. Data are presented as 10 minute averages, with filters used to ensure sufficiently steady and homogenous wind conditions over the average. Data are first sorted into wind condition classes and averaged, then compared with fitted model predictions. A Jensen two parameter model fit is performed for each individual 10 minute recording, where the two parameters are wind direction and the wake-decay constant. This model describes intra-farm wind flow as a static superposition of linearly spreading wakes.

Downwind wake velocity is modeled as a function of "overlap area" between wake and rotor areas in an attempt to estimate partial wake scenarios. Downstream velocity deficit is calculated by the sum of squared deficits from each upstream wind turbine.

Wind speeds are obtained from averaged powers of first-row turbines and the inverse power curve. Three options are compared for determining the wind direction using meteorological masts, turbine orientation, and best-fit parameters produced from the measured power of the turbines. Each of these methods produces different directions. Actual wind direction was determined by comparison of the first and second row turbines power output as a function of the estimated direction. This curve is ideally symmetric around the alignment direction of turbines however a misaligned turbine induces a small sideways movement of the wake. The best fit wind directions and the corrected turbine orientation can be thought of as good estimates of the true wind direction, on average. Fit quality of the Jensen model is increased with precision of the wind direction.

Using this approach, it was found that the distribution of the wake decay parameter peaks around 0.02 for the offshore wind farm and extends up to 0.1. The average of 0.028 is less than current standard value of 0.04 for offshore wind farms indicating that offshore wakes are narrower than previously expected. This value changes to 0.032, 0.037, and 0.044 when using other fits for the wind direction. The effect of atmospheric stability is revealed by the data producing an average of k=0.03 versus k=.026 for stable conditions. Unstable flows result in weaker velocity dependence with height which agrees better with the model assumptions, resulting in an improved fit.

The fit quality of the Jensen model is better for full than for partial wake situations, as expected. Even for full wake situations the Jensen model is not fully consistent where different wake decay constants (0.3, 0.5) are observed for different turbine spacing’s, which is a measure of model strength. Further analysis of modeling with more data is suggested.

Frandsen proposed an analytical model for small and large wind farms [34]. Models typically applied for calculating production losses due to wake effects are based on local "unit by unit" momentum equations disregarding the two-way interaction with the atmosphere. Array efficiency of infinitely large wind farms is typically calculated by viewing the wind turbines as roughness elements and applying CFD schemes. In the analysis, wake rotation is neglected and assumptions for self-similarity in a constant wake flow speed profile are made. The model includes assumptions which are only valid in the far wake. A model for expansion of the wake cross-sectional area as a function of downstream distance is described with values which must be determined experimentally.

For an infinitely large number of wind turbines it must be assumed that there is an asymptotic, non-zero wake flow speed. If flow speed became zero then thrust on the wind turbines becomes zero and the flow would accelerate. An asymptotic relationship for an infinitely large wind farm is derived with a wake expanding linearly with axial distance. The asymptotic wake flow speed deficit was said to be constant within approximation, the value of which is only moderately dependent on freestream flow speed but likely highly dependent on turbine spacing. A consequence of the asymptotic value not depending on the wind speed is that the wake decay constant must be proportional to the thrust coefficient, which also describes the initial wake deficit.

Frandsen included a model where the wake meets side wakes and can only expand vertically. The solution procedure begins with finding the asymptotic relative wake speed deficit experimentally and using this value to determine the wake decay constant. When wakes merge with lateral wakes or meet the ground, the merged wake expands completely upward. This is modeled by conserving the momentum deficit with a changed area, which results in disproportionately tall wake areas, likely implying the inability of the model to describe the actual flow physics – despite its reasonable performance results. A comparison was made with data for a row of 7 wind turbines at a set spacing and produced good agreement for the different wind speed cases.

Troldberg modeled a wind turbine wake with a numerical method which combines large eddy simulations and an actuator line technique using 8.4 million grid points [35]. Advanced CFD methods have shortcomings regarding inaccurate turbulence and transition modeling, in addition to being computationally expensive. The work addresses these shortcomings by making numerical simulations of wind turbine wakes using an actuator line technique coupled with Large Eddy Simulation to predict the region up to 7 diameters downstream, showing both near and far wake regions. Actuator line model adds body forces from the blade-element momentum theory and two-dimensional airfoil data onto rotating lines in the three-dimensional Navier-Stokes solver representing the blades. The advantage is that many fewer points are needed to describe the influence of the blades compared with simulating the actual geometry. The biggest drawback to this method is its dependency on accuracy and availability of airfoil data.

Operating in wakes of upstream wind turbines causes a reduced power production and increased turbulence level in the inflow. Ebert and Wood [36] found that at high TSR the tip speed vortices contain a large part of the angular momentum in the wake. Experiments showed that tip vortices could be detected up to approximately 3 rotor diameters downstream. Whale made PIV measurements of a model rotor at different tip speed ratios and compared the results with a simulation using inviscid free vortex wake method [37]. It was shown that as long as similarity is obtained in TSR, that the wake behavior might only be minimally sensitive to Reynold's number. The simulation by Troldberg was carried out with a uniform inflow and for varying tip speed ratios.

Results showed that the axial induction factor varies with the tip speed ratio (TSR) – i.e., changing wind speed or rotational speed – and with radius in each case. For the lowest TSR the bound circulation is seen to vary along the entire length of the blade, indicating that a large amount of vorticity will be shed into the wake from the entire span of the blade. The bound vorticity of the blades is primarily shed downstream of the root and the tip regions, which was consistent with the method's radial distribution of circulation. For TSR’s of 5 and 7, the tip-vortex pattern was visible 5 and 1 rotor diameters behind the turbine. For TSR's of 3 and 2 the tip-vortex remains distinct in the entire computational region due to the high pitch of the vortex system. These results are valid qualitatively and not as absolute reference due to the lack of atmospheric turbulence in the model which would cause the wake to dissipate faster. The heaviest loaded rotor's wake expansion is significant and the dissolution of the tip vortices results in a rapid transition to a fully turbulent wake. Wake rotation seems to reduce as the wake becomes unstable. Axial (and tangential) induction factors in the far-wake reach a value about twice that in the rotor plane, which agrees with the actuator disk theory. An important result of the study is that the instability of the wake is an intrinsic part of its dynamics and that no external turbulence is needed to create the transition from a laminar to turbulent wake, and is a function of the blade loading and TSR.

1.4 Research Objectives

- Approximate wind turbine optimum theoretical performance for single and double rotor configurations using the Actuator Disk Theory.
- Describe measured wind speed seasonal variation and distribution and relate to approximate and compare wind turbine performance.
- Experimentally quantify wind turbine performance losses due to aerodynamic interaction from wakes produced by upstream wind turbines in the wind farm setting.
- Develop an empirical relationship between turbine-turbine spacing and performance losses and compare to model predictions.
- Test wind turbine wake model predictions against data for wind farm wake scenarios.

CHAPTER 2: EXPERIMENTAL FACILITY

2.1 Micro Reconfigurable Wind Farm Test Facility

A facility has been constructed directed at investigating wind turbine wake interactions in an in-field wind farm setting.

2.1.1 Micro Reconfigurable Wind Farm Instrumentation

The Purdue University Micro Reconfigurable Wind Farm consists of four wind turbines mounted on movable carts located in a field north of Maurice J. Zucrow Laboratories, as displayed in Figure 2.1. Southwest Windpower Whisper 100 model wind turbines are used in this facility which have a 900W rated power and a 7-ft diameter. The turbines have a hub height of approximately 35-ft above the ground level. Two of the four turbines are instrumented and data collected on the cart. Produced power is used to power the instrumentation with additional power sent to a dump load resistor bank.

Figure 2.1: Micro Reconfigurable Wind Farm Facility.

The Southwest Windpower Whisper 100 wind turbines are three-bladed wind turbines which have an actual airfoil shape along their blade length. The turbines rotate at speeds up to 1000 rpm and produce 900 W at their rated wind speed of 28-mph. These turbines are described by the manufacturer's power curve given in Figure 2.2. Alignment with the wind is controlled passively through a tail fin extending from the rear of the nacelle. Overspeed protection is produced through a passive mechanism caused by the misalignment of the rotor thrust center and rotor holding pin, where the thrust produces a torque that causes the rotor and generator to lift up and furl out of the wind at sufficient wind speeds.

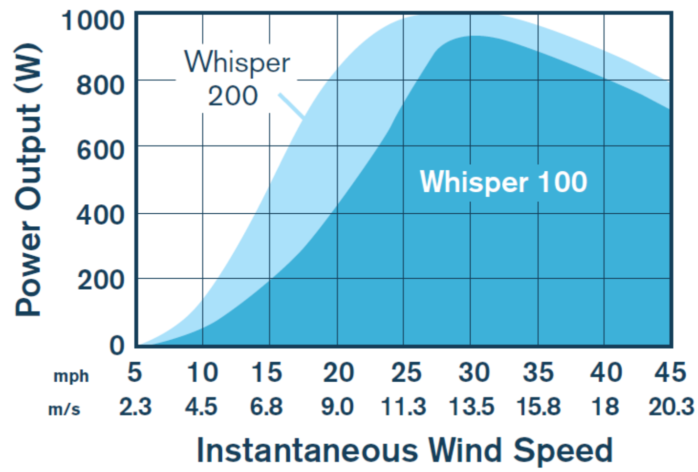

Figure 2.2: Southwest Wind Power Whisper 100 Power Curve.

Wind farm arrays are configured and tested within the completely variable array layout by positioning the wind turbines in the desired array within the given wind condition. The upstream instrumented wind turbine's position remains fixed while the other required turbines are positioned around it. The turbine carts have wheels which allow them to be pulled by a truck into the desired position. Once in the position, the turbine is leveled and supported by the four adjustable jacks on each corner as shown in Figure 2.3. No additional support is needed for the 1700-lb carts at any point of operation or maintenance with the Whisper 100 wind turbines.

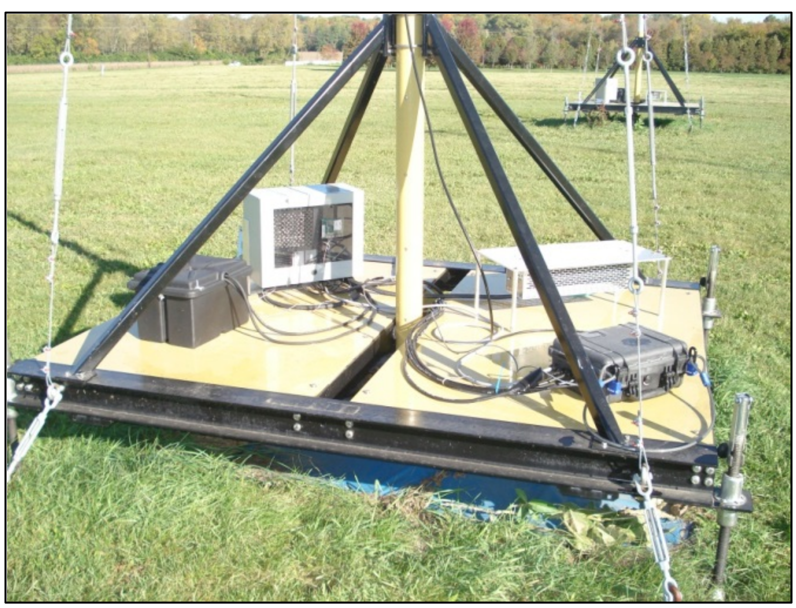

Figure 2.3: Wind Turbine Cart and Electrical Systems.

Power from the wind turbine is transferred through multiple conditioning and controlling electronic devices. The power from the wind turbine is variable voltage, variable frequency AC electricity. This power is sent to the Whisper 100 charge controller which rectifies it to a 24 V nominal DC output, which is then sent to a charge a 24 V battery bank. If this bank voltage reaches a maximum power, the turbine controller stops the wind turbine to prevent damaging the batteries. To prevent this feature from engaging, a secondary controller was added across the batteries which is set up as a diversion load to a resistor bank capable of dissipating the maximum input power of the wind turbine at a voltage that is beneath the maximum set voltage of the Whisper 100 charge controller. Wind turbine instrumentation and data acquisition (DAQ) is all powered from the battery bank charged by the wind turbines. This voltage is regulated with a DC-DC converter to 24V prevent a voltage over the instrumentation limit from being sent from the charging battery. The electrical systems are also shown in Figure 2.3.

The wind farm is located in a large, flat open area with 40-ft or smaller trees around 600-1000 ft North and South of the wind farm, but mostly open from the East and West. The surrounding terrain during testing was short grass with some 1-2 ft sparsely located throughout the field further away. A satellite image of the field is shown in Figure 2.4, showing the four wind turbines within the red square (the southeast turbine position is fixed).

Figure 2.4: Micro Reconfigurable Wind Farm Location and Surroundings.

Wind farm wind speed is measured with an anemometer mounted at the same height as the turbines 200-ft west of the instrumented turbines. The anemometer is a Lufft two-dimensional sonic anemometer capable of measuring the wind speed in the two horizontal directions at up to 15 hz with a maximum 1-second average output signal. The anemometer is configured to measure wind speed and direction during testing, and the output current signal is sent to the stationary upstream instrumented wind turbine DAQ through buried conduit. A current output on the channels is used due to its capability to transfer a signal accurately over long distances. This anemometer is shown in Figure 2.5.

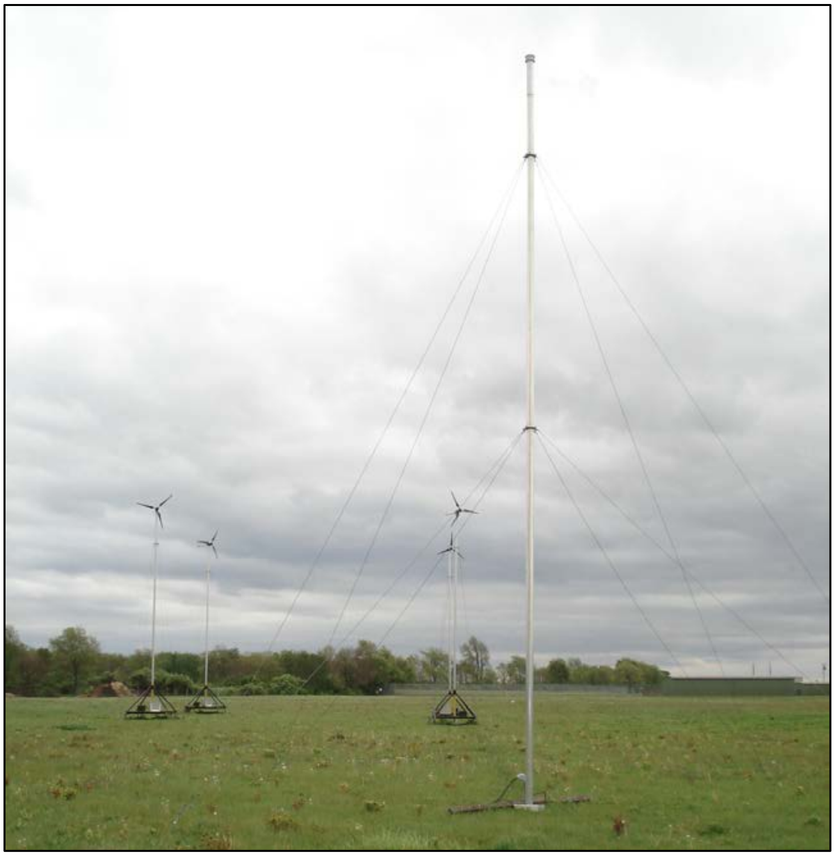

Figure 2.5: Micro Reconfigurable Wind Farm Anemometer Tower.

2.1.2 Wind Turbine Performance Instrumentation

Of the four total wind turbines in the Micro Reconfigurable Wind Farm two are instrumented to measure the performance on the rotor aerodynamically and produced electrically. The instrumented wind turbines are used in conjunction to quantify performance losses in wind farm settings when operated in the wake of an upstream wind turbine. A view of one instrumented wind turbine mounted on the cart tower is given in Figure 2.6.

Figure 2.6: Micro Reconfigurable Wind Farm Wind Turbine.

<u>The instrumented wind turbines have instrumentation capabilities as follows:</u>

- Rotor aerodynamic torque
- Rotor rotational speed
- Electrical current sent to the battery from the turbine charge controller
- Battery voltage/charging voltage
- Cart located data acquisition system

Torque is measured on the rotor with a reaction torque sensor mounted between the rotor and generator load. An Interface TQ30-600 torque sensor is used which is calibrated to 300 lb-in and has a compensated temperature range from 15 to 115°F. This sensor produces a low voltage signal and is amplified and conditioned at the rotor in an effort to minimize noise effects. An Interface CSC-8 signal conditioner is mounted under the turbine nose cap and this conditions the input voltage and generates a 4-20mA bipolar output. Pictures of the configuration are shown in Figure 2.7.

Figure 2.7: Torque Measurement Instrumentation.

In order to pass the torque measurement cables through the rotating frame of the rotor to the stationary nacelle a slip ring mounted on the bearing shaft is used, as shown in Figure 2.8. A Meridian Lab's MM4 mercury slip ring is used for its compact size and robustness. Rotational speed is measured on this shaft using an Encoder Products, Inc. model 15T incremental encoder, mounted between the bearings and the slip ring. The whole assembly fits within a recessed region in the turbine nacelle which is sealed and weatherproofed.

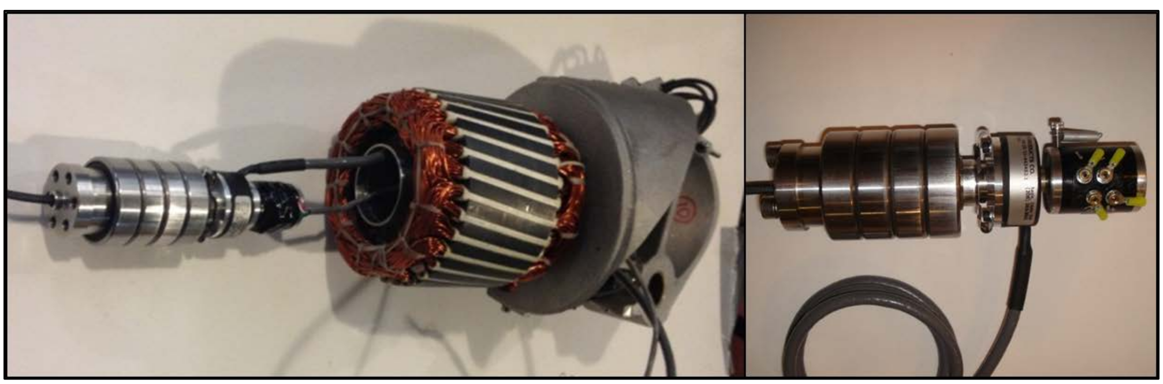

Figure 2.8: Encoder and Slip Ring Shaft Mounting.

The torque and encoder cables were initially passed through the yaw axis which spins relative to the turbine tower using an additional slip ring. It was determined that capacitive noise was picked up from have the torque signal exposed to the digital encoder signal with no shielding within the slip ring. The noise level was high enough to reduce the experimental uncertainty values outside of the acceptable range. This slip ring was removed and the center of the yaw rotation shaft was machined out to allow for cable passage without snagging on the power cables. These sets of cables were kept separate immediately behind the turbine exit with a counduit section. The assumption behind this design was that while the turbine will rotate frequently and the wind will be from all directions at times, the turbine will not go through many turns. Each turn is stored in twisting or untwisting of the torque and encoder cables. This configuration was found to reduce noise levels significantly and to within an acceptable value.

Electrical power measurements are made after the turbine AC power is converted by the turbine charge controller and sent to the DC battery bank. Current is measured with a Flex-Core CTH-050 Hall Effect current transducer which passes the battery positive cable and measures up to 50A. The voltage sent to the battery is measured directly by the data acquisition system, after connecting it to a voltage divider (with a division value of 7) to reduce the voltage to within the range of the DAQ.

A Gantner Q.series data acquisition system is used for data collection and analog to digital conversion. The DAQ system is comprised of a Q.gate controller, an A109 module for measuring the digital encoder frequency, and an A108 for the analog current and voltage measurements. Two independent units are used on each of the instrumented wind turbine carts, both with GPS devices set up as the clock on the two data acquisition (DAQ) systems to ensure proper time stamp synchronization of the data. Proper grounding is enabled through 8-ft ground rods driven in the ground in various locations within the wind farm. The DAQ systems are enclosed and sealed from the environment using pelican boxes with environmentally sealed cable glands to pass the cables through the box.

CHAPTER 3: TECHNICAL APPROACH

3.1 Wind Turbine Nomenclature

Power Coefficient:

$$C_p = \frac{P_T}{{}^1\!/_2 \rho A_T U^3}\,. \tag{3.1}$$

Thrust Coefficient:

$$C_T = \frac{Drag}{{}^1\!/_2 \rho A_T U^2}\,. \tag{3.2}$$

Axial Induction factor:

$$a, b, c = \frac{V_{in} - V_T}{V_{in}}\,. \tag{3.3}$$

Tip Speed Ratio:

$$TSR = \frac{\Omega_{rotor} R_T}{U}\,. \tag{3.4}$$

Aerodynamic Power:

$$P_{T,aero} = \tau_{rotor} \Omega_{rotor}\,. \tag{3.5}$$

Electric Power:

$$P_{T,elec} = I_{charge} V_{charge}\,. \tag{3.6}$$

Normalized Power:

$$P_{norm} = \frac{P_{downstream}}{P_{upstream}}\,. \tag{3.7}$$

3.2 Wind Turbine Optimum Theoretical Performance Derivations

Optimizing the design of wind turbines is a complicated problem with physical interactions which are unknown or difficult to model. Air flow surrounding a wind turbine is highly three-dimensional requiring approximations and empirical results to estimate inputs and performance. Optimum theoretical wind turbine performance is derived in Sections 3.2 with simplifying approximations for a single rotor and a dual rotor wind turbine. The results provide the maximum theoretical wind turbine performance, within the limitations of the particular model approximations.

3.2.1 Single Rotor Wind Turbine Optimum Theoretical Performance

Wind turbine performance can be predicted using the conservation equations of mass, momentum, and energy along with state relations. Froude's actuator disk theory is an idealized approach to solving these equations. Simplifying assumptions are made which model a rotor as an infinitely thin disk with no area change across it, in which flow properties are one-dimensional passing through it, and a pressure gradient is present across its surface in the direction of the flow (pressure drop for energy extracting turbines). For the following theoretical analysis, steady, inviscid, one-dimensional flow is assumed throughout and performance is predicted in these calculations in terms of the maximum theoretical power output for a wind turbine.

The steady, incompressible, one-dimensional governing equations are given below for reference:

$$V_i A_i = V_e A_e \tag{3.8}$$

$$p_i A_i + \dot{m} V_i + F - \int_{x_i}^{x_e} p_{sides}\, dA_{x,sides} = p_e A_e + \dot{m} V_e \tag{3.9}$$

$$h_i + \frac{V_i^2}{2} + w_s = h_e + \frac{V_e^2}{2}\,. \tag{3.10}$$

The derivation for the optimum, idealized, power coefficient is described below. The derivation subscripts correspond to Figure 3.1.

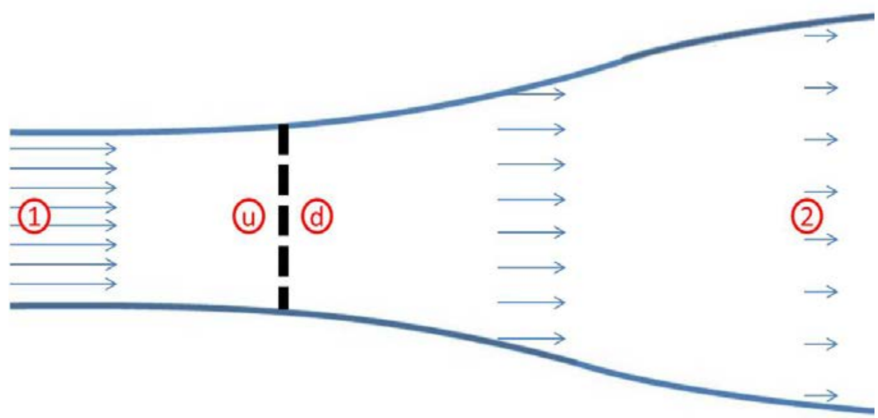

Figure 3.1: Single Rotor Actuator Disk Model Diagram.

Section (u) to (d):

Conservation of mass is solved for the infinitely thin disk with a constant area across it for incompressible flow:

$$V_u A_u = V_d A_d \rightarrow V_u = V_d \equiv V_T \,. \tag{3.11}$$

Solving the momentum equation, now with velocities set equal:

$$p_u + \rho V_u^2 - \frac{D}{A_T} = p_d + \rho V_d^2 \rightarrow \frac{D}{A_T} = p_u - p_d \,. \tag{3.12}$$

The energy equation is solved using an isentropic state relation and solved for the specific wind turbine work:

$$h_u + \frac{V_u^2}{2} - w_T = h_d + \frac{V_d^2}{2} \rightarrow -w_T = h_d - h_u = \Delta h \tag{3.13}$$

$$\Delta h_{isentropic} = \frac{\Delta p}{\rho} \rightarrow w_T = \frac{p_u - p_d}{\rho} \,. \tag{3.14}$$

Sections (1) to (u) and (d) to (2):

Bernoulli's form of the energy equation is applied to these two sections where there is no work:

$$p_1 + {}^1\!/_2\, \rho V_1^2 = p_u + {}^1\!/_2\, \rho V_u^2 \tag{3.15}$$

$$p_d + {}^1\!/_2\,\rho V_d^2 = p_2 + {}^1\!/_2\,\rho V_2^2\,. \qquad (3.16)$$

Section 2 is taken to be at a location downstream where the wake pressure has been fully recovered to the atmospheric value, so setting p_1 and p_2 equal and using the earlier result that V_u=V_d yields:

$$p_u - p_d = {}^1\!/_2\,\rho(V_1^2 - V_2^2)\,. \qquad (3.17)$$

Section (1) to (2):

The momentum equation is derived between sections (1) and (2):

$$p_1 + \rho V_d V_1 - \frac{D}{A_T} - \int_{x_1}^{x_2} p_{sides}\, dA_{x,sides} = p_2 + \rho V_d V_2\,. \qquad (3.18)$$

The integral is approximated from the known pressure relations that upstream of the turbine the pressure is above atmospheric and downstream the pressure is below atmospheric. When looking at the gage pressure this integral of the x-component of the pressure force is therefore approximated to a zero value. Solving the equation with section (1) and (2) having equal pressures and equal mass flow rates, and using the section at the disk to describe the mass flow rate since the area is known:

$$\frac{D}{A_T} = \rho V_d (V_1 - V_2)\,. \qquad (3.19)$$

A relation between the unknown velocities (V_1, V_2) is obtained by setting the two equations involving the drag (thrust) force equal and substituting the result for the disk pressure drop to relate V_1 and V_2:

$$\rho V_d (V_1 - V_2) = \frac{D}{A_T} = p_u - p_d \qquad (3.20)$$

$$\rho V_d (V_1 - V_2) = p_u - p_d = {}^1\!/_2\,\rho(V_1^2 - V_2^2) \qquad (3.21)$$

$$V_d (V_1 - V_2) = {}^1\!/_2\,(V_1^2 - V_2^2) \rightarrow V_d = {}^1\!/_2\,(V_1 + V_2)\,. \qquad (3.22)$$

Rewriting in terms of the velocity perturbation, described in Equation 3.23, yields an interesting result which will be implemented in the remaining derivation:

$$\begin{Bmatrix} V_1 \equiv U \\ V_u = V_d \equiv U - u_T \\ V_2 \equiv U - u_2 \end{Bmatrix} \tag{3.23}$$

$$U - u_T = {}^1\!/_2\left(U + (U - u_2)\right) \rightarrow \;\; u_T = {}^1\!/_2\, u_2 \tag{3.24}$$

$$u_2 = 2u_T\,. \tag{3.25}$$

This relation is used with the definition of the power coefficient to derive the value of the optimum performance:

$$w_T = \frac{p_u - p_d}{\rho} = \;{}^1\!/_2\,(V_1^2 - V_2^2) \tag{3.26}$$

$$P_T = w_T \rho V_T A_T \tag{3.27}$$

$$C_p = \frac{P_T}{{}^1\!/_2\rho U^3 A_T} = \frac{{}^1\!/_2(V_1^2 - V_2^2) * \rho V_T A_T}{{}^1\!/_2\rho U^3 A_T} \tag{3.28}$$

$$C_p = \frac{(V_1^2 - V_2^2)V_T}{U^3}\,. \tag{3.29}$$

Rewriting in the perturbation velocity format and using the relation, $u_2 = 2u_T$, found above yields the final statement for maximum power coefficient:

$$C_p = \frac{\left(U^2 - (U - u_2)^2\right)(U - u_T)}{U^3} \tag{3.30}$$

$$C_p = \left[4\left(\frac{u_T}{U}\right)^2 - 4\left(\frac{u_T}{U}\right)\right] * \left[\left(\frac{u_T}{U}\right) - 1\right]. \tag{3.31}$$

The perturbation velocity divided by the incoming velocity is defined as the axial induction factor, a. This variable represents the degree to which the incoming wind speed is slowed down by the presence of the wind turbine. Rewriting this equation and taking the derivative and setting it to zero is done to determine the optimum wind turbine performance and the axial induction factor which yields the optimum performance:

$$\frac{dC_p}{da} = (4a^2 - 4a)(1) + (a - 1)(8a - 4) = (3a - 1)(4a - 4) \stackrel{\text{def}}{=} 0\,. \tag{3.32}$$

From this optimization maxima/minima are found at a=1/3 and a=1. Calculating the power coefficient using these values reveals that the maximum theoretical C_p=16/27=59.3% occurs at an axial induction factor of a=1/3. The power coefficient is plotted versus the axial induction factor to highlight the dependency upon this variable, shown in Figure 3.2. It should be noted from Equation 3.25 that an axial induction factor greater than a=0.5 produces a backflow at region 2 which is not realistic. Therefore this model does not predict the region for a>0.5 accurately, and should not be used beyond that range.

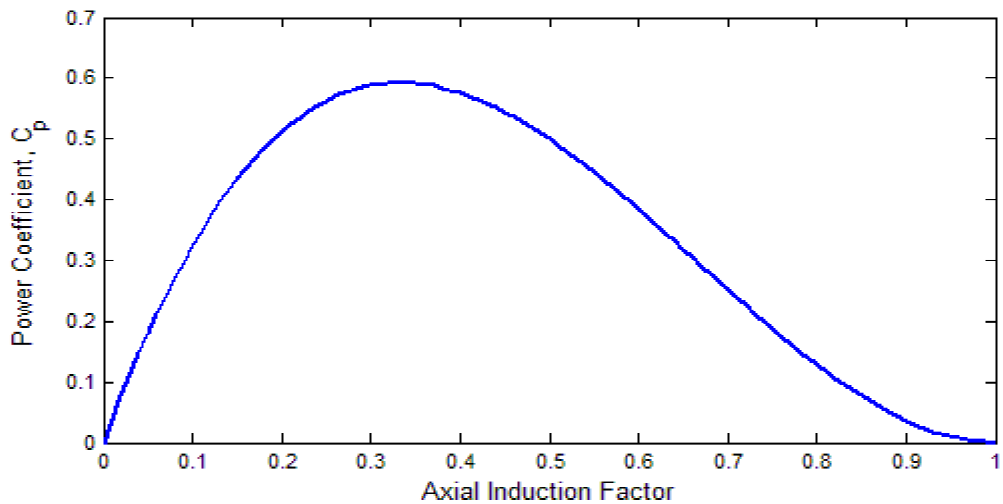

Figure 3.2: Single Rotor Actuator Disk Solution.

3.2.2 Double Rotor Wind Turbine Optimum Theoretical Performance

The actuator disk theory can be applied to the counter-rotating wind turbine case with the same approach and governing equations as used above. The results from the derivation for the single rotor are added into this analysis to simplify the following derivation. The analysis is performed with two concentric stream tubes as the boundaries. The outer stream tube produces the same optimum results as before, defined at the outer radius of the first rotor. The inner stream tube is defined at the outer radius of the second rotor at the rotor plane downstream of the first rotor. The inner stream tube is assumed to expand from a smaller area within the upstream rotor disk to the entire second rotor disk area, due to power extraction of the upstream rotor inner region. The model assumes an equal first and second rotor diameter for optimum power coefficient. Spacing between the two rotors is assumed to be sufficient to allow for full pressure recovery to atmospheric conditions between the two rotors. The results from the single disk analysis regarding the velocity at the disk plane and at the region of full pressure recovery are included initially in this analysis. The known relations for velocity are inserted into the model description, with three independent axial induction factors (a, b, c) and their relations listed, shown in Figure 3.3.

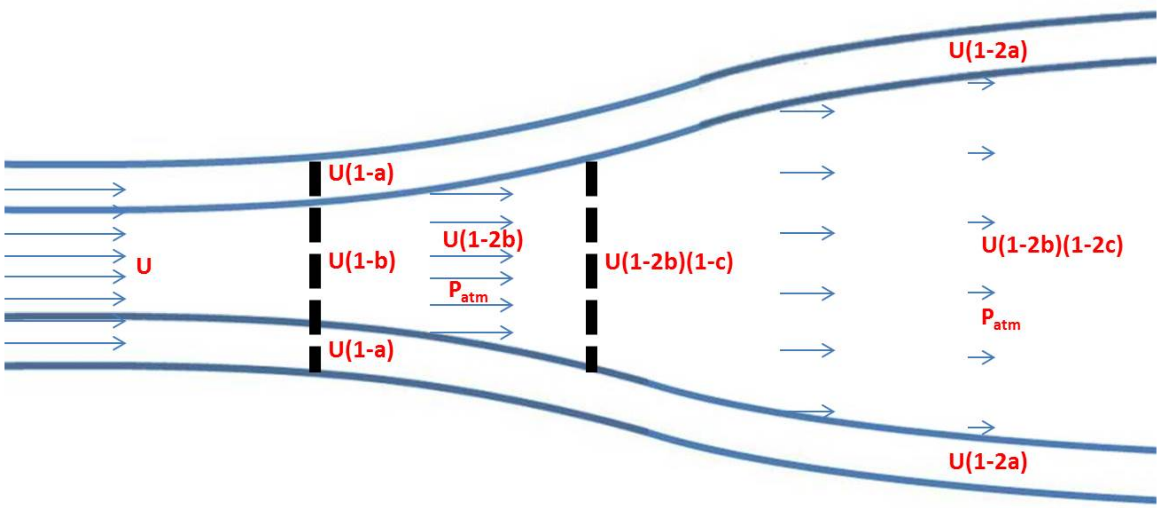

Figure 3.3: Double Rotor Actuator Disk Model Diagram.

The total power for this two-disk wind turbine comes from three contributions for this analysis. The power from the first rotor is split into the region within the inner streamtube, P_1^{in}, and from the outer portion between the two streamtubes, P_1^{out}. The power from the second rotor, P_2, is all within the inner streamtube per its definition. Each of these power components can be calculated from the energy equation within the respective streamtube derived from the locations of fully recovered atmospheric pressure upstream (location, i) and downstream (location, e) of the rotor disk. The derivation of the maximum power coefficient describing a counter-rotating wind turbine follows beginning with solving the energy equation:

$$h_i + \frac{V_i^2}{2} - w_T = h_e + \frac{V_e^2}{2} \rightarrow \;\; w_T = \frac{(V_i^2 - V_e^2)}{2} \tag{3.33}$$

$$P_{T,disk} = \dot{m} * w_{T,disk} = \rho V_{disk} A_{disk} * {}^1\!/_2 \, (V_i^2 - V_e^2)\,. \tag{3.34}$$

The 'disk' values are for the velocity and area of the respective region within the streamtubes, i.e., A_1^{in}, A_1^{out}, A_2. The power coefficient is then calculated according to its definition as follows, with the total power equaling the sum of the power produced from each of the three regions. A formula for the contribution to the power coefficient of each region is then presented:

$$C_p = \frac{P_T}{{}^1\!/_2 \rho U^3 A_T} = \frac{\sum P_{t,disk}}{{}^1\!/_2 \rho U^3 A_T} = \sum \frac{V_{disk} A_{disk} (V_i^2 - V_e^2)}{U^3 A_T} \tag{3.35}$$

$$C_{p,disk} = \frac{A_{disk}}{A_T} \frac{V_{disk}(V_i^2 - V_e^2)}{U^3}\,. \tag{3.36}$$

The power coefficients are written for each rotor using the known velocity relations in terms of the axial induction factors as described in the model:

$$C_{p,1}^{out} = \frac{A_1^{out}}{A_T} \frac{U(1-a)[U^2 - U^2(1-2a)^2]}{U^3} = \frac{A_1^{out}}{A_T} 4a(1-a)^2 \tag{3.37}$$

$$C_{p,1}^{in} = \frac{A_1^{in}}{A_T} \frac{U(1-b)[U^2 - U^2(1-2b)^2]}{U^3} = \frac{A_1^{in}}{A_T} 4b(1-b)^2 \tag{3.38}$$

$$C_{p,2} = \frac{A_2}{A_T} \frac{U(1-2b)(1-c)[U^2(1-2b)^2 - U^2(1-2b)^2(1-2c)^2]}{U^3} = \frac{A_2}{A_T}(1-2b)^3 * 4c(1-c)^2\,. \tag{3.39}$$

The total two-disk wind turbine power coefficient is the sum of each of the individual values:

$$C_p = \frac{A_1^{out}}{A_T} 4a(1-a)^2 + \frac{A_1^{in}}{A_T} 4b(1-b)^2 + \frac{A_2}{A_T}(1-2b)^3 * 4c(1-c)^2\,. \tag{3.40}$$

The optimum performance for the outer disk region of the first rotor can be solved independently of the other regions because it is not coupled to other variables. The solution for this region is the same as for the single rotor derivation, resulting in an optimum axial induction factor of a=1/3. In this formulation of the optimum counter-rotating wind turbine the two rotors have equal areas, meaning $A_2 = A_t$, and $A_1^{in} + A_1^{out} = A_t$. Adding this information into the power coefficient equation reduces the number of variables:

$$C_p = \left(1 - \frac{A_1^{in}}{A_T}\right) {}^{16}\!/_{27} + \frac{A_1^{in}}{A_T} 4b(1-b)^2 + (1-2b)^3 * 4c(1-c)^2 \,. \qquad (3.41)$$

The unknown area can be related to the rotor area by applying conservation of mass along the inner streamtube between the two rotors:

$$U(1-b)A_1^{in} = U(1-2b)(1-c)A_2 \;\rightarrow\; \frac{A_1^{in}}{A_2} = \frac{A_1^{in}}{A_T} = \frac{(1-2b)(1-c)}{1-b} \,. \qquad (3.42)$$

The fully reduced equation for calculating the optimum power coefficient is now given:

$$C_p = \left[1 - \frac{(1-2b)(1-c)}{1-b}\right] {}^{16}\!/_{27} + \left[\frac{(1-2b)(1-c)}{1-b}\right] 4b(1-b)^2 + (1-2b)^3 * 4c(1-c)^2 \,. \qquad (3.43)$$

This solution was solved and produced a maximum power coefficient of C_p = 81.4% at axial induction factors of b=0 and c=0.418. A contour plot is shown in Figure 3.4 for reference of the power coefficient variation with induction factors, b and c.

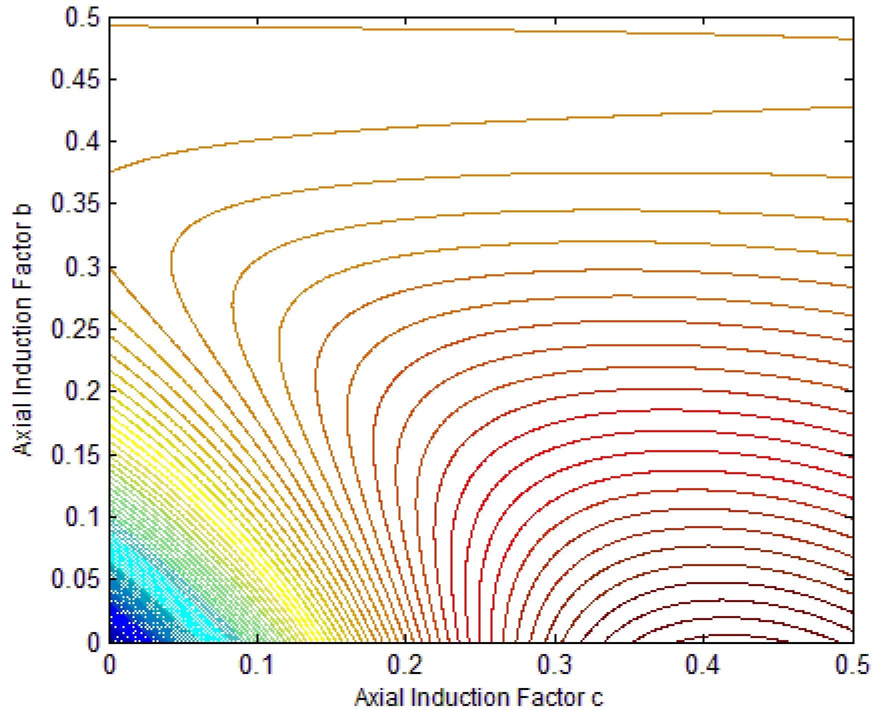

Figure 3.4: Double Rotor Actuator Disk Model Intermediate Solution.

This result produces the highest power coefficient for this model. However, a very important physical constraint is violated. The model was derived assuming power extraction from the inner region of the first rotor ($b \neq 0$) which produced the wake expansion of the inner streamtube from the inner region of the first rotor to the outer diameter of the second rotor. When the model result forces b=0 it violates the model as derived. With b=0 there will be no wake expansion of the inner streamtube because momentum is not removed by that disk. The wake expansion for b=0 would require momentum flux addition from the wall boundary, meaning the linear momentum equation is violated.

To fix this problem, an additional constraint must be added for constant momentum flux within the region of the inner streamtube between the two rotors. This region is diagrammed in Figure 3.5 with the known velocity relations restated.

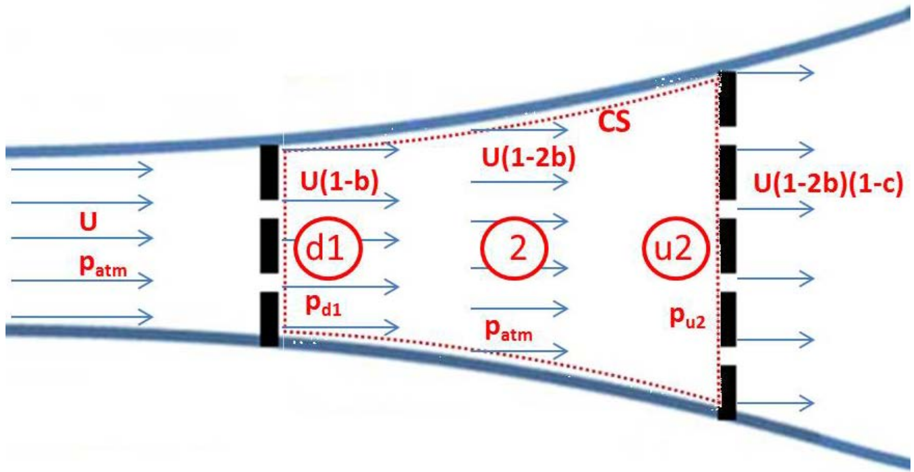

Figure 3.5: Double Rotor Actuator Disk Model Inner Streamtube Diagram.

The continuity equation is solved within the control surface region to gain a relation between the two areas:

$$\frac{A_{d1}}{A_{u2}} = \frac{V_{u2}}{V_{d1}} \,. \qquad (3.44)$$

The linear momentum equation is derived for within the control surface, Equation 3.45. The pressure at the two disks, downstream of disk 1 and upstream of disk 2, are both non-zero and the x-component of the pressure along the sides of the control surface are assumed to become negligible when using the gage pressure for all of the values. This assumption is supported as $p_{d1,g} < 0$ and $p_{u2,g} > 0$.

$$-\left(p_{u2,g}A_{u2} - p_{d1,g}A_{d1}\right) - \int_{x,d1}^{x,u2} p_{sides,g}\, dA_{sides} = \dot{m}(V_{u2} - V_{d1}) \qquad (3.45)$$

with,

$$\int_{x,d1}^{x,u2} p_{sides,g}\, dA_{sides} \approx 0 \,. \qquad (3.46)$$

Bernoulli's equation is then solved within the control surface to relate the two pressure values with known velocity relations:

$$p_{u2,g} = p_{d1,g} + {}^{1}\!/_{2}\,\rho(V_{d1}^2 - V_{u2}^2) \,. \qquad (3.47)$$

Combining these three governing equations yields the result for the inner streamtube region:

$$\frac{2p_{d1,g}}{\rho}\left(\frac{V_{d1}}{V_{u2}} - 1\right) = (V_{d1} - V_{u2})^2\,. \tag{3.48}$$

Bernoulli's formulation of the energy equation is then used to get a relation for $p_{d1,g}$, solving between the region just downstream of the first rotor to the region where the pressure is fully recovered to $p=p_{atm}$ between the two rotors:

$$^2/_\rho\, p_{d1,g} = V_2^2 - V_{d1}^2\,. \tag{3.49}$$

This result for the pressure in the upstream region within the control surface is added to Equation 3.48 and is reduced as follows:

$$(V_2^2 - V_{d1}^2)\left(\frac{V_{d1}}{V_{u2}} - 1\right) = (V_{u2} - V_{d1})^2 \tag{3.50}$$

$$\left(\frac{V_2}{V_{d1}}\right)^2 = \frac{V_{u2}}{V_{d1}}\,. \tag{3.51}$$

Inputting the velocities in terms of the axial induction factors, restated in Equation 3.52 produces the final relation which conserves momentum flux for the inner rotor region:

$$\begin{Bmatrix} V_{d1} = (1-b)U \\ V_2 = (1-2b)U \\ V_{u2} = (1-c)(1-2b)U \end{Bmatrix} \tag{3.52}$$

$$c = 1 - \left(\frac{1-2b}{1-b}\right). \tag{3.53}$$

The momentum flux constraint on the inner streamtube produces a one-to-one relationship between the two rotor disk velocities within this streamtube, meaning that they are not actually independent of each other. The power coefficient can then be solved for the two-disk model using the same formulation as before with the added constraint relating axial induction factors b and c. The solution is shown in Figure 3.6, along with the dependence of factor c upon b. Due to the constraint, b only has a solution up to where is produces a value for $c < 0.5$, therefore $b \leq 1/3$. The optimum power coefficient for a double rotor, counter-rotating wind turbine as corrected predicts a C_p = 66.9% for b=0.196, with corresponding c=0.244.

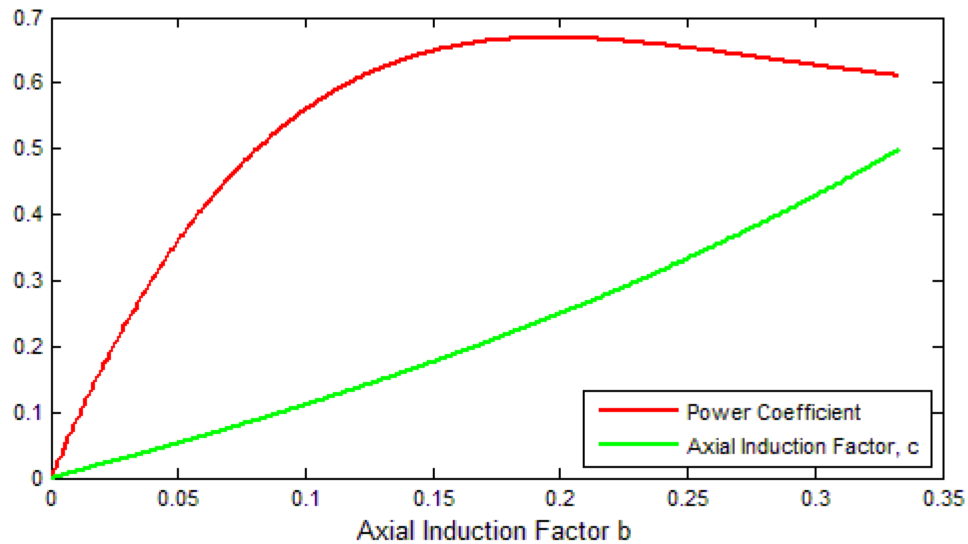

Figure 3.6: Double Rotor Actuator Disk Model Final Solution.

3.3 Wind Turbine Wake Modeling

Wind turbine operation in a wind farm setting exposes the turbines to several wake scenarios which all reduce the performance of the downstream turbine. Considering a rectangular layout there will be wake operation from the nearest aligned upstream wind turbine, wake operation in multiple upstream wind turbines, and there are lateral wakes from other wind turbines which alter the aligned wakes. Analytical models are derived and discussed in Sections 3.3 which describe these different wake scenarios and how they relate to wind turbine performance losses.

3.3.1 Wind Turbine Single Wake Model

The wake behind a wind turbine can be approximated analytically with some simplifying assumptions. The first assumption is for one-dimensional, inviscid, steady flow. This assumption treats the wake velocity as a uniform velocity at some deficit value in every region behind the wind turbine. The second major assumption addresses wake expansion and estimates this process with a linear approximation. The slope of this approximation is called the wake decay constant, k, commonly defined to have a value of 0.1 for wind farms on land. The model produced from these assumptions is shown in Figure 3.7.

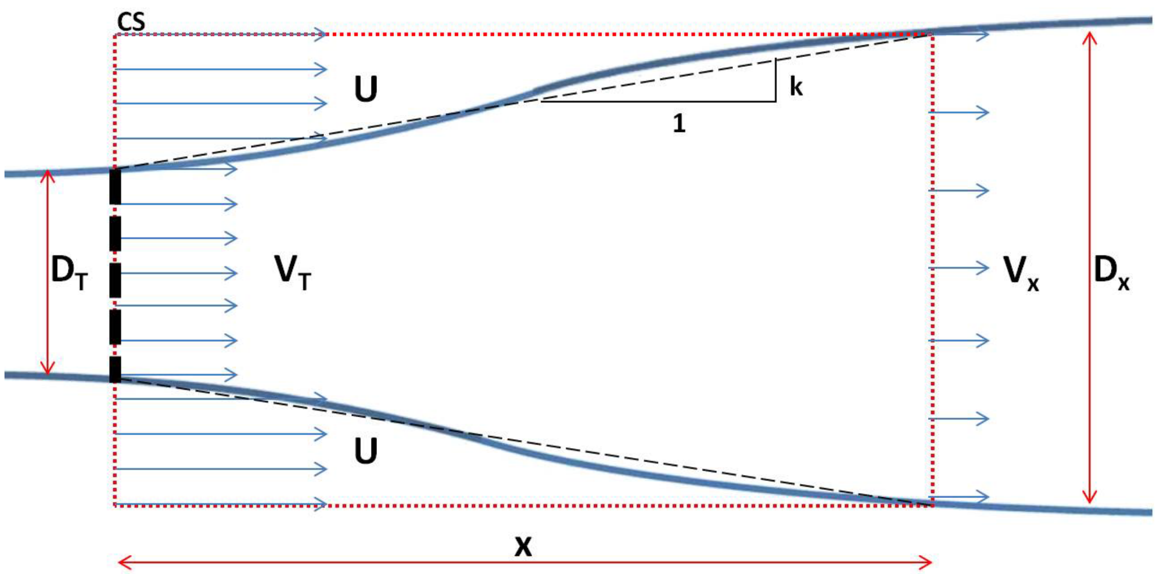

Figure 3.7: Single Wake Model Diagram.

To predict the energy losses arising from operation in the wake of upstream wind turbines, the velocity at the location of the downstream turbine plane is needed. The linear wake model can be used to predict that velocity loss, using the continuity equation to relate the unknown variables to the known variables, resulting in Equation 3.56 for the wake velocity ratio, V_x/U:

$$\int_{CS} \rho \vec{V} \cdot d\vec{A} = 0 \rightarrow \sum \rho_i V_i A - \rho_e V_e A = 0 \qquad (3.54)$$

$$U\,{}^{\pi}/_{4}\,(D_x^2 - D_T^2) + V_T\,{}^{\pi}/_{4}\,D_T^2 - V_x\,{}^{\pi}/_{4}\,D_x^2 = 0 \qquad (3.55)$$

$$1 - \frac{V_x}{U} = \left(\frac{D_T}{D_x}\right)^2 \left(1 - \frac{V_T}{U}\right). \tag{3.56}$$

This standard derivation isn't actually calculating a streamtube analysis for the wake, because by the formulation mass flow crosses the linear wake expansion boundary. This model is written such that there is no mass transfer from the outer cylindrical surface, meaning that all of the momentum in the upstream, undisturbed region is transferred into the wake region, adding significantly to the velocity predicted downstream and causing this velocity to increase with x. This assumption is at least qualitatively valid because momentum will be added from the atmosphere. A concern, however, is that the model formulation is inconsistent for this reason between the control surface used for solving continuity versus the control surface used in solving the linear momentum equation, due to mass transfer across the wake in the continuity equation.

The actuator disk analysis described in Section 3.2 can be used to produce a relation for the velocity just downstream of the rotor plane to the incoming freestream velocity, V_T/U. This relation is put in terms of the thrust coefficient, and is written using consistent nomenclature in Equation 3.64.

Relevant results from the Actuator Disk theory in consistent nomenclature are restated in Equations 3.57-59.

$$\frac{D}{A_T} = p_u - p_d \tag{3.57}$$

$$p_u - p_d = {}^1\!/_2\, \rho(U^2 - V_x^2) \tag{3.58}$$

$$\frac{D}{A_T} = {}^1\!/_2\, \rho(U^2 - V_x^2) \;\rightarrow\; \frac{D}{{}^1\!/_2 \rho U^2 A_T} = C_T = 1 - \left(\frac{V_x}{U}\right)^2. \tag{3.59}$$

This produces a relation between the wake velocity and thrust coefficient, Equation 3.60. Using the axial induction factor definition and results from the single rotor analysis in Section 3.2 produces the value of a as follows:

$$\frac{V_x}{U} = \sqrt{1 - C_T} \tag{3.60}$$

$$\frac{V_x}{U} = \frac{(1-2a)U}{U} = \sqrt{1 - C_T} \tag{3.61}$$

$$a = \begin{Bmatrix} {}^{1}\!/_{2}\left(1 - \sqrt{1 - C_T}\right) & 0 \leq a \leq 0.5 \\ {}^{1}\!/_{2}\left(1 + \sqrt{1 - C_T}\right) & 0.5 < a \leq 1 \end{Bmatrix}. \tag{3.62}$$

For standard wind turbine operation we are only interested in the region where $a \leq 0.5$, so this result is combined with the known velocity relations in solving for the wind turbine rotor plane velocity ratio:

$$\frac{V_T}{U} = \frac{(1-a)U}{U} = 1 - {}^{1}\!/_{2}\left(1 - \sqrt{1 - C_T}\right) \tag{3.63}$$

$$\frac{V_T}{U} = {}^{1}\!/_{2}\left(1 + \sqrt{1 - C_T}\right). \tag{3.64}$$

This is the correct result according to the model formulation for the velocity ratio relation to thrust coefficient. It however is a different value than that used in the standard Jensen linear wake model, and differs by the factor of 1/2. Because this is a model approximating the wake behavior, the wake decay constant can be adjusted to cause either formulation to closely agree with the experimental data of performance losses versus spacing. In order to more accurately predict the physical wake decay constant, however, it is best to use the correct physics as derived in Equation 3.64. The limitations here are that the model already contains approximations which likewise affect the result agreement to the physical values.

Substituting the new turbine plane velocity relation into the governing continuity equation produces the final result for this model, Equation 3.69, which again varies by the same factor of 1/2 from the standard Jensen model. This means that for the same input conditions the Jensen estimated velocity deficit (U-V_x) will be reduced by a factor of 2. To compensate and achieve the same velocity deficit at x requires that k be decreased. This means that the physics from the new formulation of the wake model require smaller wake decay constants, therefore predicting lower wake expansion. The revised formulation of the single wake model is derived as follows:

$$1-\frac{V_x}{U}=\left(\frac{D_T}{D_x}\right)^2\left(1-\frac{V_T}{U}\right)=\left(\frac{D_T}{D_x}\right)^2\left(1-{}^1/_2\left(1+\sqrt{1-C_T}\right)\right) \tag{3.65}$$

$$1-\frac{V_x}{U}=\left(\frac{D_T}{D_x}\right)^2\left({}^1/_2-{}^1/_2\sqrt{1-C_T}\right) \tag{3.66}$$

$$1-\frac{V_x}{U}={}^1/_2\left(\frac{D_T}{D_x}\right)^2\left(1-\sqrt{1-C_T}\right) \tag{3.67}$$

$$\frac{D_T}{D_x}=\frac{D_T}{D_T+2kx}=\frac{1}{1+2k^x/_{D_T}} \tag{3.68}$$

$$1-\frac{V_x}{U}={}^1/_2\frac{1-\sqrt{1-C_T}}{\left(1+2k^x/_{D_T}\right)^2}\,. \tag{3.69}$$

In this equation, maximum velocity losses are associated with a thrust coefficient of 1. As stated above, the thrust coefficient relates to the axial velocity drop from freestream to the rotor plane. A thrust coefficient of one corresponds to complete energy extraction of the incoming freestream, which is never actually realized. In this analysis, the maximum C_T used was that corresponding to the optimum wind turbine performance predicted at an axial induction factor of 1/3. Beyond this value the turbine operates in what is known as the turbulent windmill state, where the axial induction factor increases (axial velocity at the rotor plane decreases) but does so with negative results for the power coefficient. This is a very uncommon domain to operate within for a wind turbine, and won't be of interest to this research so it is not considered. Equation 3.64 above is used to determine the thrust coefficient for a given rotor axial induction factor:

$$C_T = 1-(1-2a)^2\,. \tag{3.70}$$

Solving this relation using the optimum axial induction factor corresponding to maximum power coefficient, a=1/3, yields a maximum thrust coefficient of $C_{T,max}$=0.89. A relationship between the thrust coefficient and wind speed was given generically by Frandsen, and is thought to fit for most modern wind turbines [38]. This relationship is used in the calculation of the wake velocity deficit to illustrate its dependence on the incoming wind speed. This relationship was used only when the thrust coefficient produced remained below 0.89:

$$C_T = \frac{3.5(2V_x - 3.5)}{V_x^2}. \tag{3.71}$$

The velocity loss in the wake, at spacing x, according to this model is illustrated in Figure 3.8, with various values of C_T compared, with a wake decay constant of k=0.07.

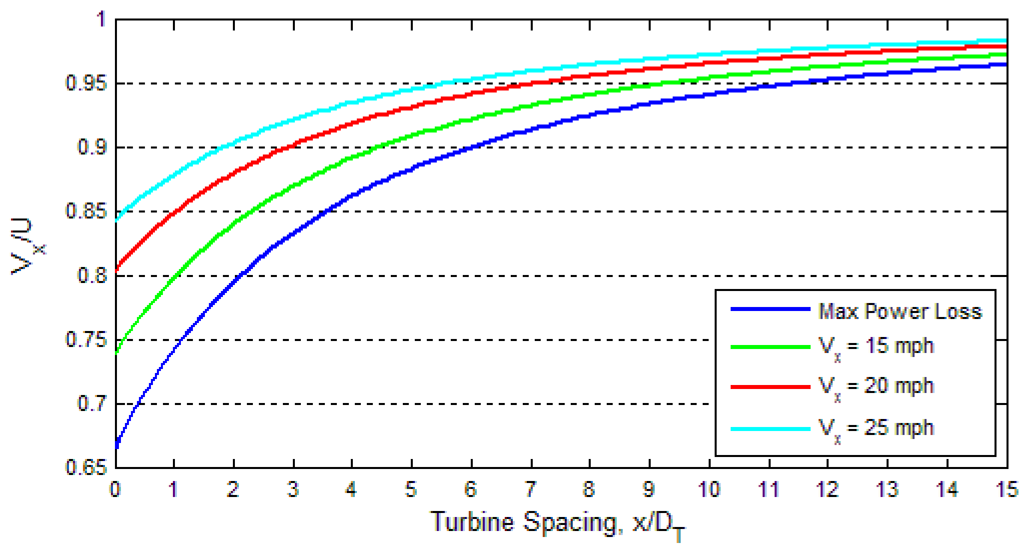

Figure 3.8: Single Wake Model Velocity Deficit, Revised Formulation.

The calculated velocity deficit can be used to determine the power deficit when the turbine power's relationship to the wind speed is known. The generic wind turbine power curve is described below [39], where V_C, V_R, V_F, and P_R all describe the wind turbine performance and are the cut-in speed, rated-speed, cut-out speed, and rated power. The exponent n describes the power relationship and typically has a value of 2 to 3:

$$P_T(U) = \begin{Bmatrix} 0 & U < V_C \\ P_R\left(\frac{U^n - V_C{}^n}{V_R{}^n - V_C{}^n}\right) & V_C \le U \le V_R \\ P_R & V_R < U \le V_F \\ 0 & U > V_F \end{Bmatrix}. \tag{3.72}$$

Using this relationship for the operation range ($V_C \le U \le V_R$) of the turbine, a relationship is derived between the velocity deficit and the power deficit as follows:

$$\frac{P_x}{P_{ref}} = \left(\frac{V_x}{V_{ref}}\right)^n . \tag{3.73}$$

For this analysis the exponent, n, is needed to derive the wake performance losses and is found for the Southwest Windpower Whisper 100 turbine, the wind turbine used in the Micro Reconfigurable Wind Farm. From Figure 3.9, it is seen that this turbine's power curve more closely follows the n=2 relationship.

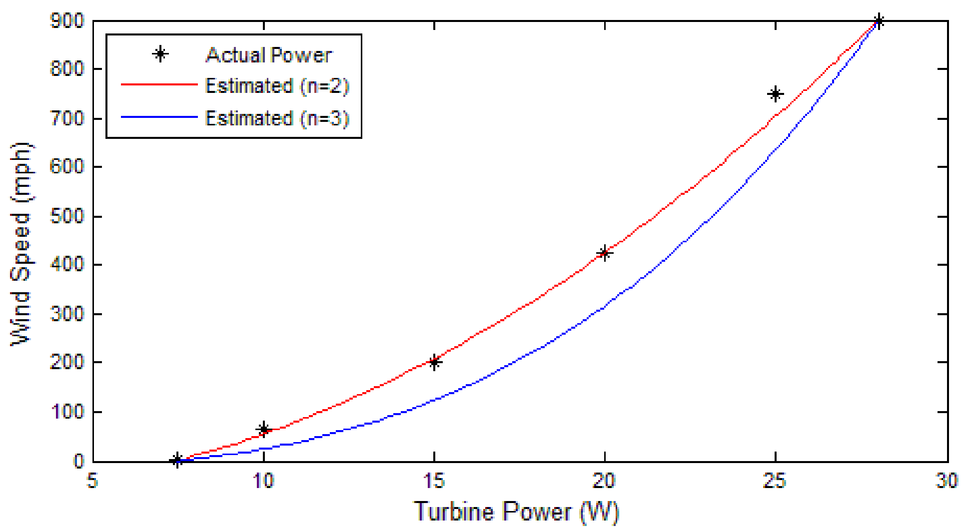

Figure 3.9: Whisper 100 Power Curve Velocity Relationship.

Using this value for n and the relationship from Equation 3.69, the power deficit was determined for the revised formulation when operating in a wake from another wind turbine spaced x/D upstream, as illustrated in Figure 3.10.

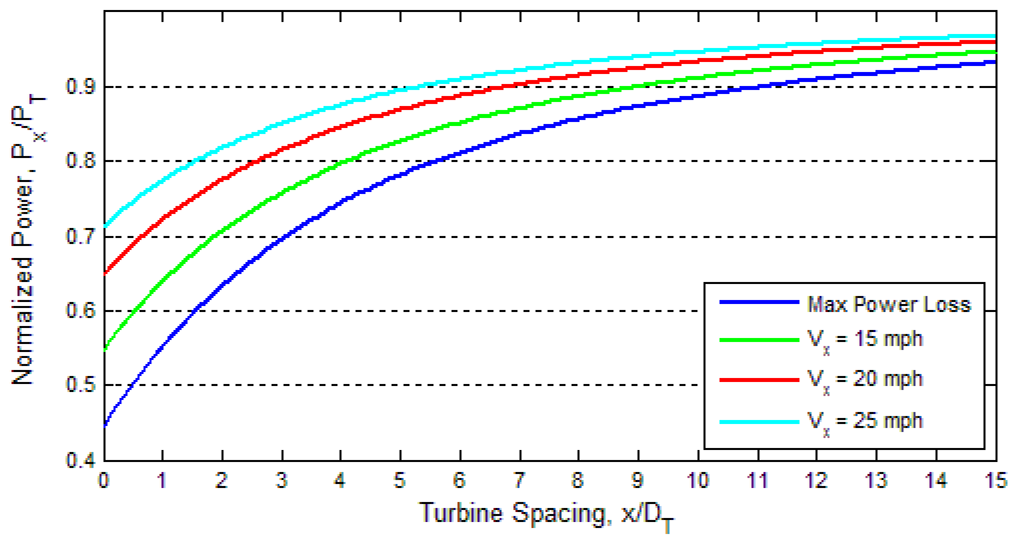

Figure 3.10: Single Wake Model Normalized Power, Revised Formulation.

Using the standard Jensen model formulation for the wind turbine wake performance losses, listed in Equation 3.74, with a wake decay constant of k=0.07 is shown Figure 3.11 for comparison.

$$1 - \frac{V_x}{U} = \frac{1-\sqrt{1-C_T}}{\left(1+2k^{x}/_{D_T}\right)^2}. \tag{3.74}$$

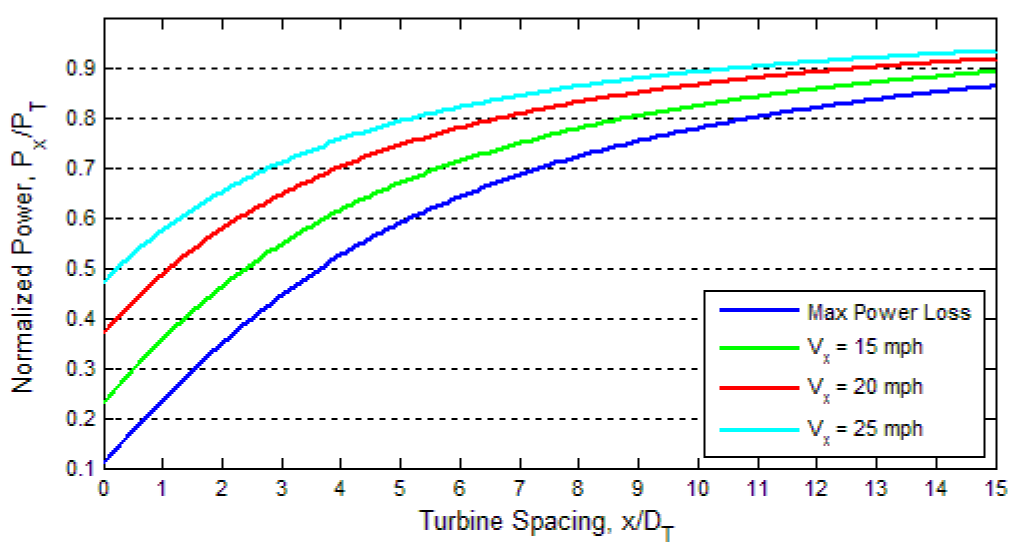

Figure 3.11: Single Wake Model Normalized Power, Jensen Formulation.

Estimates using the two models with the same wake decay constant produce results which are similar for larger turbine-turbine spacing's, however predictions vary significantly at low spacing's. The Jensen formulation predicts overall higher performance losses than the revised formulation. This result requires lower wake decay constants be used with the revised formulation to yield the same loss as the Jensen model at any given spacing.

3.3.2 Wind Turbine Multiple Wake Model

The performance of a wind turbine operating within wakes from multiple upstream wind turbines will be modeled using the single wake model and a sum of squares method, shown in Equation 3.75. A diagram of this multiple wake scenario using the nomenclature is given in Figure 3.12.

$$\left(1-\frac{V_x}{U}\right)^2=\sum_i\left(1-\frac{V_{x,i}}{U}\right)^2. \tag{3.75}$$

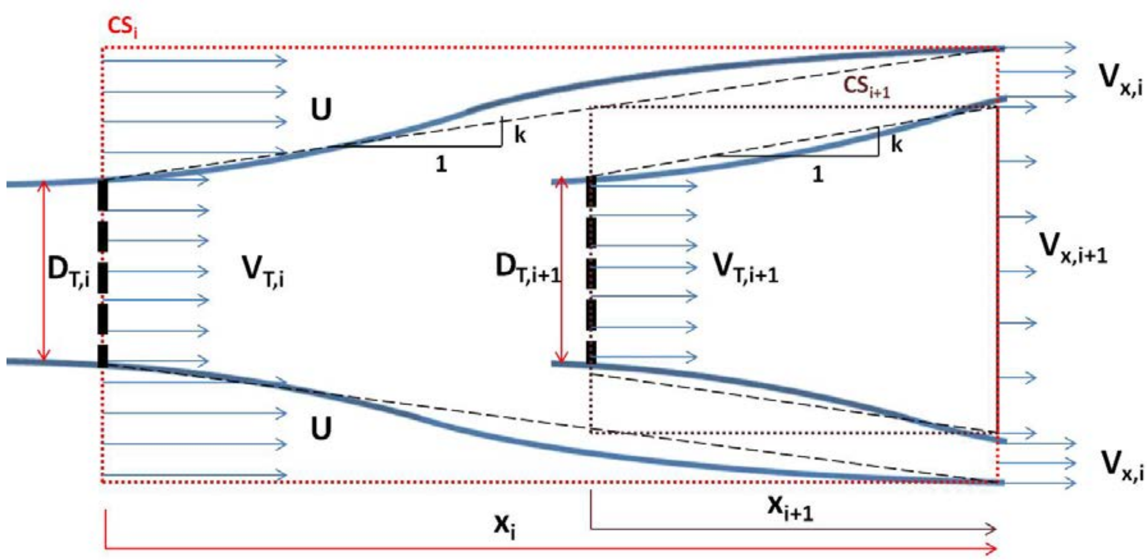

Figure 3.12: Multiple Wake Model Diagram.

This method is widely used and commonly accepted, and produces at least qualitatively correct results for a given spacing. This approach treats the multiple-wake interaction on the downstream turbine as the sum of squares combination of multiple single wake interactions at the respective spacing from the upstream turbines. This model is purely mathematical in its derivation to generate a desired trend, but does so with sufficient agreement. The model therefore does not necessarily accurately describe the physics of the multiple wake scenario.

Using the single wake model formulation in Equation 3.69, the multiple wake scenario results are found and displayed in Figure 3.13 for three different turbine spacing's. In these calculations, the thrust coefficient is treated as a constant for each of the upstream wind turbines, at the maximum value C_T=0.89 used previously. This assumption is not necessarily correct as the turbines operating within a wake do so at a reduced performance, meaning less velocity is extracted and therefore less thrust produced on the turbine. Additionally, the wake decay constant is assumed to be a constant in this analysis on each of the upstream wind turbine wakes, set to k=0.07. This again is not a necessary assumption, but a simplifying one given that the variation of the wake decay constant is not known with turbine number.

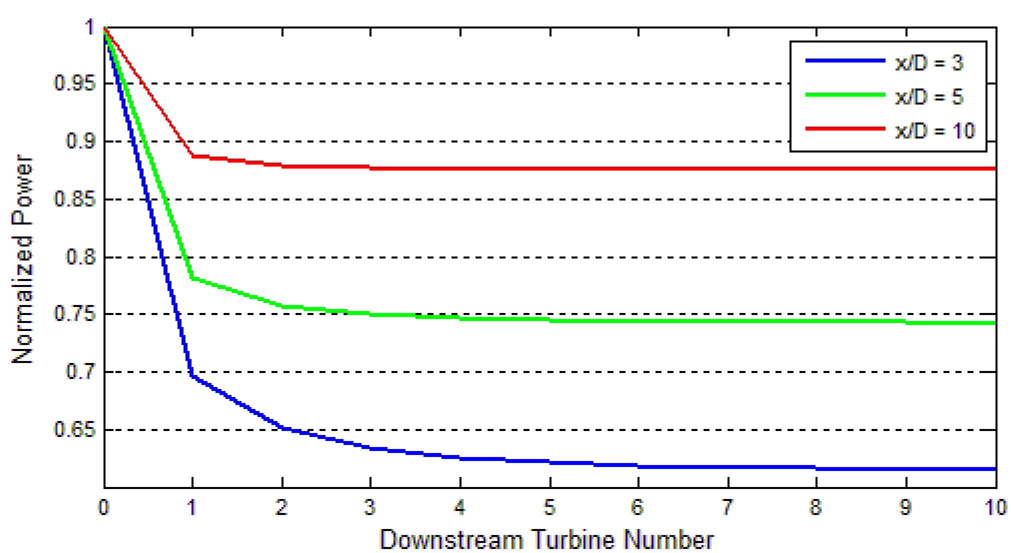

Figure 3.13: Multiple Wake Model Power Deficit, Revised Formulation.

This analysis is performed using the standard Jensen linear wake model with a wake decay constant k=0.1 and is included in Figure 3.14.

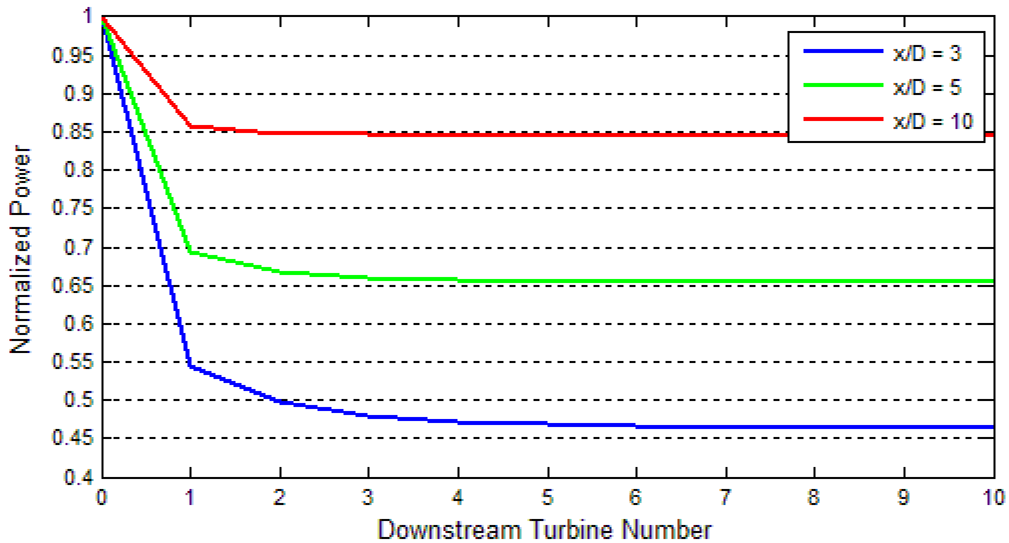

Figure 3.14: Multiple Wake Model Normalized Power, Jensen Formulation.

3.3.3 Wind Turbine Lateral Wake Model

Another scenario that is present in large wind farms is to have lateral upstream wind turbines whose wakes aren't necessarily operated within but which affect the wake of the upstream, aligned wind turbine(s). The model, shown in Figure 3.15, is for a single wake scenario with the downstream turbine at a location, $x = s^*D_T$, downstream, with lateral wakes produced upstream from wind turbines at a location, $y = w^*D_T$, on either side of the upstream wind turbine. The lateral wakes produce symmetry planes which suppress wake expansion in the lateral direction beyond the x-location where the upstream lateral wakes merge. Multiple upstream wake scenarios with lateral wakes would be treated using the resultant single wake scenario with lateral wakes and the sum of squares formulation in Section 3.3.2.

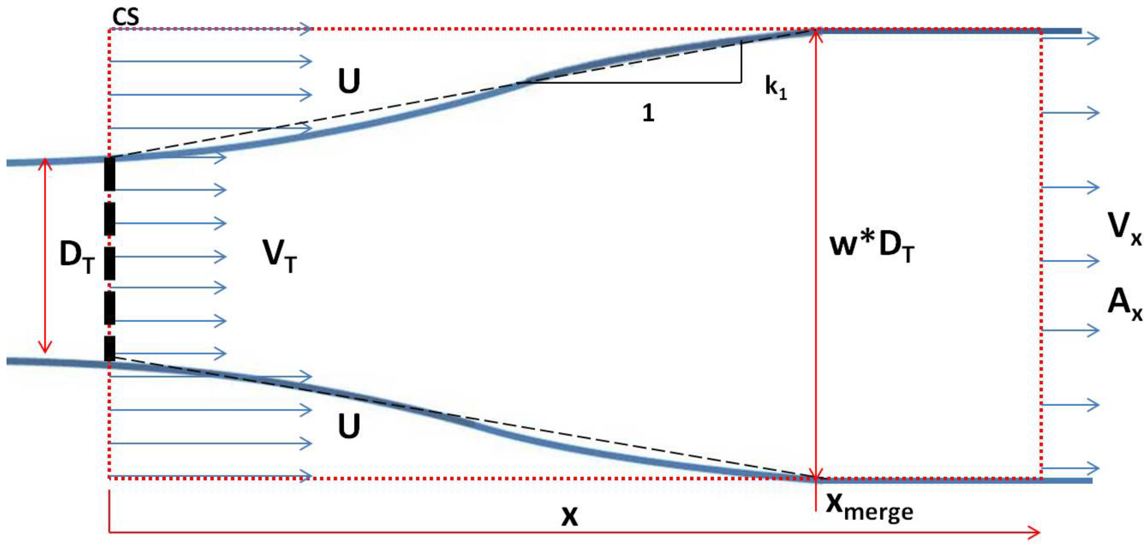

Figure 3.15: Lateral Wake Model Diagram.

In this model, the lateral wakes begin to interact with each other starting at a distance from the upstream rotor of x_{merge} as defined:

$$D_T + 2k_1 x_{merge} = wD_T \quad (3.76)$$

$$x_{merge} = \frac{w-1}{2k_1} D_T \; . \quad (3.77)$$

For $x < x_{merge}$ the model behaves identically to the single wake model described in section 3.3.1, only with a new wake decay constant k_1, which is expected to have a lower value than in the single wake scenario due to the lateral wakes suppressing expansion. When $x > x_{merge}$, the area at the downstream turbine plane needs to be corrected for the presence of lateral wakes. This model treats the presence of the lateral wakes in two ways; using a reduced wake decay constant which accounts for wake suppression due to the symmetry plane, and by including a variation in the area calculation beyond $x>x_{merge}$ which removes the symmetry overlap area. A schematic showing a front view of the wake expansion beyond $x>x_{merge}$ is presented in Figure 3.16, defining the symmetry overlap area, A_{sym}.

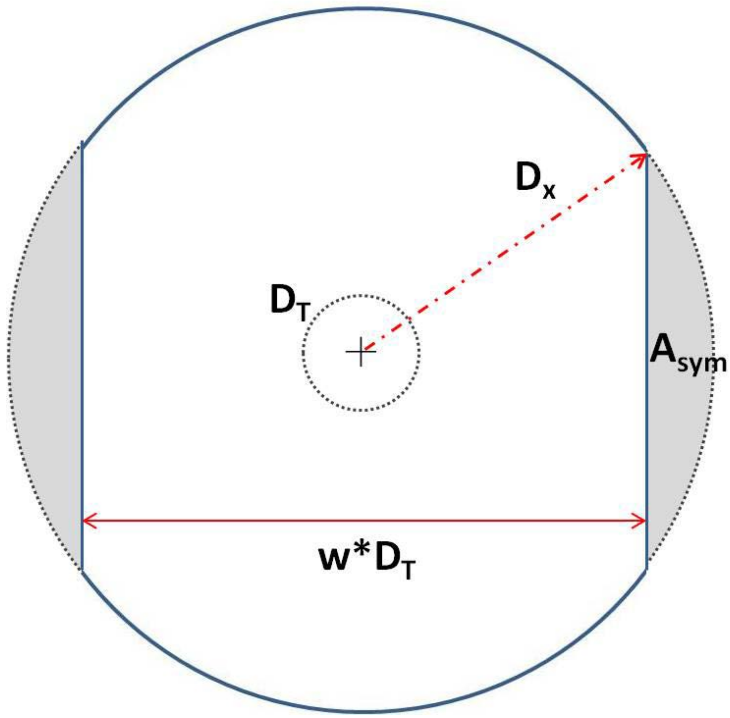

Figure 3.16: Lateral Wake Model Merged Wake Area.

The area calculation of the downstream turbine section, at location x, is piecewise defined as presented in Equations 3.78-79. Additionally, the model formulation allows for a different wake decay constant for the two regions, k_1 and k_2, to account for potential increased expansion in region $x>x_{merge}$:

$$A(x) = \begin{Bmatrix} \pi/_4 D_x^2 & x < x_{merge} \\ \pi/_4 D_x^2 - A_{sym} & x \geq x_{merge} \end{Bmatrix} \tag{3.78}$$

$$D(x) = \begin{Bmatrix} D_T + 2k_1 x & x < x_{merge} \\ wD_T + 2k_2(x - x_{merge}) & x \geq x_{merge} \end{Bmatrix}. \tag{3.79}$$

The symmetry overlap area is found by assuming a constant radial expansion with x, and defined as the total area outside of the symmetry planes produced by the laterally spaced wakes, located at $y = \pm wD_T/2$:

$$A_{sym} = \pi/_4 D_x^2 \times \frac{\alpha}{180} - 1/_2 (wD_T)^2 \tan(\alpha/_2) \tag{3.80}$$

where,

$$\alpha = 2\cos^{-1}\left(\frac{wD_T}{2D_x}\right). \tag{3.81}$$

The lateral wake model is now the combination of the single wake model from Section 3.3.1, written using the area ratio, and the lateral wake dependent downstream area from Equation 3.78. This model is described by Equation 3.82, with results plotted using the Jensen formulation in Figure 3.17 for varying axial and lateral wind turbine spacing, with $k_1 = k_2 = 0.1$.

$$1 - \frac{V_x}{U} = \beta\left(\frac{A_T}{A(x)}\right)\left(1 - \sqrt{1 - C_T}\right) \tag{3.82}$$

$$\beta = \begin{Bmatrix} 1/2 & Revised \\ 1 & Jensen \end{Bmatrix}. \tag{3.83}$$

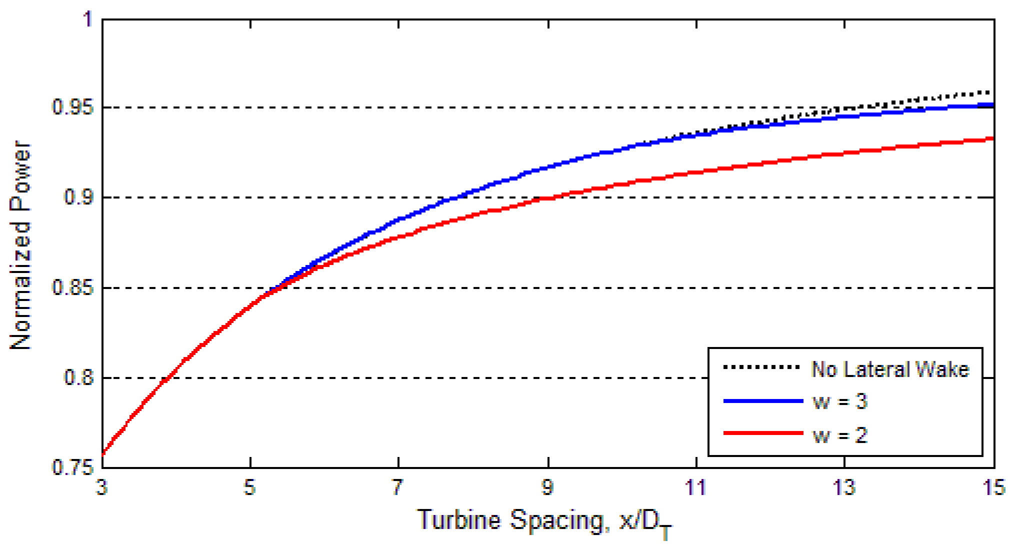

Figure 3.17: Lateral Wake Model Normalized Power, Jensen Formulation.

Based solely on these results, it seems as though this wake scenario produces negligible additional performance losses compared to simply a single wake model without lateral wind turbines. However, this plot only accounts for one expected component of the performance losses due to lateral wakes, the area change due to symmetry planes. The second component of the lateral wake loss is due to wake suppression, modeled with a reduction in the wake decay constant, k_1. Variation of the wake decay parameter for a single wake analysis is shown to change the results more significantly than with the area change due to lateral wakes alone, shown in Figure 3.18. This alteration of the upstream wake that acts on the downstream wind turbine is expected to dominate the results, more so than the area reduction due to symmetry. Comparison to experimental results will reveal the significance of wake suppression compared to area reduction by comparison to Figure 3.17.

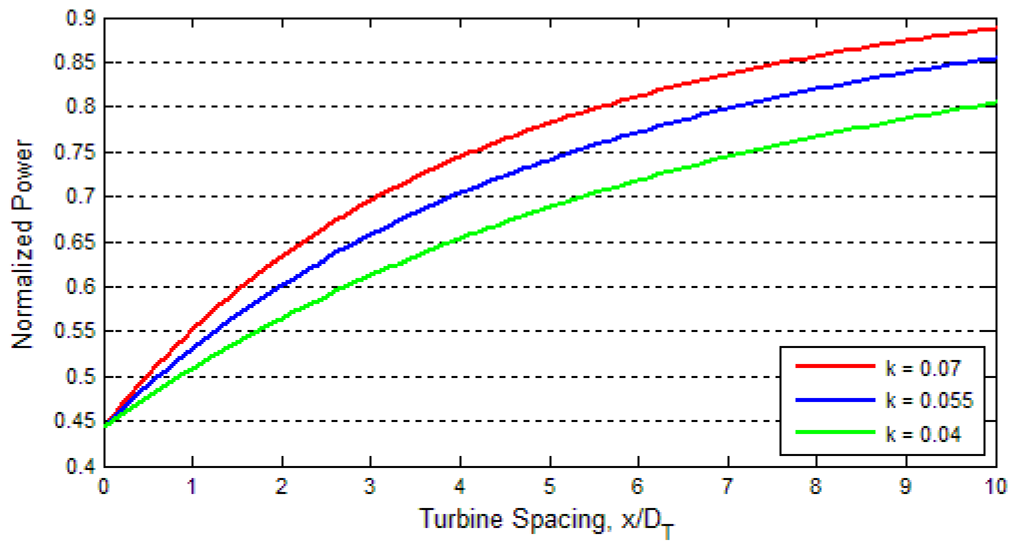

Figure 3.18: Single Wake Model with Varying Wake Decay Constants.

3.4 Micro Reconfigurable Wind Farm Technical Approach

The Micro Reconfigurable Wind Farm is purposed for quantifying wake interaction of wind turbines in farm array settings. The four turbines belonging to this facility are configured appropriately to measure this interaction for the three test cases modeled in Sections 3.3. The processes for acquiring and analyzing data collected from the facility's experiments will be described in detail in Sections 3.4.

3.4.1 Micro Reconfigurable Wind Farm Data Acquisition

Wake interaction data acquisition is accomplished by positioning the wind turbine carts in the desired test case array on a sufficiently windy day. Days with a minimum of a 15mph average wind speed were required, with a higher average typically meaning more usable data would be collected. Data acquisition requires that the turbine-turbine interaction axis be aligned with the wind direction so that the center of the upstream wake hits the center of the downstream turbine within an acceptable tolerance for that test case. Repositioning of the wind turbines to maintain alignment with shifting wind direction would be necessary on most days.

The two instrumented wind turbines are always positioned to measure the power of the upstream turbine and of the furthest downstream turbine, to produce its normalized power. The two wake generating wind turbines are used to create additional test cases while measuring the normalized power on the wind turbine of interest. In all of the test cases the upstream instrumented turbine is the same and is stationary, and the other turbines are positioned around it. It was observed that the downstream turbines would behave erratically and yaw significantly out of the wind direction when operating within the wake of the upstream turbine. This was addressed by attaching "yaw collars" on all but the upstream instrumented wind turbine which prevented yaw rotation on these turbines. A yaw collar wasn't used on the upstream instrumented wind turbine so that it could rotate with the wind, in order to observe periods of alignment.

The single wake test case uses the two instrumented wind turbines to quantify the effect that spacing from an upstream wind turbine has on performance losses, when operating within its wake. The test is performed by testing one or multiple spacing's on the same day and by testing each of the spacing's on multiple days. This test case is diagrammed in Figure 3.19.

Figure 3.19: Single Wake Test Case Layout.

The multiple wake test case adds wind turbines between the instrumented turbines to quantify additional losses due to turbines further upstream and wake persistence in the array setting. The wake generating turbines extract power from the air additional to the upstream instrumented wind turbine so that the downstream instrumented wind turbine operates within the combined wake of both upstream wind turbines. Due to the low predicted magnitude of the loss after the third wind turbine combined with the experimental limitations on accuracy, this scenario was used for two wake number tests only. The configuration for this test case is shown in Figure 3.20.

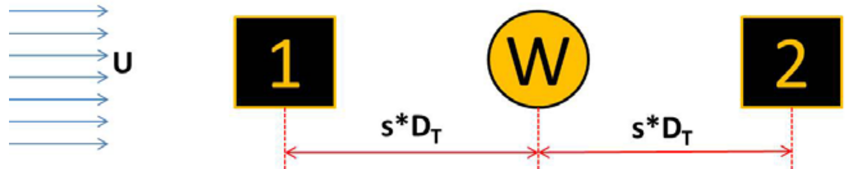

Figure 3.20: Multiple Wake Test Case Layout.

The lateral wake test case complements the single wake test case by combining its effect with wind turbines upstream perpendicular to the turbine-turbine wake interaction axis spaced from the axis. This case quantifies the effect of having lateral wakes which suppress wake expansion and wake recovery from atmospheric momentum addition. This case tests both the axial spacing and lateral spacing independently, and its layout is shown in Figure 3.21.

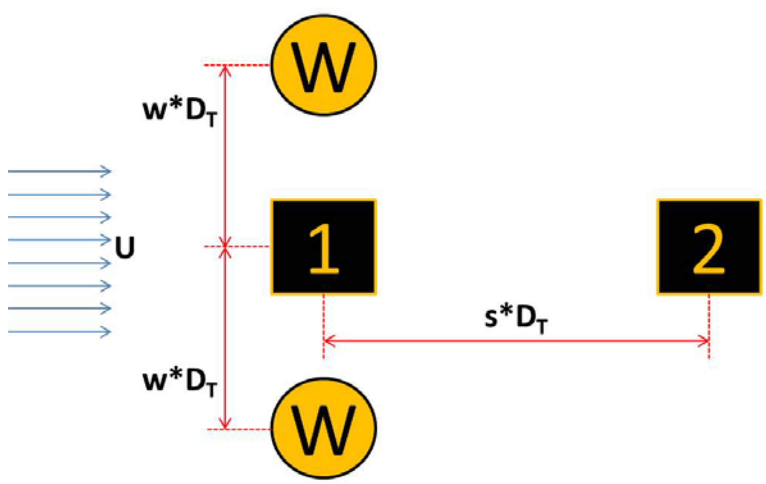

Figure 3.21: Lateral Wake Test Case Layout.

Instrumented wind turbine sensor output was recorded independently on the two instrumented wind turbines and logged to removable memory drives on the DAQ systems. The DAQ system is set with a sample frequency of f_s= 4-hz. White noise is seen on the channels from the DAQ hardware and is eliminated by adding an averaging feature on the affected channels which reduces the 10-khz internal DAQ sample rate to the 4-hz sample rate by averaging the full data set into the samples. For the torque sensor channels this is done after first low-pass filtering the signals at f_c= 200-hz. The cut-off frequency of this filter was chosen after sampling at f_s=2500-hz and looking at the torque signal spectrum to locate forcing frequencies, and was chosen to be sufficiently above the highest input forcing frequency. The digital encoder signal is converted to a rotor rotational speed using a digital frequency channel and the A and A^* reciprocal channels. Encoder frequency was determined using the DAQ system's digital method which sums the number of encoder counts and the time from the first edge to the last edge within a selected 1-sec time window. This produces accurate rotational speed measurements every 1-sec. Wind condition measurements are received at the anemometer's maximum output rate of 1-hz. The anemometer has two analog current output channels which were set to output the actual wind speed and actual wind direction (channels 400 and 500). The wind speed output range was set to [0.3, 25] m/s corresponding to the [4, 20] mA sensor output. Wind direction range was set to [0, 359.9]° with 0° representing wind from the North, 90° for wind from the East, and so on. The channel properties for the data acquisition are summarized in Table 3.1.

Table 3.1: Data Acquisition Channel Properties.

Sensor	**Channel Type**	**Range**	**Additional Information**
Encoder	Frequency 2-wire		Time Base = 1-sec
Torque	Analog Input	[10, 20] mA	Average/Auto; 200-hz LPF
Battery Voltage	Analog Input	[-1, 10] V	Average/Auto
Battery Current	Analog Input	[-1, 10] V	Average/Auto
Wind Speed	Analog Input	[4, 20] mA	No Filter
Wind Direction	Analog Input	[4, 20] mA	No Filter
Align Logic	Analog Input	[-1, 10] V	Average/Auto

Data are recorded constantly from the two DAQ units, however, the wind direction doesn't necessarily always line up with the array layout. Status of this alignment was stored in the logged data using a switch which sends a voltage to the DAQ unit on the downstream instrumented turbine for positive alignment. The switch is controlled manually by an operator sitting along the turbine-turbine interaction axis downstream of the downstream instrumented turbine. Alignment is checked visually, and required the wake center to be less than 1-2 feet off-axis of the downstream wind turbine for close to far axial spacing's. The condition was stored in the "Align Logic" variable.

3.4.2 Micro Reconfigurable Wind Farm Data Analysis

In order to determine the wake operation performance loss from the experiments, the time-stamped data from the DAQ systems on the instrumented wind turbines need to be time synchronized and converted from the analog values to the sensor physical values. The conversion procedure for each sensor is listed in Table 3.2.

Table 3.2: Sensor Conversion to Physical Values.

Sensor	Analog Value	Conversion	Physical Value
Encoder	counts/sec	(A*600/60)	rpm
Torque	mA	(A- τ_0)*300/8	lb-in
Battery Voltage	V	(A*7)	volts
Battery Current	V	(A-I_0)*50/10	amps
Wind Speed	mA	(A-4)*24.7/16+0.3	m/s
Wind Direction	mA	(A-4)*360/16	degrees from N

The measured physical values are used to describe the wind turbine performance in two ways. The first measure is the aerodynamic power. This power is the total power from the wind removed by the wind turbine, and is the product of the torque and rotational speed on the rotor:

$$P_{T,aero} = \tau_{rotor}\Omega_{rotor} \,. \tag{3.84}$$

A sample data set of the constituents of the aerodynamic power is shown in Figure 3.22. The minor fluctuations in the torque sensor zero level for the two sensors would be determined in part from this data at times where the physical torque on the rotor is zero.

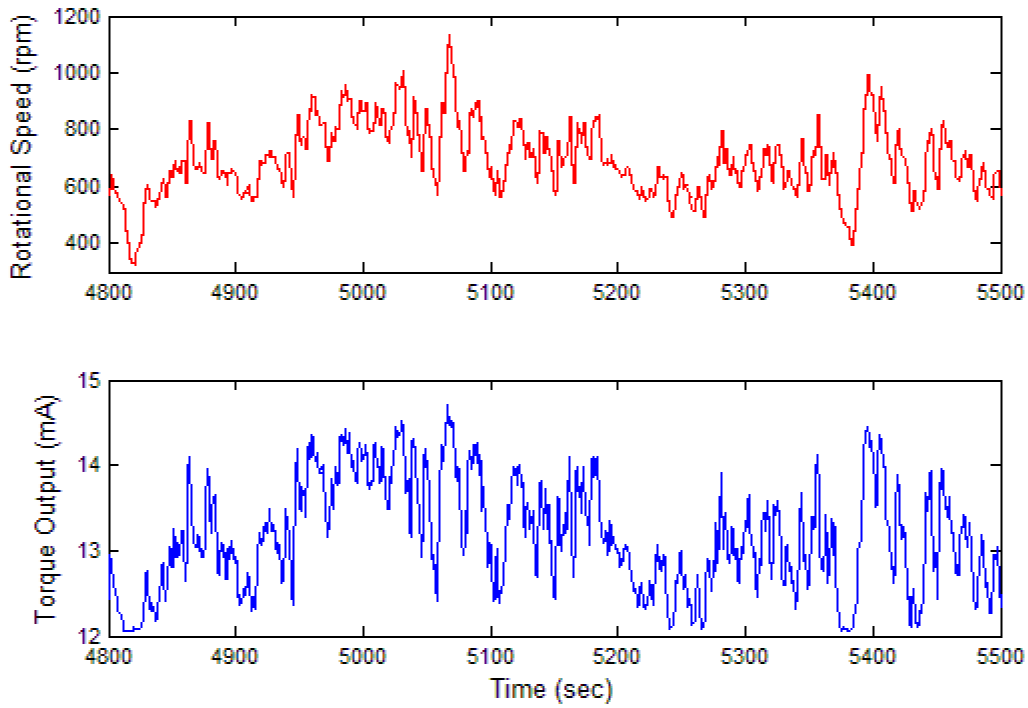

Figure 3.22: Aerodynamic Power Sample Data.

Another performance measure is the electric power produced by the wind turbine. This power describes the amount of electrical energy produced by the wind turbine which varies from the aerodynamic power by the efficiencies of the generator and of the conversion from 3-phase AC power to a rectified DC power. Electric power components are the DC charging current from the turbine charge controller to the battery bank and the voltage measured across the battery terminals:

$$P_{T,elec} = I_{charge} V_{charge} \ . \tag{3.85}$$

A sample of the electric power components is shown in Figure 3.23. The battery voltage has sharp drops when the wind turbine stops charging because the charge voltage is higher than the actual battery voltage.

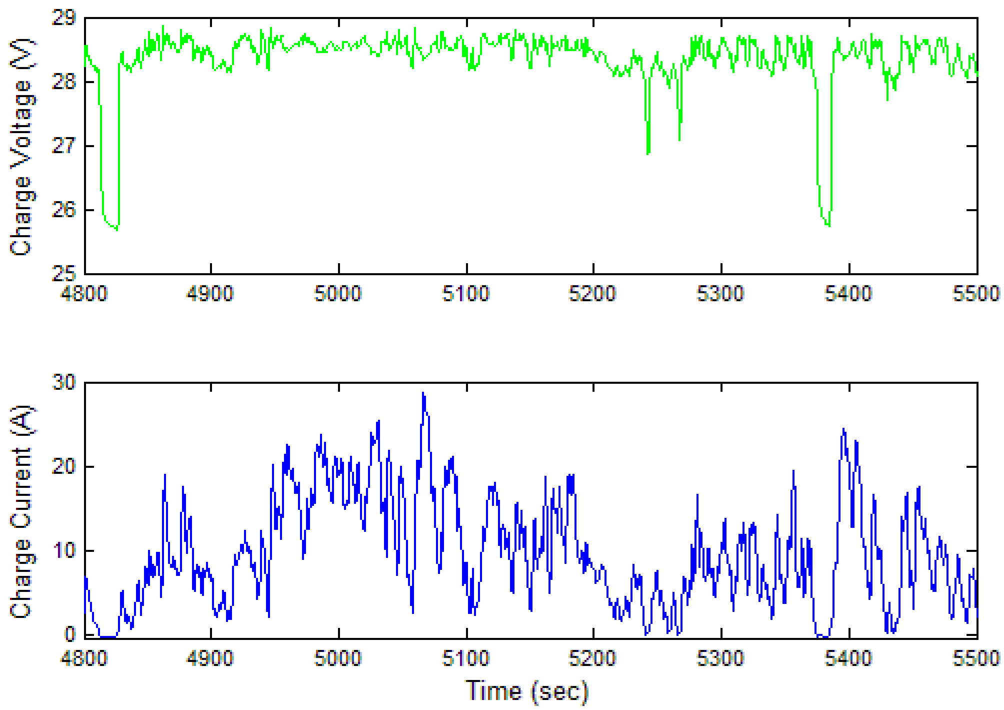

Figure 3.23: Electric Power Sample Data.

Comparison of the two wind turbine power measures captures the electrical power conversion efficiency of the wind turbine system. This conversion efficiency is defined as the quotient of the two powers, Equation 3.86. The components of this efficiency are shown together in Figure 3.24.

$$\eta_{conversion} = \frac{P_{T,elec}}{P_{T,aero}}. \tag{3.86}$$

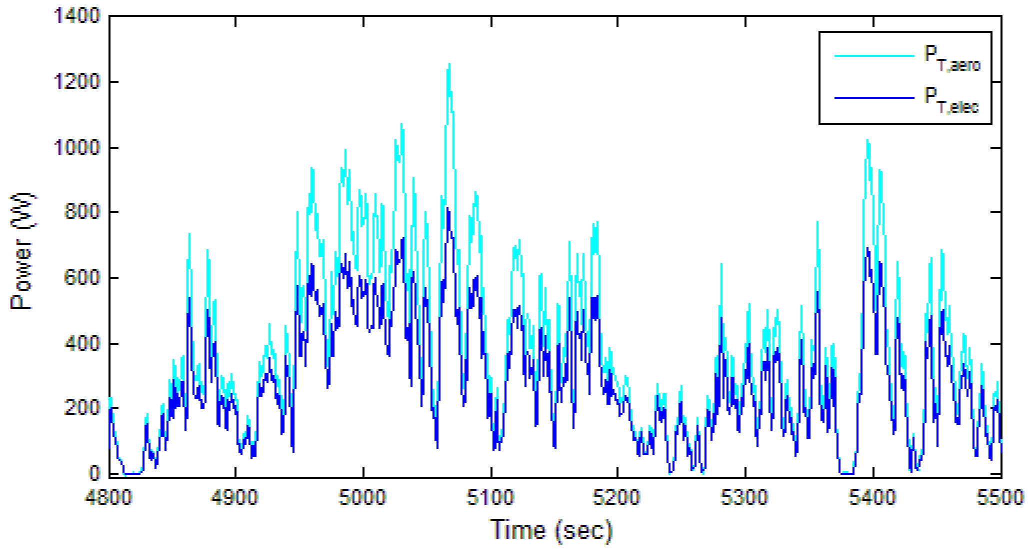

Figure 3.24: Conversion Efficiency Sample Data.

Data for the wind farm flow conditions measured by the anemometer are shown for completeness in Figure 3.25. The high resolution instantaneous velocity measurement from this sensor enables estimation of turbulence levels, described by turbulence intensity. This describes the level of variation of the mean wind speed and is calculated as the quotient of the standard deviation of the instantaneous wind speeds and their average:

$$TI = \frac{\sigma_u}{\bar{u}}. \tag{3.87}$$

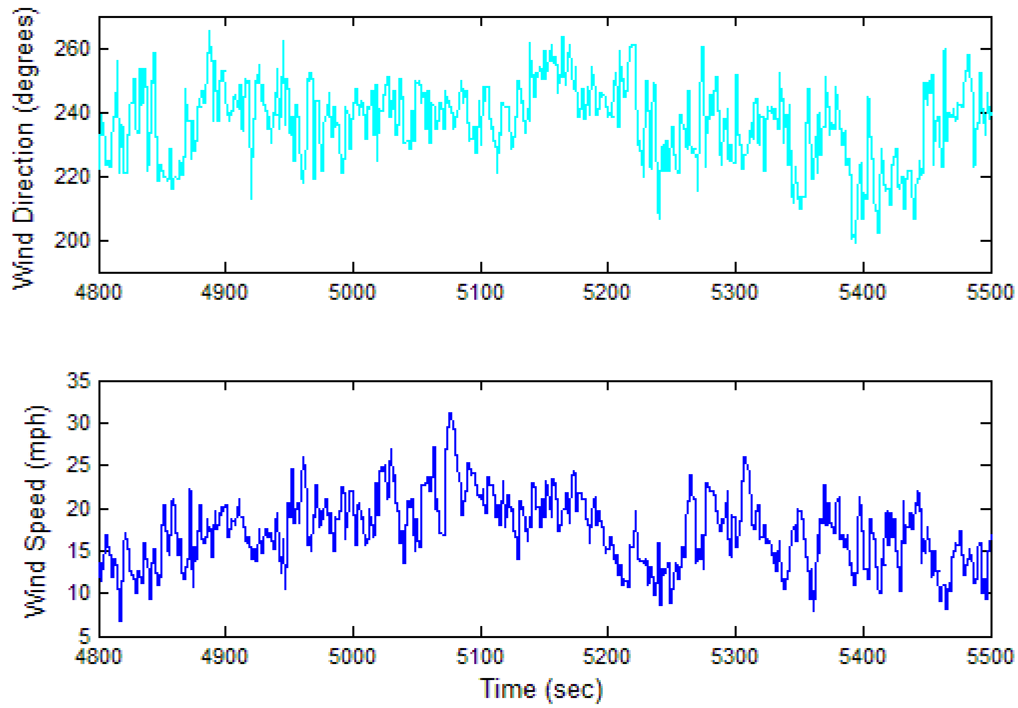

Figure 3.25: Wind Speed and Direction Sample Data.

The desired wake interaction results compare the performance of the two instrumented wind turbines. The data are first sorted into bins based on the Align Logic variable status, which filters the full set of data for times where the turbines are aligned with the wind direction. An additional filter is added which then removes data bins below a minimum time length, T_{bin}. This constraint ensures that proper alignment was sustained and additionally reduces errors from generator dynamics and minor phase misalignment when averaging larger time sets. Data bins which are larger than the minimum bin length are sorted into smaller bins of an independent time length, T_{sort}, where the conditional length is met. This function produces more precise sorting of the data when the bin performance is plotted against characteristic bin averages. The data processing from this point on is done within the sorted bins.

The wind farm DAQ output is time synchronized but the events at the different locations actually correspond to different times. To address the time offsets, data produced from the anemometer and the downstream wind turbine are both shifted to the upstream wind turbine time. The anemometer conditions are shifted based on the known alignment direction of the two wind turbines and known spacing and direction from the upstream wind turbine to the anemometer, 200-ft due East. The spacing then from the anemometer plane to the upstream wind turbine is determined as shown in Figure 3.26, and Equation 3.88. This estimation assumes that the wind conditions are 1-D, therefore constant in the direction perpendicular to the wind direction.

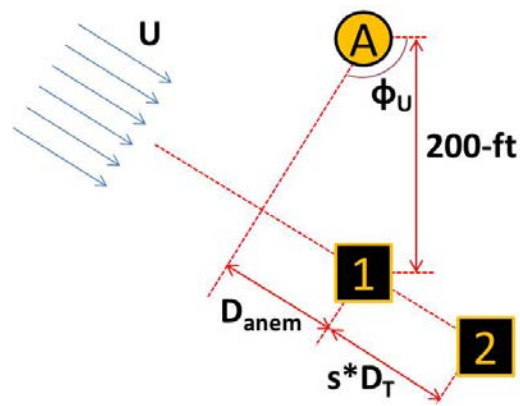

Figure 3.26: Wind Speed Measurement Time Shift Diagram.

$$D_{anem} = 200 * \sin(\phi_U - 180°)\,. \tag{3.88}$$

With the distance known, the time delay is a function only of the wind speed. The wind speed at the upstream turbine time is not known due to the time delay. The time delay must then be solved for iteratively by shifting the bin indices, in a direction dependent upon the sign of D_{anem}, until $\overline{U}_{bin+shift} * t_{shift} > D_{anem}$ and then using the previous index as the time shift and its corresponding bin averaged wind speed to describe the bin. This shift is negligible when the wind speed is constant where $\overline{U}_{bin+shift} \approx \overline{U}_{bin}$. The shifted bin wind speed average along with the turbine-turbine spacing are used to shift the downstream wind turbine data to correspond to the same wind condition as the upstream wind turbine by a value $t_{12} = sD_T/\overline{U}_{bin+shift}$. This shifted time is used to change the bin indices for the downstream turbine to correspond to the upstream turbine bin data set. For the remaining sections, when referring to the downstream wind turbine it will be referring to the shifted time value of that variable corresponding to the upstream wind turbine flow conditions, so the shifted condition will no longer be stated. Additionally, the remaining variables in the analysis will all be described only as bin averages within the upstream bin and the appropriately shifted downstream bin. For example, when a variable is mentioned in the remaining sections for the results, its value is the bin average of the appropriate bin.

Wake performance losses are described with a performance variable of the downstream turbine normalized by the same variable of the upstream turbine. The normalized power is calculated using the sum of the normalized power indices within the bin:

$$P_{norm} = \frac{\sum_i^{N_{bin}} P_{downstream,i}}{\sum_i^{N_{bin}} P_{upstream,i}} = \frac{\sum_i^{N_{bin}} (\tau * \Omega)_{downstream,i}}{\sum_i^{N_{bin}} (\tau * \Omega)_{upstream,i}}. \quad (3.89)$$

A different formulation of the normalized power can be performed as well, Equation 3.90. This does not produce the same value but based on comparison of the two results the estimation has a high accuracy:

$$P_{norm} = \frac{\sum_i^{N_{bin}} (\tau * \Omega)_{down,i}}{\sum_i^{N_{bin}} (\tau * \Omega)_{up,i}} \approx \frac{\sum_i^{N_{bin}} \tau_{down,i} * \sum_i^{N_{bin}} \Omega_{down,i}}{\sum_i^{N_{bin}} \tau_{up,i} * \sum_i^{N_{bin}} \Omega_{up,i}} = \tau_{norm} \Omega_{norm}\,. \quad (3.90)$$

Using this approximation, calculation of the relative contribution to the power loss in the wake due to the torque and due to the rotational speed can be determined. These values approximately describe the percentage of the power loss solely from the torque reduction due to the wake and rotational speed reduction due to the wake, respectively, shown in Equations 3.94 and 3.95:

$$P = \tau\Omega \rightarrow dP = \frac{\partial P}{\partial \tau} d\tau + \frac{\partial P}{\partial \Omega} d\Omega \quad (3.91)$$

$$\frac{dP}{P} = \frac{d\tau}{\tau} + \frac{d\Omega}{\Omega} \rightarrow \frac{P_{up} - P_{dn}}{P_{up}} \approx \frac{\tau_{up} - \tau_{dn}}{\tau_{up}} + \frac{\Omega_{up} - \Omega_{dn}}{\Omega_{up}} \quad (3.92)$$

$$1 - P_{norm} \approx 1 - \tau_{norm} + 1 - \Omega_{norm} \rightarrow 1 \approx \frac{1 - \tau_{norm}}{1 - P_{norm}} + \frac{1 - \Omega_{norm}}{1 - P_{norm}} \quad (3.93)$$

$$P_{loss,torque} \approx \frac{1 - \tau_{norm}}{1 - P_{norm}} \quad (3.94)$$

$$P_{loss,rotation} \approx \frac{1-\Omega_{norm}}{1-P_{norm}}. \quad (3.95)$$

The aerodynamic power is shown for the sample data set for both wind turbines, plotted with the wind turbine alignment logic variable (green curve) in Figure 3.27. This sample set presents a single wake test case at a 5 rotor diameter spacing. The necessity of the status variable is made clear where noticeable differences in the relative power occur when the alignment is positive (~5000s) and when it is not (~5400s). The bins which are evaluated for the filtered final results are derived from this status variable, as described above. The normalized power is essentially the ratio of these two power curves.

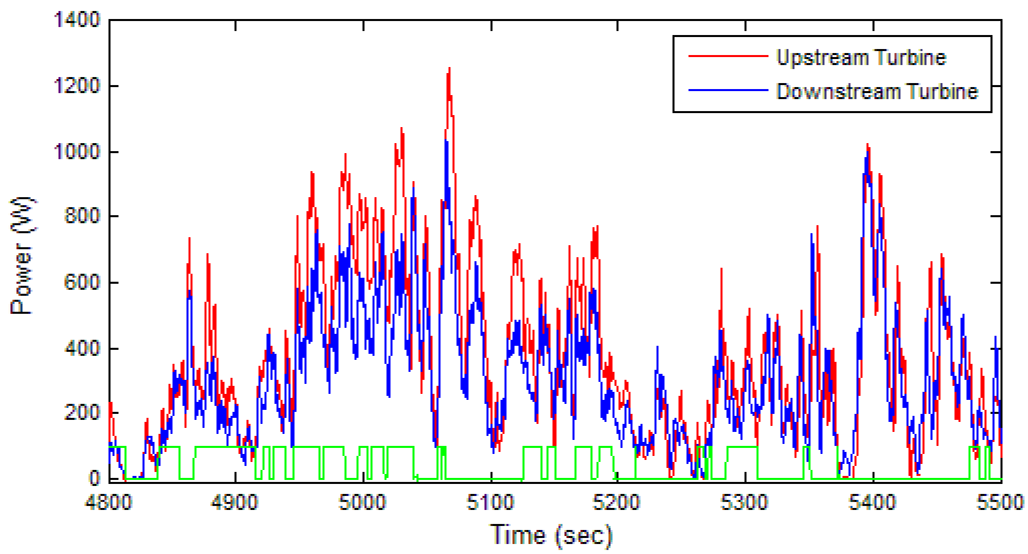

Figure 3.27: Wake Interaction Power Reduction Sample Data.

For completeness, the rotor torque and rotational speed comparison plots are shown for the same test case, Figures 3.28 and 3.29. These plots contain the information for normalized torque and normalized rotational speed.

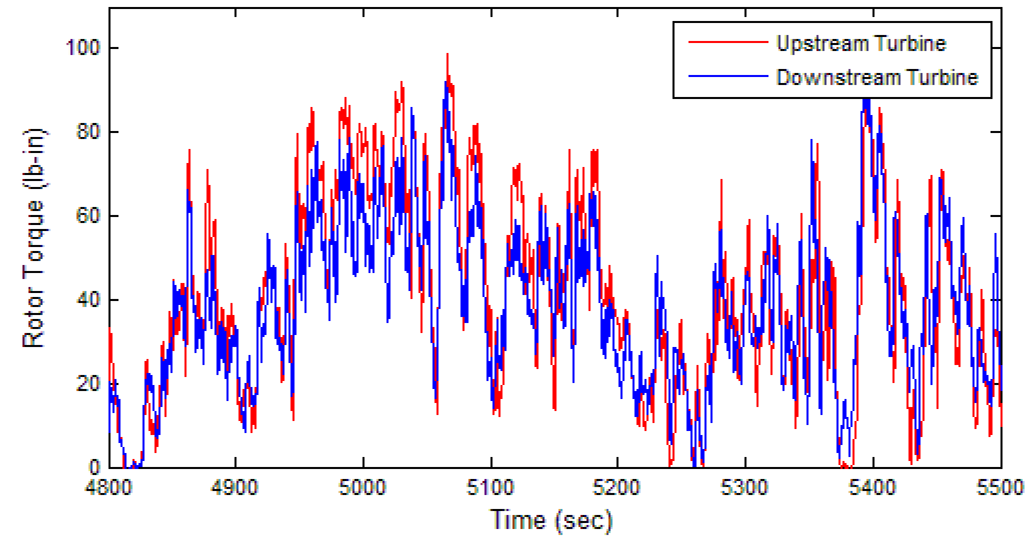

Figure 3.28: Wake Interaction Torque Reduction Sample Data.

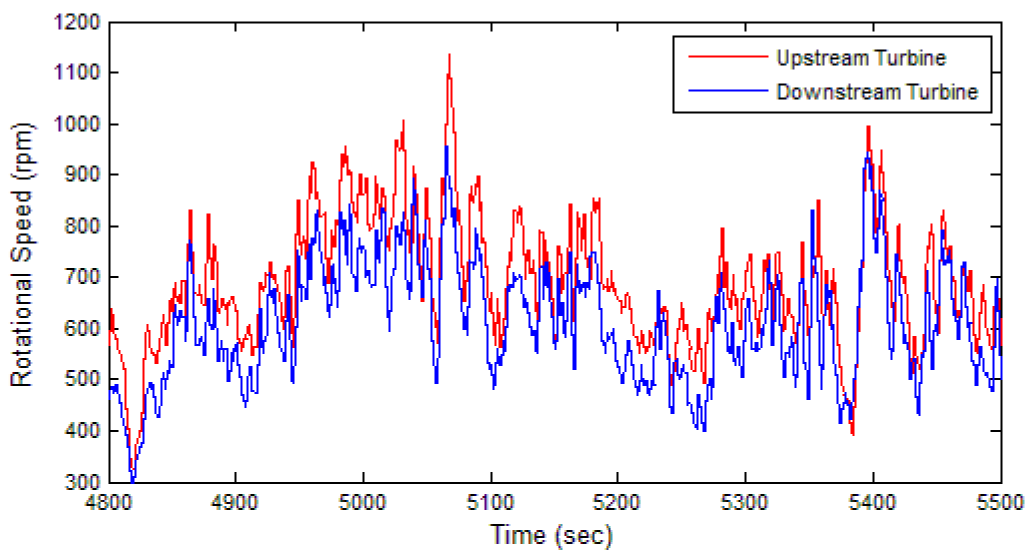

Figure 3.29: Wake Interaction Rotational Speed Reduction Sample Data.

A constraint is added, in addition to bin length, which filters the usable data set further. This constraint is a condition on the upstream wind turbine power average within the range, $P_{upstream} \geq P_{min}$. This constraint is necessary as experimental uncertainty begins to dominate below a certain value of the wind turbine power, producing fictitious results for the normalized power ratio. Normalized power is summarized within a power range [P_1, P_2] of the upstream turbine power using a weighting based on the bin time length according to Equation 3.96. When one value for normalized power is given with no mention of the power bin it is assumed to describe the entire filtered data set from [P_{min}, ∞).

$$P_{norm,wt} = \frac{\sum_i^{N_{bins}}(P_{norm,i} * t_{bin,i})}{\sum_i^{N_{bins}} t_{bin,i}}. \quad (3.96)$$

Data from multiple days and multiple spacing's will be present for most of the different test cases. Data for the different days will be combined, and then data for the different spacing's will be separated. One manner in which the data results will be described is by the average within a power range [$P_{1,i}$, $P_{2,i}$] of the upstream turbine power, and its standard deviation. The power average will be the weighted average as described above, and the standard deviation will also be a weighted standard deviation based on the bin length for each sample. Weighting for the standard deviation is done by creating a vector with the bin average repeated 'bin-length' times for each value within the upstream turbine power range for that set. This method will be used to describe the wake interaction losses as a function of the upstream turbine power for the different test cases and different spacing's.

3.4.3 Micro Reconfigurable Wind Farm Experimental Uncertainty

The results from the wind turbine wake performance measurements all contain a level of experimental uncertainty sourced from the component sensor accuracy's and due to the digital conversion. The experimental uncertainty on the aerodynamic power measurement is derived starting with the definitions of the power and the standard formulation for propagation of error:

$$P = \tau\Omega \quad (3.97)$$

$$\delta P = \sqrt{\left(\frac{\partial P}{\partial \tau}\,\delta\tau\right)^2 + \left(\frac{\partial P}{\partial \Omega}\delta\Omega\right)^2}. \quad (3.98)$$

The experimental uncertainty of the power is sourced from the uncertainties of the measured torque and rotational speed:

$$\delta P = \sqrt{(\Omega * \delta\tau)^2 + (\tau * \delta\Omega)^2}\,. \tag{3.99}$$

The rotational speed itself isn't an analog measurement but rather a quotient of two measured values, number of counts (N) and sample average time (t). The rotational speed uncertainty is therefore determined using a propagation of error analysis of these two variables:

$$\Omega = {}^{N}\!/_{t} \tag{3.100}$$

$$\delta\Omega = \sqrt{\left(\frac{\partial\Omega}{\partial N}\,\delta N\right)^2 + \left(\frac{\partial\Omega}{\partial t}\delta t\right)^2} \tag{3.101}$$

$$\delta\Omega = \sqrt{\left({}^{1}\!/_{t}\;\delta N\right)^2 + \left(\frac{N}{t^2}\delta t\right)^2}\,. \tag{3.102}$$

The sensor uncertainties are described by the physical hardware accuracies, which combine to form the overall measurement uncertainty. The uncertainty of the torque measurement depends on several accuracies. Hardware accuracies for non-linearity, hysteresis, and non-repeatability of 0.1, 0.25, and 0.05% calibration full scale (calibration = 300 lb-in) produce an uncertainty of 1.2 lb-in. This is combined with uncertainties due to the temperature effect on the sensor zero and on output of 0.002% capacity/F (capacity = 600 lb-in) and 0.002% reading/F over the total used temperature range. Using a temperature range of 30F to describe the experimental conditions, and 100 lb-in for the reading value (a worst case analysis), the contribution from temperature effect is 0.42 lb-in. From this analysis, the uncertainty in the torque measurement is, as a worst case, $\delta\tau$ = 1.62 lb-in.

The uncertainty in the rotational speed is caused by uncertainty in the number of counts and in the counting time measurement. The uncertainty in the number of counts is due to data acquisition and the encoder mechanical accuracy. Uncertainty in number of counts due to the data acquisition is at most 1-count, if a pulse edge is just outside of the count time range. This value adds with the mechanical error which is 0.017° for the encoder used. These combine for the 600 count/rev encoder to produce δN = 1.0283 counts. The accuracy of the DAQ clock determines the uncertainty in the time measurement where N is counted. For DAQ system has a 48 MHz resolution, producing an uncertainty in the time measurement of δt = 20.8-ns.

The actual uncertainty in a measurement will depend on both the uncertainty of the different components and on the nominal values from the sensors. These values will be calculated and given with the results, but to get an estimate of how the uncertainty varies with the aerodynamic power certain approximations will be made. The wind turbine torque sensor output is plotted versus the aerodynamic power of this turbine for a six hour time set on one wind turbine, and is shown in Figure 3.30. This curve is used to estimate the relationship between torque and aerodynamic power, and was done so using a cubic fitting, given in Equation 3.103.

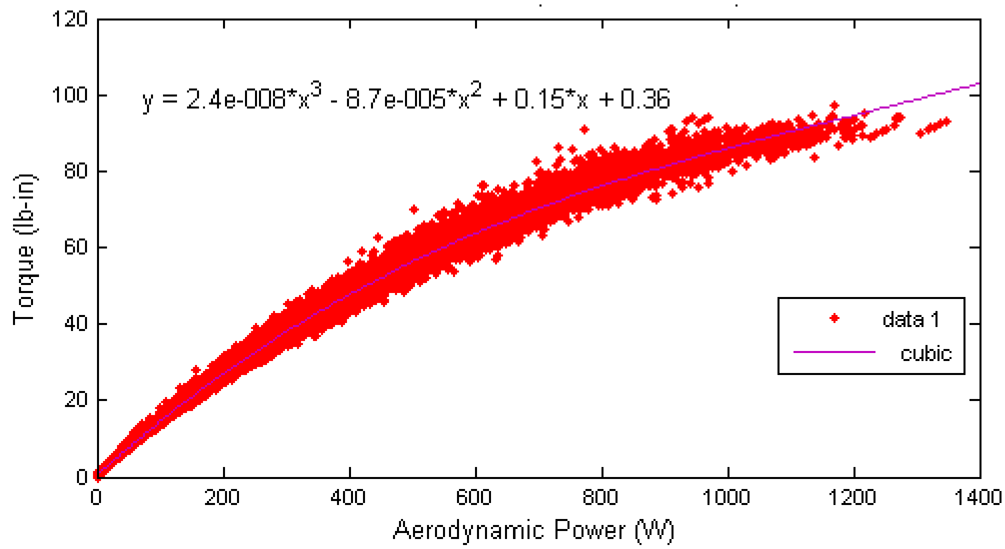

Figure 3.30: Wind Turbine Torque vs. Power Data Set.

$$\tau = 2.4e - 8 * P_T^3 \; - 8.7e - 5 * P_T^2 + 0.15 * P_T + 0.36\,. \qquad (3.103)$$

This approximation of the torque at a given turbine power enables calculation of a generic uncertainty curve as a function of turbine power. Rotational speed is calculated from the known power and torque values, and measurement uncertainties use the nominal values where needed. The results from this uncertainty analysis are shown in Figure 3.31, showing both the absolute power uncertainty in Watts and the uncertainty percentage of the nominal power.

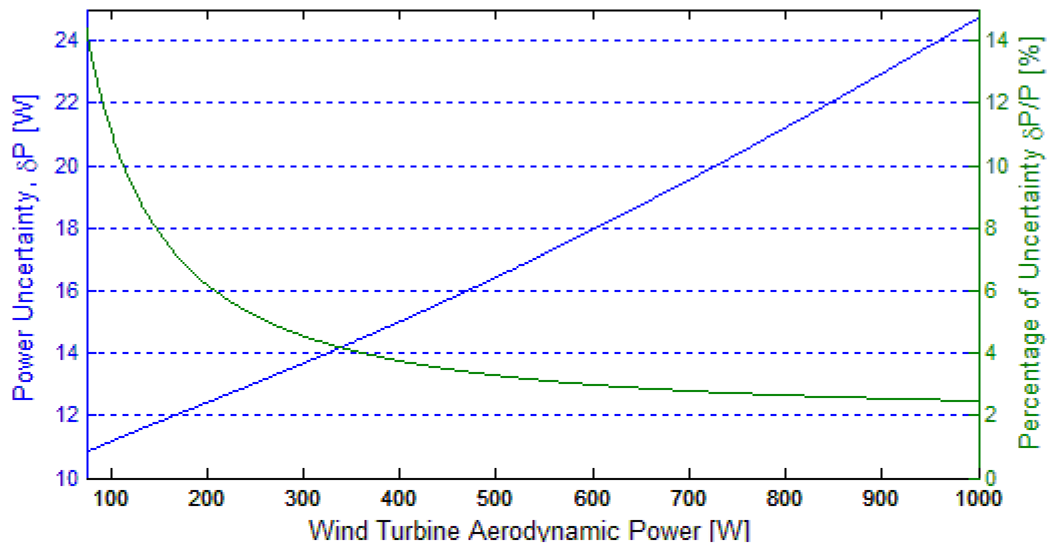

Figure 3.31: Aerodynamic Power Experimental Uncertainty Estimate.

CHAPTER 4: WIND DATA ANALYSIS RESULTS

Abstract

Wind speeds were recorded in West Lafayette, Indiana from October 1st, 2008 to December 31st, 2009 and analyzed to determine the wind speed trends both throughout the year and throughout the day. A Weibull function is fit to the data and its accuracy proven in the quality of the Weibull calculated average wind speed. The five anemometer height locations are used to describe the atmospheric velocity profile which is studied to understand its trends. The wind speed data are used to calculate performance for both residential and utility-size wind turbines. Two leading manufacturers of small wind turbines are compared at varying hub heights, and three utility size wind turbines from one manufacturer are compared which vary in rotor diameter and generator size.

Nomenclature

V	Wind speed
$f(V)$	Probability density function
k	Weibull shape parameter
c	Weibull scale parameter
V_{MP}	Most probable wind speed
$V_{MAX,E}$	Wind speed with most energy
P_W	Power in the Wind
ρ	Density of Air
Γ	Gamma function
e_D	Wind power density distribution
H_k	Hermite polynomial
$g(z_D)$	Gaussian probability distribution

z_D	Scaled wind speed, centered on wind power density
$v(i)$	Wind speed value from *i*-th data point
μ_D	Mean value of z_D
σ_D	Standard deviation of z_D
α	Velocity profile power law coefficient
z	Height in velocity profile
P_T	Wind Turbine Power Production
V_C	Wind turbine cut-in wind speed
V_R	Wind turbine rated wind speed
P_R	Wind turbine rated power
n	Wind turbine power curve exponent
V_F	Wind turbine cut-out wind speed
CF	Capacity factor
Cp	Power coefficient
A_T	Wind turbine rotor swept area

4.1 Introduction

Northern Indiana, in the counties surrounding West Lafayette, has proven to possess a favorable environment for the implementation of wind energy. Over the past 5 years, 4 large wind farm projects have been constructed with over 1.8 GW of current total installed capacity. Future wind farm projects are currently being developed as well. The placement of these farms depends on many variables, including local policy and relative location to transmission lines, among other factors. The variable of ultimate concern for the success of the wind farm is the fuel - the wind resource. The resource for a given area is not a constant value throughout the year, but rather is stochastic by nature. Apart from the difficult predictability of wind conditions at any given moment, there are trends in every area which are derived from the global and local location. Globally, the location relative to the equator and hemisphere of study are of significant contribution to the wind patterns. Locally, mountain ranges, relative altitude, and nearby obstructions all affect the average wind speed and wind direction trends, even when compared to nearby locations. Understanding of these trends in the fuel for wind turbines has impact in determining whether the energy created will be sufficient and if it will be available when most needed, when the loads are high in summer and during the day.

Akpinar and Akpinar [39] collected and statistically analyzed wind data, collected in hourly time intervals, taken over a period of six years from 1998 – 2003 in four different regions in Turkey. Wind speeds were taken every 10m up to 100m in each of these regions. Seasonal averages were made to compare the trends of the four seasons. Probability distributions were compared with the actual frequency bins of these seasons in order to verify the fit. Weibull and Rayleigh (a one-parameter Weibull fit) distributions were compared. Both probability functions produced acceptable fits in each season, with the Weibull function more closely representing the data for 12 out of the 16 season/locations. The shape factor in the Weibull function was between 1.44 and 1.80 for the four seasons in the four locations over the six year period. The averages for each season for each of the 10 anemometers were plotted versus the anemometer height to reveal the velocity profile for the four areas, revealing appreciable velocity changes with height throughout the entire range even up to 100m in all seasons. The wind data were used to determine the energy output of 6 different wind turbines, ranging from 300 to 2300 kW, by using their actual power curves. The capacity factors for all the machines were found to vary between 16 and 30% seasonally in the optimum wind location among the four regions studied.

Celik [40] performed a study in Iskenderun, Turkey to statistically analyze 1 year of hourly wind speed data. Weibull and Rayleigh density functions were compared to the measured probability density on a monthly basis. This comparison was done by calculating correlation coefficient values which measure the fit of the estimations to the measured data, with 1 being a perfect fit. These values ranged from 0.66 to

0.96 for the Weibull estimates, 0.88 average, and 0.46 to 0.96 for the Rayleigh estimate, 0.80 average. The Weibull yielded higher coefficient values for 7 of the 12 months. Celik shows how to calculate the power density from the known Weibull parameters. The power density was plotted for each month and was seen to vary significantly throughout the year, from about 10 to 70 W/m2. The average yearly error in power density from using the probability models were 4.9% for the Weibull model, whereas this value averaged to 36.5% for the year and reached over 50% using the Rayleigh model in some months.

Liu and Jiang [41] analyzed 15 years of wind speed data from weather stations at two locations in China located in the southwest coastal region. The anemometers were both located at a 10m height. Weibull distributions were applied to the wind data to obtain the mean wind speeds for the two regions, which varied from 2.308 to 3.03 m/s and 2.651 to 3.608 m/s for the two areas. The Weibull shape parameter varied from 2.08 to 2.905 and 2.08 to 3.031. Weibull estimated power density and its error were calculated according to the method by Celik [2] with a 4.74% and 9.83% error from measured power density in the two locations. This area was found to be in Wind Power class I with a wind power density less than 100 W/m^2.

Li et al. [42] studied data from a 325m meteorological tower in Beijing containing 30 anemometers at 15 different heights taken during 12 windstorms. Wind speed profiles are presented and compared with predictions from different models. Atmospheric turbulence information was also derived from this analysis recorded by 3 ultrasonic anemometers at different heights. Wind speed profiles were calculated using the Log law, Power law, and Deaves and Harris model. The log law contains 3 to 4 parameters describing the environment that is being modeled, and is seen to work for elevations up to 100m, but not greater than 200m. The power law is an empirical formulation that operates on the assumptions of (1) constant ground roughness exponent and (2) gradient height is a function of ground roughness alone. This model may not describe the vertical distributions of wind speed at low heights well, and is generally applied between 30 and 300 m. The power law profile is widely used in many standards, despite its stated drawbacks.

The Deaves and Harris model is described by three parameters and contains more of the physics of the atmospheric boundary layer. An explanation of how to calculate the relevant parameters of the models is detailed. The turbulence parameters of turbulence intensity, gust factor, and turbulence integral length scale are calculated and displayed for the three ultrasonic anemometer locations.

Morrissey et al. [43] proposed an improvement on calculating the wind power density using a Gauss-Hermite expansion. This model calculates the power density directly rather than first relying on a probability distribution with inherent errors in the velocity determination which are multiplied when used to determine the power ($\sim V^3$).

In this paper, a Weibull analysis is applied to wind speed data from five sampled anemometer heights acquired over a year in Northern Indiana. This analysis determines the wind speed trends throughout the year and throughout the day as well as the atmospheric velocity profile. The wind speed data is then used to calculate performance parameters for both residential and utility-size wind turbines.

4.2 Data Acquisition

Wind data were recorded in Northern Indiana, in West Lafayette, in an open clearing of agriculture plots utilizing a 50 meter meteorological tower. Measurements were taken using 6 NRG Systems #40C anemometers, 2 NRG #200P wind direction vanes, and 1 NRG #110S Temperature Sensor with Radiation Shield. Positions for these sensors are given in Table 4.1, with all wind sensors installed using a 20 in. mounting boom. Data were acquired and stored by an NRG Symphonie 12-channel Data Logger.

Table 4.1: Wind Data Sensor Descriptions.

Sensor	Height (m)	Orientation (deg.)
Anemometer	50	270, 180
Anemometer	40, 30	270
Anemometer	12, 3	180
Direction Vane	50, 40	0
Thermometer	1	N/A

The data set was taken from October 1, 2008 to December 31, 2009. Data points are in the form of ten minute averages performed on each of the sensor channels, calculated from the interval's data set which included data sampled every two seconds. The mean and standard deviation were recorded for this ten minute period, along with the maximum and minimum values for the sensor. The data collection procedure resulted in 144 total data points for each day, with 457 days in the data set viewed.

4.3 Mathematical Procedure

The ten minute data points were sampled using a moving average scheme with the index value being the center of that bin. The data were placed into bins where divisions of both the number of days and number of hours could be made to group the data. For this analysis, the number of days in a bin range from 1 to 90, and hour divisions used are for a whole day (24 hours) and down to every hour. This sampling was performed to add insight into the seasonal trends, those that vary with date, and the daily trends, those that vary within each day of the wind data.

The statistical characteristics of the wind were determined using a Weibull probability estimation, Equation 4.1. The Weibull function is a two parameter distribution which describes the probability of a certain value (wind speed) occurring. The parameters describe the shape or spread k and the scale c of the distribution. The shape factor is said to vary from 1.5 to 3 [1] for most wind conditions and describes the variability of the wind:

$$f(V) = \left(\frac{k}{c}\right) \times \left(\frac{V}{c}\right)^{k-1} \times exp\left[-\left(\frac{V}{c}\right)^{k}\right]. \tag{4.1}$$

The two parameters are calculated using the MATLAB® function *wblfit* which calculates the *Maximum Likelihood Estimate* of the shape and scale factors given a data set. From this distribution, two important wind speeds are derived; the most probable wind speed and the wind speed carrying maximum energy. The most probable wind speed V_{MP} occurs at the peak of the Weibull distribution:

$$V_{MP} = c\left(\frac{k-1}{k}\right)^{1/k}. \tag{4.2}$$

The wind speed which carries the maximum energy $V_{MAX.,E}$ will always occur at a higher value than the most probable wind speed. The power in the wind is proportional to the wind speed cubed, balancing with the lower frequency of higher wind speeds to produce the energy maximum. This wind speed is of particular interest to the wind turbine designer:

$$V_{MAX,E} = c\left(\frac{k+2}{k}\right)^{1/k}. \tag{4.3}$$

Total power production in the wind can be estimated using this distribution along with known Weibull parameters for the period of interest, with Γ representing the gamma function:

$$\frac{\mathrm{P_W}}{\mathrm{A}} = {}^{1}\!/_{2}\,\rho \times \Gamma\left[\mathrm{c}^3\left(1 + \frac{3}{\mathrm{k}}\right)\right]. \tag{4.4}$$

A direct method of determining the Wind Power Density Distribution (e_D) was predicted using a Gauss-Hermite expansion of the sampled wind speed data as detailed by Morrissey et al. [6]:

$$\hat{e}_D(v|n,m) = \sum_{k=0}^{m\to\infty} \hat{\psi}_D(k) H_k(z_D) \frac{g(z_D)}{\sigma_D}. \tag{4.5}$$

The terms H_k and $g(z_D)$ represent the Hermite polynomial and the standard Gaussian, respectively. The intermediate term $\hat{\psi}_D$ is calculated using the wind data, with n samples:

$$\hat{\psi}_D(k,n) = {}^1\!/_2\, \rho \left(\frac{\sqrt{\pi}}{2^{k-1}k!}\right) \frac{1}{n} \sum_{i=1}^{n} \{v(i)^3 H_k[z_D(i)] g[z_D(i)]\} \tag{4.6}$$

where,

$$z_D = \frac{v-\mu_D}{\sigma_D};\ \mu_D = \frac{\sum_{i=1}^{n} v(i)^4}{\sum_{i=1}^{n} v(i)^3};\ \sigma_D = \left\{\frac{\sum_{i=1}^{n} v(i)^3 [v(i)-\mu_D]^2}{\sum_{i=1}^{n} v(i)^3}\right\}^{1/2}. \tag{4.7}$$

The five height locations of the anemometer tower were used to describe the atmospheric velocity profile below the 50 m height. The power law profile shape assumption, Equation 4.7, was used due to its simplicity and the relatively low height of the tower. Calculations for this parameter were made in the raw data at each point before sampling. The power coefficient was determined from the 6 data points using a polynomial fitting tool which minimized error in ($\ln V$) and not (V) itself.

$$\frac{V}{V_{ref}} = \left(\frac{z}{z_{ref}}\right)^{\propto}. \tag{4.8}$$

The particular interest of this study of the yearly wind conditions is its interplay with wind turbine operation. This determination begins with the wind turbine power calculation, and the normalized performance measures of capacity factor and power coefficient are then derived. Wind turbine power production is calculated using the actual, non-sampled, wind speed and the wind turbine of interest's power curve. For this study two of the leading wind turbines in the "small wind-turbine" classification (<100kW) are compared, along with three utility size wind turbines from the same manufacturer which vary rotor size and generator capacity. A generic wind turbine power curve is also used following its accepted definition. This standard wind turbine power curve [1] is given in Equation 4.8, where V_C, V_R, V_F, and P_R describe the wind turbine performance and are the cut-in speed, rated-speed, cut-out speed, and rated power. The exponent n describes the power relationship and has a typical value between 2 and 3:

$$P_T(V_W) = \begin{cases} 0 & V_W < V_C \\ P_R\left(\frac{V_W{}^n - V_C{}^n}{V_R{}^n - V_C{}^n}\right) & V_C \leq V_W \leq V_R \\ P_R & V_R < V_W \leq V_F \\ 0 & V_W > V_F \end{cases}. \tag{4.9}$$

The performance measures of the wind turbine are capacity factor CF and power coefficient C_p, Equations 4.9. They were calculated from the full data set and then sampled to smooth out the curve as desired and to gain insight into the seasonal and daily trends.

$$CF = \frac{P_T}{P_R};\;\; C_p = \frac{P_T}{{}^1\!/_2 \rho A_T V_W{}^3}. \tag{4.10}$$

4.4 Results

The data set for the wind speed is reduced through averaging to remove some of the inherent stochastic properties of wind and to reveal more of the overall seasonal and daily trends. The averaging scheme was performed and compared with one day, month (30 day), or season (90 day) as the bin size, Figure 4.1. The one day averages contain much of the stochastic characteristics of the wind, which for the sake of this review is undesirable, making the prediction of overall yearly trends more difficult. Monthly and seasonal averages reduce the high variability of the wind to reveal a clear trend for yearly averages of wind speed. The monthly averaging was selected over seasonal averaging due to the presence of some of the higher frequency trends that the seasonal averaging smoothed out. For the remainder of this review, 30 day averages will be used in the plots and tables where applicable. Also, the following results and figures describe the wind data at a 50m height if not stated otherwise

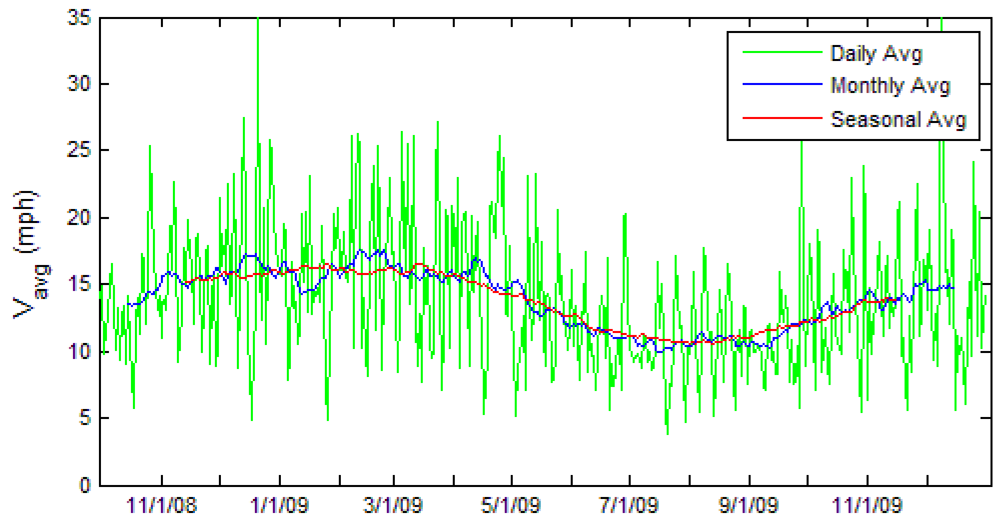

Figure 4.1: Averaged Wind Speed of Data Set Comparison.

In addition to periodic variation throughout the year there is also a daily variation component superimposed on this seasonal trend, Figure 4.2. The averaging scheme was carried out to also divide the sample bins throughout the day, ranging from 1 to 24 hour selected intervals. The hourly variation is illustrated below with the thick black line displaying the mean velocity when no daily sampling was performed (24 hour bin).

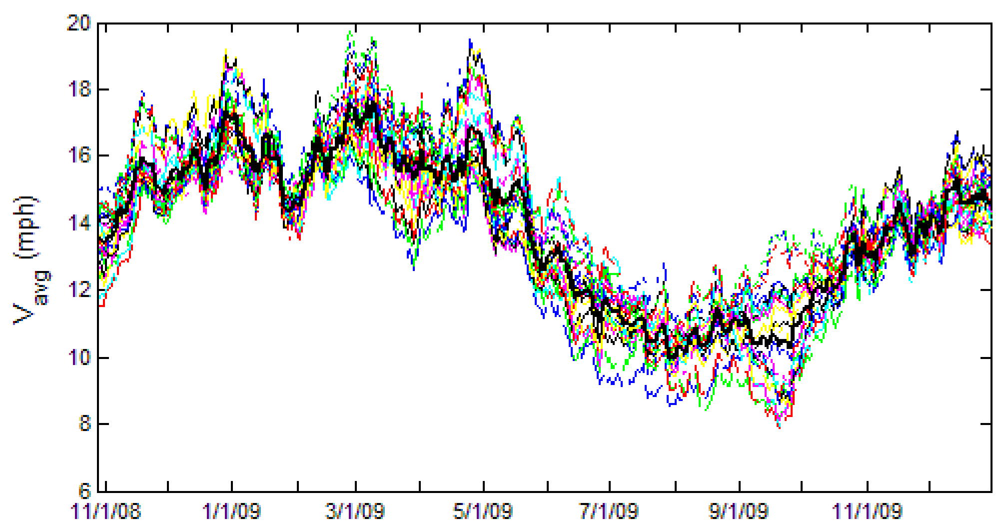

Figure 4.2: Averaged Wind Speed with 1-hour Sample Bins.

This analysis reveals significant variations in the average wind speed both throughout the year and throughout the day. Daily variations fluctuate throughout the year and range from about 1.5 to 5 mph differences in the average wind speed, with the underlying yearly average varying 7 mph throughout the year. Table 4.2 adds insight into the physical properties of the monthly and daily variation. The data representing the month is from the 30 day average whose center is located on the 15th day of that month. The average velocity for that month is given (as displayed by the thick black line in Figure 4.2), and minimum and maximum values for that average were found for each month from the hourly sampled data. The times where the wind is at a minimum and maximum are also given for each month. All of these values were averaged together to yield yearly averaged values. The minimum wind velocity in the day for this area typically occurs early in the morning averaged to 7 a.m. (with the exception of November) and the maximum occurs in the second half of the day averaged to after 4 p.m.

Table 4.2: Monthly Averaged Wind Speed Data, 50m (mph).

Month	*V,max*	*t,max*	*V,min*	*t,min*	*V,avg*	*ΔV,avg*
January	15.41	14:00	13.78	0:00	14.46	1.63
February	18.98	22:00	15.64	7:00	17.21	3.33
March	17.00	16:00	12.62	7:00	15.29	4.38
April	19.19	12:00	14.96	1:00	16.67	4.23
May	13.97	17:00	11.39	7:00	12.63	2.58
June	13.42	16:00	9.58	7:00	11.76	3.84
July	11.39	14:00	8.51	7:00	10.00	2.88
August	11.87	14:00	9.65	8:00	11.17	2.22
September	13.36	22:00	9.22	9:00	11.00	4.14
October	14.78	15:00	12.34	8:00	13.23	2.44
November	14.42	22:00	12.78	16:00	13.58	1.64
December	15.86	13:00	13.45	9:00	14.67	2.42
AVERAGE:	14.97	16:25	11.99	7:10	13.47	2.98

The monthly averaged wind speed data tables for the four other anemometer height locations are given in Section 4.7. A summary table of the yearly averages for each of the anemometer heights is given in Table 4.3.

Table 4.3: Yearly Averaged Wind Speed Data.

Height	*V,max*	*t,max*	*V,min*	*t,min*	*V,avg*	*ΔV,avg*
50m	14.97	16:25	11.99	7:10	13.47	2.98
40m	14.38	16:10	11.33	5:50	12.78	3.05
30m	13.62	15:05	10.18	7:40	11.78	3.44
12m	11.46	14:20	6.94	7:40	8.93	4.52
3m	9.86	13:40	5.49	10:20	7.38	4.37

Figure 4.3 illustrates this trend visually where eight 3-hour sample bins were used to more easily observe the hourly trends throughout the day. It is observed how the maximum wind speeds throughout the year typically come from the second half of the day, and the minimum wind speeds from the first. The thick black curve of averaged wind speed with no daily sampling division was also plotted for comparison.

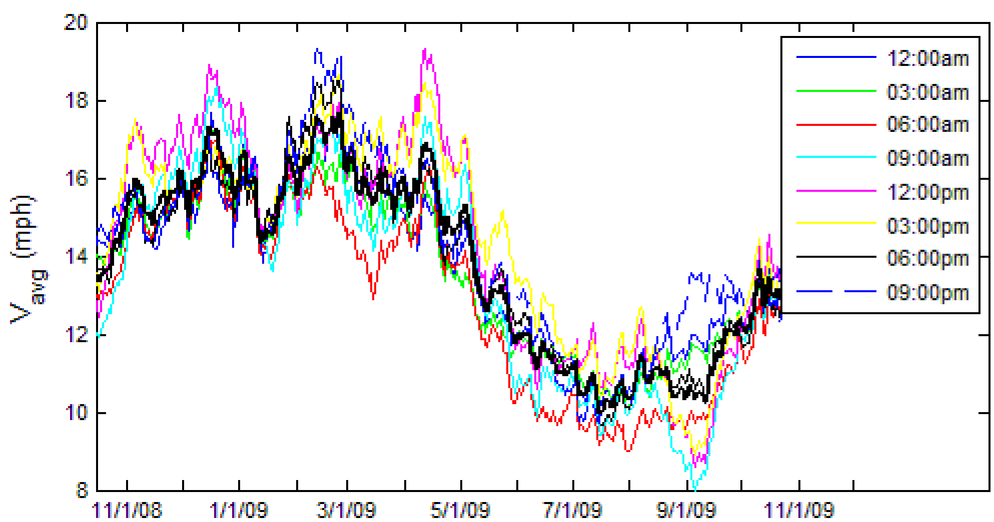

Figure 4.3: Averaged Wind Speed with 3-hour Sample Bins.

The variability throughout the day differs with the height in the atmosphere as well as seasonally, Figure 4.4. The daily fluctuations, defined as the difference in the minimum and maximum averaged wind velocity from hourly sampling, are plotted for the five anemometer locations. A trend is observed that these daily fluctuations are stronger closer to the ground.

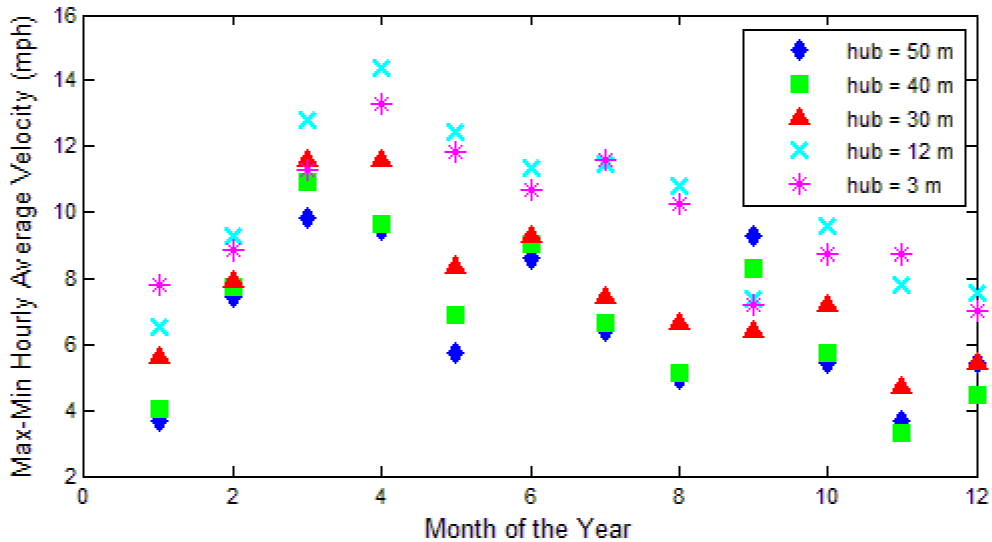

Figure 4.4: Daily Variation in Average Wind Speed at Different Heights.

The Weibull probability distribution was applied to the sampled data to prove its reliability in accurately describing the wind speeds in this location, Figures 4.5 and 4.6. The two parameters to this function were determined, with the shape factor being of particular interest. The shape factor hourly averages were seen to vary from 1.48 to 5.77 throughout the year of interest with significant variation between the months of June and October. This parameter remains within the typical range describing wind statistics of 1.5 to 3.0 [1] when averaging within the entire day, with the data varying from 1.77 to 3.05 throughout the year, represented by the thick black line.

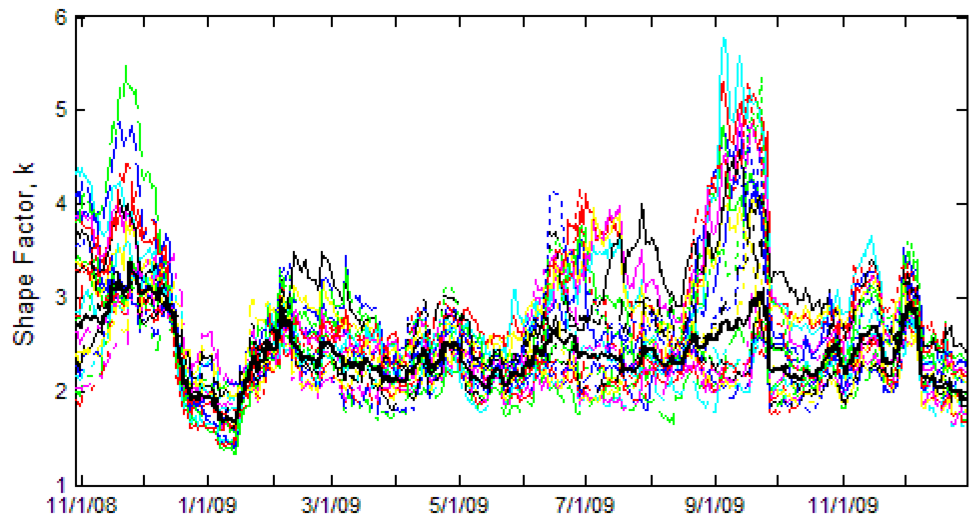

Figure 4.5: Weibull Shape Factor, k, with 1-hour Sample Bins.

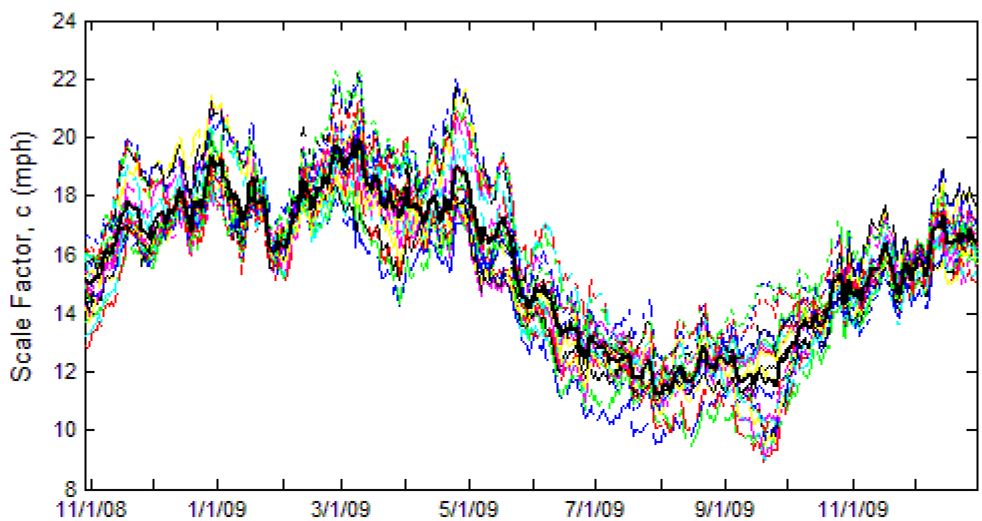

Figure 4.6: Weibull Scale Factor, c, with 1-hour Sample Bins.

The shape factor calculated for each month is summarized in Table 4.4, including the maximum and minimum average values found from 1-hour samples with the time of day where they occur. The scale factor is also given for reference. The monthly shape factors average to 2.49 on the year and vary only by about 0.5 from this mean throughout the year. Unlike with the average wind speed, the shape factor doesn't seem to have any noticeable trends throughout the day for when it is highest and lowest.

Table 4.4: Monthly Averaged Weibull Shape Factor Description.

Month	*k,max*	*t,max*	*k,min*	*t,min*	*k,avg*	*Δk,avg*	*c,avg (mph)*
January	3.01	19:00	2.25	9:00	2.56	0.76	16.14
February	3.26	6:00	2.13	18:00	2.56	1.13	19.33
March	2.58	2:00	1.72	15:00	2.18	0.86	17.25
April	3.00	22:00	2.20	1:00	2.60	0.80	18.72
May	2.87	3:00	1.84	8:00	2.25	1.03	14.22
June	3.99	23:00	1.81	8:00	2.70	2.18	13.19
July	3.58	6:00	1.81	0:00	2.53	1.77	11.23
August	4.19	2:00	1.91	10:00	2.94	2.27	12.49
September	3.29	6:00	1.79	9:00	2.39	1.50	12.36
October	3.08	3:00	2.01	12:00	2.51	1.07	14.86
November	3.32	23:00	2.16	16:00	2.70	1.16	15.14
December	2.47	6:00	1.63	17:00	1.98	0.84	16.47
AVERAGE:	3.22	10:05	1.94	10:15	2.49	1.28	15.12

The Weibull statistical analysis was performed at all five anemometer height locations within the data set with the remaining heights given in Section 4.8. A summary of the yearly averages at the five different heights of the Weibull parameters and trends is listed in Table 4.5.

Table 4.5: Yearly Averaged Weibull Parameter Comparison.

Height	*k,max*	*t,max*	*k,min*	*t,min*	*k,avg*	*Δk,avg*	*c,avg (mph)*
50m	3.22	10:05	1.94	10:15	2.49	1.28	15.12
40m	3.20	5:40	1.98	11:25	2.50	1.22	14.37
30m	2.99	8:10	1.92	10:25	2.39	1.06	13.26
12m	2.45	12:35	1.50	9:25	1.91	0.95	10.02
3m	2.80	13:00	1.46	10:20	2.00	1.34	8.29

The Weibull parameters were used to predict an average wind speed, which is a measure for the distribution's ability to accurately describe the wind data. Figure 4.7 presents the Weibull calculated average wind speed which very nearly resembles that corresponding to the data. The error of this estimate compared to the direct average of the wind speed was calculated and is less than 0.85% in each of these months at each anemometer location, with average errors for each location under 0.3%.

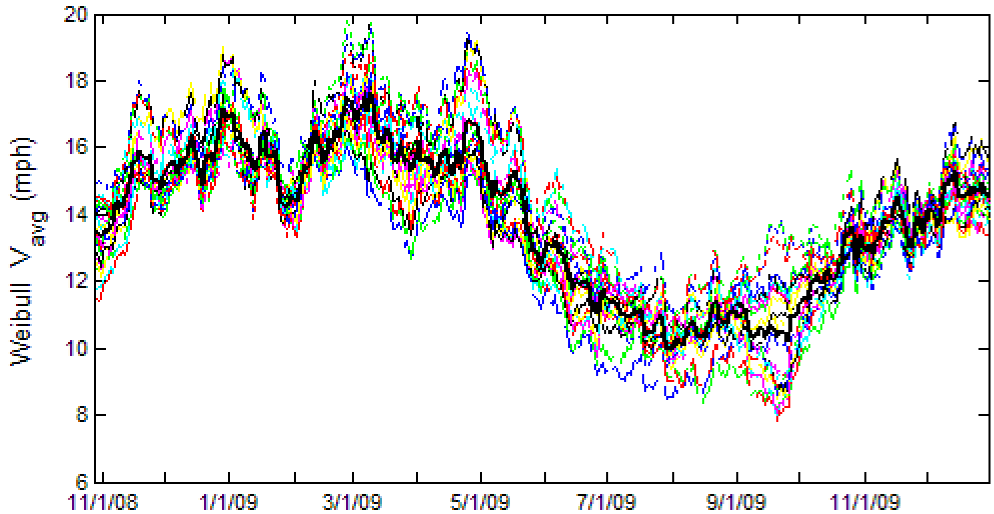

Figure 4.7: Weibull Calculated Average Wind Speed with 1-hour Sample Bins.

The Weibull parameters were used to determine the most probable wind speed and the wind speed carrying the most energy, Figures 4.8 and 4.9. A more significant wind speed regarding wind turbines is that corresponding to highest energy output (the highest frequency of the cube of the velocity). For the area studied, the most probable wind speed varied seasonally with the yearly average listed for each anemometer height in the figure legend, ranging from 5.3 to 12.2 mph. The maximum energy wind speed was over twice the value of the most probable wind speed for the 3m and 12m cases, and its yearly average ranged from 13.1 to 20.3mph. The effect of height on the values is notable with the 3m and 12m locations, but far less significant between 30 and 50m. The implications of this result affect the tower height selection for a wind turbine and help to understand the trade-off between power production and the installation height.

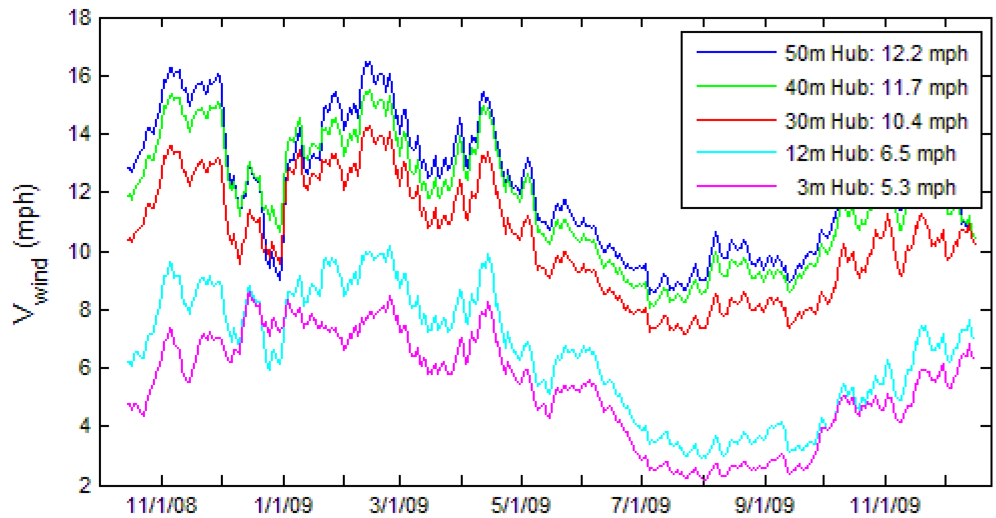

Figure 4.8: Weibull Parameter Calculated Most Probable Wind Speed.

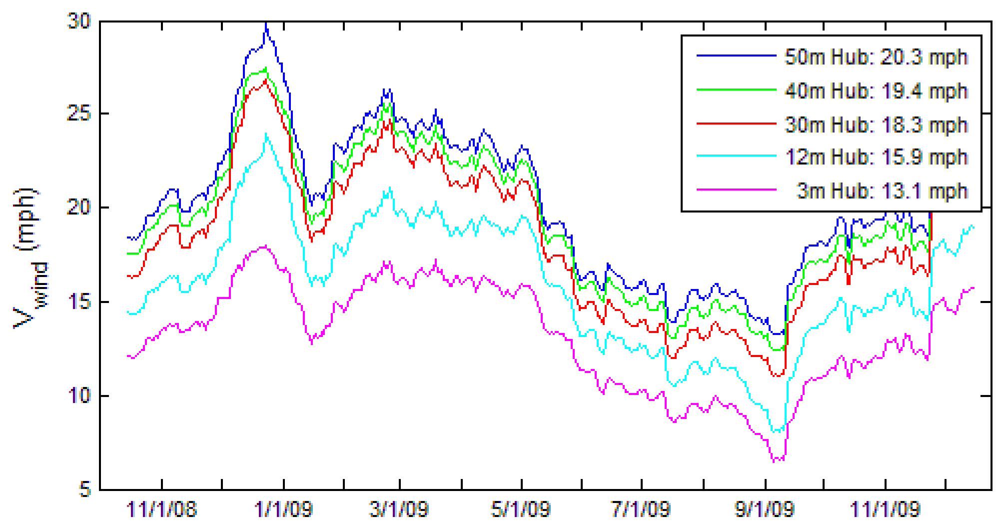

Figure 4.9: Weibull Parameter Calculated Maximum Energy Wind Speed.

The ability of a distribution to predict the average velocity of the wind is a useful tool for areas where these parameters are known or can be estimated. The prediction of the wind's power density is however a more significant value for wind turbines. Power density describes the power contained in the wind and is used to define the wind class environment. The distribution's prediction of velocity has an inherent error which is then multiplied when describing the power density; proportional to velocity cubed ($\sim V^3$). The comparison was made between the power density calculated directly from the wind data and that estimated with the three sampling periods chosen: 1, 30, and 90 day, Figure 4.10. The error in estimating the wind power density remained below a maximum error of about 4% using the Weibull distribution, confirming its acceptable description of this wind data. The Gauss-Hermite expansion method of calculating the power density of the wind distribution directly was also used to verify the results from Morissey et al. [6] which indicates the improvement of this method over the Weibull analysis, with a maximum error value observed of 1.09%, Table 4.6.

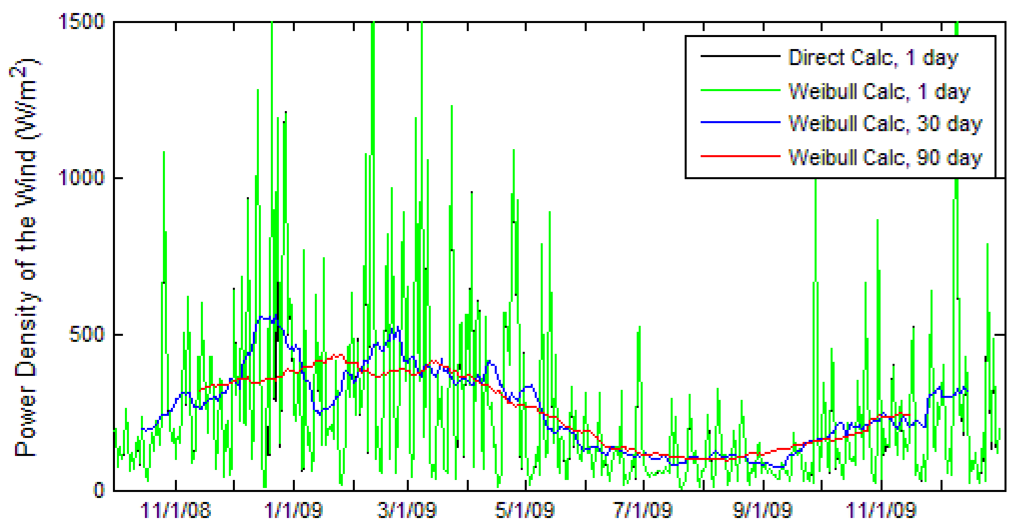

Figure 4.10: Power Density Comparison, Direct vs. Weibull Estimated Comparison.

Table 4.6: Wind Power Density Estimation and Error Comparison.

	50m	*40m*	*30m*	*12m*	*3m*
ACTUAL	253.0	226.1	187.0	103.0	58.0
WBL - 365 day	251.2	221.6	182.3	105.4	59.6
%error	0.75%	1.96%	2.54%	2.30%	2.78%
GH - 365 day	250.9	223.8	185.3	103.0	58.0
%error	1.15%	0.99%	0.89%	0.00%	0.01%
WBL - 1 day	259.2	229.4	189.9	107.2	60.2
%error	2.45%	1.50%	1.57%	4.01%	3.81%
GH - 1 day	251.1	224.0	185.7	103.4	58.2
%error	0.76%	0.89%	0.70%	0.34%	0.35%

Table 4.6: Continued.

WBL - 30 day	255.0	226.4	187.6	107.0	59.9
%error	0.79%	0.14%	0.33%	3.86%	3.33%
GH - 30 day	250.3	223.8	185.7	103.3	58.3
%error	1.09%	1.00%	0.72%	0.31%	0.52%

The wind power density was determined at the five anemometer height locations and is shown for the year in Figure 4.11. Based on the average throughout the year this location has a Wind Rating of between Class I and II at 10m (borders at 100 W/m^2), and a Class II rating at 50m (200-300 W/m^2) as defined by the National Renewable Energy Laboratory. Class II rating is typically thought of as a minimum for operating a wind turbine.

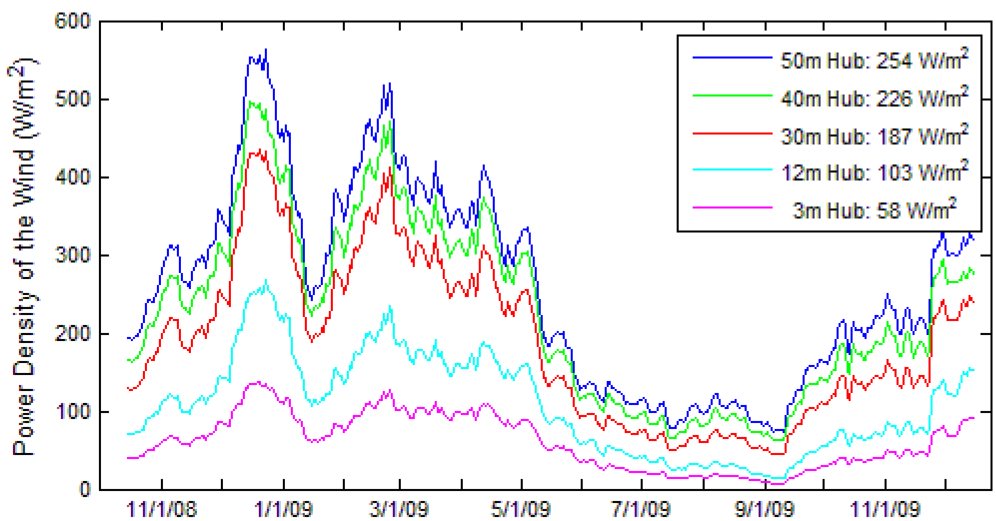

Figure 4.11: Wind Power Density Comparison with Height.

The relationship between the performance of a wind turbine and its hub height is regulated by the atmospheric velocity profile. For this analysis a power law velocity profile was assumed and the power law coefficient was derived following the procedure detailed by Equation 4.7. This coefficient is illustrated with hourly samples in Figure 4.12 to reveal the nature of the velocity profile throughout the year and day. In this analysis a lower coefficient describes a fuller velocity profile and is associated with turbulence, and a higher coefficient corresponds to a more gradual profile as present with laminar flow conditions. The power law coefficient typically lies in the range from 0.05 - 0.5, with 0.14 being a commonly accepted value which is widely applicable to open sites with low surfaces [39].

Figure 4.12 reveals the dichotomous power law coefficient where there is an upper and lower cluster of hourly averages with minimal transient time between them, around 2 hours. The year of study displays a transition from the high to low cluster at around 6 – 10 am throughout the year, and transitioning up to the high cluster between 4 – 6 pm. These results correlate well with what was found for the average wind speed daily trends which had a minimum occur at 7:10am and maximum at 4:25pm. This correlation means that the power law coefficient is in the low cluster at the minimum wind speeds in the first half day (turbulent conditions) and in the high cluster at the maximum wind speeds in the second half of the day (laminar conditions).

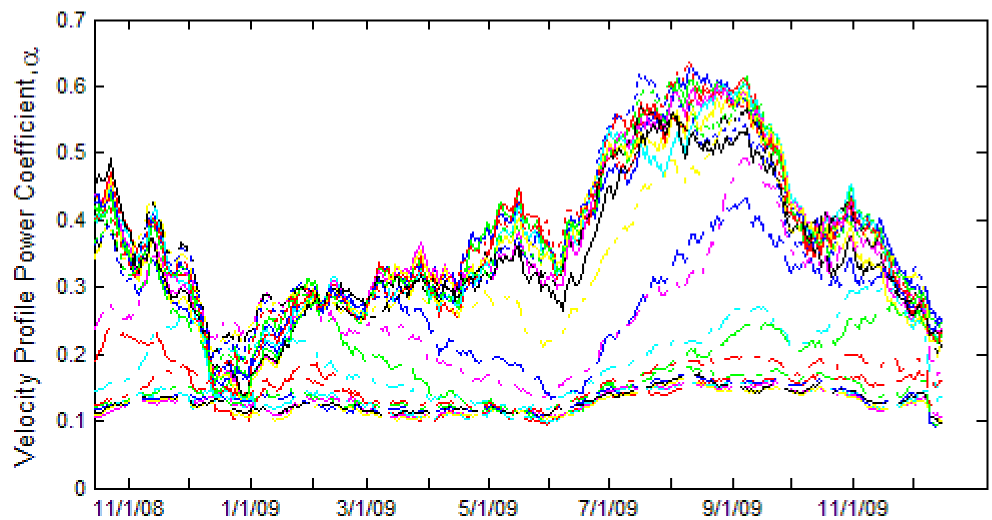

Figure 4.12: Velocity Profile Average Power Law Coefficient with 1-hour Sample Bins.

Average monthly wind data were used to show the effect of the velocity profile and how it changes throughout the year, Figure 4.13. The higher wind speed months subscribe to a more turbulent looking profile and lower wind speed months to more laminar profiles. The velocity profile power law coefficient was calculated based on these average wind speeds and given in Table 4.7.

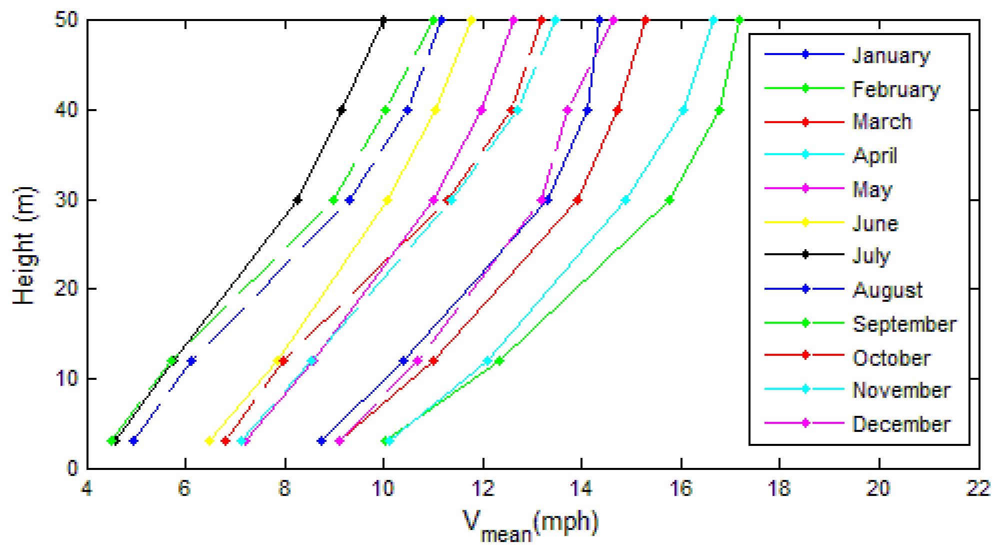

Figure 4.13: Averaged Monthly Wind Speed Velocity Profiles.

Table 4.7: Monthly Power Law Coefficients.

Month	α	Month	α
January	0.19	July	0.28
February	0.2	August	0.3
March	0.19	September	0.33
April	0.18	October	0.25
May	0.2	November	0.23
June	0.21	December	0.17

The wind data was used directly to calculate the performance of two of the industry leading small wind turbines to give quality measures of their performance. Power production of the wind turbines was determined using the manufacturer's power curve which relates the wind turbine power with wind speed. The small wind turbines studied are described in Table 4.8.

Table 4.8: Small Wind Turbine Specifications.

Model	Power Capacity (W)	Rotor Diameter (ft)
SWWP Whisper100	900	7
Bergey XL.1	1000	8.2

The capacity factor of the two wind turbines is calculated to display their performance fluctuations within the year, also revealing the effects of installation height. The capacity factor is lowest during the summer months for the two turbines, following the wind speed trend. The variability in performance for both wind turbines is around 20-30% throughout the year which would need to be known to size the turbine appropriately to get the power output required during the year or during specific times of the year. The yearly averaged capacity factors calculated from 365 successive days within the data set are given in the legend for each height position for the two wind turbines in Figures 4.14 and 4.15. The Southwest Windpower Whisper 100 yearly averaged capacity factor ranges from 24.5% to 6.5% for hub heights ranging from 50m to 3m, where the Bergey XL.1 varies similarly from 32.8% to 9%. The Southwest Windpower Whisper 100 model wind turbine was outperformed by the Bergey XL.1 at every height and by about 33% at 50m. Both models revealed low capacity factors for this study's wind conditions which was especially true at 3m and 12m.

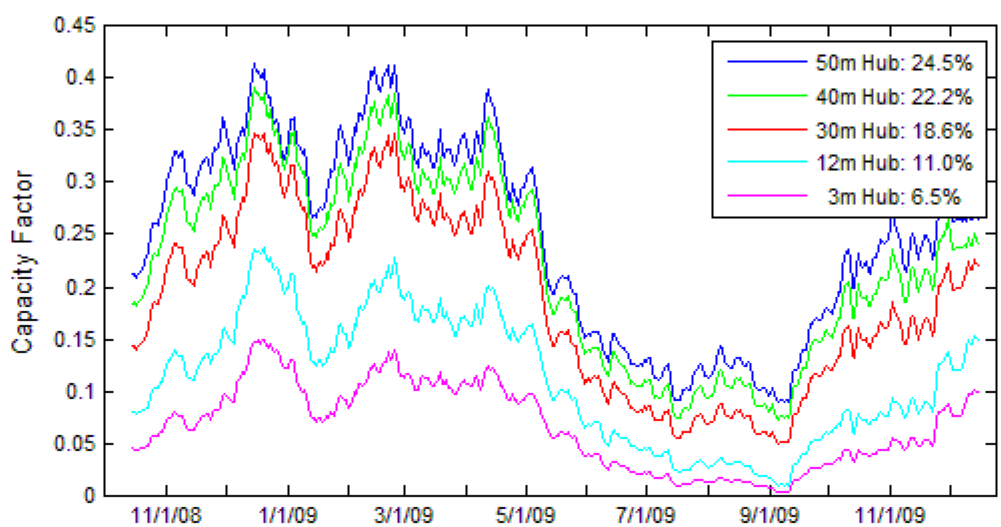

Figure 4.14: SWWP Whisper 100, Capacity Factor Averages.

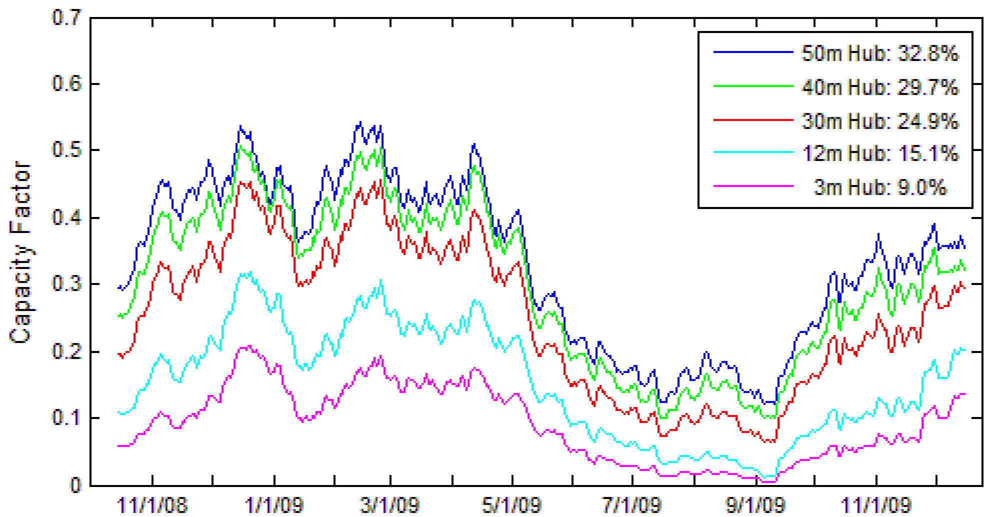

Figure 4.15: Bergey XL.1, Capacity Factor Averages.

The yearly average capacity factor for the two commercial small wind turbines shown above is summarized versus tower height in Figure 4.16, clearly illustrating the XL.1's increasing improvement with tower height and higher wind speeds over the Whisper 100.

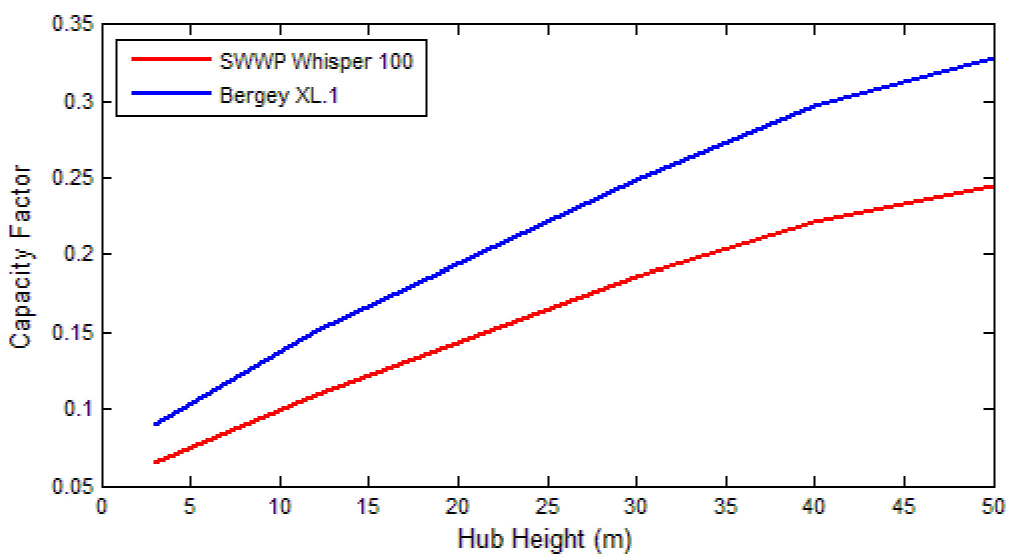

Figure 4.16: Yearly Average Small Wind Turbine Capacity Factor Comparison.

The ratio of the power density of a wind turbine to the power density of the wind is described by the power coefficient, C_p, which was calculated for the two small wind turbines over the year of study, Figure 4.17. There is a significant discrepancy between the amount of power in the wind and that captured by the wind turbine, which varies between 18-34% for 30 day averages throughout the year for the Bergey XL.1. The Bergey XL.1 is seen to perform with a higher power coefficient than the Whisper 100, however less significantly than with the capacity factor due to its larger area.

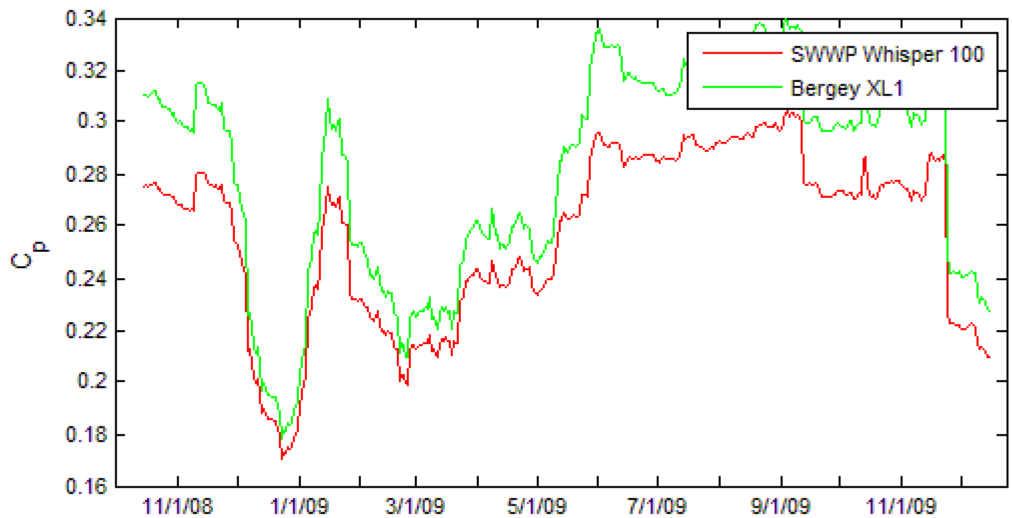

Figure 4.17: Small Wind Turbine Power Coefficient Averages.

The power coefficient value varies with wind speed following the wind turbine's power curve relationship, Figure 4.18. The maximum power coefficients for the Whisper 100 and XL.1 are found to be 35.8 and 38.4%, respectively, as compared to the Betz value of 59%. These maxima occur at about 11.5 and 14 mph for the Whisper 100 and XL.1, after which there is a negative trend with wind speed and power coefficient C_p. The maximum power coefficient occurs at a notably lower wind speed than the maximum power production for the two wind turbines (28 and 24.6 mph).

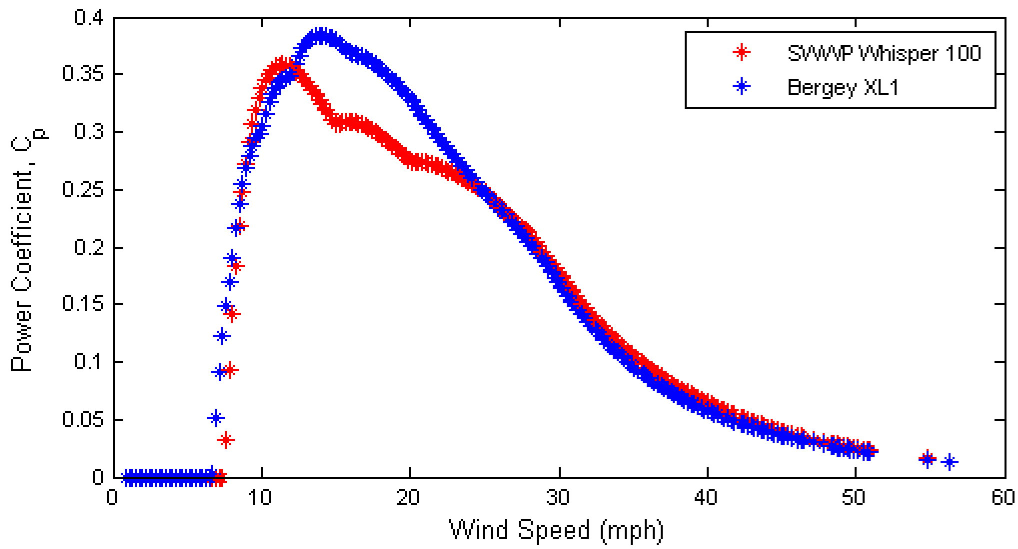

Figure 4.18: Small Wind Turbine Power Coefficient Comparison.

The power coefficient variation throughout the year is shown for the five anemometer heights for the Bergey XL.1 wind turbine, Figure 4.19. The yearly average of this parameter varies from 29.8% to 21.7% for a 50m to 3m height. High wind speed portions of the year result in the 50m height location representing the lowest value amongst the five heights due to the power coefficient trend with wind speed shown in Figure 4.18.

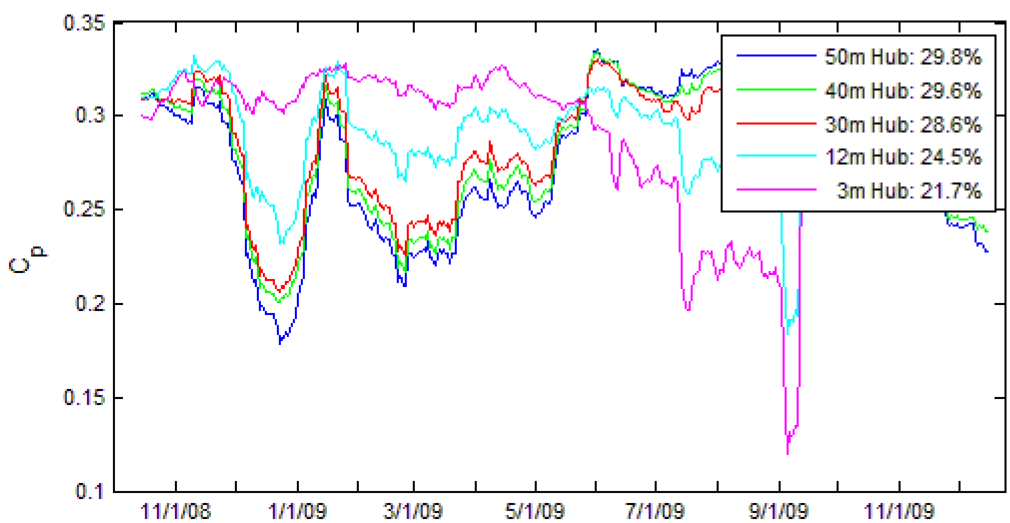

Figure 4.19: Bergey XL.1 Power Coefficient Comparison with Hub Height.

Table 4.9 below summarizes the performance results for the two small wind turbines studied listing the yearly averaged performance measures at the five wind speed height locations from the data set along with the maximum power coefficient for each wind turbine.

Table 4.9: Small Wind Turbine Comparison Performance Results.

	CF_{year} (%)					$C_{p,year}$ (%)					$C_{p,max}$
Model	50m	40m	30m	12m	3m	50m	40m	30m	12m	3m	
SWWP Whisper100	24.5	22.2	18.6	11	6.5	27.1	27	26.2	22.3	19.6	35.8
Bergey XL.1	32.8	29.7	24.9	15.1	9	29.8	29.6	28.6	24.5	21.7	38.4

This performance analysis was also extended to large utility size wind turbines to compare the effects of rotor diameter and generator size on the machine's performance in this wind condition. Three wind turbines from General Electric were compared which have a power rating and rotor diameter that vary independently from a control (GE 1.6-100), shown in Table 4.10.

Table 4.10: Utility Size Wind Turbine Specifications.

Model	Power Capacity (MW)	Rotor Diameter (m)
GE 1.6-100	1.6	100
GE 1.6-82.5	1.6	82.5
GE 2.5-103	2.5	103

The three wind turbines analyzed all share one tower height option commercially at 80 m. To make the study more realistic this common height is used for the analysis. Wind speeds were not recorded at 80m so the velocity at this height was calculated by extrapolating the velocity at 50m using the velocity profile power law estimation and average power coefficients as discussed earlier. The yearly average of the power density from the wind data extrapolated to 80m was found to be 348 W/m^2.

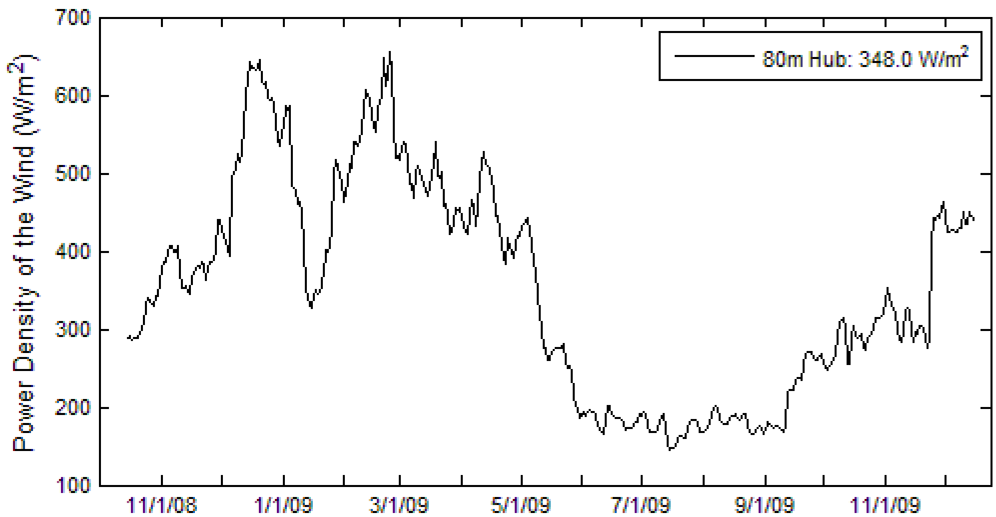

Figure 4.20: Wind Power Density Extrapolated to 80m Height.

Turbine performance was calculated again using the power curves for the three utility-size turbines and the wind speed and is described using the identical measures as before. Capacity factor for the three turbines is compared using the yearly data with a 30 day sample bin, Figure 4.21. The yearly average of the capacity factor was also determined by averaging the power output of the turbine for 365 successive days. The order of highest capacity factor was the GE 1.6-100 at 46.8% its rated power, GE 1.6-82.5 at 39.3% its rated power, and finally the GE 2.5-103 at 36.6% its rated power. Dependent upon the cost of the turbines and installation, an economic decision could be made using this information to either buy more of the less expensive turbines which perform at a higher capacity factor or less of the more expensive turbines with the higher rated power and lower capacity factor. If the cost was a constant function of only the power capacity of the machine then the analysis would conclude to purchase the turbine with the highest capacity factor. The cost for a wind turbine does depend on more than just its capacity however, and additional (relatively) fixed costs like installation and land usage push towards fewer, higher power capacity wind turbines.

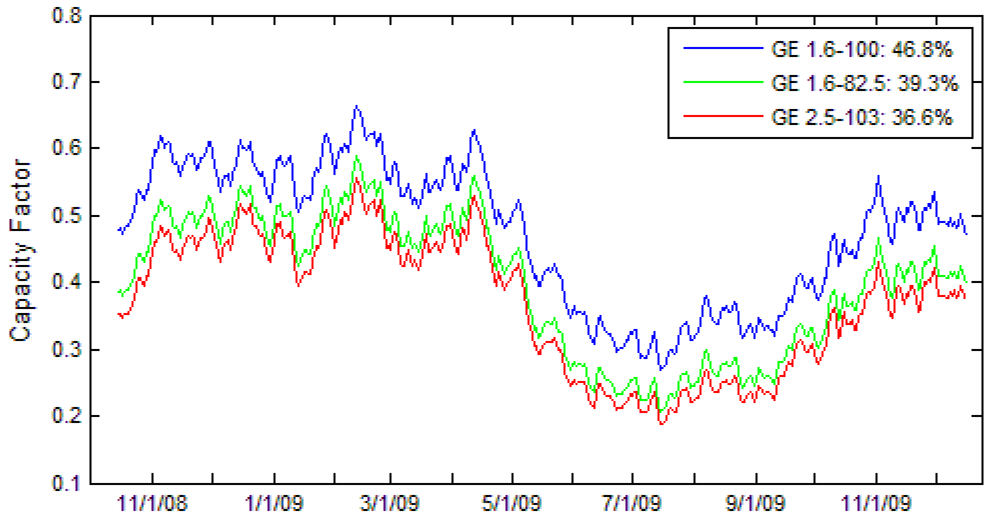

Figure 4.21: Utility Size Wind Turbine Capacity Factor Comparison (80m Height).

The second measure of turbine performance, the power coefficient, is also compared for the three utility turbines throughout the year using the 80m extrapolated wind data, Figure 4.22. This measure does not duplicate the information shown by the capacity factor above as clearly seen in this comparison, where the turbine with the highest capacity factor also has the lowest power coefficient. The smaller area GE 1.6-82.5 has the highest power coefficient, which depends on the turbine area, followed by the GE 2.5-103 and then the GE 1.6-100. There is nearly a 10% increase in this efficiency measure for the 1.6 MW wind turbines for the smaller rotor diameter compared with the larger diameter machine. The higher rated wind turbine has a 2% increase in machine efficiency than the lower rated turbine with nearly the same rotor diameter.

Power coefficient versus wind speed plots are shown for the three utility wind turbines as calculated from the individual turbine power curves. Figure 4.23 shows how the power coefficient varies with wind speed for these three turbines. An important thing to note, the GE 1.6-100 has a higher maximum power coefficient than the GE 2.5-103, but a lower yearly average, due to the broader curve for the GE 2.5-103 and the distribution of wind speed. Higher peak efficiency doesn't mean the turbine will perform better if the alternative is a broader, flatter peak region.

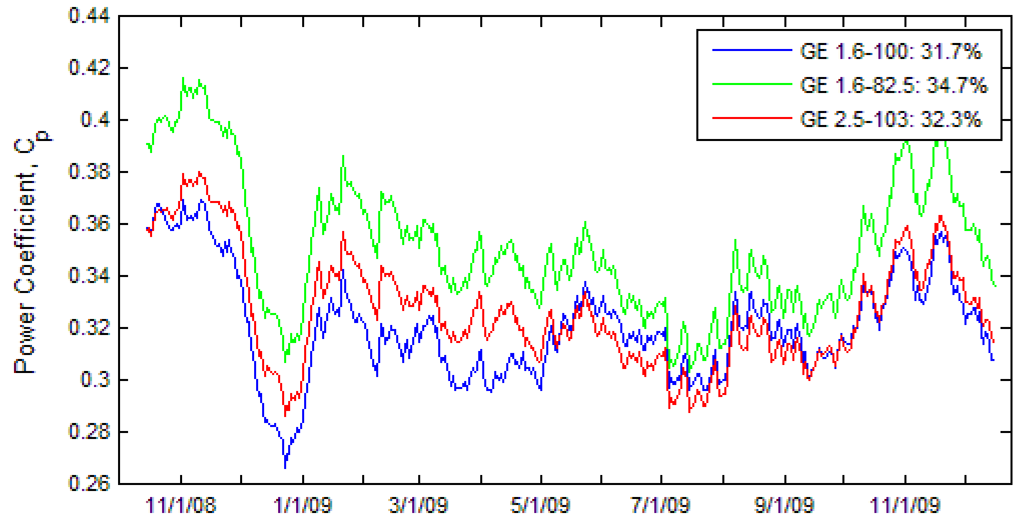

Figure 4.22: Utility Size Wind Turbine Power Coefficient (80m Height).

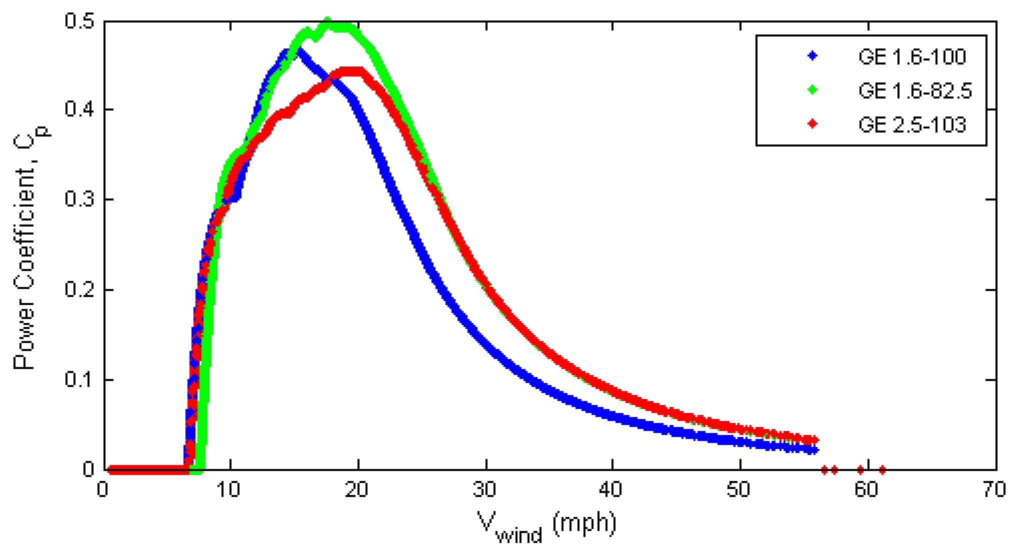

Figure 4.23: Utility Size Wind Turbine Power Coefficient Comparison.

The results of the performance comparison for the three utility-size wind turbines are summarized in Table 4.11 with the machine characteristics restated.

Table 4.11: Utility Size Wind Turbine Comparison Performance Results.

Model	P_{rated} (MW)	D_{rotor} (m)	CF_{year}	$C_{p,year}$	$C_{p,max}$
GE 1.6-100	1.6	100	46.8	31.7	46.6
GE 1.6-82.5	1.6	82.5	39.3	34.7	49.8
GE 2.5-103	2.5	103	36.6	32.3	44.4

A sensitivity analysis was performed using the generic wind turbine power curve from Equation 4.8 to determine the effect of changing the three defining speeds of a wind turbine's power curve; cut-in, rated, and cut-out wind speeds. These values are the wind speeds where power is first produced by the turbine, where the turbine produces its rated power, and where the turbine is stopped due to high winds, respectively. In this analysis, the three speeds were changed independently with the other two speeds held constant. The nominal values (where that speed was not the test subject) are: Cut-in speed = 6 mph, Rated speed = 25 mph, and Cut-out speed = 45 mph. Additionally, the exponent n in the generic wind turbine equation was set to a value of 3 and the study was performed using 365 days of the wind speed data at 50m. Figure 4.24 reveals that changing the rated speed has the greatest influence on the capacity factor for a wind turbine. The capacity factor is relatively insensitive to the cut-in and cut-out speeds when they remain within current common values. Extending the range of operation by decreasing the cut-in and increasing the cut-out speeds has a negligible effect on the capacity factor over much of the range in this wind condition.

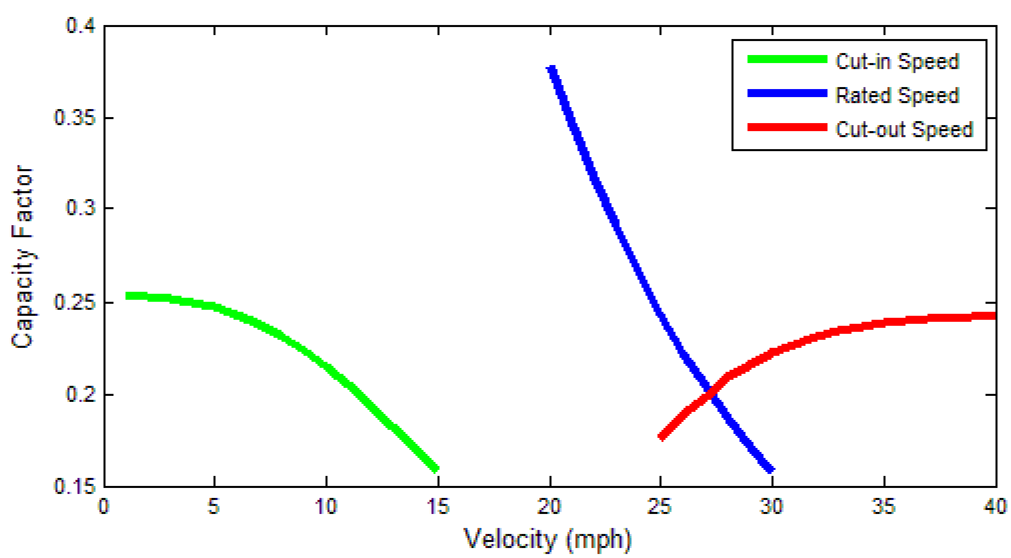

Figure 4.24: Wind Turbine Capacity Factor Sensitivity Study.

4.5 Conclusions

The analysis of wind speed data for West Lafayette, Indiana holds strong seasonal and daily trends. Within the day and throughout the year wind speeds are observed that fluctuate as a substantial percentage of the average. The trends hold that highest wind speeds occur seasonally in winter and early spring, and the lowest values are during the summer months. Daily variations are such that the lowest wind speeds occur in the first half of the day where the highest values are in the second half. The time within the day averages out from the year to occur at 7:10 am and 4:25 pm for the minimum and maximum. The distribution of the wind speed was described using the Weibull probability function and the accuracy of this method is again proven for both estimating the average velocity from calculated parameters and from estimating the power in the wind with maximum errors around 0.85% and 4%. The atmospheric velocity profile was estimated using a power law approximation and coefficients determined. Wind turbine performance within the measured wind conditions were calculated for small residential wind turbines and for utility-size wind turbines to compare. The two small wind turbines compared differed by about 33% on the year at 50m in capacity factor with a 32.8% maximum value average on the year. A comparative study between rotor diameter and rated power was performed for utility-size wind turbines, with 100m and 1.6 MW as the benchmark. Performing in the wind conditions of this study revealed that the low capacity, large rotor diameter had the highest capacity factor, but also the lowest power coefficient on the year. The low capacity, small rotor diameter had the highest power coefficient on the year. Increasing the rotor diameter by 21% resulted in a 19% increase in the power production for the 1.6 MW machines, therefore an 8.6% decrease in average power coefficient. For the turbine with a 56% increase in the rated capacity, the capacity factor decreased by only 28%.

4.6 Highlights

- Wind speed averages on the year at heights of (50, 40, 30, 12, 3)-m were found of (13.5, 12.8, 11.8, 8.9, 7.4)-mph.
- November to May and times centered around 4:30pm contain the highest wind speeds on the year, while June to October and the time of day centered around 7am produced the lowest wind speeds on the year.
- Weibull probability analysis yearly average coefficients were calculated at heights (50, 40, 30, 12, 3)-m producing shape factors of k = (2.5, 2.5, 2.4, 1.9, 2.0) and scale factors of c = (15.1, 14.4, 13.3, 10.0, 8.3)-mph.
- Wind Power class at the studied location is determined to be Class II at 50-m height with a wind power density average of 254 W/m^2, and between Class I-II at 10-m with an average wind power density at 12-m of 103 W/m^2.
- Small wind turbine performance was estimated for two leading manufacturer's models with yearly average capacity factors at 50-m height of 24.5% and 32.8% and yearly power coefficient values of 27.1% and 29.8%.
- Utility-size wind turbines were compared for three models at an extrapolated 80-m height with yearly averages of the capacity factor of (46.8, 39.3, 36.6)% and of the power coefficient of (31.7, 34.7, 32.3)%

4.7 Additional Monthly Averaged Wind Speed Data

Table 4.12: Monthly Averaged Wind Speed Data, 40m (mph).

Month	*V,max*	*t,max*	*V,min*	*t,min*	*V,avg*	*ΔV,avg*
January	15.23	14:00	13.43	0:00	14.14	1.80
February	18.36	21:00	14.90	7:00	16.80	3.46
March	16.70	16:00	11.83	7:00	14.70	4.87
April	18.65	12:00	14.35	2:00	16.06	4.30
May	13.74	17:00	10.66	3:00	11.98	3.08
June	13.09	16:00	9.05	7:00	11.02	4.04
July	10.68	14:00	7.69	7:00	9.13	2.99
August	11.55	14:00	9.24	7:00	10.46	2.31
September	12.08	21:00	8.38	8:00	10.03	3.70
October	14.28	14:00	11.71	6:00	12.58	2.56
November	13.37	22:00	11.89	7:00	12.71	1.47
December	14.87	13:00	12.88	9:00	13.75	1.99
AVERAGE:	14.38	16:10	11.33	5:50	12.78	3.05

Table 4.13: Monthly Averaged Wind Speed Data, 30m (mph).

Month	*V,max*	*t,max*	*V,min*	*t,min*	*V,avg*	*ΔV,avg*
January	14.94	14:00	12.42	23:00	13.31	2.52
February	17.16	16:00	13.59	7:00	15.78	3.56
March	16.14	16:00	10.96	7:00	13.88	5.18
April	17.95	12:00	12.78	2:00	14.86	5.18
May	13.03	17:00	9.27	3:00	11.02	3.75
June	12.39	16:00	8.23	7:00	10.07	4.16
July	10.18	14:00	6.86	7:00	8.28	3.32
August	10.85	15:00	7.87	6:00	9.31	2.98
September	10.43	21:00	7.57	8:00	8.99	2.86
October	13.44	14:00	10.21	6:00	11.33	3.23
November	12.37	13:00	10.27	7:00	11.40	2.10
December	14.53	13:00	12.12	9:00	13.20	2.42
AVERAGE:	13.62	15:05	10.18	7:40	11.78	3.44

Table 4.14: Monthly Averaged Wind Speed Data, 12m (mph).

Month	*V,max*	*t,max*	*V,min*	*t,min*	*V,avg*	*ΔV,avg*
January	12.20	14:00	9.29	23:00	10.48	2.91
February	14.25	15:00	10.10	7:00	12.35	4.16
March	13.74	16:00	8.01	7:00	10.98	5.73
April	15.98	12:00	9.55	4:00	12.13	6.43
May	11.42	15:00	5.86	2:00	8.60	5.55
June	10.81	16:00	5.74	5:00	7.86	5.07
July	8.73	14:00	3.61	21:00	5.76	5.12
August	8.84	14:00	4.02	1:00	6.12	4.83
September	7.47	15:00	4.17	4:00	5.69	3.31
October	10.68	14:00	6.39	3:00	8.00	4.29
November	10.63	14:00	7.13	7:00	8.56	3.50
December	12.79	13:00	9.40	8:00	10.67	3.39
AVERAGE:	11.46	14:20	6.94	7:40	8.93	4.52

Table 4.15: Monthly Averaged Wind Speed Data, 3m (mph).

Month	*V,max*	*t,max*	*V,min*	*t,min*	*V,avg*	*ΔV,avg*
January	10.79	13:00	7.30	21:00	8.74	3.49
February	12.10	15:00	8.14	7:00	10.05	3.96
March	11.72	15:00	6.68	6:00	9.09	5.04
April	13.67	12:00	7.72	4:00	10.10	5.95
May	9.87	15:00	4.59	2:00	7.20	5.28
June	9.14	16:00	4.36	22:00	6.47	4.78
July	7.31	14:00	2.13	21:00	4.57	5.18
August	7.45	14:00	2.85	1:00	4.93	4.59
September	6.32	12:00	3.10	19:00	4.47	3.22
October	9.24	14:00	5.35	20:00	6.80	3.89
November	9.52	11:00	5.62	0:00	7.11	3.90
December	11.15	13:00	8.01	1:00	9.08	3.14
AVERAGE:	9.86	13:40	5.49	10:20	7.38	4.37

4.8 Additional Monthly Averaged Weibull Parameter Data

Table 4.16: Monthly Weibull Averaged Wind Speed Data, 40m.

Month	*k,max*	*t,max*	*k,min*	*t,min*	*K,avg*	*Δk,avg*	*c,avg (mph)*
January	3.70	3:00	2.55	18:00	2.90	1.15	15.84
February	3.10	6:00	2.17	18:00	2.54	0.93	18.90
March	2.45	2:00	1.67	14:00	2.10	0.78	16.60
April	2.84	6:00	2.19	1:00	2.56	0.65	18.09
May	2.91	3:00	1.92	8:00	2.28	0.99	13.51
June	3.78	2:00	1.90	10:00	2.57	1.88	12.38
July	3.53	6:00	1.89	8:00	2.59	1.64	10.27
August	4.15	2:00	1.97	10:00	2.91	2.18	11.72
September	3.15	6:00	1.80	9:00	2.36	1.35	11.30
October	3.02	3:00	2.08	8:00	2.54	0.94	14.16
November	3.19	23:00	2.09	16:00	2.66	1.10	14.26
December	2.58	6:00	1.53	17:00	2.01	1.05	15.43
AVERAGE:	3.20	5:40	1.98	11:25	2.50	1.22	14.37

Table 4.17: Monthly Weibull Averaged Wind Speed Data, 30m.

Month	*k,max*	*t,max*	*k,min*	*t,min*	*k,avg*	*Δk,avg*	*c,avg (mph)*
January	3.66	3:00	2.46	18:00	2.79	1.19	14.92
February	2.86	6:00	2.13	19:00	2.43	0.73	17.77
March	2.33	1:00	1.65	14:00	2.02	0.68	15.67
April	2.74	16:00	2.10	1:00	2.43	0.64	16.75
May	2.66	3:00	1.84	0:00	2.18	0.82	12.42
June	3.82	2:00	1.78	8:00	2.54	2.03	11.31
July	3.21	6:00	1.87	8:00	2.53	1.34	9.30
August	3.68	23:00	1.96	10:00	2.74	1.72	10.43
September	2.85	6:00	1.75	9:00	2.20	1.10	10.12
October	2.76	3:00	1.80	8:00	2.36	0.96	12.74
November	2.79	23:00	2.07	16:00	2.44	0.72	12.81
December	2.50	6:00	1.69	14:00	2.03	0.81	14.85
AVERAGE:	2.99	8:10	1.92	10:25	2.39	1.06	13.26

Table 4.18: Monthly Weibull Averaged Wind Speed Data, 12m.

Month	*k,max*	*t,max*	*k,min*	*t,min*	*k,avg*	*Δk,avg*	*c,avg (mph)*
January	2.67	15:00	1.89	23:00	2.24	0.78	11.74
February	2.53	9:00	1.69	3:00	2.10	0.83	13.91
March	2.23	9:00	1.56	22:00	1.77	0.67	12.33
April	2.89	16:00	1.64	0:00	2.22	1.25	13.64
May	2.32	14:00	1.25	0:00	1.77	1.07	9.59
June	2.47	17:00	1.45	6:00	1.98	1.03	8.84
July	2.94	14:00	1.28	2:00	1.88	1.66	6.45
August	2.38	13:00	1.42	6:00	1.82	0.96	6.86
September	1.92	12:00	1.34	7:00	1.60	0.58	6.38
October	2.48	16:00	1.46	4:00	1.83	1.02	8.96
November	2.59	10:00	1.56	21:00	1.92	1.04	9.59
December	2.00	6:00	1.48	19:00	1.72	0.52	11.95
AVERAGE:	2.45	12:35	1.50	9:25	1.91	0.95	10.02

Table 4.19: Monthly Weibull Averaged Wind Speed Data, 3m.

Month	*k,max*	*t,max*	*k,min*	*t,min*	*k,avg*	*Δk,avg*	*c,avg (mph)*
January	3.32	15:00	1.71	18:00	2.53	1.61	9.82
February	2.85	13:00	1.63	3:00	2.12	1.22	11.30
March	2.61	9:00	1.45	0:00	1.78	1.16	10.18
April	3.14	16:00	1.57	0:00	2.28	1.57	11.34
May	2.63	14:00	1.16	23:00	1.87	1.47	8.03
June	2.74	17:00	1.64	20:00	2.06	1.10	7.29
July	3.34	14:00	1.26	1:00	1.99	2.08	5.12
August	2.66	13:00	1.41	0:00	1.87	1.25	5.52
September	2.25	12:00	1.25	18:00	1.68	1.00	5.01
October	2.84	10:00	1.52	1:00	2.03	1.32	7.63
November	3.13	10:00	1.41	21:00	1.94	1.72	7.96
December	2.10	13:00	1.50	19:00	1.80	0.61	10.21
AVERAGE:	2.80	13:00	1.46	10:20	2.00	1.34	8.29

CHAPTER 5: MICRO RECONFIGURABLE WIND FARM EXPERIMENTAL RESULTS

5.1 Limitations and Assumptions

Comparison of the performance of the wind turbines in wake operation requires a set of assumptions. The first assumption is that the two wind turbines operate at the same power output in equivalent wind conditions. This assumption depends on the repeatability of blade manufacturing and generator and electrical system repeatability. The effect of any error from this assumption's violation is limited by always placing each wind turbine in the same relative position, upstream or downstream of the other, and by averaging the power samples over T_{bin} to reduce differences in the power caused by the generator. In addition to this assumption, the torque/rotational speed split of the produced power is also assumed equal for both wind turbines at a given input so that these values can also be compared.

Variations in performance measurements with wind speed and with the upstream wind turbine's aerodynamic power are treated synonymously in this analysis. This assumption is justified by the manufacturer's power curve which displays a one-to-one relationship with the wind speed and output power. This, however, is not the true power curve with wind speed due to the generator dynamics which produce regular transients as the load is cycled. Grouping the performance measures within aerodynamic power bins is treated as having the same effect as with wind speed, but producing more accurate results due to the generator dynamics.

5.2 Wind Turbine Single Wake Results

Wake performance data were collected for the single wake case on five windy days over a three week span. The data set includes repeated tests for three different turbine spacing's of 3-, 5-, and 7-rotor diameters. An example test case facility configuration for a 3-rotor diameter turbine spacing is shown in Figure 5.1.

Figure 5.1: Facility Configuration with a Single Wake, 3-Rotor Diameter Spacing.

As detailed in Section 3.4.2, the data were processed and filtered into the final usable data set using three filters; T_{bin}, T_{sort}, and P_{range}. T_{bin} describes the minimum sample bin time length for alignment that would be included in the final data set. These bins are then divided into T_{sort} length bins, when the initial length is large enough. The upstream wind turbine aerodynamic power is averaged within each bin, and data whose averages are within P_{range} are collectively averaged together to give the final result describing that variable within P_{range}. For the single wake test case it was determined that using values of T_{bin} = 10-sec and T_{sort} = 10-sec produced accurate results. The total data set averages of the normalized power and data set time for the single wake test case for a P_{range}= [75 W, ∞) are summarized for the three wind turbine spacing's tested in Table 5.1. In all of the results, the normalized averages are the time weighted averages of the bins within the particular P_{range}.

Table 5.1: Single Wake Test Case Performance Results (t_{bin}= 10s/t_{sort}= 10s).

3-Rotor Diameter Wind Turbine Spacing

Date	Filtered Data Set Time (min)	Normalized Power Data Set Average
Day2	9.5	0.353
Day3	15.1	0.453
Day4	22.3	0.499
total	46.9	0.455

5-Rotor Diameter Wind Turbine Spacing

Date	Filtered Data Set Time (min)	Normalized Power Data Set Average
Day1	16.4	0.72
Day2	19.1	0.676
Day5	33.9	0.799
total	69.4	0.746

7-Rotor Diameter Wind Turbine Spacing

Date	Filtered Data Set Time (min)	Normalized Power Data Set Average
Day1	2.7	0.876
Day4	31.7	0.832
Day5	23	0.85
total	57.4	0.841

The variable filter times affect the results of the single wake test case. Choosing a larger T_{bin} means that you are only looking at the data bins where the wind turbine was aligned over a larger portion of time. A larger time also means that the generator dynamics would be averaged more appropriately to account for the transients of the rotor as it is loaded by the generator. The higher bin requirement however comes at a cost of total data time in each set. Reducing the amount of data for a set results in less certainty of the validity of the results, and can produce erroneously large or small distribution statistics. The T_{bin} condition was made to ensure that the turbines were actually aligned during the sample and not simply passing through from on one side of the turbine to the other side. The time condition would also need to be sufficient enough to overcome generator dynamics, if present. Additionally, larger conditional time lengths reduce the error inherent with using a time shift from the upstream wind turbine to the second based on the bin average velocity. With this noted, there were many sub- 10-sec bins of constant alignment which would accomplish the goals of this filter. It was observed that 10-sec is a fairly long time considering input wind variations and the tight conditions placed on alignment. T_{bin}= 10-sec was taken as a sufficient time length to produce valid results, and more total filtered data with improved statistics.

The total averaged results are seen to vary from about 1-4% for the three tested spacing's depending upon the bin length chosen, shown in Table 5.2. In each of the cases, the loss is increased with the larger bin length. The P_{range}= [75 W, ∞) averages are lower, but when plotted with further sub-divided power ranges, the averages are consistent within statistical variation for the three spacing's at each of the compared bin time values. The reduced normalized power trend with bin time is likely a result of the longer bins happening during strong gusts where the upstream turbine is removing more momentum from the air causing a lower normalized power, shifting the weight of the data average to higher powers.

The T_{sort} bin division length is seen to have little effect on the average results when taken over large power ranges. This variable is more important for dividing up large bins which may actually contain high and low power averages to ensure proper averaging when the ranges are divided. By comparison, the 10-sec sort time produced the smoothest results for comparison over a finer sorting of power bins. For this reason and considering the justification for the bin time value, a 10-sec sort time was chosen for the final results.

Table 5.2: Normalized Power Data Processing Comparison.

Bin Time	Sort Time	s/D = 3	s/D = 5	s/D = 7
10 sec	unsorted	0.453	0.749	0.841
10 sec	10 sec	0.455	0.746	0.841
10 sec	30 sec	0.453	0.746	0.842
20 sec	10 sec	0.429	0.726	0.826
20 sec	20 sec	0.431	0.727	0.832
30 sec	10 sec	0.417	0.717	0.832
30 sec	30 sec	0.412	0.72	0.834

Filter conditions using T_{bin}= 10-sec and T_{sort}= 10-sec are used for describing the results of the single wake test case. This processing scheme is seen to sufficiently average the generator dynamics and any error due to using bin-averaged time shifts, while maintaining enough data points and time for accurate power range division averaging. Two additional cases of (T_{bin}, T_{sort}) = (20-sec, 20-sec) and (30-sec, 30-sec) are shown for completeness and comparison of the total filtered data time in Tables 5.3 and 5.4. The total amount of time meeting P_{bin} > 75W was reduced for (3, 5, 7) diameter spacing sets from (47, 69, 57) minutes for 10-sec bin requirement to (38, 56, 42) and (23, 37, 25) minutes for 20- and 30-sec bin requirements. Comparison of these times reveals the amount of data within the 10-sec minimum bin requirement data set which has a bin time greater than 20-sec, and greater than 30-sec. Outside of these two tables, all remaining results use the final data processing conditions described.

Table 5.3: Single Wake Test Case Performance Results (t_{bin}= 20s/t_{sort}= 20s).

3-Rotor Diameter Wind Turbine Spacing

Date	Filtered Data Set Time (min)	Normalized Power Data Set Average
Day2	9.4	0.327
Day3	11.4	0.451
Day4	17	0.475
total	37.8	0.431

5-Rotor Diameter Wind Turbine Spacing

Date	Filtered Data Set Time (min)	Normalized Power Data Set Average
Day1	16	0.716
Day2	17	0.669
Day5	22.5	0.779
total	55.5	0.727

7-Rotor Diameter Wind Turbine Spacing

Date	Filtered Data Set Time (min)	Normalized Power Data Set Average
Day1	2.1	0.886
Day4	23.8	0.834
Day5	15.7	0.823
total	41.6	0.832

Table 5.4: Single Wake Test Case Performance Results (t_{bin}= 30s/t_{sort}= 30s).

3-Rotor Diameter Wind Turbine Spacing

Date	Filtered Data Set Time (min)	Normalized Power Data Set Average
Day2	7	0.314
Day3	6.77	0.445
Day4	9.4	0.462
total	23.17	0.412

5-Rotor Diameter Wind Turbine Spacing

Date	Filtered Data Set Time (min)	Normalized Power Data Set Average
Day1	14.1	0.707
Day2	10.9	0.68
Day5	11.9	0.771
total	36.9	0.720

7-Rotor Diameter Wind Turbine Spacing

Date	Filtered Data Set Time (min)	Normalized Power Data Set Average
Day1	2	0.918
Day4	14.3	0.832
Day5	8.9	0.817
total	25.2	0.834

The single wake performance total data sets and range averages are shown in Figures 5.2-7. The filtered and sorted bins are averaged individually for the normalized power, torque, and rotational speed with each bin plotted for the three spacing's versus the upstream wind turbine power –a measure of the incoming wind speed. Additionally, the range averages are compared using 100-W power ranges with the center value as the index. The averages are plotted with $\pm$ 1 standard deviation of the range data set to reveal its distribution. The total data set plot reveals the range and number of samples for each of the three spacing's. From this plot, it is clear that the final 3-diameter spacing range [450, 550] W is not a statistically significant result which explains the final point in the range average plots for this spacing going against the downward trend with upstream turbine power. Outside of this point the results are determined to be statistically significant.

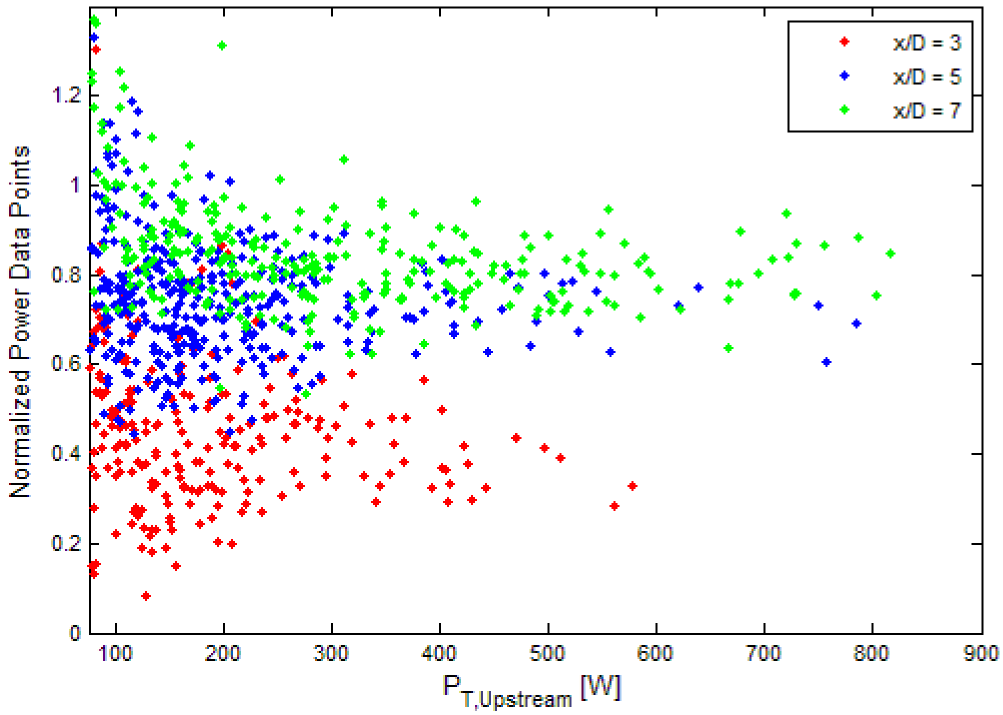

Figure 5.2: Single Wake Power Losses with Turbine Spacing Data Set.

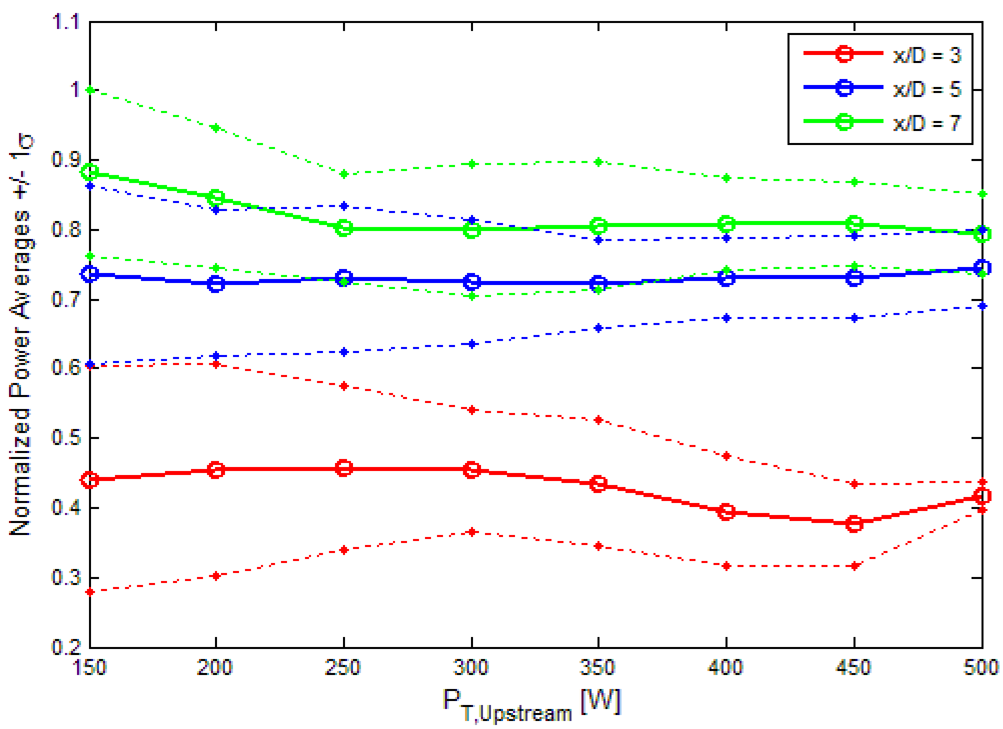

Figure 5.3: Single Wake Average Power Losses with Turbine Spacing.

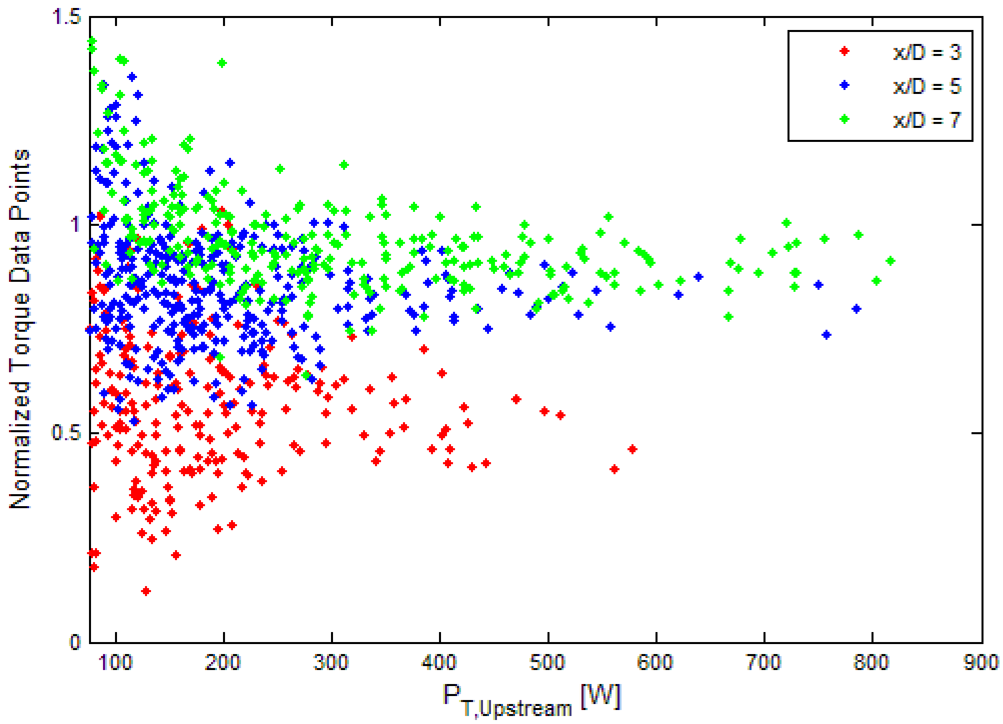

Figure 5.4: Single Wake Torque Losses with Turbine Spacing Data Set.

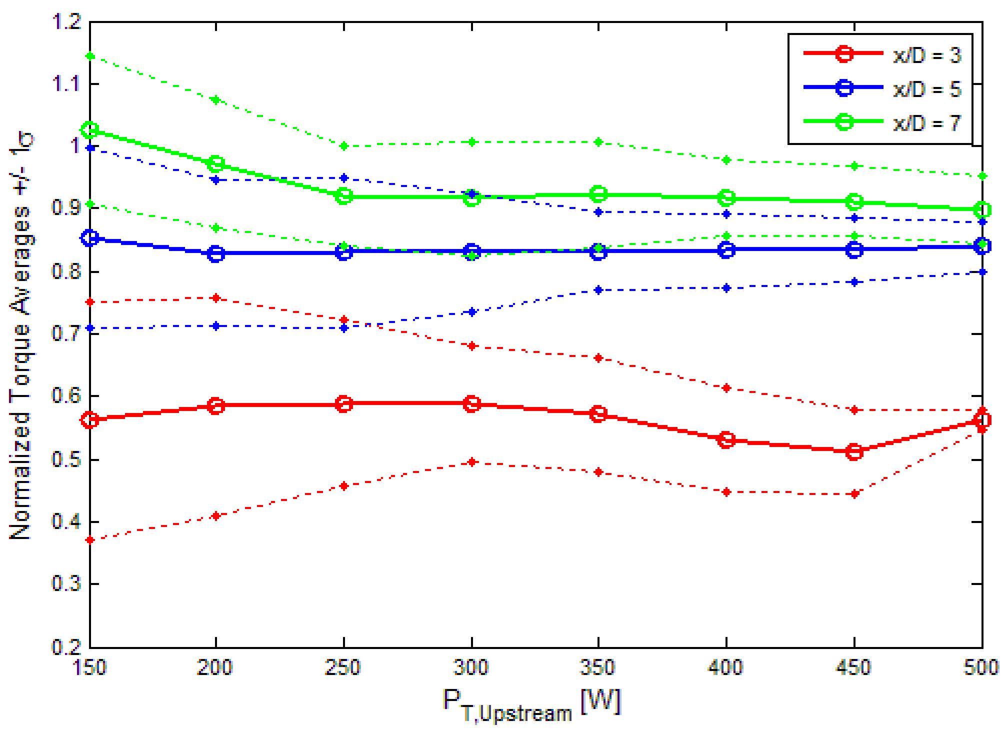

Figure 5.5: Single Wake Average Torque Losses with Turbine Spacing.

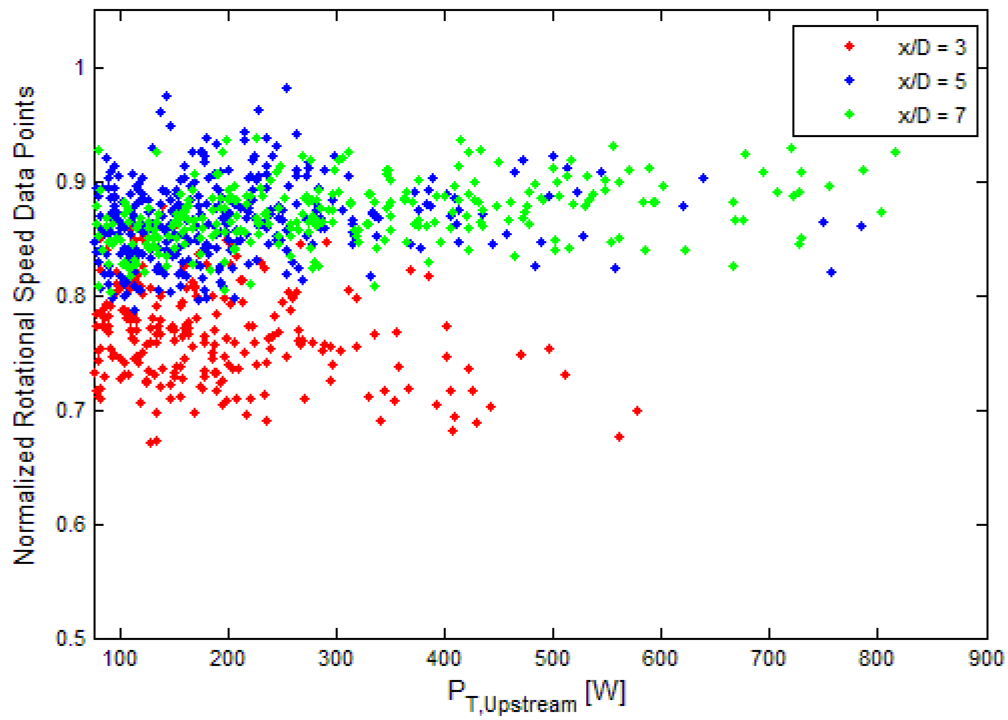

Figure 5.6: Single Wake Rotational Speed Losses with Turbine Spacing Data Set.

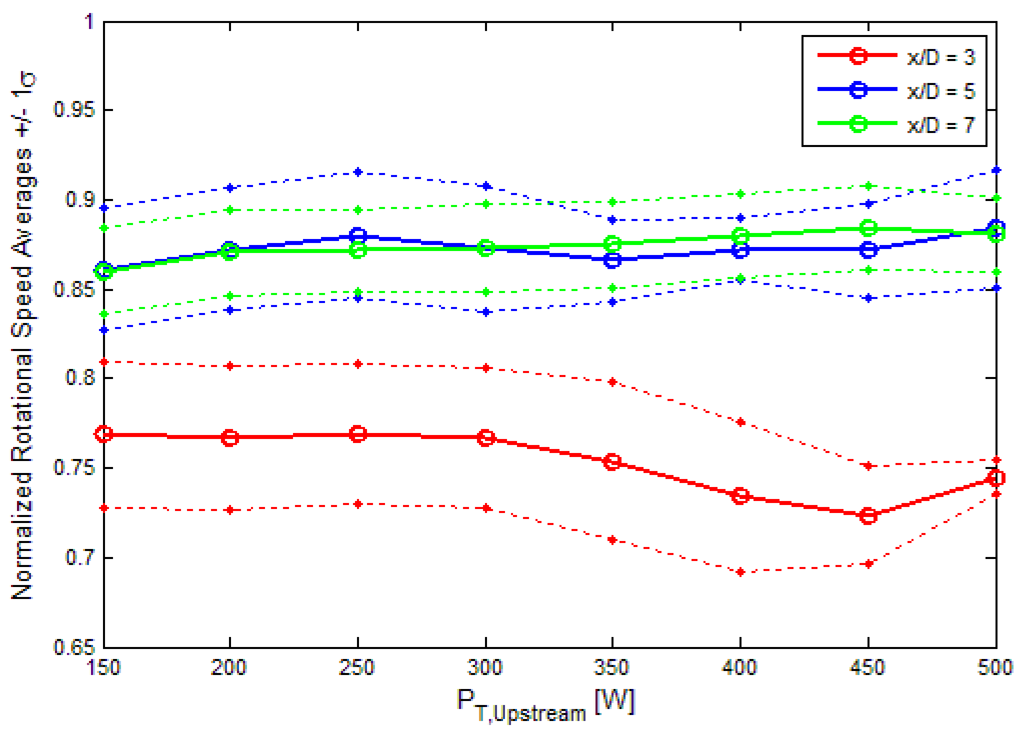

Figure 5.7: Single Wake Average Rotational Speed Losses with Turbine Spacing.

Trends are apparent from the results, namely through comparison of the data set averages. Comparing overall power losses in Figure 5.3 for the three different turbine-turbine spacing's reveals a trend that at larger spacing's the downstream turbine operates at a higher percentage of the upstream turbine's extracted power. This relationship is clearly non-linear where the reduction in normalized power in 2-diameter increments from spacing's of 7 to 5 and 5 to 3 are on the order of 0.07 and 0.3. The 3-diameter spacing location is likely operating in a region of the upstream turbine wake called the near-wake region. This region extends up to around 2 to 5-rotor diameters downstream and is characterized by large structure turbulence with swirling flow containing a helical swept trajectory of the tip vortices, which are highly rotational. Within this region, downstream turbine losses are not due simply to a reduction in momentum from the freestream by the upstream turbine, but also due to the 3-dimensional rotational and turbulent flow conditions which both work to reduce power capture by the downstream turbine. Beyond the near wake region the wake begins to propagate in a self-similar manner with only small scale turbulence. The data statistics point to a valid result for the spacing trend where the ± 1 standard deviation curve from the one spacing's average typically falls outside of the other spacing's average. Considering the varying atmospheric conditions which could produce widely different results for the same wake scenario, this standard deviation is seen as a highly acceptable result that validates the significance of the data.

The normalized power also displays a trend in response to increasing power range bins. As the upstream wind turbine extracts more power (at higher wind speeds) the normalized power of the downstream wind turbine decreases. This trend is noticed with the 7- and 3-diameter spacing cases, but not with the 5-diameter case which is mostly constant. The decrease with upstream power capture for the 7-diameter case only persists up to 200 W. This can be explained in several ways. The upstream turbine produces increased power in response to increased wind speed. The power in the wind has a cubic relationship to its velocity, whereas the turbine extracts power as a square of the velocity. This means that as wind speed increases, more power is in the atmosphere than is extracted at a divergent rate. The addition of momentum in the freestream potentially compensates for the additional momentum extraction by the upstream turbine. The thrust coefficient also can be used to possibly explain the near constant normalized power for power ranges greater than 200 W for 7- and 5-diameter spacing's. One-dimensional theory used in deriving the single wake model in Section 3.3.1 reveals that the wake performance loss depends on the spacing, wake expansion properties which vary with atmospheric conditions, and on the thrust coefficient of the upstream turbine. At a constant spacing in the same, or near the same, atmospheric conditions, the only variable that can alter the downstream wind turbine performance is the thrust coefficient of the upstream turbine. It is possible that the upstream turbine begins operating in a region of near constant thrust coefficient after about 200-W. At 200-W power output the wind turbine is operating at an average of over 600 rpm, so it is likely that the thrust coefficient beyond this point has only negligible changes. The wind turbine is operating within the "turbulent windmill state" beyond its maximum efficiency point as defined in Figure 5.8 with support given Figure 5.9 which reveals that the test wind turbine reaches its maximum power coefficient at a very low wind speed, from where the thrust coefficient potentially nears a constant value.

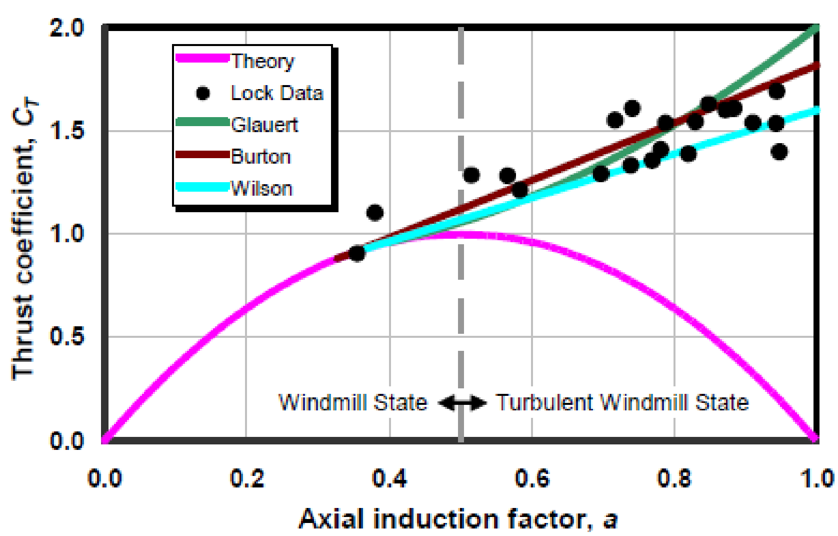

Figure 5.8: Thrust Coefficient Operating Regions with Empirical Fits [38].

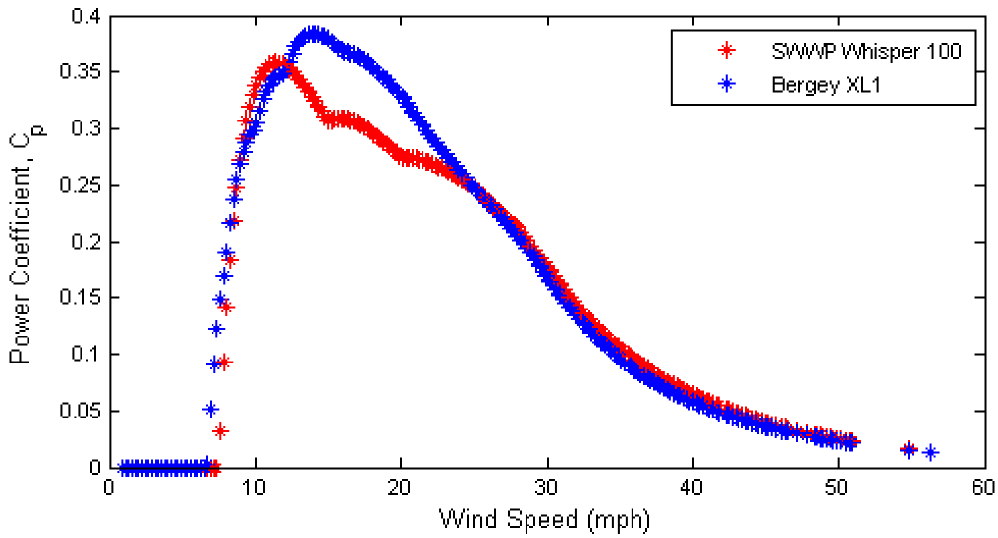

Figure 5.9: Whisper 100 Power Coefficient versus Wind Speed.

The smaller upstream power region produces more suspect measurements due to increased percentages of experimental uncertainty. It is possible that the first data point in the averages [100, 200] W has a variation due to these effects. The data will be presented later in a Table, but the time content in the data range for 3, 5, and 7-diameter spacing's is 22.7, 35.1, and 17.4 minutes. The 5-diameter spacing which has a constant normalized power does have more content, but it is determined that the 3- and 7-diameter spacing data sets contain a large enough sample to validate their results. Experimental uncertainty is not thought to be an explanation to this trend.

The normalized torque data, Figures 5.4 and 5.5, display trends similar to the normalized power trends discussed, and follow the same discussion. Differences are that the normalized torque occurs at a value on the order of 0.1 greater than the normalized power values. This means that the torque comparisons between the upstream and downstream turbines are more similar in magnitude than the power comparisons. The average normalized torque values are also mostly constant beyond 200 W upstream turbine power, with averages for the (3, 5, 7) diameter spacing's of around (0.6, 0.8, 0.9). The normalized torque again follows a non-linear trend with turbine spacing as it approaches the upstream turbine near-wake region.

To a high level of agreement for these data, the normalized power is approximated as the product of the normalized torque and normalized rotational speed. While the torque trend closely followed that of the power, the rotational speed trend with upstream turbine power for the three spacing's tested is nearly constant. One implication of this is that the overall power trends with upstream turbine power are due to changes in the torque, not the rotational speed. For the 3- and 7-diameter spacing cases which saw a downward trend in the normalized power with upstream turbine power, the variation of normalized power compared with the variation of normalized rotational speed between the different power range averages was on the order of 4 times greater. This indicates that the reduction in rotational speed is much more consistent at varying upstream wind turbine power than the reduction in the power due to the upstream wake.

The normalized rotational speed data points in Figure 5.6 also show very low variability for each of the three spacing cases, with slightly more at the near-wake 3-diameter spacing location. This low level of scatter results in standard deviations 2-3 times smaller than for the torque measurements. The low variability of the rotational speed implies that it is nearly a function of the spacing alone, and less dependent upon atmospheric conditions or wake variations of the upstream turbine. This seemingly makes the rotational speed an ideal indicator of turbine performance in wake operation. The difficulty however is that it appears that there is not a one-to-one relationship between normalized rotational speed and normalized power as the normalized rotational speed for the 5- and 7- diameter spacing cases are nearly identical and average to within 0.001 of each other. This is a significant result which reveals that between 5- and 7-diameter spacing the mechanism which causes a reduction in rotational speed of a wake-operated wind turbine operating ceases to decrease it further and has reached a constant value for the normalized rotational speed around 0.87.

A summary of the averages for the non-repeated power bins for normalized power, torque, and rotational speed for the three tested spacing's is given in Table 5.5. This table also shows standard deviation and time in the power range sample of each calculated value to support the conclusions drawn about the statistical significance of the data. An additional average is given which contains all of the data with an upstream turbine power greater than 200 W, and its standard deviation. Due to the discussed nearly constant wake performance with upstream turbine power beyond 200 W, this average is considered as the most representative single value for describing wake operation. Observation of the low standard deviations combined with the large time samples within this averaging range prove the results within the average, and also the similar magnitude normalized value results in the bins which combine into this average. The comparison between the three spacing's reveals that the standard deviation of this average gets smaller as more data time is included, another validation of the facility's instrumentation and measurements.

Table 5.5: Single Wake Normalized Performance Data Statistical Summary.

3-Diameter Turbine Spacing Single Wake Summary

Power Bin [W]:	[100,200]	[200,300]	[300,400]	[400,500]	[200,∞)
Power Avg	0.440	0.457	0.435	0.376	0.437
Power Sdev	0.162	0.117	0.091	0.058	0.109
Torque Avg	0.562	0.589	0.571	0.512	0.571
Torque Sdev	0.190	0.132	0.091	0.066	0.119
Omega Avg	0.769	0.769	0.754	0.723	0.757
Omega Sdev	0.041	0.039	0.044	0.027	0.043
Data Time	22.7	10.1	3.2	2.3	16.1

5-Diameter Turbine Spacing Single Wake Summary

Power Bin [W]:	[100,200]	[200,300]	[300,400]	[400,500]	[200,∞)
Power Avg	0.735	0.729	0.722	0.731	0.728
Power Sdev	0.129	0.106	0.064	0.059	0.092
Torque Avg	0.854	0.830	0.832	0.834	0.830
Torque Sdev	0.144	0.119	0.062	0.051	0.101
Omega Avg	0.861	0.880	0.866	0.872	0.876
Omega Sdev	0.034	0.035	0.023	0.026	0.033
Data Time	35.1	15.8	4.0	3.1	25.0

Table 5.5: Continued.
7-Diameter Turbine Spacing Single Wake Summary

Power Bin [W]:	[100,200]	[200,300]	[300,400]	[400,500]	[200,∞)
Power Avg	0.882	0.803	0.806	0.807	0.803
Power Sdev	0.119	0.078	0.091	0.060	0.076
Torque Avg	1.026	0.920	0.922	0.911	0.914
Torque Sdev	0.119	0.079	0.085	0.056	0.072
Omega Avg	0.860	0.872	0.875	0.884	0.877
Omega Sdev	0.024	0.023	0.024	0.023	0.025
Data Time	17.4	13.5	8.1	6.6	36.7

The power loss of a wind turbine operated within a wake of an upstream turbine is a result of the loss in torque and/or loss in rotational speed. Using the performance averages for the [200,∞) W power range along with the results of Equations 3.94 and 3.95, the power loss due to torque loss and to rotational speed loss can be estimated and compared to give insight into the physics of the wake and performance loss mechanisms as a function of the turbine spacing:

$$P_{loss,torque} \approx \frac{1-\tau_{norm}}{1-P_{norm}} \tag{5.1}$$

$$P_{loss,rotation} \approx \frac{1-\Omega_{norm}}{1-P_{norm}}\,. \tag{5.2}$$

The results from this analysis are given in Table 5.6. The equation used to solve for the loss components is only an approximation where the contributions ideally add up to 1. The contribution sum is seen to stray from this ideal, particularly for the 3-diameter case. With this caveat, the loss components can be thought of as percent contributions to the total power loss. The results do show a trend with spacing, where the contribution of the torque loss to the total power loss decreases with spacing (meaning the torque recovers to its non-wake value). Rotational speed losses are seen to likewise increase, but at a lower rate than with torque losses, and reach a constant value as discussed between 5- and 7-rotor diameters. The overall trend produce, seen in the loss ratio ($L_{torque}/L_{rotation}$), is that as the turbine moves further downstream from the wake generating turbine that the power loss originally dominated by a torque loss begins to be dominated by a rotational speed loss.

Table 5.6: Single Wake Power Loss Components.

x/D_T	P_{norm}	τ_{norm}	Ω_{norm}	$P_{loss,torque}$	$P_{loss,rotation}$	$L_{torque}/L_{rotation}$
3	0.437	0.571	0.757	0.76	0.43	1.77
5	0.728	0.830	0.876	0.62	0.45	1.38
7	0.803	0.914	0.877	0.43	0.62	0.70

In order to understand this result, consideration is given to flow property changes caused by the wake of a wind turbine and their variations with distance from the turbine. The wake of a wind turbine changes the flow in essentially three ways, treated independently in this qualitative analysis; momentum extraction causing a reduced velocity at the rotor disk and reduced pressure immediately downstream of the rotor, tangential swirl velocity addition to the flow produced from torque generation opposite the direction of the turbine rotation, and turbulence addition to the flow mostly radiating from the blade tip region due to blade loading and tip vortices. These properties and their variation with distance downstream of a wind turbine are what produce the power loss contribution differences at the three tested spacing's. Axial velocity loss due to momentum extraction predicted in the wake is highest in the near-wake region and the loss is recovered downstream with an expanding wake and momentum addition from the atmosphere. The added swirl velocity due to torque generation is again most distinct near the wind turbine and at some point downstream, near the onset of the far-wake region, this swirl velocity returns to zero. Turbulence added to the flow from the solid airfoil boundaries initially occurs in large length scale helical structures with rotation but is resolved into small length scale turbulence in the far wake region with further reduction in turbulence levels with distance downstream, ultimately recovering completely but at a further distance than velocity recovery.

In order to understand the effect of the changing wake flow on torque and rotational speed a two-dimensional blade strip analysis is considered, as diagrammed in Figure 5.10.

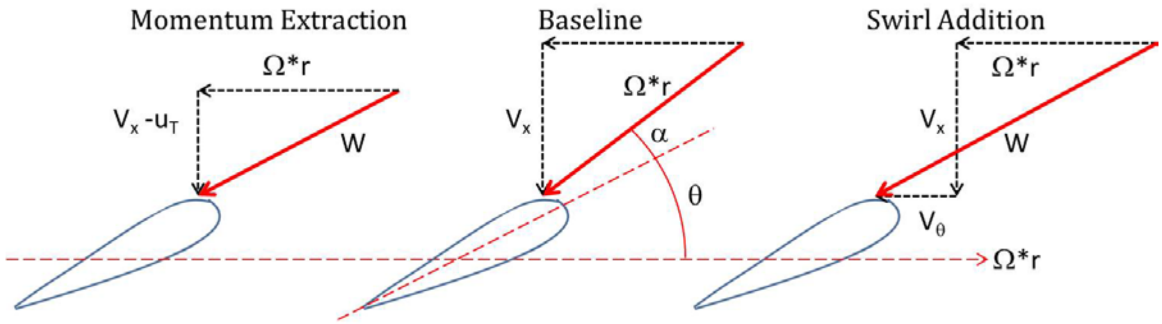

Figure 5.10: Wind Turbine Strip Analysis Diagram.

The differential rotor torque contribution at each radial location is determined, with C_L and C_D representing the lift and drag coefficients:

$$d\tau = {}^{1}/_{2}\,\rho W^2 * \{C_L \cos(90 - (\theta + \alpha)) - C_D \cos(\theta + \alpha)\} * dA\,. \qquad (5.3)$$

For reference, the relationship of torque and rotational speed for a stand-alone wind turbine not operating within a wake is given in Figure 5.11. Points plotted are for sampled data at 4-hz. There is a nearly linear relationship visible between the two power variables with scatter mostly arising from the wind turbine generator dynamics, with an approximated slope of between 0.2-0.23 lb-in/rpm. In order for the relative influence of torque versus rotational speed on the combined power loss to fluctuate in a manner that can match the data, this curve would need to change when considering the downstream wind turbine, and is not meant to be a quantitative reference.

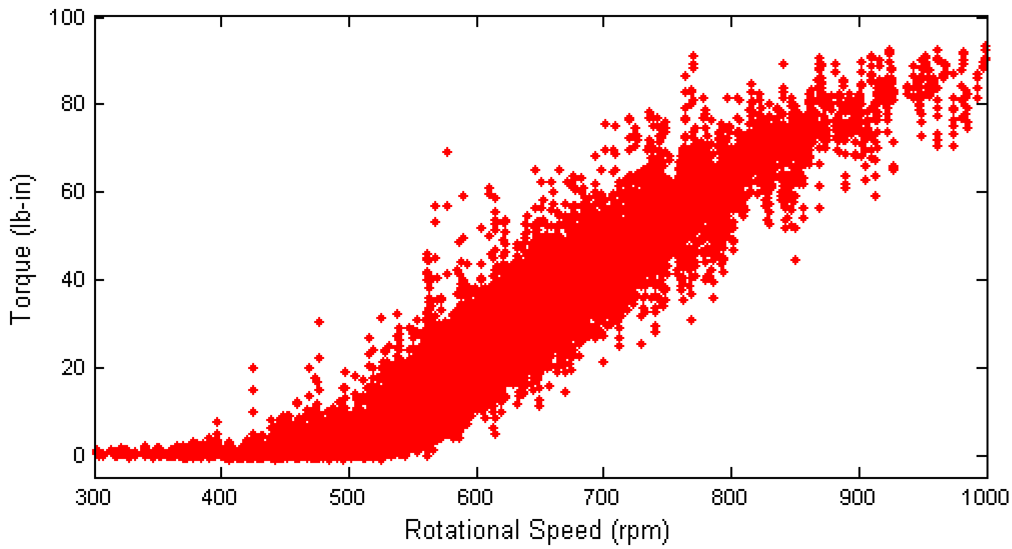

Figure 5.11: Wind Turbine Torque vs. Rotational Speed Data Set.

The axial velocity loss due to momentum extraction (assuming a starting rotational speed as without the loss) would act to reduce the angle of attack of the airfoil and reduce the relative velocity flow over the airfoil. The change in the angle of attack has two main effects which both degrade performance. Given a blade set angle selection which is optimized for the design angle of attack the blade performance will move to a less optimum range, and additionally the reduced angle of attack also shifts the direction of the lift force so it has a smaller component in the rotation/torque plane. Reduction in the relative speed over the airfoil would act to reduce the magnitude of the lift force. This wake phenomenon causes less torque to be generated by the blades, which would in turn require a reduction in the rotational speed so that the generator load matches the rotor aerodynamic forcing input.

Swirl velocity addition (initially assuming a rotational speed as the case without swirl) will also cause a reduction in the angle of attack but with an accompanied increase in the relative airfoil flow speed. Assuming an equivalent angle of attack change between the momentum extraction and swirl addition components, the difference in performance will be described completely by the difference in the relative velocity between the two cases. Higher lift forces produced by the increased relative velocity from the swirl flow would mean higher performance for the swirl case relative to the momentum extraction case. It is unclear as to whether the two phenomena will produce similar angle of attack reductions required to qualitatively compare their relative contributions. The increase in relative velocity caused by the swirl addition also makes approximation of its effect on the flow difficult, it is considered however to produce a reduction in torque and therefore rotational speed of a small value, lesser than with momentum extraction.

Turbulence superimposed on flow over an airfoil can increase or decrease its performance. When operated near stall conditions, turbulence will extend the range before flow separation is incurred preventing substantially reduced performance. If not operating near stall conditions, turbulence will only act to degrade performance. Stall conditions occur at high angles of attack and for high relative velocities seen by the airfoil. While stall may be present over the outer portion of the wind turbine blades during its operation, the majority of power production likely arises from the inner- to mid-span portions of the blades. Turbulence will be considered overall as a contributor to power losses in the present analysis. These losses are thought to be especially prevalent in the region downstream where the turbulence has reduced to smaller length-scale which is more isotropic in nature. As mentioned, the turbulence losses will persist longer than momentum extraction losses and also will decrease with downstream spacing once fully developed.

Single wake performance loss results for the three spacing's tested are summarized graphically in Figure 5.12. In this figure a dividing line is plotted which distinguished the torque dominated loss region from the rotational speed dominated loss region, describing the relative contribution of torque and rotational speed to the overall power loss.

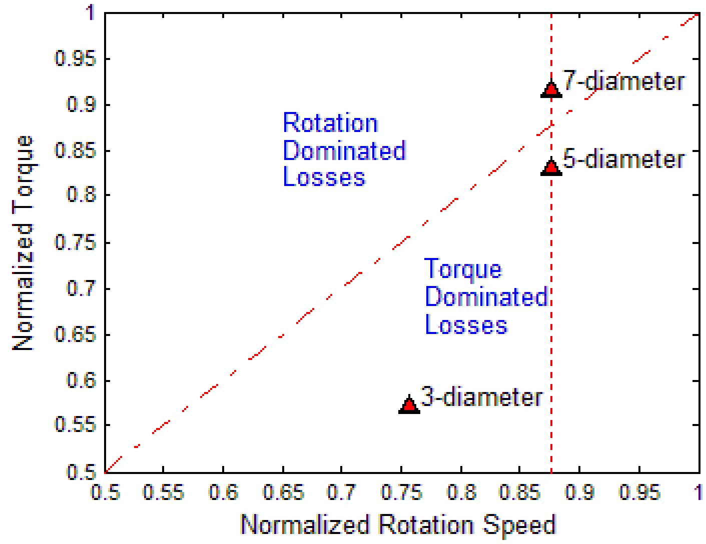

Figure 5.12: Single Wake Normalized Power Component Losses.

An interesting result for this analysis occurs between the 5- and 7-diameter spacing cases where the rotational speed seems to hit a constant for the loss, but that the torque loss is decreased for the larger spacing. This result clearly requires an explanation beyond the wind turbine torque-rpm curve can provide. The linear torque-rpm curve approximates that an input torque reduction would likewise produce a rotational speed reduction. This trend breaks down when comparing the 5- and 7-diameter spacing's, where the increased torque loss from 7- to 5-diameter is not accompanied with a rotational speed loss. If rotational speed loss is thought to be due to momentum extraction and swirl addition alone then this result would suggest that there is no further axial velocity reduction or swirl component present beyond 5-diameters downstream. In this scenario, turbulence would then be the only varying component meaning that turbulence causes a reduction in torque with spacing, but not so or less so with rotational speed. The reasoning that turbulence would decrease the torque but not rotational speed is unclear.

The results from Figure 5 show that a 3-diameter spacing wind turbine is clearly operating in a high loss region. This case has a power reduction both due to torque losses and rotational speed losses. These losses are considered to be sourced by each of the three mechanisms. Rotational speed losses are thought to be dominated by both axial velocity reduction and swirl velocity addition from the upstream wind turbine which both have high magnitudes at this close spacing. This location produces torque dominated losses considered in part from the reduced performance due to axial speed reduction and in part from turbulence reduced torque – if the possible result from the 5- and 7-diameter spacing comparison holds.

The wind turbine single wake operation power loss results versus turbine spacing are summarized in Figure 5.13. This plot includes two power ranges in order to reveal the role of upstream power extraction on the downstream turbine power loss, where up to a 5% additional loss is observed at the higher upstream power condition. This result can, in part, be described by the reduced thrust coefficient in the lower power range. The averages are plotted with ± 1 standard deviation of the averages.

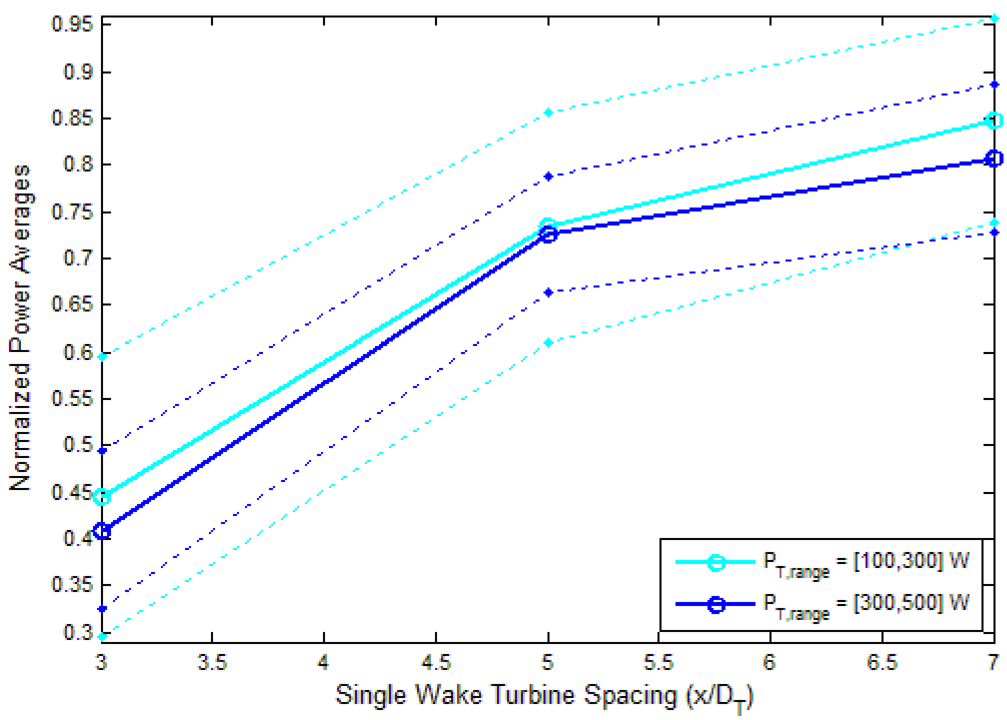

Figure 5.13: Single Wake Average Power Losses vs. Turbine Spacing.

The exact values from the single wake power losses with spacing are listed, with the total time of data within the average, in Table 5.7. The time included in the [100, 300] W power range is naturally more substantial, however the [300, 500] W curve follows the expected trend where a higher momentum capture from the upstream turbine will result in greater power losses in the downstream turbine so the data time is viewed as sufficient.

Table 5.7: Single Wake Spacing Normalized Power Comparison.

Data Range:	P_{range} = [100, 300] W		P_{range} = [300, 500] W	
Spacing (x/D_T)	Data Time (min)	$P_{norm,wt}$	Data Time (min)	$P_{norm,wt}$
3	32.8	0.446	5.5	0.410
5	51	0.733	7.2	0.726
7	30.9	0.848	14.7	0.806

Comparison of the overall single wake results for the three spacing's to the models described in Section 3.3.1 will now be made. The model formulation from the revised analysis in addition to the standard Jensen model will both be used to compare to the data, and compare the model's results. The models will be solved and fit to the experimental results over a range of thrust coefficient. The model formulation from Equations 3.69 and 3.74 are solved for k and rewritten, again using n=2 to describe the test wind turbine:

$$k = \frac{1}{2s}\left[\sqrt{\frac{\beta\left(1-\sqrt{1-C_T}\right)}{1-\left({}^{P_x}/_{P_1}\right)^{1/n}}} - 1\right] \tag{5.4}$$

$$\beta = \begin{Bmatrix} 1/2 & Revised \\ 1 & Jensen \end{Bmatrix}. \tag{5.5}$$

Results for the revised formulation model for the wake decay constant fit to the data point as a function of the required input thrust coefficient are shown in Figure 5.14. The associated wake decay constants for the six data points, 3 spacing's and 2 power bins each, were each solved for with the small power bin, [100, 300] W, plotted using the dashed lines and the large power bin, [300, 500] W, displayed using the solid lines. The power bins are associated with the thrust coefficient where the lower power bin would be expected to have a lower thrust coefficient.

Additionally, it would be expected for the same power bin at different spacing's to have the same thrust coefficient since this is dependent upon only the upstream wind turbine and not on the spacing. This assumption is especially true in comparing the 5- and 7- diameter spacing's. Given validity of the constant linear wake expansion assumption, this would require intersection of the two spacing's curves at (C_T, k). To an approximation, the wake decay constant can be thought of as a strong function of the atmosphere, and a weak function of the upstream turbine power range or spacing. With this approximation, the thrust coefficient can be compared for the two power bins, by maintaining a constant k, when one thrust coefficient is determined.

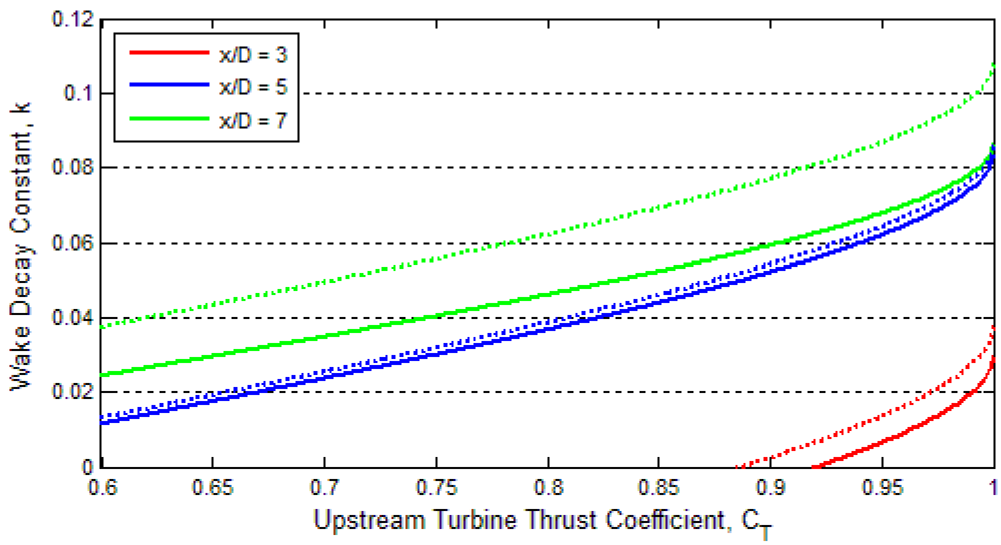

Figure 5.14: Single Wake Model Fit to Data, Revised Formulation.

This model's results do not match the expectations for the single wake analysis. In order for the thrust coefficients to have the same value, with an assumed constant k from the atmosphere produced at that particular C_T, the curves for 5- and 7- diameter spacing's would need to intersect. For the large power bin, the curves for k come within 0.01 of each other for thrust coefficients greater than C_T = 0.76. The constant wake decay assumption bin for the two spacing's within the same power bin may be inaccurate to within 0.01 since the testing was partially done on different days and with different weigthing. The model is not invalidated by this comparison. With a known thrust coefficient, the wake decay constant can be determined. For values of C_T = [0.8, 0.9] resultant wake decay constants are approximately between k = [0.04, 0.06].

Comparison of the curves for the three spacing's reveals a stark disagreement between this model and what's physically possible from the 3-diameter spacing. This spacing requires a wake contraction (negative k) for thrust coefficients less than 0.92 for the high power bin – the actual C_T is likely beneath this value. The one-dimensional formulation of the model makes assumptions on the flow that are not physical, and these assumptions are especially violated within the near-wake region of the flow where large structure turbulence and swirling velocities make significant contributions to the overall flow conditions. The model formulation does not capture the physics of the near-wake region and therefore it is not appropriate to use this model near that region.

The Jensen model results for the wake decay constant fit to the experimental data are derived in the same way, presented in Figure 5.15.

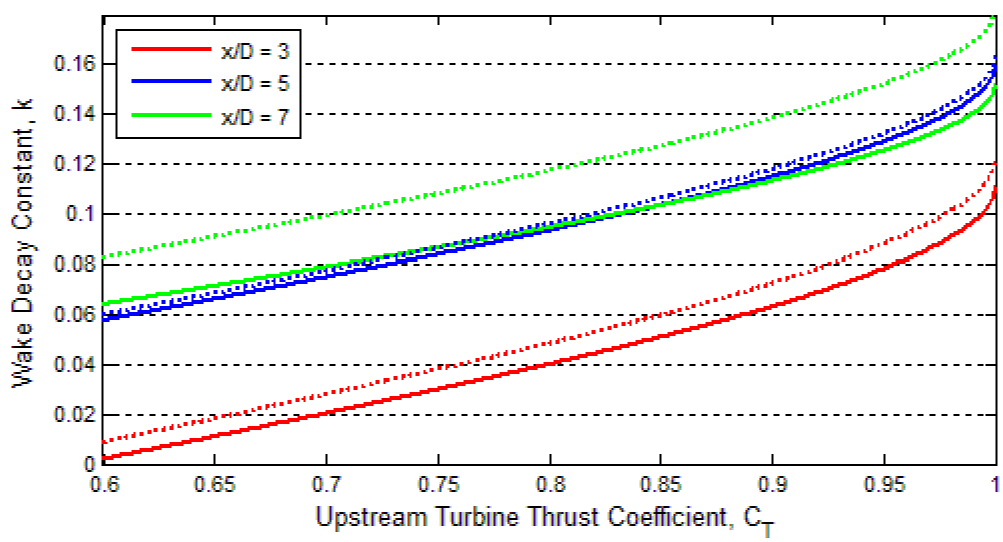

Figure 5.15: Single Wake Model Fit to Data, Jensen Formulation.

The Jensen model curves for the 5- and 7-diameter spacing's do intersect as expected for the high power bin. The intersection, and therefore the results for the large power bin, occurs at C_T = 0.848 with k = 0.103. This result is significant because a wake decay constant of k = 0.1 is a commonly accepted value using the Jensen model, further verifying the experimental results. The Jensen model does a better job at approximating the 3-diameter turbine spacing case than the revised formulation, however the model still does not describe the near wake region physics appropriately. The 3-diameter spacing result requires a wake decay constant of k = 0.05 at the intersection C_T = 0.85, which is the actual thrust coefficient for the upstream wind turbine within the [300, 500] W power bin, according to this model. In order to describe all of the spacing's appropriately the model would have to be formulated with a non-linear wake expansion, expanding slowly at first (low k) and then more rapidly expanding with axial location, eventually reaching a linear expansion region with constant k.

For both models, the small power bin cannot be accurately compared due to the reduction in power for 7-diameter but not for the 5-diameter spacing. If the 7-diameter spacing small power bin is treated as correct, the thrust coefficient change can be compared as predicted by the two models. This change is calculated using the known thrust coefficient from the Jensen model at the high power range (C_T=0.85) along with the assumption of nearly constant k for the same spacing case between the two power bins described earlier. With these assumptions, the revised formulation predicts a C_T=0.85 reducing to C_T=0.72 for the [100, 300] W power range, with a wake decay constant k=0.044. The Jensen model predicts the [300, 500] W power range C_T=0.85 will reduce to the exact same value of C_T=0.72 for the [100, 300] W power range, at the wake decay constant k=0.1. Due to the model formulation, at a constant k (that can vary for the two respective models) the two model equations will produce the same resultant C_T value if the starting value is the same. Accordingly, for both models this reduction in the thrust coefficient is reasonable at the lower power range.

The revised model was created as a more theoretically correct derivation of the linear wake model, but the more fundamentally correct model is the ultimate goal for the single wake model. The Jensen model more nearly captured the near-wake region as opposed to the wake contraction predicted by the revised formulation in this region, where using the resulting k=0.1 value predicts a normalized power of 0.58 for the 3-diameter spacing result compared to the actual result of 0.41. This deviation is minor compared to the model violation within this region and is considered to be in good agreement for that reason. The Jensen model was in complete agreement with the normalized power results for 5- and 7-diameter spacing's which was where the two curves intersected and the values for C_T=0.85 and k_{Jensen}=0.103 were derived. The revised model formulation, using the C_T solution from the Jensen model and solving for $k_{revised}$=0.044 predicts normalized power value for spacing's (3, 5, 7) of (0.65, 0.73, 0.78) compared to the experimental results of (0.41, 0.73, 0.81). The results of the two models and their predictions beyond the spacing's tested are shown and compared in Figure 5.16.

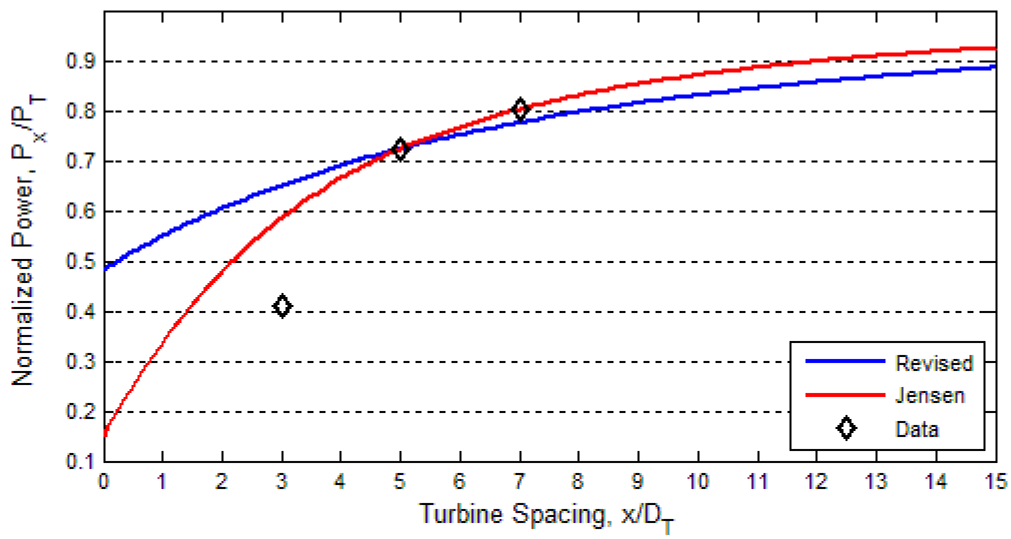

Figure 5.16: Single Wake Model Comparison with Data.

This figure shows that the formulation of the Jensen model fits best with the data over the range it was collected. The revised formulation predicts a higher normalized power in the near-wake region, and more sustained power loss with lower normalized power values at higher turbine spacing's. The appropriateness of either model formulation could also be compared by considering the resulting wake decay constants from both. For an assumed C_T=0.85, these constants differ from k=0.044 for the revised formulation to k=0.1 for the standard Jensen formulation.

The values predict expansion rates with difference of a factor of two, which is substantial. Comparison to actual wake flow measurements may reveal the more accurate physics of wake expansion rate for one of the models.

5.3 Wind Turbine Multiple Wake Results

Wake performance data was collected for a double wake test case on one windy day. The data set contains a double wake (three turbine) 7-rotor diameter spacing multiple wake test. The test case facility configuration for the 7-rotor diameter, double wake turbine spacing is shown in Figure 5.17.

Figure 5.17: Facility Configuration with a Double Wake, 7-Rotor Diameter Spacing.

A comparison of the data processing parameters for the double wake was performed as with the single wake analysis comparing the effects of T_{bin}, T_{sort}, and P_{range}. This comparison produced the same conclusion with the same justification as for the single wake scenario. The T_{bin} with 30-sec didn't contain enough points to be accurate and the plots were erratic when plotted in the divided power bins for this reason. The 20-sec bin requirement plots look very similar to the 10-sec requirement, only with less data. The concern for this analysis was that the double wake scenario doubles the mandatory time shift increasing the magnitude of its errors in a smaller time bin. The agreement between the 20-sec and 10-sec curves disproved the concern for increased loss in the double wake with T_{bin} = 10-sec. For these reasons, the double wake analysis also uses T_{bin} = 10-sec and T_{sort} = 10-sec to filter the data set, over various P_{range} values.

Table 5.8 details the justification for selection of T_{bin} = 10-sec, where the results were similar to the 20-sec case only with more total data. The 8.0 minutes of data collected on one day is not as statistically significant as would be hoped for, however it was seen in the single wake case where reduced 100 W sample data bins with small time content (< 5 minutes) would repeatedly produce consistent results with the larger set (> 15-25 minutes). These data for that reason are justified as correct in regards to their trend.

A significant difference between the processing of the single wake scenario and the double wake scenario is seen in the variation of its average with respect to the power range, shown in Table 5.8. For P_{range} = [75 W, ∞) results seemingly point to a constant value for the normalized power from wake number 1 to wake number 2, comparing with results from Table 5.9. When processed for P_{range} = [200 W, ∞) the results change and the normalized power for the double wake scenario (wake number 2) changes from 0.861 to 0.738 for the data processing scheme of interest. This results in a difference in single to double wake normalized power of approximately 0.07, compared with no change for the larger power range.

Table 5.8: Double Wake Normalized Power Comparison (7-diameter Spacing).

Data Processing Scheme		P_{range} = [75 W, ∞)		P_{range} = [200 W, ∞)	
Bin Time	Sort Time	Data Time (min)	$P_{norm,wt}$	Data Time (min)	$P_{norm,wt}$
10 sec	unsorted	33.3	0.861	8.4	0.731
10 sec	10 sec	31.2	0.861	8.0	0.738
10 sec	30 sec	33.3	0.862	7.3	0.736
20 sec	unsorted	22.9	0.839	5.9	0.717
20 sec	20 sec	22.6	0.836	5.2	0.730
30 sec	10 sec	6.9	0.807	1.5	0.659
30 sec	30 sec	7.6	0.817	1.5	0.677

Table 5.9: Single Wake Normalized Power Comparison (7-diameter Spacing).

Data Processing Scheme		P_{range} = [75 W, ∞)		P_{range} = [200 W, ∞)	
Bin Time	Sort Time	Data Time (min)	$P_{norm,wt}$	Data Time (min)	$P_{norm,wt}$
10 sec	10 sec	57.4	0.841	36.7	0.803
10 sec	30 sec	60.9	0.841	36.9	0.803
20 sec	10 sec	39.4	0.826	26.5	0.796
20 sec	20 sec	41.6	0.832	27.1	0.799
30 sec	10 sec	23.1	0.832	16.9	0.793
30 sec	30 sec	25.2	0.834	16.0	0.788

The total filtered data set results are displayed in Figures 5.18-23 for normalized power, torque, and rotational speed. These data are presented in the same manner as for the single wake scenario, only now comparing the 7-diameter spacing data set from the single wake case above with data for the 7-diameter double wake test case.

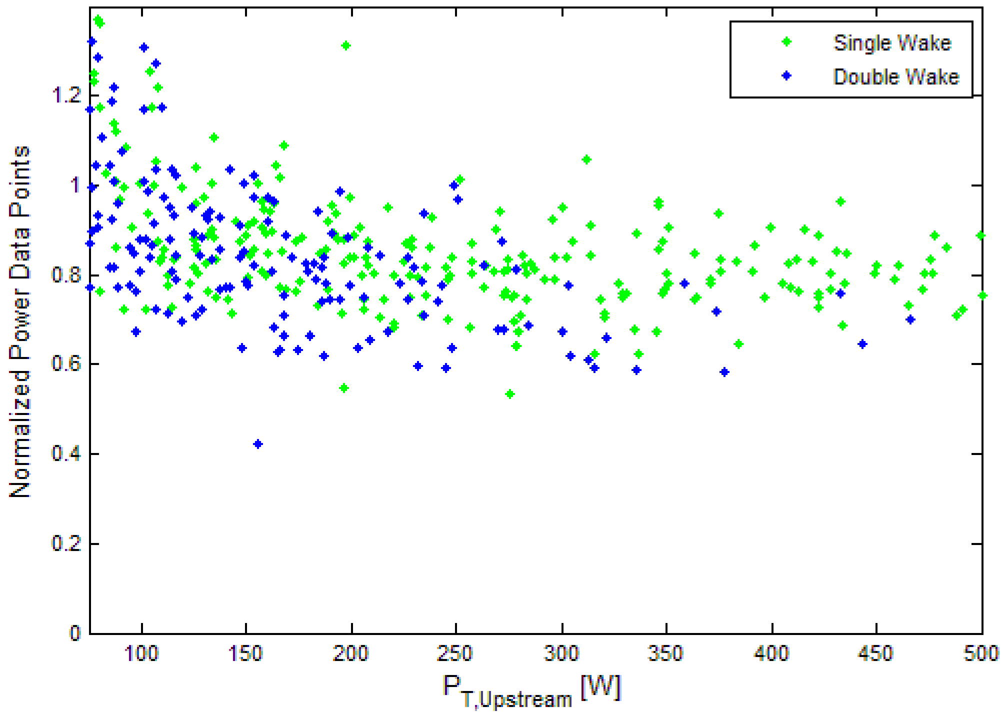

Figure 5.18: Wake Power Losses with Wake Number Data Set.

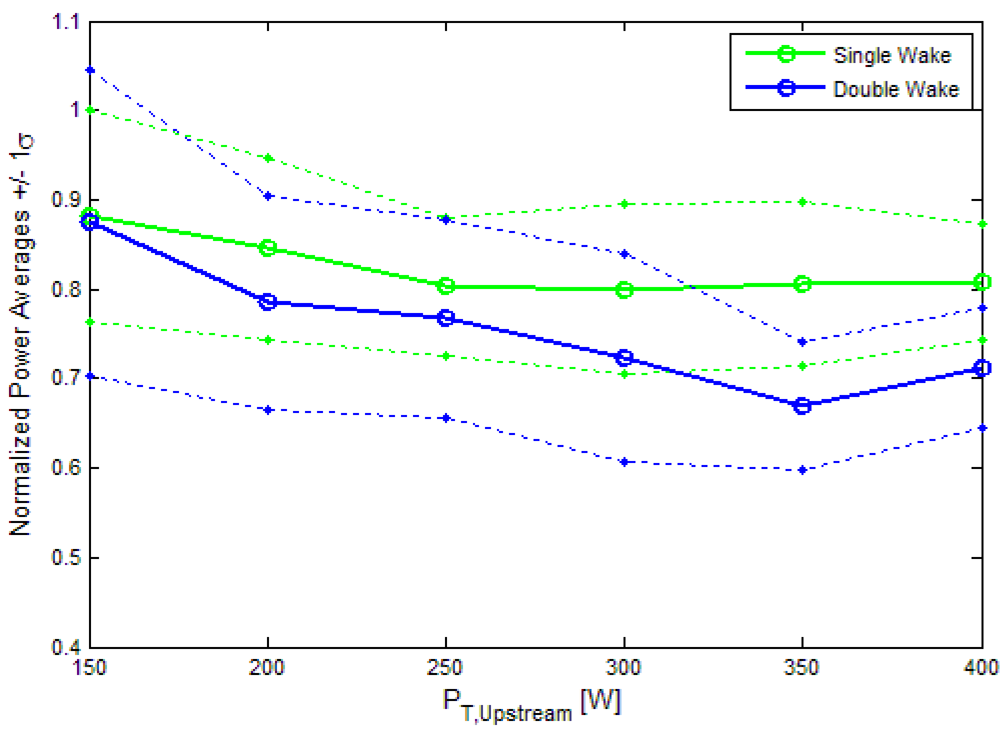

Figure 5.19: Wake Average Power Losses with Wake Number.

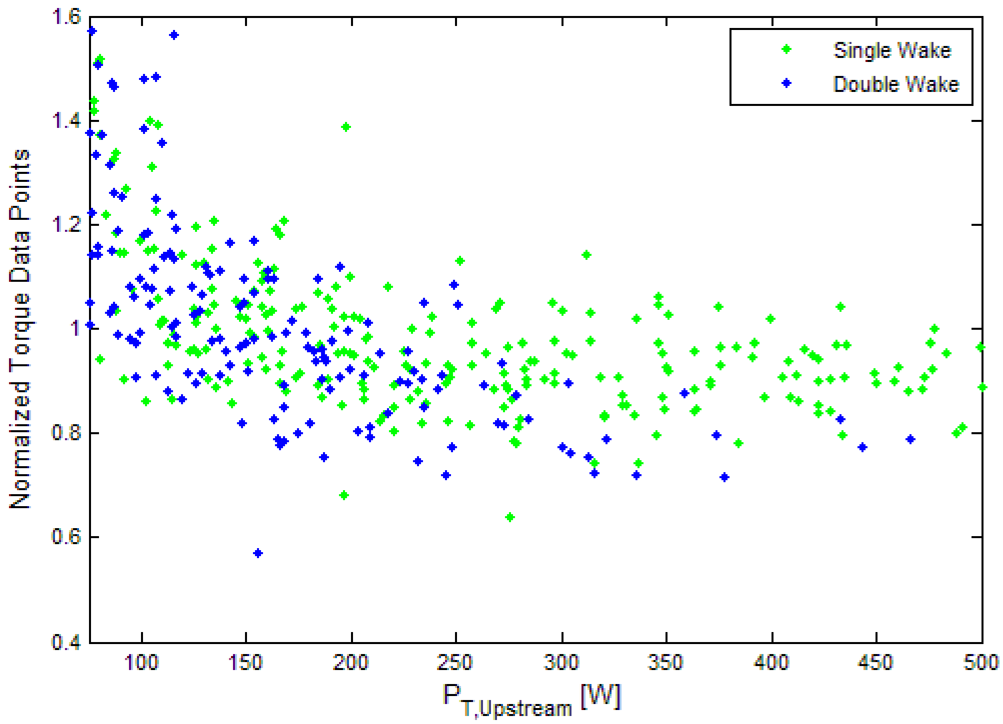

Figure 5.20: Wake Torque Losses with Wake Number Data Set.

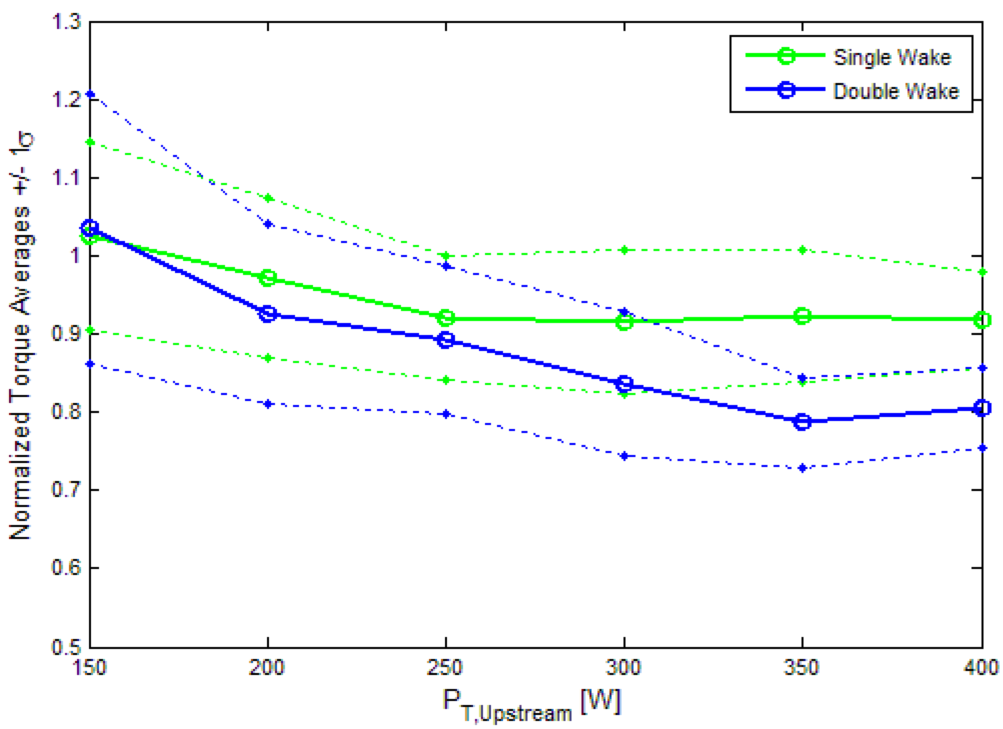

Figure 5.21: Wake Average Torque Losses with Wake Number.

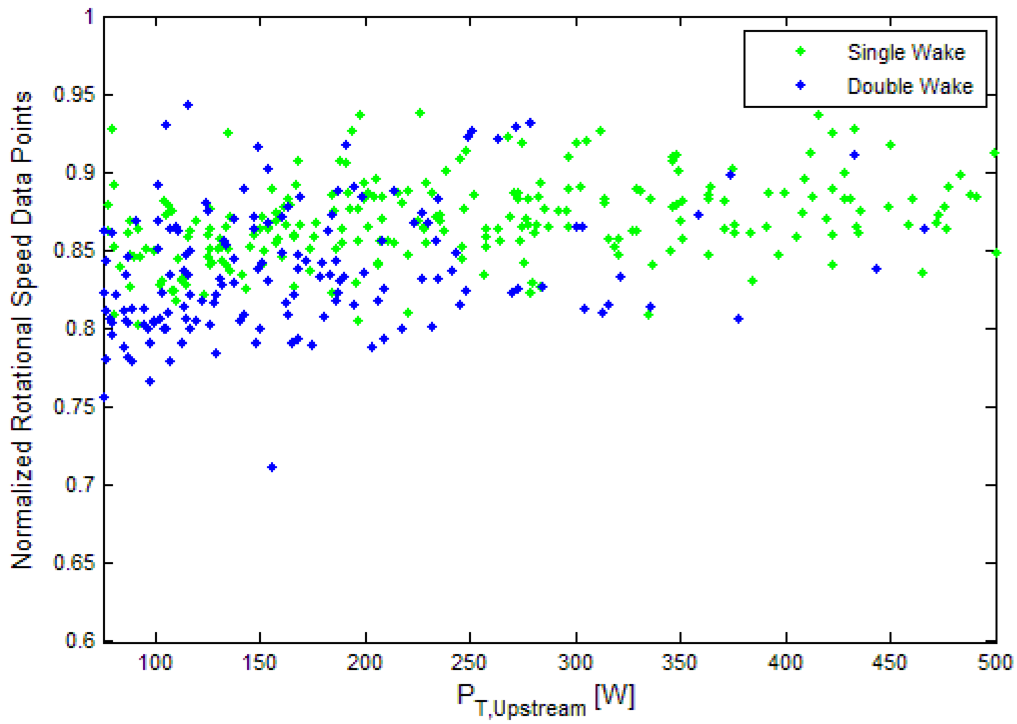

Figure 5.22: Wake Rotational Speed Losses with Wake Number Data Set.

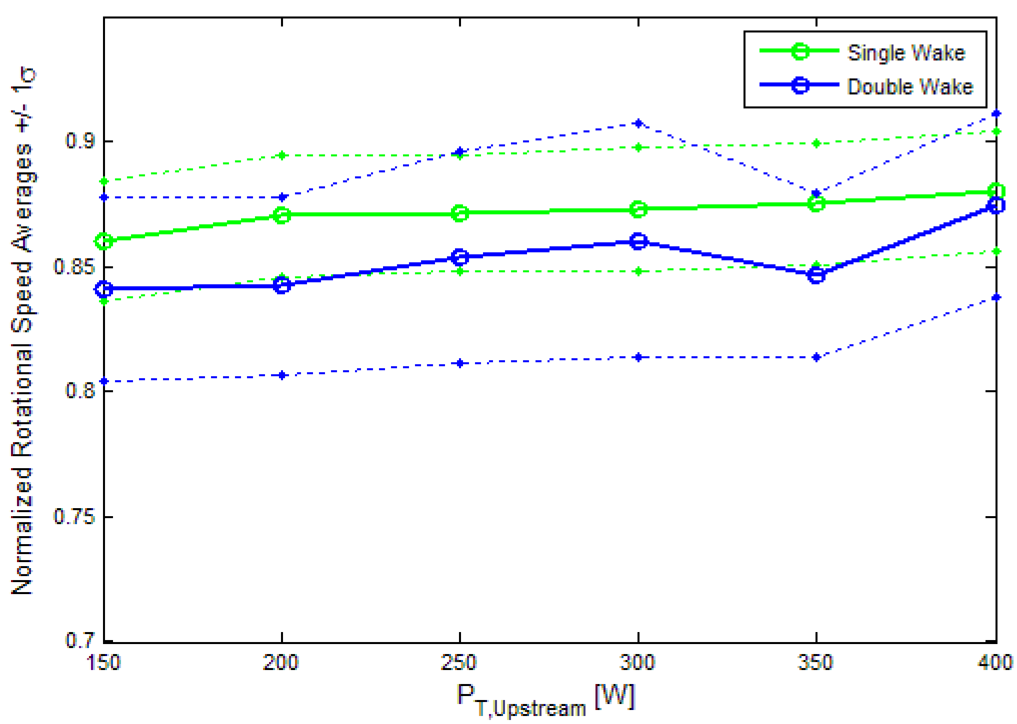

Figure 5.23: Wake Average Rotational Speed Losses with Wake Number.

The comparison plots of the performance for single- and double-wake 7-diameter spacing scenarios reveal some conclusive trends. Comparisons are made using the bin average plots, which are averaged over a 100 W range with the plotted point being the center of that range. Observation of the total data set plot reveals that in the final range [350, 400] W there aren't very many total points which makes the final point plotted in the averages suspect, and may not well describe the actual average for this bin or its statistics.

One clear trend in both the normalized power and normalized torque plots is that as the power range increases, the separation between the curves for a single and double wake increases. This is best explained by the momentum extraction increasing with the power range (as explained with the single wake), only now in the double case there is a multiple effect because of the second wake. The normalized power in the small power range bins for the torque and power are very near that of the single wake results. This agreement verifies the quality of the results for the double wake because at very low power extraction, the first turbine (14-diameters upstream) would only be expected to contribute a small amount to the power loss of the third turbine, meaning the results would be very near those of the single wake. Although the average given in Table 5.8 for the [75 W, ∞) range seemed to point to a negligible reduction for the second wake number from the first, it is seen from this plot that the trend with power range is correct, meaning that the high average was due to a disproportionate weighting towards low upstream wind turbine power averages (where the normalized power for single and double wake scenarios is about 0.88). At the high power range, the single and double wake scenarios seem to reach a limit in the normalized power of approximately 0.8 and 0.72, meaning the additional loss is 0.08 from the second wake.

As with the single wake test cases, the rotational speed for the double wake scenario is also nearly a constant with little scatter, Figure 5.23, with the same justification as before. For the double wake scenario, this value is reduced further, from an average of about 0.88 to 0.86 for the double wake test case. The addition of the second wake upstream causes a small reduction in the rotational speed, which is thought to be due to a further decrease in the freestream wind speeds, with the wind turbine rotating more slowly in this lower wind condition.

Following Equations 5.1 and 5.2 as before, the contribution to the loss from the torque and rotational speed components for comparison of the single and double 7-diamter spacing scenarios is summarized in Table 5.10. The comparison reveals that adding a wake only slightly increases the rotational speed loss, but disproportionately increases the torque loss of the downstream wind turbine. The ratio of torque loss to rotational speed loss is nearly doubled with the addition of the second wake, from 0.68 to 1.29. For a single wake number the power loss was mostly due to rotational speed loss whereas with a wake number of 2 the torque loss dominates the overall power loss. Following the explanation given in the single wake scenario, a shifting towards greater torque losses is explained with the added turbulence, where now the second turbine operates with incoming turbulence in addition to its own production.

Table 5.10: Double Wake Power Loss Components.

Wake #	P_{norm}	τ_{norm}	Ω_{norm}	$P_{loss,torque}$	$P_{loss,rotation}$	$L_{torque}/L_{rotation}$
1	0.803	0.914	0.877	0.43	0.62	0.70
2	0.738	0.859	0.854	0.54	0.56	0.97

An additional summary including the amount of time within the data bin averages and listed values for the normalized wake performance variables is given in Table 5.11. For the double wake scenario, due to the persisting decrease of normalized power and normalized torque as seen in Figures 5.19 and 5.21, the best single value summary is thought to be the [250, 500] W range averages.

Table 5.11: Wake Number Normalized Performance Summary (x/D=7).

Single Wake Summary (7-Diameter Spacing)

Power Bin [W]:	[100,350]	[250,500]	[200,∞)
Power Average	0.842	0.803	0.803
Power Standard Dev.	0.111	0.081	0.076
Torque Average	0.972	0.916	0.914
Torque Standard Dev.	0.116	0.078	0.072
Omega Average	0.867	0.876	0.877
Omega Standard Dev.	0.025	0.024	0.025
Data Set Time [min]	35.5	21.2	36.7

Double Wake Summary (7-Diameter Spacing)

Power Bin [W]:	[100,350]	[250,500]	[200,∞)
Power Average	0.838	0.719	0.738
Power Standard Dev.	0.168	0.102	0.107
Torque Average	0.988	0.825	0.859
Torque Standard Dev.	0.173	0.082	0.095
Omega Average	0.844	0.865	0.854
Omega Standard Dev.	0.038	0.043	0.040
Data Set Time [min]	29.7	3.9	8.0

The multiple wake results are plotted as the averages ± 1 standard deviation for power range bins of [100, 350] and [250, 500], shown in Figure 5.24. The bins were chosen to overlap so that they would include more data. The bins are large when considering the variation of normalized power for the double wake seen for the 100 W bin ranges in Figure 5.19, which explains the large variation on the wake number 2 data. The plot average data, along with its time content, is listed in Table 5.11.

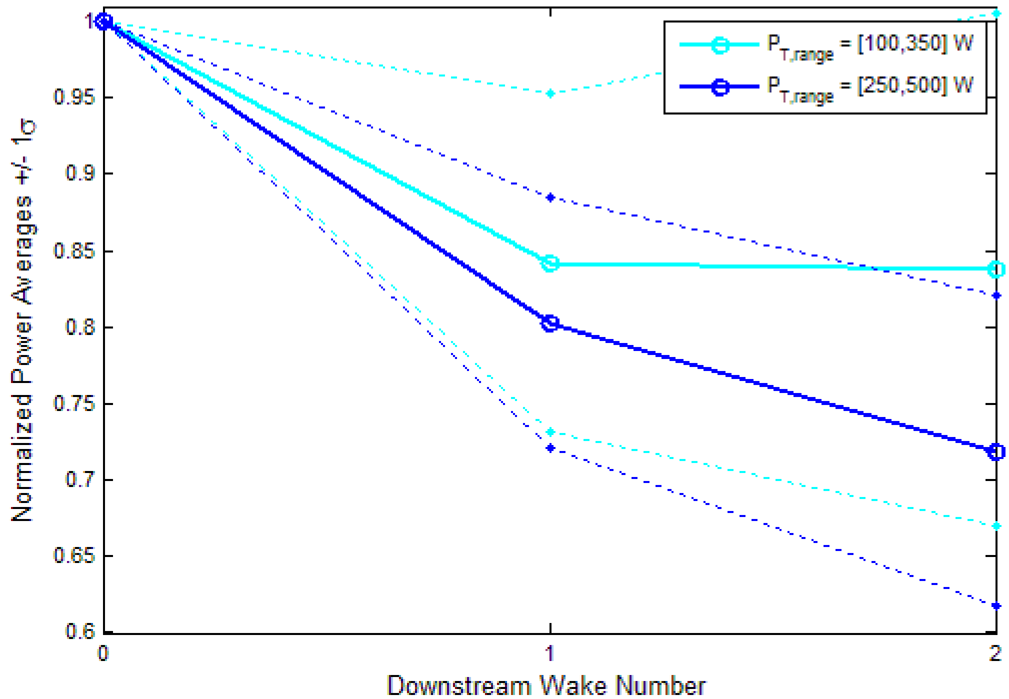

Figure 5.24: Multiple Wake Average Power Losses vs. Wake Number.

This plot reveals what was identified in Table 5.11 earlier, that the wake number has a significant effect for a 7-diameter spacing up to at least a wake number of 2 when comparing the data within a high power bin to avoid over-averaging the repeated low power data into the result. For the high power range [250, 500] W the normalized power decreases 0.084 with the second wake from the single wake test case. For the low power bin [100, 350], there is nearly no effect of adding the second wake upstream.

The results for normalized performance with number of wakes are compared with the multiple wake model described in Section 3.3.2. The first method of comparison is using this sum of squares approach to combine the wake number effects independently while assuming that the values for the wake decay constant and the thrust coefficient are constant for each successive upstream wind turbine. The normalized power results of the turbine at the wake number one position are used to determine the k, C_T values for the overall formulation. The single wake solution for k at a given turbine spacing and with known normalized power is plotted in Figure 5.25 versus the thrust coefficient, which needs to be selected for this model. A value of C_T=0.85 is selected for the high power bin, as found from the single wake results using the Jensen model. The small power bin thrust coefficient is approximated as the thrust coefficient at the same wake decay constant as for $C_{T,high}$=0.85 of the high power range. For this analysis, the high power range produces a wake decay constant of k = 0.05, which then corresponds to a $C_{T,low}$=0.74 for the [100, 350] W power range.

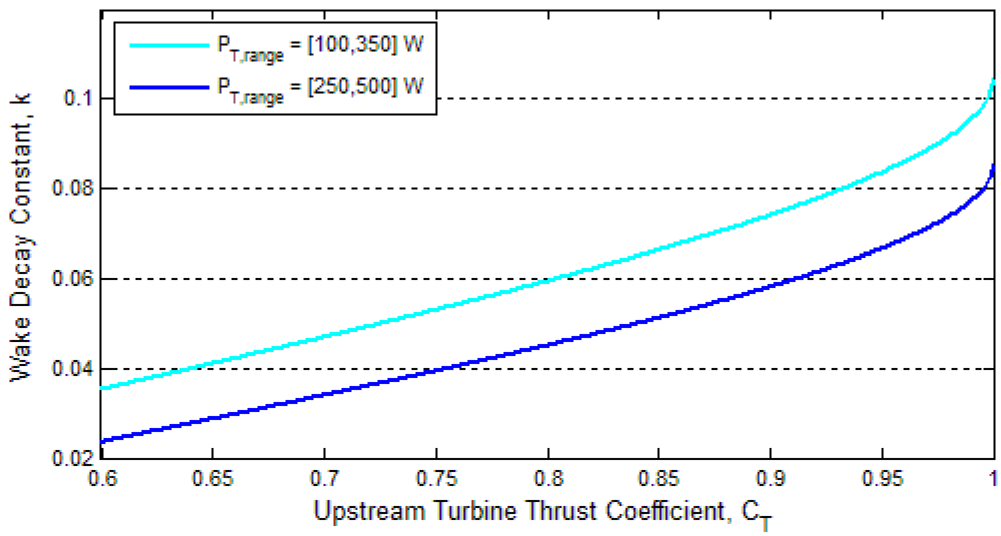

Figure 5.25: Single Wake Model Fit for Wake Number 1, Revised Formulation.

With the thrust coefficient, wake decay constant pairs of (k, C_T) = (0.85, 0.05) and (0.74, 0.05) for the low and high power ranges, the second wake number can be added. The multiple wake scenario is solved using these values and treating them as a constant with wake number, and is compared to the actual data results for wake numbers of 1 and 2, with the model being fit to the wake number 1 turbine, displayed in Figure 5.26.

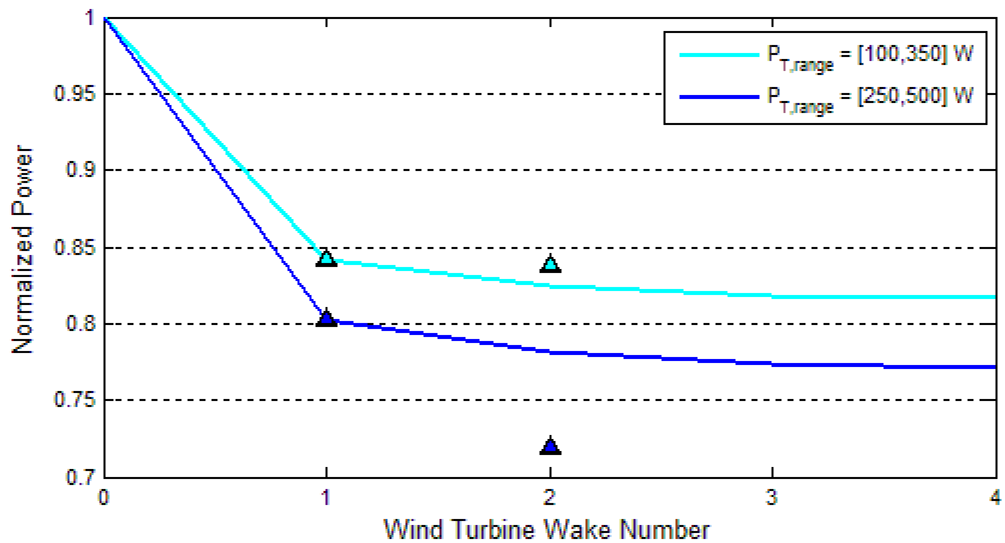

Figure 5.26: Multiple Wake Model Fit to Wake Number 1, Revised Formulation.

The Jensen model is also used with a fit to the wake number 1 turbine at C_T=0.85 for the high power range, resulting in the same value of C_T= 0.74 for the low range. The Jensen plot comparison of the wake decay constant with power range is shown in Figure 5.27. The thrust coefficients correspond to a wake decay constant of k=0.1.

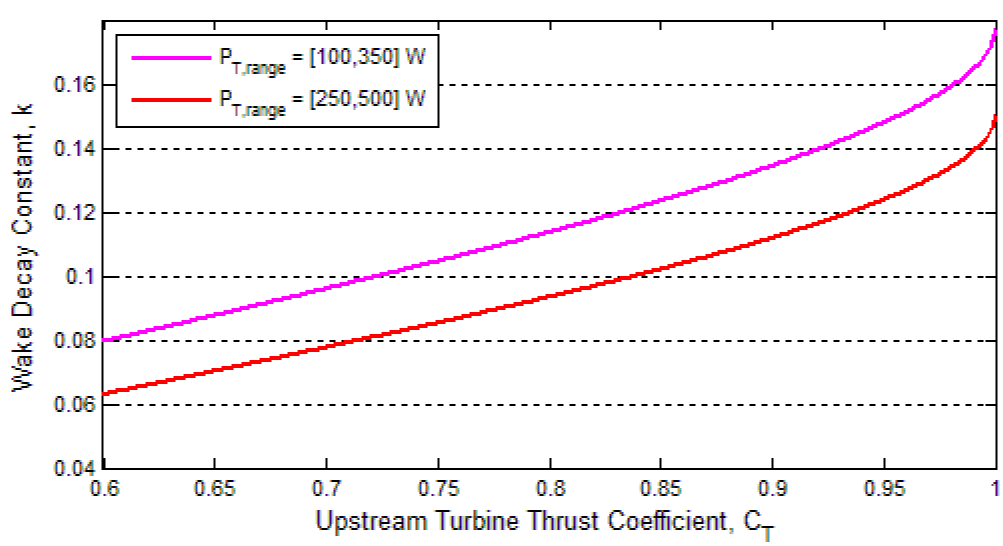

Figure 5.27: Single Wake Model Fit for Wake Number 1, Jensen Formulation.

Using the input parameters and assuming a constant k and C_T with wake number within the model produces the results shown in Figure 5.28.

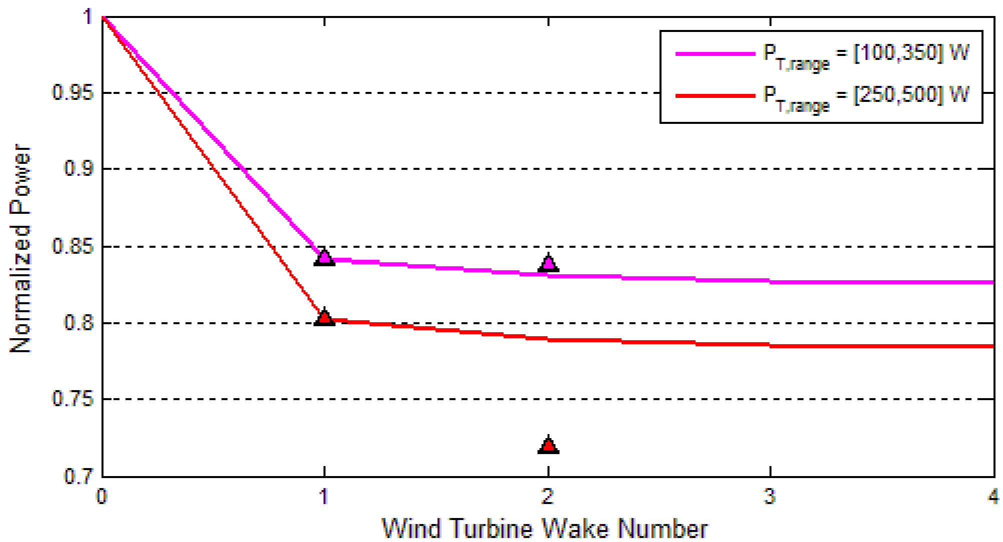

Figure 5.28: Multiple Wake Model Fit to Wake Number 1, Jensen Formulation.

The multiple wake model is fit to the data at wake number 1, and treated as constant, using the revised linear wake single wake model and the Jensen single wake model. Using this approach to determine the (k, C_T) inputs to the model produces results that are very constant with wake number. This trend is in agreement with the low power range [100, 350] W averages for both models due to this data point's minor reduction from wake number 1 due to the low power extraction. The multiple wake model however, should not be solved in this manner when making predictions for higher power ranges, under most standard conditions. The models, in both cases, over predict the performance of the wake number 2 turbine. The revised formulation and the Jensen model over predict the normalized power by 0.06 and 0.07, respectively.

The multiple wake model does not capture the additional loss caused by wake number 2 by around 0.07 normalized power. In the formulation to reach the model predictions it was however assumed that there would be a constant C_T and k input for each upstream turbine. To relax this assumption, the second wake number turbine is allowed to have an independent k, C_T pair from the first wake number turbine. With known values from the data for single and double wake scenarios, it is possible to solve for the k vs. C_T relationship for the isolated wake from wind turbine #2 to wind turbine #3 using the multiple wake model sum of squares approach. Rewriting the single wake formulation and solving for $k_{1\to 2}$:

$$k_{w\#1\to w\#2,s=7} = \frac{1}{2s}\left[\sqrt{\beta\frac{1-\sqrt{1-C_T}}{\sqrt{P^*}}} - 1\right] \tag{5.6}$$

where,

$$P^* = \left(1-\left(\left.{P_x}\middle/{P_1}\right.\right)_{w\#2}^{1/n}\right)^2 - \left(\beta\left(\frac{1-\sqrt{1-C_T}}{1+2k^x/D_T}\right)_{w\#1,s=14}\right)^2. \tag{5.7}$$

The results using this approach for the revised model and for the Jensen model are given in Figures 5.29 and 5.30.

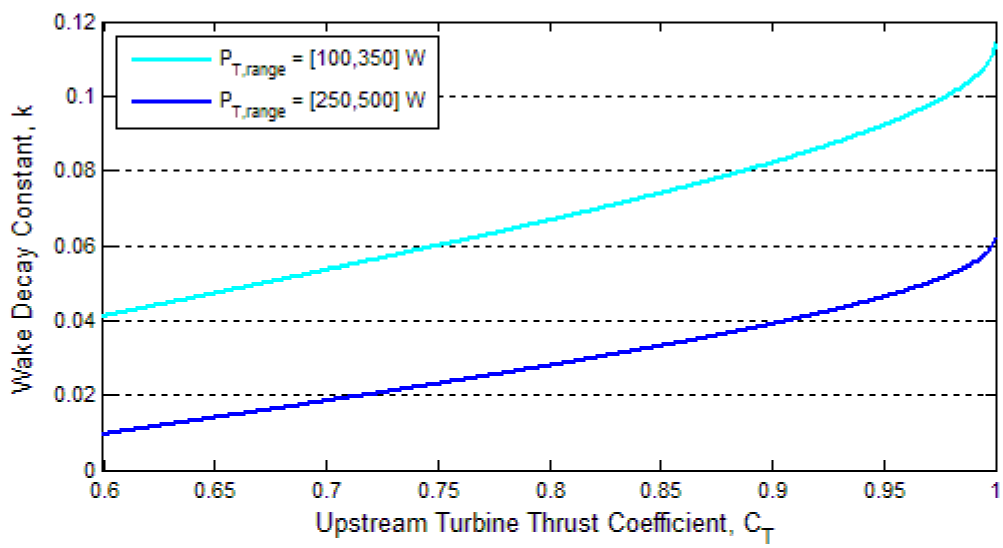

Figure 5.29: Double Wake Model Fit for Wake Number 2, Revised Formulation.

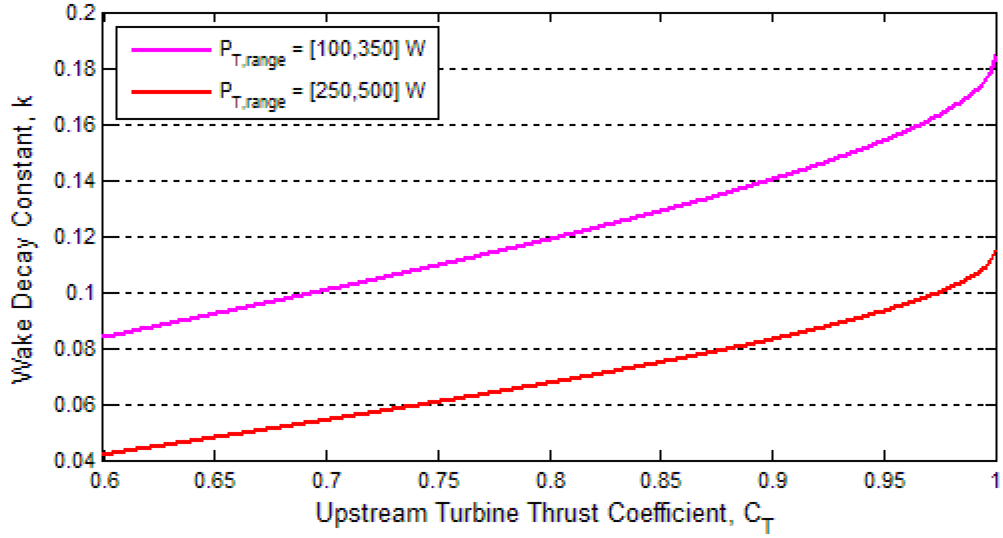

Figure 5.30: Double Wake Model Fit for Wake Number 2, Revised Formulation.

Selection of a thrust coefficient for the 2nd wind turbine reveals the necessary accompanying wake decay constant produced by this wind turbine. For the smaller power bin, the requirement is for greater expansion which would increase the velocity downstream according to the model to match the data that is higher than the model. For the high power range, whose data point was well below the model, k would need to be decreased in order to reduce the power of the turbine at wake number 2.

5.4 Wind Turbine Lateral Wake Results

Wake performance data were collected for a lateral wake test case on one windy day. The data set contains a 7 rotor diameter single wake downstream of a row of three turbines spaced laterally with a 2 rotor diameter width spacing. This spacing was chosen as it was the closest width spacing obtainable with predicted losses at a 7-diameter wake spacing. The instrumented upstream wind turbine was the center turbine in the row with the downstream instrumented wind turbine directly behind it when aligned with the wind direction. The test case facility configuration for the 7x2-diameter spacing lateral wake configuration is shown in Figure 5.31.

Figure 5.31: Facility Configuration with a Lateral Wake, 7x2-Diameter Spacing.

The findings from the single wake analysis for selection of the data processing variables were used for the lateral test case (T_{bin} = 10-sec, T_{sort} = 10-sec). These variables depend mostly on the turbine-turbine spacing for the two instrumented wind turbines, which is the same for the two test cases justifying the use of the result here. Comparison is made of the lateral wake 7x2-diameter spacing with the 7-diameter spacing data from the single wake test case, which has no lateral wakes. Plots of the total data sets and their 100 W power bin averages ± 1 standard deviation are given in Figures 5.32-37.

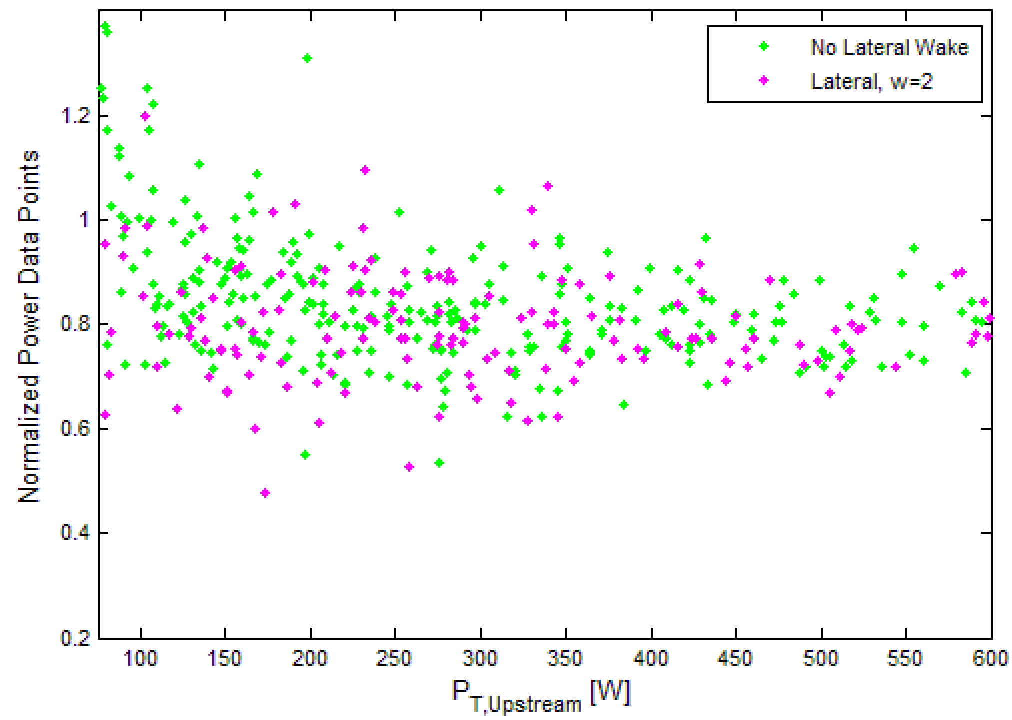

Figure 5.32: Wake Power Losses with Lateral Wakes Data Set.

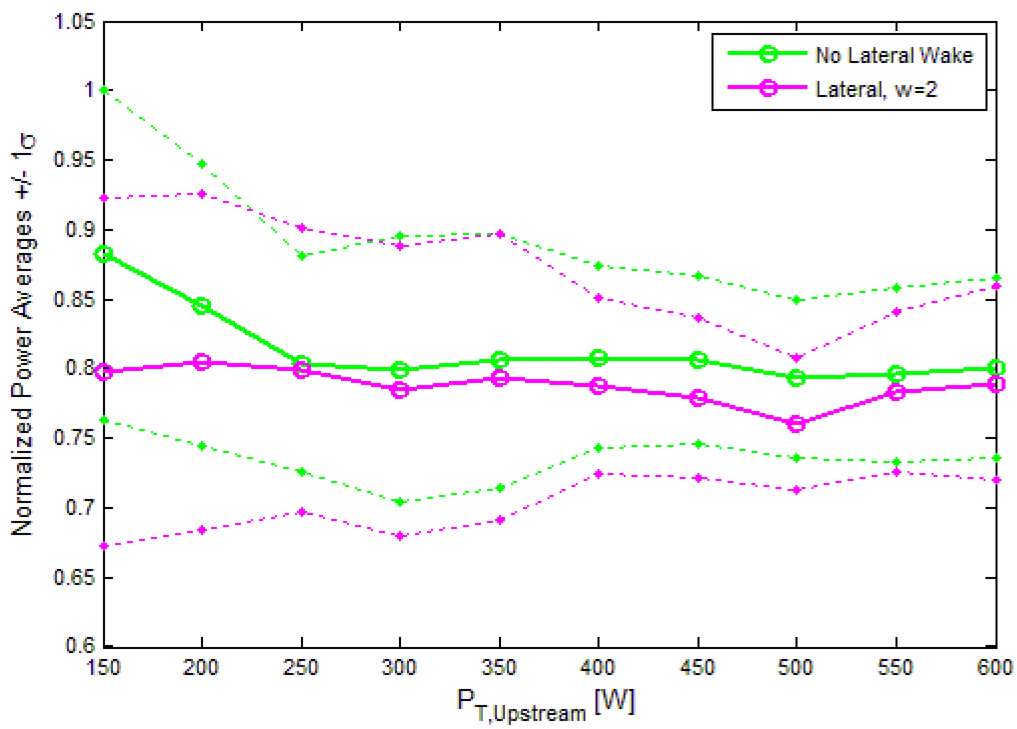

Figure 5.33: Wake Average Power Losses with Lateral Wakes.

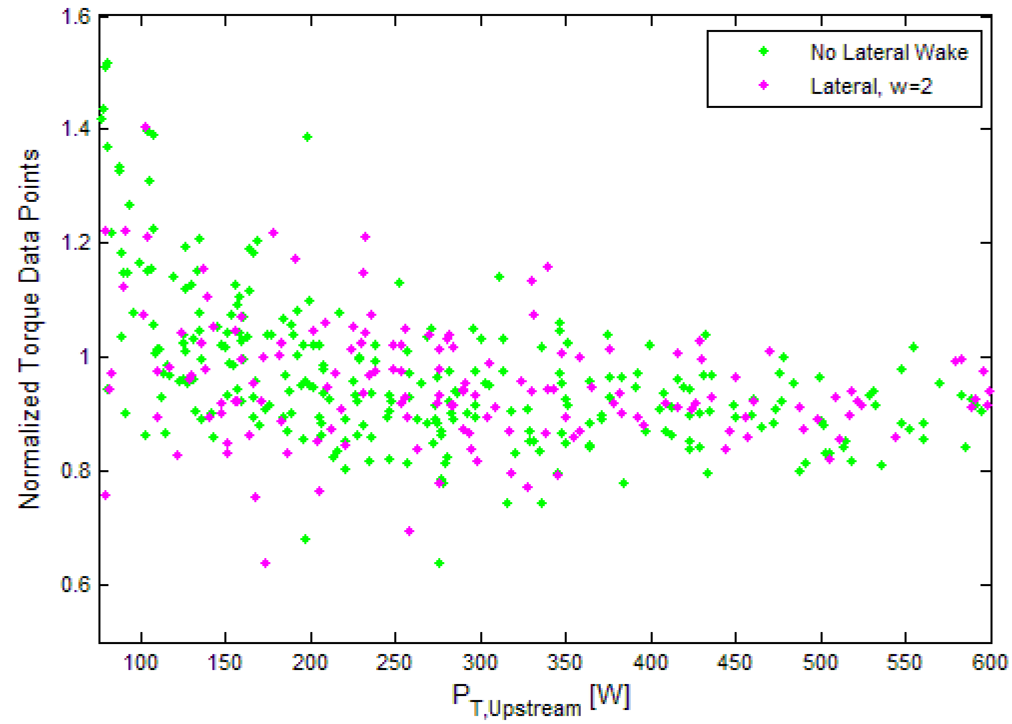

Figure 5.34: Wake Torque Losses with Lateral Wakes Data Set.

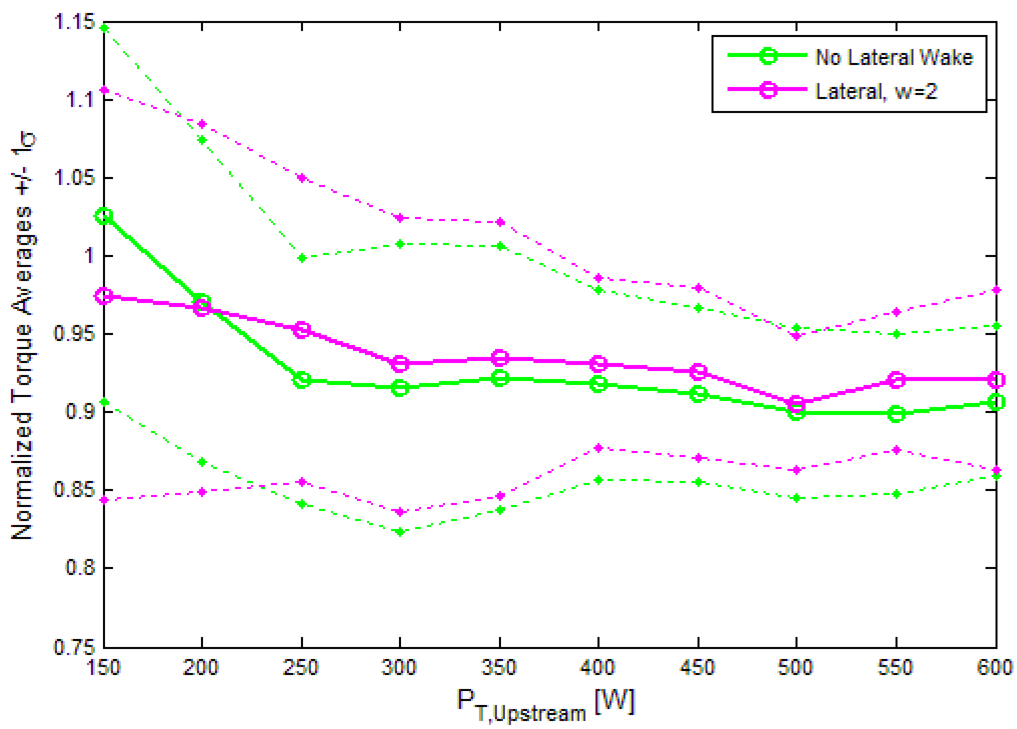

Figure 5.35: Wake Average Torque Losses with Lateral Wakes.

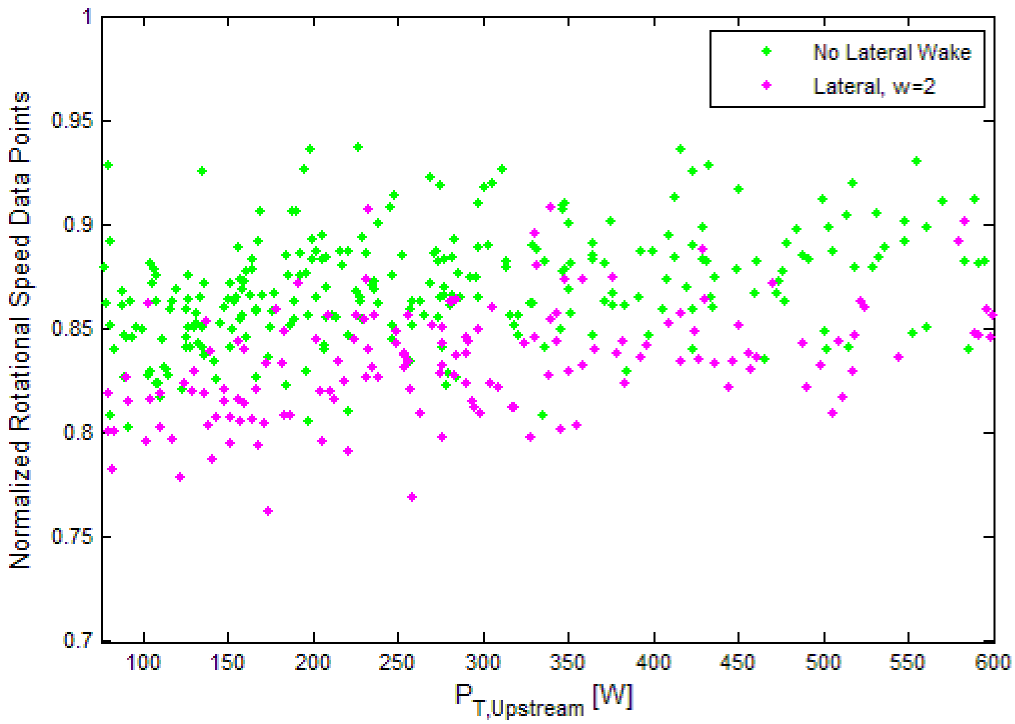

Figure 5.36: Wake Rotational Speed Losses with Lateral Wakes Data Set.

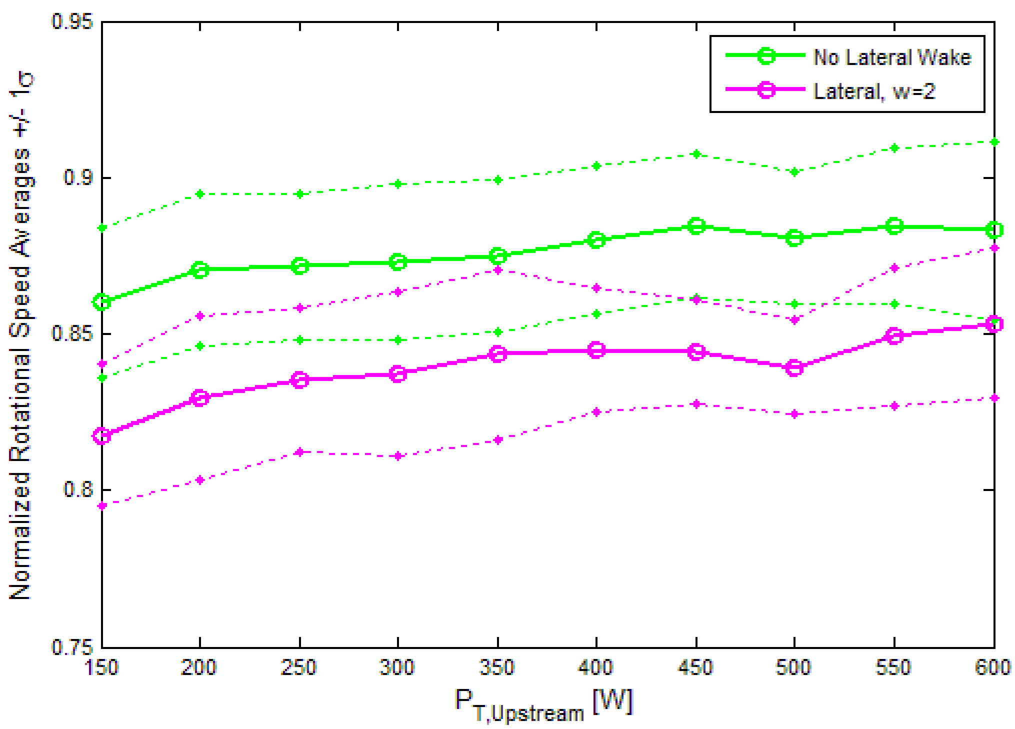

Figure 5.37: Wake Average Rotational Speed Losses with Lateral Wakes.

The results from this study show, within atmospheric variation and experimental uncertainty, that there is only a small change in the performance of a 7-diameter spaced turbine when 2-diameter lateral wakes are added upstream. The normalized power shows an average 1-2% decrease with the lateral wakes present over the high power ranges, Figure 5.33. There is a distinction present at the low power ranges in which the lateral wakes produce an average 5-8% decrease from the case without wakes. The total data sets of normalized power can also be compared and there is almost no discernible distinction between the two test cases except for at the lower power ranges. The two cases appear to occur within approximately the same range of values for the individual data points, but with a higher weighting of the lower values for the w=2 lateral wake case.

The increased power losses at lower power ranges are not fully understood. From the normalized torque and normalized rotational speed plots it is clear that the additional loss is due mostly to a further torque reduction, where the rotational speed loss is constant relatively. Torque reduction alone, without rotational speed reduction, was determined to be sourced from added turbulence in the wake. If this analysis is true, then it would mean that the wake has higher turbulence levels in the low power ranges when a lateral wake is added. This could possibly be due to the increased time of wake development for a given spacing with a lower freestream velocity. The distinction between these results at the low power range is not simply the low power range, but that in the presence of upstream lateral wakes. This would imply that the lateral wakes generate losses mostly due to turbulence addition versus axial flow reduction or swirl addition.

The normalized torque data set reveals a similar result to the power where data points occur over the same range for both test cases with no clear difference between the two. The average shown in Figure 5.35 is used to reveal the overall trend, where the downstream turbine is seen to perform at a higher torque value by about 1% in the high power ranges. The environmental and experimental accuracy constraints limit this result to a statement that the torque values are essentially constant between the two cases. The rotational speed may be a better indicator of relative performance due to the nature of the measurement's reliability, produced by the experimental uncertainty and its substantially lower response rate, as discussed earlier. The accuracy of this measurement produces a factor of two to four times less variation than with the torque measurement. The normalized rotational speed loss averages in Figure 5.37 reveal a nearly constant 5% absolute decrease from the no lateral wake to the w=2 lateral wake case. The averages are all outside of the 1 standard deviation variation making this additional loss a conclusive result.

A summary and comparison of the lateral wake test case results averaged over low, high, and total power ranges is included in Table 5.12. For the high and total power ranges, it is noted that the loss due to the lateral wake may be slightly larger than shown due to the torque average having a higher value with the lateral wake scenario in these cases which is an unexpected result. This variation could be on the order of an absolute 2% difference, resulting in around a 3-4% absolute loss with the addition of lateral wakes, spaced at 2-diameters.

Table 5.12: Lateral Wake Normalized Performance Summary (x/D =7).

Single, No Lateral, Wake Summary (7-Diameter Spacing)

Power Bin [W]:	[100,350]	[350,600]	[200,∞)
Power Average	0.842	0.803	0.803
Power Standard Dev.	0.111	0.063	0.076
Torque Average	0.972	0.911	0.914
Torque Standard Dev.	0.116	0.058	0.072
Omega Average	0.867	0.881	0.877
Omega Standard Dev.	0.025	0.023	0.025
Data Set Time [min]	35.5	14.7	36.7

Lateral Wake Summary (7x2-Diameter Spacing)

Power Bin [W]:	[100,350]	[350,600]	[200,∞)
Power Average	0.798	0.782	0.791
Power Standard Dev.	0.114	0.059	0.091
Torque Average	0.959	0.924	0.938
Torque Standard Dev.	0.112	0.050	0.084
Omega Average	0.830	0.845	0.841
Omega Standard Dev.	0.026	0.020	0.024
Data Set Time [min]	23.8	8.9	25.7

Relative contributions for the studied test cases to the power loss of operating in the wake of an upstream wind turbine within the influence of lateral wakes are summarized in Table 5.13.

Table 5.13: Lateral Wake Power Loss Components.

Width, w	P_{norm}	τ_{norm}	Ω_{norm}	$P_{loss,torque}$	$P_{loss,rotation}$	$L_{torque}/L_{rotation}$
∞	0.803	0.914	0.877	0.43	0.62	0.70
2	0.791	0.938	0.841	0.30	0.76	0.39

These results suggest that the presence of lateral wakes reduces performance losses due to increased torque on the downstream wind turbine, and increases performance losses due to rotational speed losses, among increasing performance losses all around for this spacing layout. The shift of overall loss contribution with the addition of lateral wakes seems to further increases relative contribution to the overall power loss by rotational speed losses. The percentages of which discussion is made for the torque measurement are within experimental uncertainty values and therefore cannot be definite statements.

The results from the lateral wake test case are compared using the model described in Section 3.3.3. The data listed in Table 5.12 for power ranges of [100, 350] W and [350, 600] W are used for the comparison with experimental results. This comparison is made for both power ranges using the two formulations of the lateral wake model. In each of the formulations it is assumed that the wake decay constant does not change value after the wakes merge. This is a reasonable assumption if the wake expansion is driven more by the interface with the atmosphere than by the internal volume of fluid. Regardless, for these comparisons it will be assumed that the wake-atmosphere interface is the controlling factor for wake expansion rate and that the wake decay constant has the same value before and beyond the merged wake region.

The first method of comparison to model results is done by fitting the case without a lateral wake to the single wake model to first determine a value for the wake decay constant, k, and then using this value to describe the lateral wake case. The thrust coefficient is again needed as an input to this equation and the results from the single wake case describe the lateral cases studied, C_T=0.72, 0.85 for the low and high power ranges. The two additional contributions to wind turbine performance loss when considering lateral wake scenarios are that due to area change caused by wake merging and that due to wake suppression caused by the symmetry planes. This first analysis compares the effect of modeled performance losses due to area change alone with the experimental data for the two power bins.

Results are first shown using the revised formulation of the linear wake model in Figure 5.38. This formulation of the linear wake model produces a wake decay constant k=0.05, which is one half of the value of the Jensen model at the same thrust coefficient. Due to this low wake decay constant there is no predicted loss at the 7-diameter spacing from wake area change. For this reason, only the low power bin from this formulation is shown in this section.

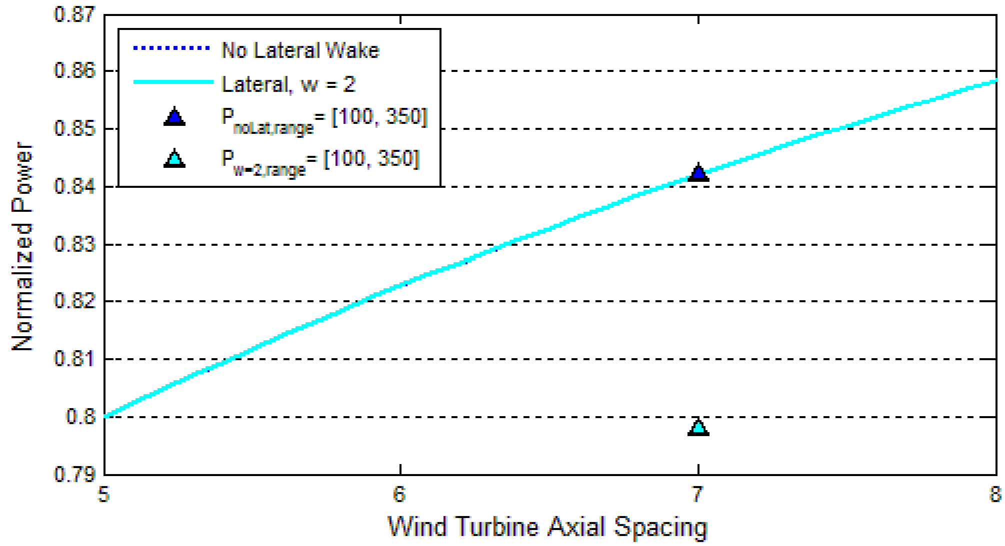

Figure 5.38: Lateral Wake Model Fit to Low Power Data, Revised Formulation.

This same approach was used with the Jensen model formulation for both low and high power range cases with the results shown in Figures 5.39 and 5.40. This model's wake decay constant has a sufficient value to predict a wake area change due to lateral wakes at the tested 7-diameter spacing, as seen by the divergence of the lateral wake case (solid magenta line) from the single wake case, with no lateral wakes (dashed red line).

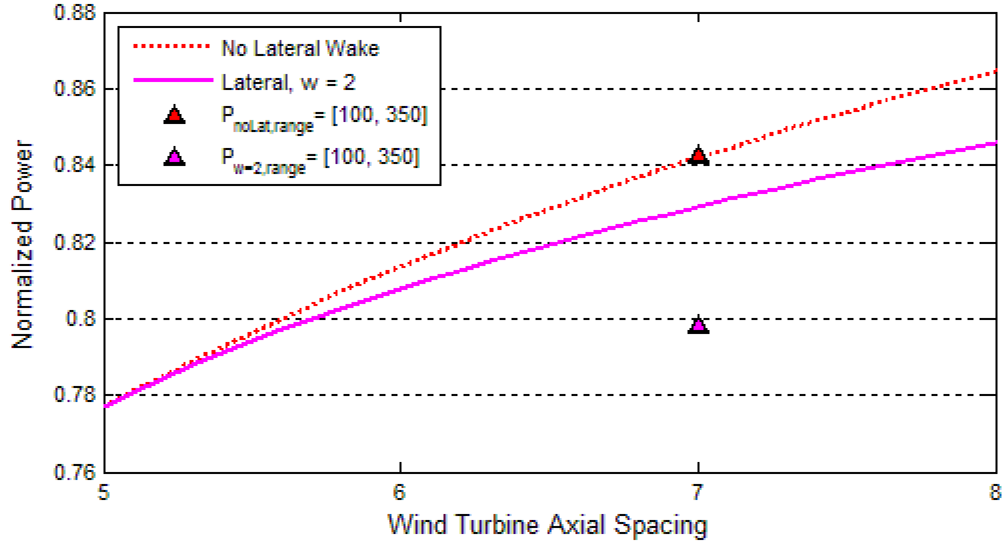

Figure 5.39: Lateral Wake Model Fit to Low Power Data, Jensen Formulation.

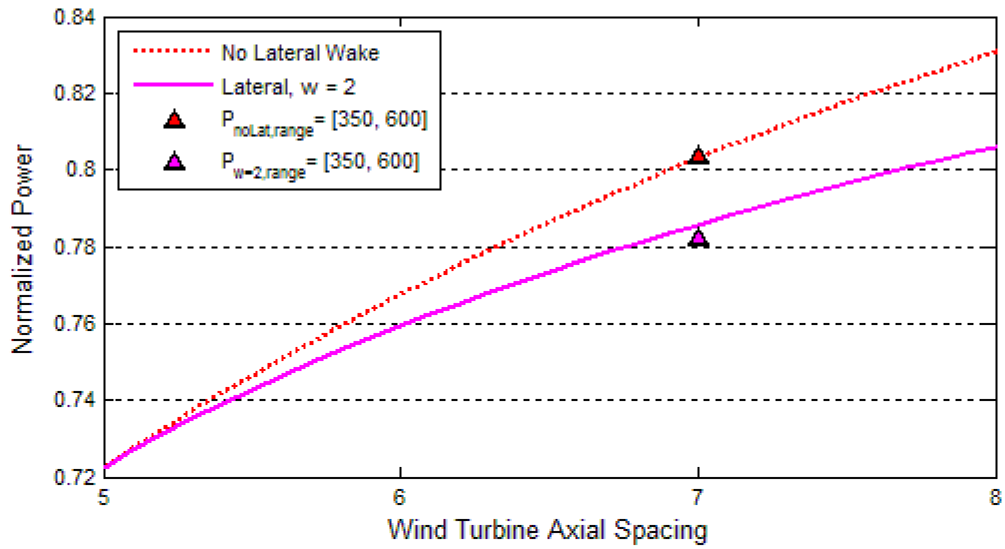

Figure 5.40: Lateral Wake Model Fit to High Power Data, Jensen Formulation.

The model comparison plots show a reasonable level of agreement with the experimental results for the two power bins. The low power bin deviates from the experimental result for the 2-diameter lateral wake case when using the wake decay constant fit from the single wake data assuming C_T=0.72, estimated from the single wake analysis. The high power comparison produces a high level of agreement with the lateral wake model with the assumed C_T=0.85.

The unknown thrust coefficient of the low power range can be adjusted to yield improved results compared to the model. If the thrust coefficient of the high power range is used for the low power range analysis the prediction changes as shown in Figure 5.41. In this figure the solid lines represent the previous results for C_T=0.72 and the dashed lines for the new comparison with C_T=0.85. The dashed magenta line for the lateral wake model with the high power range thrust coefficient used reduces the discrepancy from the model and the result by a factor of two and with an absolute difference of only 1.6%.

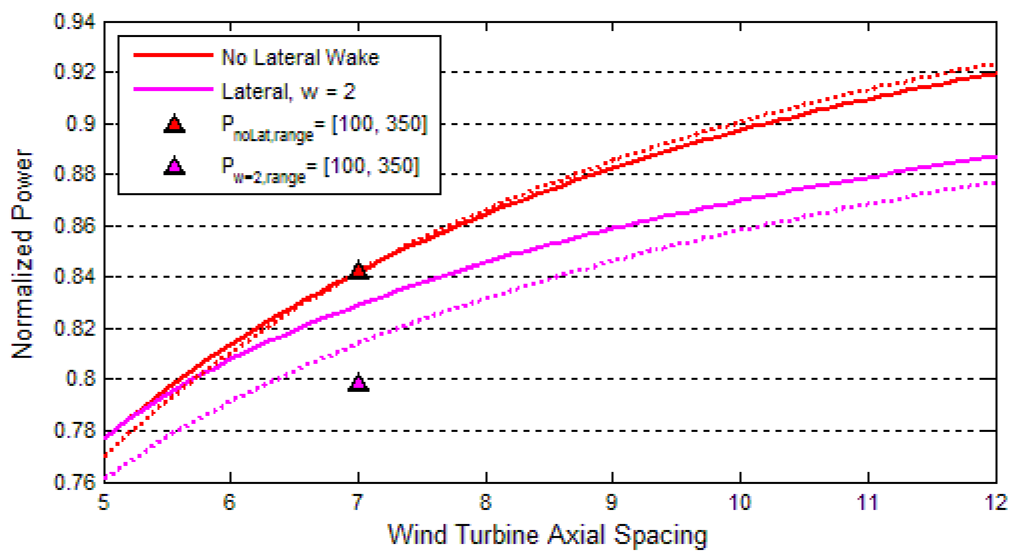

Figure 5.41: Lateral Wake Model Low Power Data C_T Comparison, Jensen.

The remaining gap between the lateral wake model and data can be accounted for with wake suppression. The presence of lateral wakes can act to suppress wake expansion due to bounded atmospheric conditions in the lateral direction. In reality, this suppression would skew the area growth of the wake based on the distinction between the atmospheric conditions at the top interfaces and the side interfaces but it will be treated as a constant radial growth with overall suppression. The presence of this effect is seen in the remaining discrepancy between the lateral wake data and model in Figures 5.42-43, which is clearly more significant for the low power range than the high. In the model this effect is accounted for by changing the wake decay constant in the lateral wake model so it will fit the experimental data point for the 2-diameter lateral wake test case.

Results from this analysis are shown using the revised linear wake model formulation with lateral wake effects, which are not present at 7-diameter spacing for this formulation. With this model, the entire performance loss due to the addition of lateral wakes is due to wake suppression, at this spacing. In order for the revised model to be accurate, given the validity of the lateral wake model, the wake decay constant has to take a suppressed value of k = 0.035 and k = 0.045 for the low and high power ranges. The values are suppressed from a wake expansion without lateral wakes of about k=0.05. As before, these are seemingly low values but the revised single wake model validity could be proven or disproven from flow measurements that quantify the wake expansion.

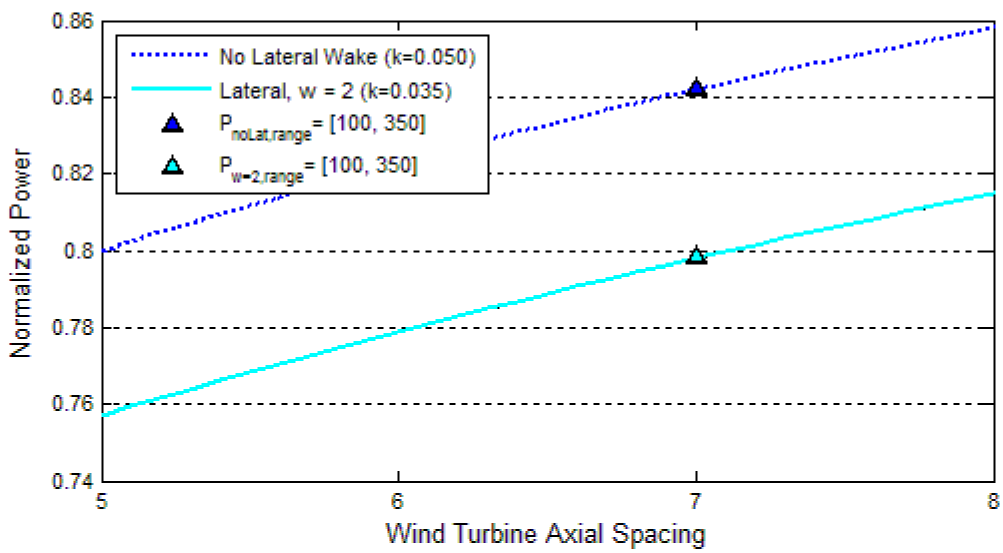

Figure 5.42: Lateral Wake Model Low Power Fit with Wake Suppression, Revised.

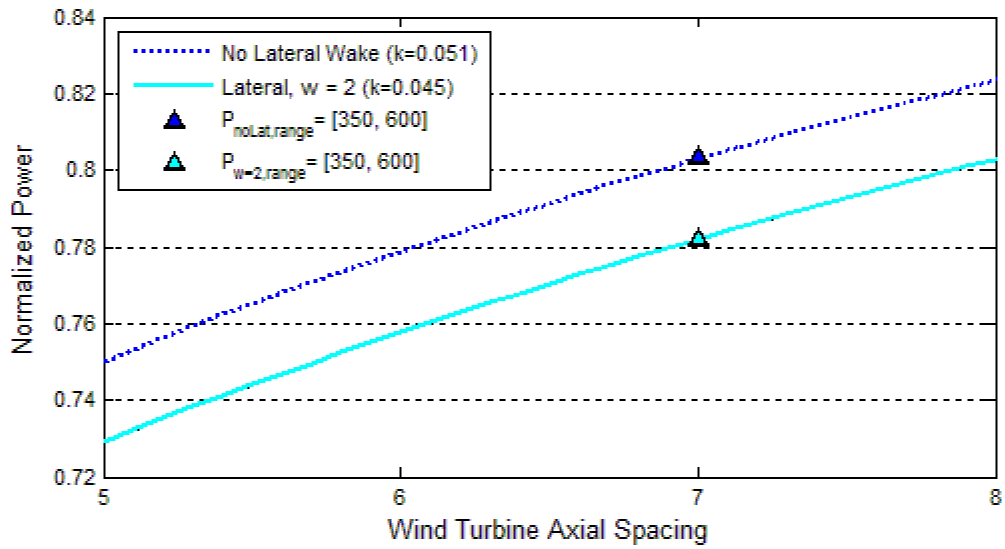

Figure 5.43: Lateral Wake Model High Power Fit with Wake Suppression, Jensen.

The Jensen formulation is also compared using this method of determining a suppressed wake decay constant from the single wake, no lateral wake, benchmark value. Figures 5.44 and 5.45 show the results using the low and high power range experimental data. These fits are calculated using the original values of C_T=0.72, 0.85 for the low and high power ranges. The suppressed wake decay constants take on values of k=0.08 and k=0.1 for these ranges, varying from the single wake value of approximately k=0.1.

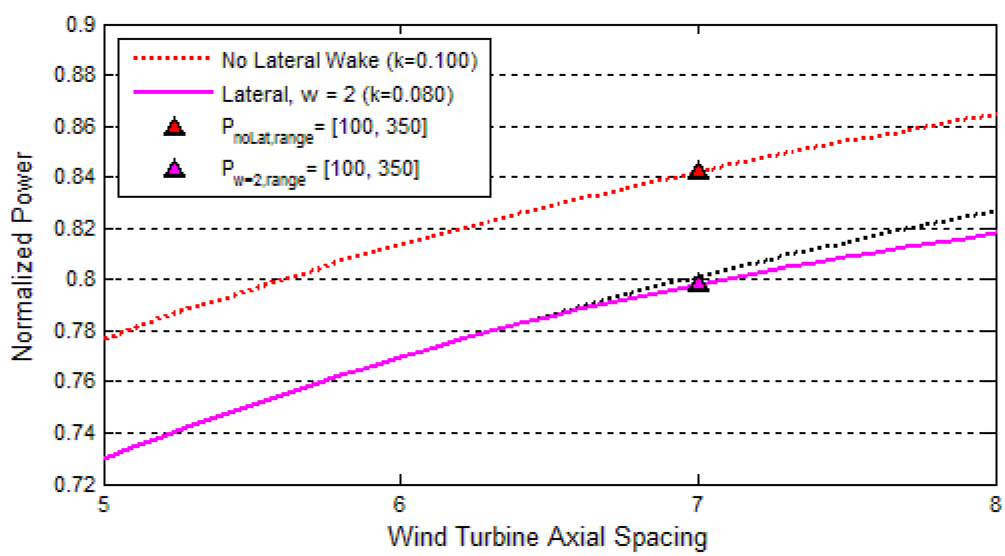

Figure 5.44: Lateral Wake Model Low Power Fit with Wake Suppression, Revised.

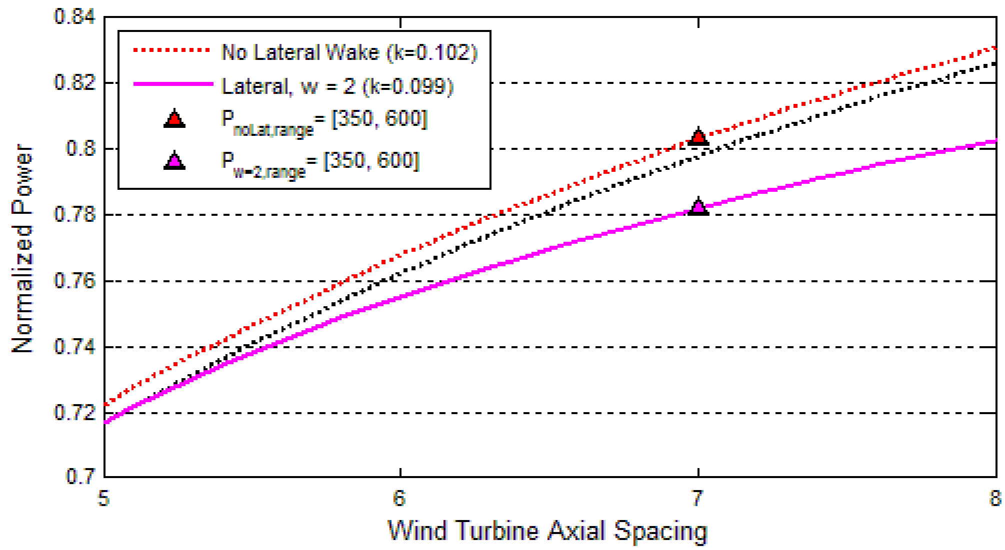

Figure 5.45: Lateral Wake Model High Power Fit with Wake Suppression, Jensen.

The main conclusion from the lateral wake results is that the model developed as part of this dissertation to describe lateral wakes seems to agree well with what is physically happening, especially when combined with the Jensen model. If the Jensen single wake model is correct, then the conclusion from this study is that the lateral wake model agrees well with experimental results with only a minor amount of wake suppression present in the lateral wake scenario. This model's validity would prove that area reduction produced by the presence of lateral wakes is the dominant source of additional performance losses. If the revised linear wake model is correct then the source of additional performance loss due to lateral wakes at 7-diameter spacing is completely due to wake suppression. A summary of the results from the lateral wake analysis is given in Table 5.14. This table lists the wake decay constants when fit to the single wake and lateral wake experimental data which highlights the level of wake suppression required. The relative additional power loss from single wake to a lateral wake case caused by area change versus by wake suppression are also given in the last two columns.

Table 5.14: Lateral Wake Model Results, 7x2-Diameter Spacing.

Jensen Model Wake Formulation

Power Range	C_T	k_{fit}-no Lat.	k_{fit}-Lat, w=2	$P_{loss,Area}$	$P_{loss,suppress}$
[100, 350] W	0.72	0.100	0.080	0.29	0.71
[100, 350] W	0.85	0.123	0.110	0.63	0.37
[350, 600] W	0.85	0.102	0.099	0.82	0.18

Revised Linear Wake Model Formulation

Power Range	C_T	k_{fit}-no Lat.	k_{fit}-Lat, w=2	$P_{loss,Area}$	$P_{loss,suppress}$
[100, 350] W	0.72	0.050	0.035	0.00	1.00
[100, 350] W	0.85	0.066	0.049	0.00	1.00
[350, 600] W	0.85	0.051	0.045	0.00	1.00

The results for the lateral wake model's effectiveness can be better concluded with additional spacing's tested at further distances which could be added to the comparison.

CHAPTER 6: SUMMARY AND CONCLUSIONS

6.1 Conclusions

Wind turbine performance has been predicted analytically and determined experimentally as part of this research. Maximum theoretical performance of individual wind turbines has been derived for single- and double-rotor, counter-rotating configurations with respective anticipated power coefficient performance merits of 59.3% and 66.9%, corrected from earlier results for a double rotor analysis. Wind turbine performance predictions, namely losses, when operated collectively in wind farm settings were modeled with single, multiple, and lateral wake scenarios. The standard Jensen single wake linear expansion model was corrected for more theoretically consistent prediction with a revised linear wake model. A model describing lateral wake scenarios due to adjacent upstream wind turbines was created as part of this research.

The Purdue Micro Reconfigurable Wind Farm facility was used to test variable array layouts in order to simulate and measure wind turbine performance in a wind farm setting. Test cases were performed to quantify the effects of turbine-turbine spacing in a single wake scenario, to quantify further performance losses when operating within the wakes of multiple upstream wind turbines, and to quantify the effect of lateral wake spacing from adjacent upstream wind turbines.

Data for the single wake test case were collected using spacing's of 3-, 5-, and 7-rotor diameters. The data analysis reveals that performance losses with single wake spacing are highest nearer to the upstream wind turbine and the power losses from upstream decrease with this spacing in a non-linear manner. The data averages show that experimental variation is well within an acceptable level for the three cases tested validating the significance of the results. The power losses with single wake spacing were presented separating low and high power ranges for the [3, 5, 7] diameter spacing's with normalized power values of [0.446, 0.733, 0.848] for the low power range and [0.410, 0.726, 0.806] for the high power range.

The data from the three spacing's for normalized power, torque, and rotational speed were averaged within power range bins to produce their dependency with upstream wind turbine power, which is a value indicative of wind speed. Normalized rotational speed loss due to wake operation was presented with very low variability for each of the tested cases, however, predictions from measurement of rotational speed alone do not necessarily produce a representative value for total power losses as they are not in a one-to-one relationship with each other. By treating the power loss as the multiple of torque and rotational speed losses the relative contribution of the two was derived for the three test cases. This analysis of the loss mechanisms yields insight into the physics of the wake flow at the tested locations downstream.

Results from the single wake test case were compared with a model which assumes a linear wake expansion to determine velocity deficits downstream. The standard Jensen model and a revised formulation of it which has a theoretically more correct derivation are both used for the comparison. This comparison split the data into two power ranges to account for the anticipated difference in thrust coefficient, which is an important input to this model. The downstream wind turbine spacing condition is not considered to affect the upstream performance, particularly for larger spacing's. An outcome of this condition was modeled correctly with the Jensen model causing the 5- and 7-diameter cases to intersect when deriving the wake decay constant fit to the experimental data as a function of the unknown thrust coefficient. This intersection occurred at a value of C_T=0.848 resulting in a wake decay constant of k=0.103. These values agree well with what would be expected providing merit to both the data and the model. The thrust coefficient of the low power range was assumed to occur at a constant k value and matched with the 7-diameter spacing low power data which resulted in C_T=0.72 for the upstream turbine. The 3-diameter spacing was not approximated accurately by this model. This location is considered within the near-wake region of the flow and its physics are not accounted for in this one-dimensional model, and should not be used in this region. For the high power range the wake decay constant is forced to take a value of k=0.05 to fit this close spacing point. It was determined that a non-linear wake expansion would have to be modeled to describe all of the spacing's tested, expanding slowly at first and then more rapidly, eventually reaching a constant linear expansion.

The revised linear wake model formulation predicted a wake decay constant using a high power range C_T=0.85 of k=0.044, which resulted in a low power range prediction of C_T=0.72. The revised formulation of the single wake model was fit to the data with wake decay constant plotted versus thrust coefficient but without intersection of the 5- and 7-diameter curves as with the Jensen model. The revised formulation of the linear wake model provided less agreement overall with the data, most notably at the 3-diameter spacing which would require wake contraction to fit to the data. Despite its more theoretically correct conception, the revised model does not predict the wake power loss data for the single wake case as well as the Jensen model. The wake decay constant predicted differs by a factor of two between the two models. The accuracy compared to physical wake expansion for either model is left to further flow-field analysis for conclusion.

A double wake case was tested with a 7-diameter spacing. The normalized power comparison with upstream wind turbine power shows power losses that differ between single- and double-wake scenarios which increase with the power range. Additional absolute power losses on the order of 8% are produced at the high power ranges with the presence of the second wake. For the low power range there was nearly no effect of adding the second wake. The additional power loss source was determined to be primarily from additional torque losses for the double wake case, with double the magnitude of additional rotational speed losses.

The double wake results were compared with the standard velocity deficit sum of squares mathematical approach. The model was first used assuming a constant wake decay constant and thrust coefficient as fit to the single wake data and then compared with the double wake results. The Jensen model and its revised formulation predicted the double wake scenario with similar accuracy where prediction for the lower power bin, low additional loss data was in good agreement but the high power range additional power loss was underestimated by about 7%. The second approach used with this model was to relax the constant (k, C_T) pair with wake number assumption and to solve for the pair that fits the experimental data at the downstream wind turbine. The relationship between wake decay constant and thrust coefficient required at the second wind turbine by the multiple wake model to fit the experimental data was determined using the two single wake formulations and two power ranges. For the high power range the requirement is for lower wake expansion to fit the double-wake data using the multiple-wake model. Reduced thrust coefficient and wake decay constant is to be expected for the downstream wind turbine as required by the multiple-wake model

The effect of the lateral wake on downstream wind turbine performance was compared for a 7-diameter downstream spacing when 2-diameter width lateral wakes were added. This case resulted in an average of 1-3% absolute decrease of power with lateral wakes over the high power range. The low power range predicted 5-8% additional power losses with the lateral wakes. The additional loss incurred by adding the lateral wakes was found to be mostly caused by rotational speed losses. The shift of overall loss contribution is increased in favoring rotational speed losses due to the lateral wakes from upstream adjacent wind turbines.

A model was created to describe power losses of a wind turbine operating in the wake of an upstream wind turbine with adjacent wind turbines producing lateral wakes. Deviation of this model from the single wake model occurs both explicitly and implicitly. Explicitly this model predicts additional power loss through wake area reduction beyond the point where the lateral wakes meet and create a symmetry plane. Additional power loss is expected by the model implicitly from wake suppression due to the lateral wake mirroring effect, reducing the wake decay constant. The relative effect of the variation sources was determined for the two linear wake model formulations. Area effects were first observed through the model derivation as written with treatment of the wake decay constant as fit to the no lateral wake data. The revised formulation predicted zero loss for the tested layout from area reduction due to its small wake decay constant (k=0.05). The analysis was additionally performed using the Jensen model which predicted an area change reduction in power for the low and high power ranges, which was in good agreement for the high power range. The low power range was found to agree better if using the same thrust coefficient as for the high power range. A measure of how well the model fit to the data without wake suppression is determined through using the model to fit a wake decay constant to the experimental data for the lateral wake case. The Jensen model predicted wake suppression on the order k=0.1 to k=0.08 for the low power range and k=0.102 to k=0.099 for the high power range. The revised formulation of the linear wake model predicted additional power loss caused by lateral wakes to arise solely from wake suppression with wake decay constant reduction from k=0.05 to k=0.035 and from k=0.51 to k=0.045 for the low and high power ranges, respectively. The derived lateral wake model has been given a level of proof from its predictions compared to the experimental results. Depending on the correctness of either linear wake model formulation, insight has been gained as to the mechanism of the additional loss – due to either area reduction or wake suppression.

6.2 Future Work

Viable results have been obtained using the Micro Reconfigurable Wind Farm facility at Purdue University which gives fundamental insight into wake behavior. Results from this facility can be used to aid model revision and derivation as done with this dissertation's research. Future studies which are believed to be significant are listed in relative high to low order of perceived significance:

- Collect multiple wake test case data with higher wake number (using all four wind turbines) for the 7-diameter configuration to determine if there are further losses that result in greater errors from the multiple wake model.
- Collect multiple wake test case data using a 3- or 5-diameter spacing to determine if the multiple wake model predicts an inverse trend with spacing for predictions beyond wake number 1 than what physically occurs; as anticipated.
- Collect lateral wake test case data at higher axial spacing's to compare to validate the lateral wake model, suggested 10x2-diameter configuration benchmarked with a 10-diameter single wake configuration.
- Collect single wake test case data at 2- and 4-diameter spacing's to provide insight into the near-wake dynamics and the far-wake transition length.
- Using the single wake 2-, 4-, and 10-diameter spacing's in addition to the 3-, 5-, and 7-diameter spacing data given to generate a more discretized grid of the wake losses with spacing in order to verify the linear wake expansion approximation.
- Combine the validated models into a wind farm prediction tool; can be used to determine significance of lateral wake spacing versus axial spacing.
- Use the 10-diameter single wake spacing data for model validation of the Jensen model or the revised linear wake model formulation.
- Collect data for partial wake flow scenarios for a single wake test case.

- Determine the physical wake expansion of a wind turbine for low and high power ranges and use the value to compare between the two formulations of the linear wake model, and to revise the model.

LIST OF REFERENCES

LIST OF REFERENCES

[1] Barthelmie RJ, et al., 'Modelling and Measuring Flow and Wind Turbine Wakes in Large Wind Farms Offshore', *Wind Energy*, 2009, Volume 12, pp. 431-444.

[2] D.J. Milborrow and J.F. Ainslie, 'Intensified study of wake effects behind single turbines and in wind turbine wakes', *Final Report of IEA, Annex IX,* National Power, London, 1992.

[3] Crespo A, Hernandez J, Frandsen S, 'Survey of Modelling Methods for Wind Turbine Wakes and Wind Farms', *Wind Energy*, 1999, Volume 2, pp. 1-24.

[4] P.J.H. Builtjes and P.E.J. Vermeulen, 'Turbulence in Wind Clusters', *Proc. 4th Int. Symp. on Wind Energy Systems*, Stockholm, 1982, Vol. 2, pp. 449-464.

[5] Adams BM, Quarton DC, Schepers JG, Bulder B, J.A. Dahlberg and E. Morfiadakis, 'Dynamic Loads in Wind Farms', *Proc. EWEC '94*, Thessaloniki, 1994, 756-761.

[6] Playle SC, Korkan KD, von Lavante E, 'A Numerical Method for the Design and Analysis of Counter-Rotating Propellers', *Journal of Propulsion*, 1986, Volume 2, pp. 57-63.

[7] Agrawal V, 'Design and Aero-Acoustic Analysis of a Counter-Rotating Wind Turbine', *Master's Thesis, Purdue University*, 2010.

[8] Denner BW, Korkan KD, 'An Approximate Model For The Performance and Acoustic Predictions of Counterrotating Propeller Configurations', *AIAA 28th Aerospace Sciences Meeting*, Reno, 1990, pp. 1-18.

[9] Lolgen Th, Neuwerth G, 'Noise Directivity of Unducted Counter Rotating Propfans', *15th AIAA Aeroacoustics Conference*, Long Beach, 1993, pp. 1-10.

[10] Chung J, Hough J, Nagel R, 'Interaction Between Rotors of a Counter-Rotating Propeller', *AIAA 13th Aeroacoustics Conference*, Tallahassee, 1990, pp. 1-9.

[11] Chung JD, Walls JL, Nagel, RT, 'Flow Interaction & Noise From a Counter Rotating Propeller', *AIAA Aerospace Sciences Meeting*, Reno, 1991, pp. 1-9.

[12] McKay BG, 'Ideal Optimization of Counterrotating Propellers', *AIAA/ASME/SAE/ASEE 24th Joint Propulsion Conference*, Boston, 1988, pp. 1-7.

[13] Lesieutre DJ, Sullivan JP, 'Unsteady Forces on Counter-Rotating Propeller Blades', *AIAA*, 1986, pp. 229-236.

[14] Page GS, Liebeck RH, 'Analysis and Design of Dual-Rotation Propellers', *AIAA*, 1989, pp. 473-480.

[15] Gazzaniga JA, Rose GE, 'Wind Tunnel Performance Results of Swirl Recovery Vanes as Tested with an Asvanced High Speed Propeller', *AIAA/SAE/ASME/ASEE 28th Joint Propulsion Conference and Exhibit*, Nashville, 1992, pp. 1-42.

[16] Squires B, 'Manipulation of Upstream Rotor Leading Edge Vortex and its Effects on Counter Rotating Propeller Noise', *AIAA 31st Aerospace Sciences Meeting & Exhibit*, Reno, 1993, pp. 1-10.

[17] Vermeer LJ, Sorensen JN, Crespo A, 'Wind Turbine Wake Aerodynamics', *Progress in Aerospace Sciences 39*, 2003, pp. 467-510.

[18] G.C. Larsen, J. Hojstrup and H.A. Madsen, 'Wind fields in wakes', *Proc. 1996 European Union Wind Energy Conf.*, Goteborg, 1996, pp. 764-768.

[19] H. Schlichting, *Boundary Layer Theory*, McGraw-Hill, New York, 1968.

[20] T. Faxen, 'Wake interaction in any array of wind-mills. Theory and preliminary results', *Proc. 2nd Int. Symp. on Wind Energy Systems*, Amsterdam, 1978, pp. 59-72.

[21] Crespo A, Manuel F, Moreno D, Fraga E, and Hernandez J, 'Numerical Analysis of Wind Turbine Wakes', *Proc. Delphi Workshop on Wind Energy Applications*, Delphi, 1985, pp.15-25.

[22] Katic I, Hojstrup J, Jensen NO, 'A Simple Model for Cluster Efficiency', *Proc. EWEC '86*, Rome, 1986, Vol. 1, pp. 407-410.

[23] van Oort H, van Gemert PH, Crespo A, 'Wind Farms in Complex Terrain', *Final Report, CEC Contract EN3W/0030/NL, MT-TNO Report 89-233*, Apeldoorn, 1989.

[24] Stefanatos N Ch, Morfiadakis EE, and Glinou GL, 'Wake Measurements in Complex Terrain', *Proc. 1996 European Union Wind Energy Conf.*, Goteborg, 1996, pp. 773-777.

[25] Helmis CG, Papadopoulos KH, Asimakopoulos DN, Papageorgas PG, Soilemes AT, 'An Experimental Study of the Near-Wake Structure of a Wind Turbine Operating in Complex Terrain', *Solar Energy*, 54, 1995, 413-428.

[26] Taylor GJ, 'Development of an Improved Eddy Viscosity Model. Wake and Wind Farm Modeling', *contribution to Final Report, CEC Contract JOUR-0087-NL (CEC), MT-TNO Report 93-374*, 1993.

[27] Magnussen M, and Smedman A-S, 'Influence of Atmospheric Stability on Wind Turbine Wakes', *Wind Engineering*, 18, 1994, pp. 139-152.

[28] Volund P, 'Loads on a Horizontal Axis Wind Turbine Operating in a Wake', *Proc. EWEC'91*, Amsterdam, 1991, pp. 605-609.

[29] Frandsen S, and Thomsen K, 'Change in Fatigue and Extreme Loading when Moving Wind Farms Offshore', *Wind Engineering*, 21, 1997, pp. 197-214.

[30] Dahlberg JA, Poppen M, and Thor SE, 'Load/fatigue Effects on a Wind Turbine Generator in a Wind Farm', *Proc. EWEC'91*, Amsterdam, 1991, pp. 251-255.

[31] Dekker JWM, Pierek JTG, 'European Wind Turbine Standards', *Energy Research Centre of the Netherlands: ECN-C-99-073*, Petten, the Netherlands, 1999, 57.

[32] Barthelmie RJ, Folkerts L, Larsen GC, Rados K, Pryor SC, Frandsen ST, Lange B, and Schepers G, 'Comparison of Wake Model Simulations with Offshore Wind Turbine Wake Profiles Measured by Sodar', *Journal of Atmospheric and Oceanic Technology*, 23, 2006, pp. 888-901.

[33] Cleve J, Greiner M, Enevoldsen P, Birkemose B, Jensen L, 'Model-based Analysis of Wake-Flow Data in the Nysted Offshore Wind Farm', *Wind Energy*, 12, 2009, pp. 125-135.

[34] Frandsen S, Barthelmie R, Pryor S, Rathmann O, Larsen S, Hojstrup J, 'Analytical Modelling of Wind Speed Deficit in Large Offshore Wind Farms', *Wind Energy*, 9, 2006, pp. 39-53.

[35] Troldberg N, Sorensen JN, Mikkelson R, 'Numerical Simulations of Wake Characteristics of a Wind Turbine in Uniform Inflow', *Wind Energy*, 2010, Volume 13, pp. 86-99.

[36] Ebert PR, Wood DH, 'The Near Wake of a Model Horizontal-axis Wind Turbine Part 3: Properties of the Tip and Root Vortices', *Renewable Energy*, 22, 2001, pp. 461-472.

[37] Whale J, Anderson CG, Bareiss R, Wagner S, ‘An Experimental and Numerical Study of the Vortex Structure in the Wake of a Wind Turbine’, *Journal of Wind Engineering and Industrial Aerodynamics*, 84, 2000, pp. 1-21.

[38] Frandsen S T, ‘Turbulence and turbulence-generated structural loading in wind turbine clusters’, *Riso National Laboratory Report, Riso-R-1188(EN)*, 2007.

[39] Akpinar EK, Akpinar S, ‘An Assessment on Seasonal Analysis of Wind Energy Characteristics and Wind Turbine Characteristics’, *Energy Conversion and Management*, 2005, pp. 1848-1867.

[40] Celik AN, ‘A Statistical Analysis of Wind Power Density Based on the Weibull and Rayleigh Models at the Southern Region of Turkey’, *Renewable Energy*, 2003, pp. 593-604.

[41] Liu J, Jiang Y, ‘A Statistical Analysis of Wind Power Density Based on the Weibull Models for Fujian Province in China’, *IEEE*, 2009.

[42] Li QS, Zhi L, Hu F, ‘Boundary Layer Wind Structure from Observations on a 325m Tower’, *Journal of Wind Engineering and Industrial Aerodynamics*, 2010, pp. 818-832.

[43] Morrissey ML, Cook WE, ‘An Improved Method for Estimating the Wind Power Density Distribution Function’, *Journal of Atmospheric and Oceanic Technology*, 2010, Volume 27, pp. 1153-1164.

VITA

VITA

EDUCATION

Purdue University, West Lafayette

Doctor of Philosophy, Mechanical Engineering 2009—2013
Master of Science Mechanical Engineering 2007—2009
Bachelor of Science Mechanical Engineering 2003—2007

ENGINEERING SKILLS

Experimental

- Six years combined research at the Aerodynamic Interaction Research laboratory
- Designed and operated the Purdue Wind Turbine Testing Facility wind tunnel and generator platform for novel design verification
- Designed and tested the Purdue Micro Reconfigurable Wind Farm
- Gained experience with Experimental Fluid Mechanics and Structural Dynamics
- Analyzed the acoustic response of a wind turbine in a wind tunnel

Analytical

- 3.84/4.0 cumulative Graduate GPA, 4.0/4.0 Undergraduate GPA
- Fluid Mechanics Coursework, with Fluid wake models and rotor modeling
- Dynamics and Aeromechanics Coursework, with unsteady aerodynamic analysis
- Acoustics and Aeroacoustics coursework
- Turbomachinery coursework, design and analysis of gas turbines

Computational

- Studied Methods for Computational Aerodynamics with some experience using CFD
- Finite Element Methods for structural dynamics with some experience using Abaqus

PROFESSIONAL ENGINEERING EXPERIENCE

General Electric • Louisville, KY May 2006—August 2006
Engineering Internship on Water Systems & Growth Team

- Simultaneously worked on projects of designing a Faucet Mount Filtration System and developing a test plan and defining failure modes for an Instant Hot Water Dispenser
- Named as Lead Engineer on design patent for Faucet Mount Filtration System
- Improved technical communication skills while demonstrating leadership by taking a lead in weekly conference calls with a Chinese sourcing company to clarify the design

eCo • Purdue University January 2007—May 2007
Team Leader on Senior Design Project

- Led a 7-member team to design/build a high-efficiency vehicle for a competition
- Managed overall team progress and handled communication with companies and advisors

COMPETITIONS

- Semi-Finalist Burton D. Morgan $100,000 Business Plan Competition (2012, 2013)
- One of 20 Global Semi-Finalists Tulane $100,000 Business Plan Competition (2012)

LEADERSHIP/TEACHING

- Involvement in Next Generation Scholars to present graduate research to middle school students
- Led a youth group for five years at Calvary Church including roles of teaching lessons, facilitating discussions, creating vision, and raising up leaders to lead others
- Developed and led a week-long summer camp for 6^{th}-8^{th} graders for two years

RESEARCH EXPERIENCE DESCRIPTION

Purdue Wind Turbine Testing Facility

Objective:

Design and build a facility for testing small wind turbine aerodynamic performance and acoustics

Involvement:

Redesigned an existing wind tunnel for free-jet testing of wind turbines
Measured and characterized the flow properties within the wind tunnel
Designed a wind turbine generator system which decouples rotor rotational speed and wind speed
Selected instrumentation to accurately measure the aerodynamic power produced by the rotor
Tested a manufacturer's 400W wind turbine blades

Skills:

Gained an understanding of experimental fluid mechanic testing practices/standards
Gained extensive experience with data acquisition using LabView and data analysis
Data collection using pressure sensors, velocity probes, microphones, and control motors
Learned the practices of research, worked through problems as they arose, worked independently

Counter-Rotating Wind Turbine

Objective:

Design and test novel rotor designs and turbine configurations to improve efficiency and beat the single rotor maximum theoretical performance limit

Involvement:

Designed an adaptable generator test platform in which a dual rotor, counter-rotating wind turbine configuration will be tested
Designed blades for a dual-rotor stage wind turbine which theoretically performs at a power coefficient greater than the 59.3% Betz Limit

Skills:

Testing modeling theory for counter-rotating wind turbines
Learned practice of quantifying aerodynamic interaction between rotors using a hot-wire thermal anemometry probe

<u>Purdue Micro Reconfigurable Wind Farm</u>

Objective:

- Quantify wind turbine power losses in a wind farm setting derived from aerodynamic interaction with impinging wakes produced by upstream wind turbines

Involvement:

- Complete design of test facility and structures for four small wind turbines on movable carts
- Selection of instrumentation fitting the high demands of both the research needs and size constraints of the 900W wind turbines
- Assembly of test structures and configuration of turbine instrumentation and data acquisition
- Analyzing performance losses and structural dynamic response as a function of array spacing

Skills:

- Gained further experience using different data acquisition and instrumentation hardware and software and their connectivity
- Utilized experimental structural dynamics testing and analysis from data on one wind turbine
- Implemented analytical models to describe wind turbine wakes predicting performance losses and farm performance
- Data collection using torque sensors, encoders, accelerometers, and ultrasonic anemometer

ACADEMIC FOCUS

Fluid Mechanics:

- Graduate courses taken related to fluid mechanics/turbomachinery of *Intermediate Fluid Mechanics*, *Turbulence and Turbulence Modeling, Gas Dynamics*, *Computational Aerodynamics*, & *Fundamentals of Wind Energy*

Structural Dynamics:

- Graduate courses taken related to structural dynamics of *Mechanical Vibrations*, *Turbomachinery II* (Aeromechanics), *Experimental Structural Mechanics*, & *Finite Element Methods in Aero Structures*

Acoustics:

- Graduate courses taken related to acoustics of *Engineering Acoustics*, & *Aeroacoustics*

TEACHING/LEADERSHIP EXPERIENCE

Technical:

- Graduate Mentor for Undergraduate Research Fellow (Summer 2008, Fall 2008, Summer 2009, Summer 2012)
- Lectured in ME514 – Fundamentals of Wind Energy, and CS490 – Software for Embedded Systems
- Developed a Course Project and Assessed student performance for ME514 – Fundamentals of Wind Energy

Developed a course project and worked with student teams for MET317 – Machine Diagnostics

SERVICE ACTIVITIES

Membership in Purdue Habitat for Humanity Club; have taken construction trips to New Orleans, LA and Beaumont, TX
Participation in Purdue Winterization Service Day (2010, 2011, 2012)

HONORS/AWARDS

Wesley A. Wood Harrison Hall Scholarship	2006—2007
Lubrizol Foundation Mechanical Engineering Scholarship	2006—2007
Grant H. Arrasmith Graduate Fellow	2007—2008
GAANN Graduate Fellow, U.S. Dept. of Education	2013

PUBLICATIONS

Ennis, B. and Fleeter, S., “Variability of Wind Speed and its Effect on Wind Turbine Performance in Northern Indiana,” 2013, submitted for publication.

Ennis, B. and Fleeter, S., “Wind Turbine Performance Losses in Array Operation as a Function of Turbine Spacing and Upstream Wake Number,” 2014, submitted for publication.